Magnetic Nozzles

Experimental characterisation of the plume expansion in the magnetic nozzle of a helicon plasma thruster

by

M. Wijnen

to obtain the degree of Master of Science
at the Delft University of Technology,
to be defended publicly on Tuesday May 9, 2017 at 11:00 AM.

Student number:	4390261	
Project duration:	June 1, 2016 – May 9, 2017	
Thesis committee:	ir. B. T. C. Zandbergen,	TU Delft, supervisor
	dr. A. Cervone	TU Delft
	prof. dr. R.J.E. Jaspers	TU Eindhoven
	dr. M. Merino Martinez,	UC3M, advisor

TU Delft

Abstract

This thesis is concerned with characterising the plume expansion in the magnetic nozzle of a helicon thruster. The investigation took place in the context of the new electric propulsion laboratory of the Space Propulsion & Plasmas Group (EP^2) of University Carlos III of Madrid (UC3M) and the test-campaign of the helicon plasma thruster HPT05 prototype that is a joint project of SENER and EP^2. The magnetic nozzle is a new plasma acceleration concept that can be used on several different electric thrusters. The helicon plasma thruster is a new type of electric thruster that aims to achieve high thrust density by using a helicon plasma source. The focus of this work is threefold: development, testing and application of electrostatic probe diagnostics for the EP^2 lab; characterising the plume expansion and comparison to DiMagNo (magnetic nozzle model) simulations. Some figures of merit about the helicon thruster performance are estimated along the way.

The diagnostics used in this thesis are simple and RF-compensated Langmuir probes, Faraday probes and emissive probes. Langmuir probe measurements were found useful for inferring the plasma density and providing the electron temperature which were found to be of the order of 10^{16}-10^{18} m^{-3} and 3-5 eV respectively. RF-compensated probes could not be verified correctly as in the low plasma densities of $n < 10^{18} m^{-3}$ one of main assumptions, $\omega_{pi} \gg \omega_{rf}$ was not valid. The emissive probe was operated in the *floating potential in the limit of large emission* method providing a fast and precise means to measure the plasma density. A Faraday probe was used to measure the ion current density. All probes are mounted on a three degrees of freedom (3-DOF) positioning system to provide spatially resolved measurements of the corresponding plasma parameters.

The plume expansion was found to be independent of the the RF-power in both radial and axial dimension; the shape of the plume is therefore mainly determined by the shape of the magnetic nozzle. Observed radial asymmetries in plasma potential and electron temperature are attributed to the shape of the antenna. The downstream evolution of the electron temperature showed signs of polytropic cooling with $\gamma_e = 1.10 \pm 0.05$ at 500 W operation while at higher power (>650 W) the observed behaviour was isothermal. The plume divergence half angle was found to remain constant downstream (>120 mm) indicating ion detachment from the magnetic fields lines. This was further corroborated by the downstream increase of the ratio of ion to magnetic flux. The presence of the magnetic nozzle significantly improved the plume divergence, decreasing the divergence half-angle with 7°.

The axial evolution of measured plasma parameters in the plume were compared to the DiMagNo simulation for the nominal (500 W) case, which showed overall good agreement of ion Mach number, plasma potential, ion current density and plasma density[1]. Including the polytropic model for electron thermodynamics into DiMagNo was necessary to achieve agreement between simulation and measurement of the ion Mach number. Results were also compared to results from similar thrusters found in literature and good agreement was found particularly with Takahashi [80] and Little [49, 50].

This work helped develop the diagnostic capabilities of the EP^2 electric propulsion lab and paved the way for future experiments on magnetic nozzles and validation of the DiMagNo code.

---

[1] As inferred from combined emissive and Faraday probe measurements

Preface

This thesis project is the proverbial crowning glory of a two year master track in space engineering at the faculty of Aerospace Engineering of the Delft University of Technology. The thesis project provides the opportunity to carry out an in-depth investigation in a particular area of interest and to make a substantive contribution to knowledge in that area. My area of interest is the intersection of the fields of plasma physics which I came to love during my BSc degree applied physics at the Eindhoven University of Technology, with the field of space exploration which has enticed me since a very young age. The particular intersection of these two fields to which I am referring is the field of electric propulsion.

The topic of this thesis is the magnetic nozzle concept that is a plasma acceleration device that can be added to many different plasma thrusters. The work for this thesis has been done in the context of the new electric propulsion facility of the electric propulsion and plasma (EP^2) research group of the University Carlos III of Madrid. The particular magnetic nozzle studied in this thesis is part of a experimental prototype of a helicon plasma thruster developed by SENER and EP^2. In this work the plume expansion in this magnetic nozzle has been characterised using spatially resolved electrostatic probes measurements. The plume was characterised in terms of the plasma density, electron temperature, plasma potential and ion current density which are used to infer secondary parameters such as the ion Mach number as well figures of merit such as the thrust efficiency.

In this work it will be shown that the magnetic nozzle determines the shape of the plasma and that the magnetic nozzle greatly affects the plume divergence. Furthermore good agreement is found between measurements and DiMagNo model simulations of the axial evolution of the aforementioned parameters. Other achievements of this thesis include development and testing of the electrostatic probe diagnostics and preliminary characterisation of the thruster performance.

I will also like to use this opportunity to thank the various people directly or indirectly involved in this work. First of all I would like to thank the committee members for taking the time to review this work, especially Dr. Roger Jaspers who has found the time to come all the way from Eindhoven to attend the defence. Furthermore I would like to thank the EP^2 group for providing their experimental facility and SENER for providing the HPT05 prototype. Then I would like to thank my thesis supervisor Barry Zandbergen of TU Delft for his advise and constructive criticism on the report and my supervisor dr. Mario Merino of UC3M for proofreading the report and making available the DiMagNo code. I would also like to thank the rest of the EP^2 group in particular dr. Jaume Navarro with which I spent many hours in the lab, dr. Pablo Fajardo, both for his help in the lab and for helping me navigate the administrative swamp of the PhD application, and lastly dr. Xin Chen for the many extensive discussions on probe theory. Mercedes Ruiz from SENER also deserves to be mentioned for her many helpful comments on the report.

Most importantly, I would like to thank my family, especially my parents, Han and Marina To them I would like to say: I am who I am because of you. Without your support I would not have not made it this far let alone been able to live a year abroad. And lastly I would like to thank Tania for her love and support, you brighten my day, everyday.

Lastly I am proud to announce that I am given the opportunity to continue this work as a PhD-candidate at UC3M.

M. Wijnen
Madrid, April 7

Contents

Acronyms

Numbers

3-DOF three degrees of freedom.

A

ABR Allen-Boyd-Reynolds.

B

BRL Bernstein-Rabinowitz-Laframboise.

C

CEX charge exchange.
CoTS commercial off-the-shelf.

D

DL double-layer.

E

ECRT electron-cyclotron resonance thruster.
EEDF electron energy distribution function.
EP electric propulsion.
EP^2 Space Propulsion & Plasmas Group.
ESA European Space Agency.

H

HDLT Helicon Double-Layer Thruster.
HET Hall-effect thruster.
HPHT High-Power Helicon Thruster.
HPT helicon plasma thruster.

I

ICRH ion cyclotron resonance heating.
IPPS iterative post-processing scheme.
I_{sp} specific impulse.

L

LCA local current ambipolarity.
LHS left hand side.
LP Langmuir probe.

M

mHTX mini-Helicon Thruster Experiment.
MN magnetic nozzle.
MPDT magneto-plasma-dynamic thruster.

N

NEP nuclear-electric propulsion.

O

OES optical emission spectroscopy.
OML orbital motion limited.

P

PM-HPT Permanent Magnet Helicon Plasma Thruster.
PPT pulsed plasma thruster.
PPU power processing unit.

R

RF radio-frequency.
RFCLP RF-compensated Langmuir probe.
RHS right hand side.
RPA retarding potential analyser.

S

SEP solar-electric propulsion.

T

TG Trivelpiece-Gould.
TLR technological readiness level.

U

UC3M University Carlos III of Madrid.

V

VASIMR VAriable Specific Impulse Magnetoplasma Rocket.

Notation

A

A Area [m^2].
a Langmuir probe radius.

B

$\mathbf{B}$ magnetic field (vector) [G].
β total wave vector.
β_0 ratio between plasma and magnetic pressure.

C

c_s ion acoustic speed [m/s].
C_{sh} sheath capacitance [F].

D

δ (momentum weighted) divergence half-angle [°].
$\delta_{0.95}$ 95% (mass cone) divergence half-angle.
Δv velocity increment [m/s].

E

$\mathbf{E}$ electric field (vector) [V/m].
e elementary charge: $1.60217662 \cdot 10^{-19}$ [C].
ϵ_0 vacuum permittivity: $8.854187817 \cdot 10^{-12}$ [F/m].
ε_e error in Langmuir probe ion current fit.
ε_i error in Langmuir probe ion current fit.
ϵ_{ion} ionisation loss factor.
ϵ_{wall} wall loss factor.
η (global) efficiency.
η_{ch} chamber efficiency.
η_{con} conversion efficiency.
η_{div} divergence efficiency.
η_i internal efficiency.

F

F force, thrust [N].
F_{ch} chamber thrust [N].
F_e electric force [N].
F_m magnetic force [N].
F_p pressure force [N].
F_z axial force.
ϕ plasma potential [V].
ϕ_e electron plasma potential.
ϕ_i ion plasma potential.
Φ_w work function [eV].

G

g_0 standard gravity [m/s^2].
γ_e polytropic coefficient for electrons.
G_e ratio of electron to magnetic flux.

H

H_e electron Bernoulli function.

I

I current [A].
i normalized current.
I_e electron current.
I_{em} emission current.
I_i ion current.
$I_{i,th}$ theoretical ion current.
I_{sp} specific impulse [s].

J

J angular momentum.
$\mathbf{j}$ current density (vector) [Am/^{2}].
j_r randomised ion current per unit density.
j_z axial ion current density [A/m].

K

k wave vector.
$k_\perp$ perpendicular wave vector.
k_z axial wave vector.
κ_F nozzle expansion factor for thrust.
κ_P nozzle expansion factor for power.

L

λ_c collisional mean free path [m].
λ_D Debye-length [m].
ℓ_e electron Larmor radius [m].
ℓ_i ion Larmor radius [m].
L_n magnetic nozzle length.

M

M ion Mach number.
$\dot{m}$ mass flow rate [sccm,mg/s].
m_d dry mass [kg].
m_e electron mass [amu].
m_i ion mass [amu].
$\overline{\overline{\mathbf{M}}}$ momentum flux (tensor).
m_p propellant mass [kg].
μ_0 vacuum permeability: $4\pi \cdot 10^{-7}$ [N/A^2].

N

n plasma number density [m^{-3}].
n_i ion number density [m^{-3}].
n_e electron number density [m^{-3}].
ν collisional frequency [s^{-1}].

O

ω angular frequency [rad/s].
Ω_i electron cyclotron frequency [rad/s].
Ω_i ion cyclotron frequency [rad/s].
ω_{lh} lower hybrid frequency [rad/s].
ω_{pe} electron plasma frequency [rad/s].
ω_{pi} ion plasma frequency [rad/s].
ω_{rf} RF driving frequency [rad/s].

P

P_T total power [W].
P_b beam power [W].
P_e power deposited on electrons [W].
P_i power deposited on ions [W].
P_{zi} axial ion power [W].
ψ magnetic stream function.
ψ_i ion stream function.

R

R radius [m].
r radial coordinate.
R_A RFCLP area ratio.
R_{sh} sheath resistance [Ω].
R_V radius of plasma-vacuum edge [m].

T

T_w emissive probe wire temperature.
T_e electron temperature [eV].
θ azimuthal coordinate; angle.
T_i ion temperature [eV].

U

$\mathbf{u}_e$ electron velocity (vector).
$\mathbf{u}_i$ ion velocity (vector).

V

V bias potential [V].
v_{ex} exhaust velocity [m/s].
V_{rf} plasma potential oscillations due to RF.
V_s space potential (see ϕ).

X

ξ probe parameter.

Z

z axial coordinate.
Z_{ck} RF choke impedance [Ω].
ζ non-dimensionalised plasma potential.
Z_{sh} sheath impedance [Ω].

Figures

Tables

1

Introduction

1.1. General

The past years the space industry has experienced a boom. Private space companies are on the rise, culminating with SpaceX as the first private company to reach orbit. While recently the Luxembourg government announced to develop a legal framework for the commercial exploitation of space resources. Commercial use of space is expanding with the increase in satellite augmented services used in many modern consumer electronics, satellite communication for commercial aviation, commercial satellite based imaging services and high throughput satellite communication. The scientific need for space flight is as strong as ever with recent successes such as the New Horizons, Rosetta and Juno missions. The space industry like any (commercial) enterprise is cost-driven and any innovation that leads to cost-reduction will be pursued. One of the main expenses of any space mission are the launch costs which depend on the target orbit and the payload mass. Mass reduction therefore equals cost reduction. This need for mass reduction has resulted in two trends, miniaturisation which aims to reduce the structural mass of the payload and high specific impulse (I_{sp}) propulsion to reduce the propellant mass. Electric propulsion (EP) is the field that emerged to provide high I_{sp} propulsion. Many technologies have been developed with varying technological readiness level (TLR), ranging from fundamental research to proven flight heritage. HPTs and magnetic nozzles (MNs) are two such technologies at the low end of the TLR scale.

1.2. Background

This section provides a general introduction to the the field of EP and introduces the helicon plasma thruster and magnetic nozzle concepts.

1.2.1. Rocket propulsion

Chemical rocket propulsion is based on the thermodynamic expansion of the propellant. The internal energies of the propellant are converted to the directional kinetic energy of the exhaust flow and thrust is produced by the gas pressure on the surfaces in contact with the hot propellant gas. Chemical rocket propulsion is powered by the combustion of fuel and oxidiser which leads to intense temperatures and pressures which cause the gas to rapidly expand along a nozzle. [77, p.4] The relationship between thrust, mass flow rate and exhaust velocity is given by:

$$F = \dot{m} v_{ex} + A_{ex}(p_{ex} - p_a) \tag{1.1}$$

The second term on the right hand side (RHS) is due to the difference between the pressure on the outer surface, p_{ex} and the ambient pressure p_a working on the exhaust area A_{ex}. (However this term is of minor importance for EP and will be neglected.) From this equation it is immediately apparent that for the same thrust level an increase in exhaust velocity leads to a decrease in mass flow rate. Noting that I_{sp} is defined as the exhaust velocity divided by the standard gravity g_0:

$$I_{sp} = \frac{v_{ex}}{g_0} \tag{1.2}$$

it is clear why I_{sp} is a figure of merit. This can also be seen from Tsiolkovsky's rocket equation:

$$\Delta v = I_{sp} g_0 \ln\left(1 + \frac{m_p}{m_d}\right) \tag{1.3}$$

which is linear in the I_{sp}. For a given mission with a specified Δv and dry mass m_d increasing the I_{sp} reduces the propellant mass m_p. It also shows that for deep space missions the very high Δv requirement can only be met by high I_{sp} thrusters.

1.2.2. Electric propulsion

In EP the energy imparted to the propellant comes from an outside electrical source rather than intrinsic chemical energy. The ways to do so are myriad and can be by means of electric and magnetic fields, electromagnetic radiation or a combination. However the energy is coupled to the propellant the goal is to generate a high-velocity directional mass flow whose momentum rate of change equals the thrust. Where the exhaust velocity of chemical propulsion is limited by the intrinsic energy, generally up to 4 km/s (400 s I_{sp}) [40] EP does not have this limitation. Instead electric thrusters are limited by the amount of electric power available and the power-to-weight ratio of their power source. The kinetic power in the thruster exhaust, the beam power is given by:

$$P_b = \frac{1}{2}\dot{m}v_{ex}^2 = \frac{F^2}{2\dot{m}} \tag{1.4}$$

Due to losses the beam power is never equal to the total available power. The ratio between beam power and the total power is the global efficiency η which is another important figure of merit for an electric thruster. Combining equations 1.1 (while ignoring the pressure contribution) and 1.4 yields the following equation for the efficiency:

$$\eta = \frac{F^2}{2\dot{m}P_T} = \frac{\dot{m}I_{sp}g_0F}{2P_T} \tag{1.5}$$

For a given I_{sp} and efficiency the thrust is limited by the available electric power. To summarise: chemical propulsion is energy limited and therefore high thrust, low I_{sp} propulsion while electric propulsion is power limited and thus produces low thrust at high I_{sp}.

Current power sources for electric propulsion are usually solar arrays and this concept is referred to as solar-electric propulsion (SEP). It is evident this is power source is limited by the efficiency, the weight and surface of the solar panels and the distance to the sun. Nuclear-electric propulsion (NEP) has been proposed but so far only exists on paper.

1.2.3. Electric thruster types

Many varieties of electric thrusters exist today and there are several ways to categorise them. A primary distinction is the way the propellant is accelerated which is either due to electrothermal, electrostatic or electromagnetic interaction.

- Electrothermal thrusters use electric currents or plasma to heat up a propellant which then expands in a conventional nozzle. In principle the acceleration is due to thermal expansion, however the energy is provided from an electric source. Examples are the resistojet and the arcjet.

- In electrostatic thrusters the propellant is accelerated by the Coulomb force using electrostatic fields. Several different concepts have been developed for this type of thruster, most importantly gridded ion thrusters, Hall-effect thruster (HET) and electrospray thrusters.

- Electromagnetic thrusters work via the Lorentz force or otherwise employ (electro-)magnetic fields to accelerate the propellant. Examples of electromagnetic thrusters are the magneto-plasma-dynamic thruster (MPDT) and the pulsed plasma thruster (PPT) as well as the VAriable Specific Impulse Magneto-plasma Rocket (VASIMR). Although the HPT uses RF-waves to ionise and heat the plasma, the acceleration mechanism is electrothermal in nature as will become evident later in this report.

Table 1.1: Typical performance data for various types of thrusters. From ref.[54]

Thruster type	specific impulse (I_{sp}) [s]	Thrust [N]	Power [kW]	Efficiency [%]
Chemical				
Cold gas	50	$0.1 - 100$	0.05	N/A
Solid	250	10^7	10^8	N/A
Liquid	$300 - 400$	10^6	10^7	N/A
Electrothermal				
Resistojet	$100 - 300$	0.2	$0.1 - 1$	> 50
Arcjet	500	0.1	1	30
Electrostatic				
Gridded ion engine	3000	$10^{-3} - 0.1$	$0.1 - 5$	> 70
Hall-effect thruster	1500	$10^{-2} - 1$	$0.2 - 20$	$50 - 60$
Electrospray [a]	$1150 - 3200$	$20 - 100 \cdot 10^{-6}$	$0.5 - 1.5 \cdot 10^-3$	$50 - 65$
Electromagnetic				
MPD thruster	$100 - 10000$	$0.5 - 50$	$100 - 10^3$	40
Ablative PPT	$500 - 1500$	$10^{-5} - 10^{-2}$	0.01	< 10
VASIMR[b]	5000	6.3	215	72

[a] Added from refs. [45][32]
[b] Added from ref. [9]

Both the electrostatic and electromagnetic thrusters need an electrically charged propellant for the electromagnetic fields to interact with. Therefore all thrusters except the Electrospray thruster ionise their propellant at some stage of the process; Electrospray thrusters extract single ions from ionic liquids or liquid metals. Apart from the acceleration mechanism the thrusters also differ widely in performance as shown in table 1.1.

1.2.4. Helicon plasma thrusters

The helicon thruster is a new type of thruster that is based on a helicon plasma source. Helicon plasmas have been studied by the plasma physics community for half a century. Its application to space propulsion can be credited to Boswell and Charles who in 2003 patented a plasma beam generator that used helicon waves and would provide a reactive propulsive thrust. [12] Their prototype was named the Helicon Double-Layer Thruster (HDLT) named after the double-layer structure then thought to be the responsible thrust mechanism. [18]

Helicon plasmas rely on helicon waves for plasma generation. These waves can be excited in an axially magnetised plasma column by a helically shaped RF-driven antenna in the MHz range. When propagating along the column the helicon wave energy is transferred to the plasma electrons by collisional and collision-less processes. Helicon plasmas have generally high densities up to 10^{20} m^{-3}. A high plasma density translates to a high thrust density allowing for more compact thrusters.

A helicon thruster consists of a cylindrical dielectric chamber, enclosed at one side by an injector plate. Wound around the chamber is a (half-helical) antenna. The thruster further incorporates (electro)magnets to produce an axial magnetic field and possibly a magnetic nozzle.

Clearly the thruster consists of very few parts it therefore excels in simplicity. Furthermore the lack of moving parts, neutralisers and electrodes give the helicon thruster a long lifetime. The thruster can also operate with a wide variety of propellants and can be throttled to provide adjustable levels of thrust. Lastly it is expected that the helicon thrusters can be easily scaled up to higher powers on the order of 10's of kW's.

Due to its inherent high plasma density and corresponding high thrust density it could prove to be a potentially compact thruster. With added benefits of robustness (i.e. long life-time), simplicity, flexibility of propellant and throttle-ability, provided the HPT can reach performance levels of current thrusters, it can become a competitive new technology in the space propulsion market. Helicon thrusters is covered in more detail in chapter 2.

1.2.5. Magnetic nozzles

The helicon thruster incorporates a magnetic nozzle, a feature also employed in other thrusters like the MPDT and the VASIMR. A MN is basically a convergence-divergence of the otherwise axial magnetic field. The section of the MN where the magnetic field peaks is regarded as the throat of the thruster. Here the plasma ion velocity here reaches a sonic point, similar to conventional nozzles. [5] In the MN of a HPT electron thermal energy is converted into ion kinetic energy thereby increasing the thrust. [1] Magnetic nozzles are covered in more detail in chapter 3.

1.3. Motivation

The magnetic nozzle concept is a plasma acceleration device that can be applied to many different electric thrusters such as the HPT, VASIMR, electron-cyclotron resonance thruster (ECRT) and MPDT. It is able to increase thrust and could even be used to provide non-mechanical thrust vector control (using a 3D magnetic nozzle [58]). For this reason the magnetic nozzle concept is worth studying independently and is the main object of study for this thesis. The performance of the helicon plasma thruster prototype that functions as the plasma source is studied concurrently.

The EP^2 group recently founded a new electric propulsion test facility that expands their experimental capabilities in the field of EP. Furthermore they have developed a helicon thruster prototype in cooperation with SENER. The new experimental facility and the prototype create a need for several new activities. Firstly the brand new test facility has to be outfitted with new plasma diagnostics that have to be developed and tested. Secondly, using these diagnostics, the plume expansion in the magnetic nozzle of the HPT prototype has to be characterised. And lastly the performance of the HPT prototype has to be characterised.

The experimental work in the new electric propulsion lab is complement to EP^{2}s recent numerical work on MNs and HPTs consisting of a 2D-model for the plasma plume expansion in a magnetic nozzle as well as a fluid model describing the plasma inside a helicon thruster.[1, 3] Characterisation of the plume expansion paves the way for validating the magnetic nozzle model.

1.4. Objectives

The objectives of this thesis are fourfold, in order of decreasing priority: develop, test and implement electrostatic probe diagnostics, characterise the plume expansion in the magnetic nozzle, characterise the helicon plasma thruster and explore the validation of the magnetic nozzle model.

In the literature study preceding this thesis several diagnostics have been identified for use in this work: Langmuir probes, RF-compensated Langmuir probes, Faraday probes and Emissive probes. It also discussed the effects of flow, magnetic fields and RF-fluctuations. which are inherent to the complex plasma of a HPT, influence the probe measurements and how they can be mitigated. This thesis is in part be devoted to design, manufacture and characterisation of the probes. Based on this literature study and prior experience in the lab, research questions have been developed that further detail the objectives and form a guideline for this research.

1.4.1. Research questions

To guide the investigation a set of research questions has been formulated. The main questions are reflective of the objective stated in the previous section. Most questions are divided into sub-questions whose answers together help to answer the main questions.

1 How adequate are the different electrostatic probes for characterising the magnetic nozzle?
  1.1 Can the Langmuir probe be used to accurately measure n, T_e, ϕ in the MN?
    1.1.1 Can the iterative parametrisation of BRL theory be successfully applied?
    1.1.2 Does it produce accurate results?
    1.1.3 Is it an improvement on existing methods (planar approximation)?
    1.1.4 What is the measurement uncertainty?
  1.2 Does the RF-compensated Langmuir probe improve on the simple Langmuir probe?
    1.2.1 Can the it accurately measure n, T_e, ϕ in the MN?
    1.2.2 How does it compare to the simple Langmuir probe?
    1.2.3 Does it mitigate the RF-fluctuations?
  1.3 Can the emissive probe accurately measure ϕ in the MN?

        - 1.3.1 Does is it improve on the simple Langmuir probe?
        - 1.3.2 What probe temperature can be reached?
        - 1.3.3 Can the probe be operated with the floating potential method?
        - 1.3.4 What is the measurement uncertainty
    - 1.4 Can the Faraday probe accurately measure the ion current density?
        - 1.4.1 What is the measurement uncertainty
        - 1.4.2 Can the divergence angle be calculated?
        - 1.4.3 Can the total current be calculated?
    - 1.5 Can propulsive figures of merit be inferred?
        - 1.5.1 Does combining Langmuir and Faraday probe measurements accurately yield the ion velocity and the thrust?

2 What are the plasma properties in the plume expansion?
    - 2.1 In terms of plasma parameters?
        - 2.1.1 What is the axial evolution of n, T_e, ϕ?
        - 2.1.2 What is the radial evolution of n, T_e, ϕ?
        - 2.1.3 What is the effect of the RF power?
        - 2.1.4 Are there signs of electron cooling?
        - 2.1.5 How does the ion Mach number develop downstream?
    - 2.2 What is the plume divergence?
        - 2.2.1 How does it develop downstream?
        - 2.2.2 Do ions detach from the magnetic field lines?
        - 2.2.3 What is the effect of the RF power?
        - 2.2.4 What is the effect of the magnetic nozzle?

3 What is the HPT05 prototype performance that can be inferred from the plume?
    - 3.1 What is the global efficiency?
        - 3.1.1 What is the thrust?
    - 3.2 What is the utilisation efficiency?
        - 3.2.1 How is it affected by the RF power?

4 Can the DiMagNo model be validated with electrostatic probe diagnostics?
    - 4.1 What quantities can be compared?
    - 4.2 How do measurement and simulation compare?
    - 4.3 What are the requirements for a rigorous validation experiment?

5 How can the EP^2 electric propulsion lab be improved?
    - 5.1 How can the diagnostic capabilities be improved?
    - 5.2 What are the limitations of the current diagnostic setup?
    - 5.3 What additional diagnostics are needed?
    - 5.4 How can the magnetic nozzle be improved?
    - 5.5 How can the HPT05 prototype be improved?

1.4.2. Limitations

Like any study this research obviously has its limitations. Firstly the diagnostic setup has been limited to four particular electrostatic probes and some auxiliary optical emission spectroscopy. This limits the diagnostic capabilities but should nonetheless yield enough novel information about the MN and the HPT05 prototype. Secondly the HPT05 is an experimental prototype and produces a poorly known plasma. Without any other validated plasma source this means that the probe diagnostics cannot be properly validated but only cross-compared to check for consistency. This means that for at least some quantities only relative results can be trusted. However for characterising trends in the plume as well as for comparison to the magnetic nozzle model simulations, which are normalised, this is sufficient. Then there is the indirect nature of the estimation of the thruster's figures of merit. Direct thrust measurements require a thrust stand or at least a momentum flux sensor [81]. Neither of these tools are available at the UC3M propulsion laboratory. Instead the ion velocity is inferred from the combined ion current and plasma density measurements. This can only provide a rough order of magnitude (ROM) estimate.

Despite these limitations this thesis provides many insights into the properties of the plume expansion and the thruster performance.

1.5. Report outline

The report consists of four parts: theory, methodology, results and conclusion. These four parts are further divide i

- The report starts of with three chapters on theory.
    - Chapter 2, *Helicon Plasma Thrusters* covers the helicon thruster in more detail including a section on the physics of helicon waves.
    - Chapter 3, *Magnetic Nozzles* briefly explains the theory behind magnetic nozzles, introduce the 2D magnetic nozzle model of EP^2 and its implementation, the DiMagNo code. It also sheds some light on the expected performance based on the model.
    - Chapter 4, *Probe Diagnostics*, introduces the various diagnostics, the theory behind them and the particular designs used in this study.
- The following two chapters are concerned with the methodology.
    - Chapter 5, *Experimental Setup*, introduces the thruster prototype, its specifics and the nominal configuration as well as the probe positioning system and the measurement equipment used in each diagnostic setup.
    - Chapter 6, *Operational and Measurement Procedures*, presents the test plans for the experiments, as well as documents other procedures used in the experiments.
- The next four chapters present and discuss the experimental results.
    - Chapter 7, *Characterisation of Probe Diagnostics*, deals with the characterisation of the (RF-compensated) Langmuir and Emissive probes.
    - Chapter 8, *Plasma Parameters in the near-Plume*, is the first chapter that looks in detail at the structure of the plume. It discusses the axial and radial evolution of n, T_e, ϕ in the near plume region.
    - Chapter 9, *Characterisation of Propulsive Properties*, looks at the figures of merit of the magnetic nozzle, such as divergence, utilisation efficiency and thrust inferred mainly from Faraday probe measurements.
    - Chapter 10, *Comparison with Rheory and Literature*, compares the results of the HPT05 with those of similar thrusters found in literature. It also compares the downstream evolution of measured and simulated plasma quantities for the nominal configuration.
- The report ends with a concluding chapter.
    - Chapter 11, *Conclusions & Recommendations*, summarises the conclusions that can be drawn from the results of this work and presents the recommendations for future work.

Unfortunately optical diagnostics, which were originally to be included in this work did not yield sufficient results to warrant a full chapter in this report and have been included in the appendix. The appendix furthermore includes a list of addenda to this report, some example raw data files, a list of the raw data files, extra images and the abstracts to two conference papers to which this work has contributed.

2

Helicon Plasma Thrusters

Introduction

This chapter provides additional information on helicon plasma thrusters, the current state of the art and the physics of helicon waves The helicon plasma thruster is an emerging technology in the field of electric propulsion. Although helicon plasma sources have existed since the 60's, it wasn't until 2003 that they entered the field of electric propulsion in 2003 when Boswell and Charles discovered the formation of current-free double layers in a plasma beam generated by a helicon source [17]. These double-layers (DLs) were thought to accelerate the ions which lead to idea of using it for propulsive means. This materialised with the creation of the HDLT prototype. Later it was shown that the DL actually does not produce a thrust gain as the total momentum over the DL is constant [2, 37]. However, due to their intrinsic high plasma density helicon thrusters remained a topic pursued by several research groups.

Several helicon thruster experiments have been conducted in the recent past working at different power levels, mass flow rates and with widely varying performances. Table 2.1 gives an overview the current state of helicon research. All of experiments used Argon as a propellant and except for the High-Power Helicon Thruster (HPHT) all of them operated at $13.56\ MHz$. Both the mini-Helicon Thruster Experiment (mHTX) and the HPHT research has been halted which is surprising considering the relatively high efficiency of the mHTX. It must be noted that the reported estimates for the HPHT had gross inconsistencies. The reported 55% efficiency contrasts starkly with the 4.7% which can be calculated from the other reported parameters. The HDLT, the first helicon thruster concept, still struggles to reach efficiencies of more than 1%. The data reported for the VASIMR is for operation without the ion cyclotron resonance heating (ICRH) which is therefore representative of the first stage helicon source. Most recent and still on-going work on helicon thrusters is done by the Tohoku university in Japan (the last two entries in table 2.1). Which is among the most 'promising' work, reporting efficiencies the order of several percent. However this is still a far cry from the several tens of percent of existing electric thruster concepts.

Table 2.1: Recent experimental helicon thrusters.

Thruster	P [kW]	F [mN]	$I_{sp}[s]$	η [%]	B [G]	$\dot{m}$ [mg/s]	year	ref.
HPHT[a]	35	4000	2200	4.7	150	7.1	2005	[84]
mHTX	0.50	10	1700	17	2000	0.60	2008	[7]
HDLT	0.65	2.8	280	< 1	138	0.74	2011	[63]
VASIMR	23.5	700	660	9.5	1500	107	2011	[52]
PM-HPT	2	15	2000	7.5	300	0.70	2013	[79]
HPT-x[b]	1	10	1360	6.8	700	0.75	2015	[29]

[a] Operated with a $1\ MHz$ pulsed RF-source.

[b] Thruster was not given a proper name and thus labeled HPT-x.

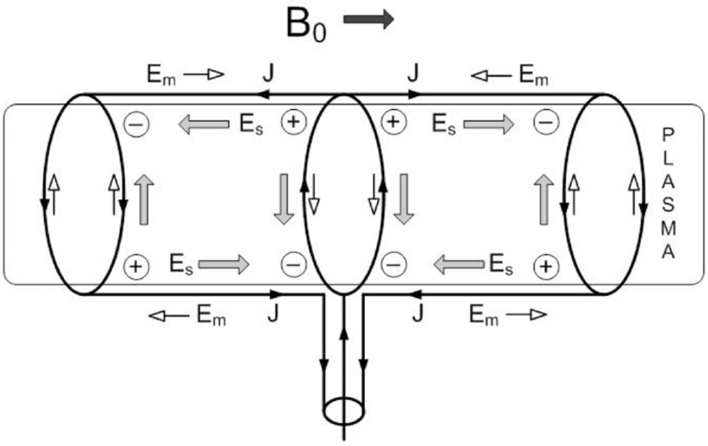

Figure 2.1: EM field pattern of a Nagoya type III antenna [36].

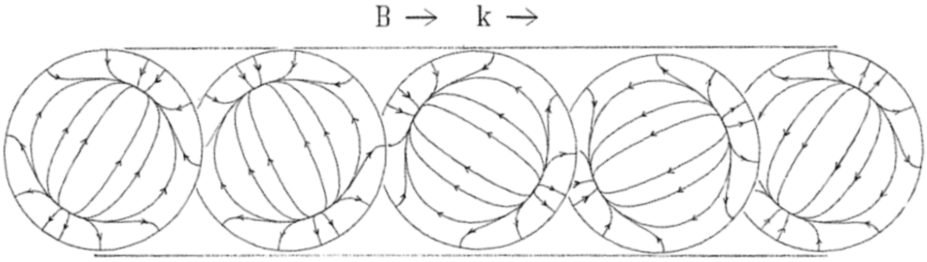

Figure 2.2: Electric field pattern of a $m = +1$ mode helicon wave [22].

Currently the only experimental work on helicon thrusters is being done by the group of Charles and Boswell at the Australian National University and by Takahashi at the Tohoku university in Japan. The university of Michigan also recently got involved in helicon thrusters focusing on miniaturisation for nano-satellites [72]. The EP^2 group of UC3M, until to now having only done numerical work on the topic, has recently started experimental work, which this thesis is part of.

The rest of chapter will be devoted to introduce underlying physics of the helicon thruster, helicon sources and helicon waves, albeit in a condensed form. For a more complete overview of the helicon plasma thruster physics the reader is referred to the literature study that preceded this MSc thesis, in particular chapter 4.

2.1. Helicon sources

Helicon sources are plasma sources that couple RF-power to the plasma by inciting helicon waves. Helicon waves have first been discovered in 1962 [47] and where further investigated into the 70's and 80's. Although their application to plasma processing has been a topic of research, commercialisation of the technology never took off.

A helicon source consists of a dielectric cylinder with an axial magnetic field and an (helically shape) antenna wound around it. (Half-)helical antenna's are basically Nagoya type III antennas that have been twisted to better fit the helicon wave pattern, which is helical in nature. As can be seen in figure 2.1 due to the current J in the wire the electrons in the plasma feel an opposing electric field E_m. Plasma electrons move against the direction of this field resulting in a charge density distribution indicated by the plus and minus signs, until the resulting electric field E_s cancels out E_m. Due to the accumulation of opposing charges on opposite sides of the cylinder, along the antenna there is now a transverse electric field in the plasma. In case of a helical antenna this transverse field matches the helical transverse field of the helicon wave shown in 2.2

Helicon sources have an unusual high plasma density in the order of $10^{18} - 10^{20}$ m^{-3}. Plasma density increases with the amount of coupled RF power as shown in figure 2.3. At low power levels

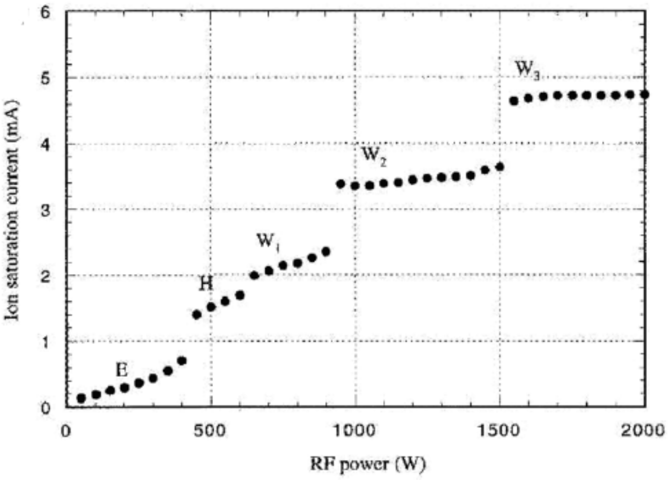

Figure 2.3: Ion current vs. RF power showing mode jumps with increasing power. E: capacitive coupling, H: inductive coupling, W: helicon wave coupling [28].

the antenna is capacitively coupled to the plasma resulting in relatively low densities. With increasing power a mode change occurs and the power is now inductively coupled to the plasma. This mode change is visible as a sudden jump in plasma density in a density vs. power plot. Further increasing the power results in another mode change, also with a corresponding density jump. This occurs when the power is high enough to generate a density matching the helicon conditions (eq. 2.2). The source now operates in helicon mode. Further mode changes can occur to other types of helicon modes.

2.1.1. Helicon waves

Helicon waves are bounded whistler waves that can be excited in a plasma with an axial magnetic field. They occur at frequencies between the lower hybrid and the ion plasma frequency: $\omega_{pi} < \omega < \omega_{lh}$. Consider waves of the form $\exp\left[i\left(m\theta + kz - \omega t\right)\right]$ propagating in a cylindrical plasma with an axial magnetic field $\mathbf{B} = B_0\hat{z}$. The dispersion relation for right-hand (R) electron cyclotron waves at an arbitrary angle θ to $\mathbf{B}$ is given by:

$$\frac{c^2\beta^2}{\omega} = 1 - \frac{\omega_p^2/\omega^2}{1 - (\omega/\Omega_e)\cos\theta} \xrightarrow[\Omega_e \gg \omega]{} \frac{\omega_p^2}{\omega\Omega_e\cos\theta} \tag{2.1}$$

where β is the total wave number such that $\beta^2 = k_z^2 + k_\perp^2$. Noting that $\beta = k_z\cos\theta$ we then end up with the following linear dispersion relation [36]:

$$\beta = \frac{\omega}{k}\frac{\omega_p^2}{\Omega_e c^2} = \frac{\omega}{k}\frac{n_0 e\mu_0}{B_0} \tag{2.2}$$

In a long thin cylinder of radius a, where $ka \ll 1$ the boundary condition is:

$$m\beta J_m(k_\perp a) = 0 \tag{2.3}$$

For the lowest radial mode, $m = +1$ which is the mode most commonly excited in experiments it follows that $J_m = 0$ and $k_\perp a = 3.83$ the first order Bessel root. Since $\beta \approx k_\perp$ in this geometry it follows that:

$$\frac{3.83}{a} = \frac{\omega}{k}\frac{n_0 e\mu_0}{B_0} \propto \frac{\omega}{k}\frac{n_0}{B_0} \tag{2.4}$$

i.e. for a given mode the density should be proportional to B which is confirmed by experiments [36].

When electron inertia is finite a second wave is excited alongside the helicon-wave. This wave is an electrostatic electron cyclotron wave which is highly damped and therefore localised near the boundary of the cylinder. The waves which are referred to as Trivelpiece-Gould (TG) waves are the main ionisation mechanism in helicon sources.

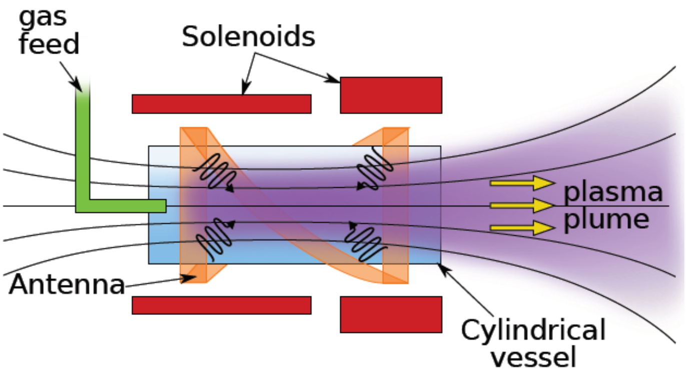

Figure 2.4: Schematic representation of the HPT concept [61].

Combining the equation of motion for electrons and Maxwell's equations, defining $\delta = (\omega + i\nu)/\Omega_e$, with ν the collision frequency and $k_w^2 = \omega n_0 e \mu_0 / B_0$ we can write:

$$\delta \nabla \times \nabla \times \mathbf{B} - k \nabla \times \mathbf{B} + k_w^2 \mathbf{B} = 0 \tag{2.5}$$

Factoring the above equation:

$$(\beta_1 - \nabla\times)(\beta_2 - \nabla\times)\mathbf{B} = 0 \tag{2.6}$$

where $\beta_{1,2}$ are the roots of:

$$\delta\beta^2 - k\beta + k_w^2 = 0 \tag{2.7}$$

For the case $\delta k_w^2 \ll k^2$:

$$\beta_{1,2} = \frac{k}{2\delta}\left[1 \mp \left(1 - \frac{4\delta k_w^2}{k^2}\right)^{\frac{1}{2}}\right] \approx \frac{k}{2\delta}\left[1 \mp \left(1 - \frac{2\delta k_w^2}{k^2}\right)\right] \approx \begin{cases} k_w^2/k \\ k/\delta \end{cases} \tag{2.8}$$

Here the upper solution (minus sign) is the dispersion for the helicon waves from eq. 2.2 while the other solution is for the TG wave.

2.2. Helicon thrusters

The helicon thruster is a space propulsion technology based on a helicon plasma. As such they consist of a dielectric cylinder, radius R, with an axial magnetic field $\mathbf{B} = B_0\hat{z}$ and an (half-helical) antenna wound around the cylinder. The source of the essentially axial magnetic field are either annular permanent magnets or solenoidal electromagnets. In addition to these magnets there is a third (electro-)magnet near the open end of the cylinder. This third magnet squeezes the magnetic field creating a convergent-divergent field that functions as a magnetic nozzle. The other side of the cylinder is closed off except for a gas-feed that provides the propellant and optionally a permanent magnet that creates a magnetic cusp shielding the back-wall. A schematic view of the helicon thruster concept is given in figure 2.4.

The function of the magnetic field is three-fold, it allows for propagation and penetration of EM-waves along/into the plasma, it shields the walls from the plasma preventing losses and the magnetic nozzle configuration provides additional thrust gain. The RF antenna ionises the plasma creating a dense plasma column in the chamber that can only leave the chamber at the open side. Due to the magnetic nozzle configuration the ions reach the sound speed $c_s = \sqrt{T_e/m_i}$ at the throat [5]. Since the RF-power is mostly coupled to the electrons and since electron-ion energy transfer is considerably less efficient than electron-electron transfer: $T_e \gg T_i$. The hot, light electrons tend to be fully magnetised $\ell_e \ll R$ while the colder, heavy ions are weakly magnetised, if at all.

The energetic electrons expand along the magnetic nozzle following the fields lines which sets up an ambipolar field that then accelerates the ions. Electron thermal energy is thus transferred into ion kinetic energy and by this mechanism the thruster could be classified as an electrothermal device

[1]. However the source of thrust is the diamagnetic force between the electrons and the thruster coils due to the electron azimuthal (Hall) current in the plasma. From the viewpoint of forces the HPT is an electro-magnetic device. In a non-uniform plasma this current results from the non-zero radial derivative of the density profile. In a uniform plasma the Hall-current is concentrated in a thin layer near the plasma-vacuum edge and is a surface current rather than a volume current [1].

Summary

This chapter presented an introduction to helicon plasma thrusters, current research and state of the art as well as the underlying physics of helicon waves, plasma sources and the thruster application. Several institutions have pursued research on helicon thrusters and currently the highest reported thrust efficiency is 10% which is insufficient to be a competitive thruster. Helicon plasmas have been in use for a very long time, but the application to space propulsion is relatively recent, mostly studied in the last decade.

The RF field of the antenna can be coupled to the plasma capacitively, inductively or using helicon waves. This last mode results in unusually high plasma densities: $\sim 10^{20}\ m^{-3}$. Helicon waves penetrate deeper into the plasma while accompanying TG-waves efficiently couple energy to the electrons which in turn ionise the neutrals.

In a helicon thruster the hot electrons expand from the source out into the vacuum following the magnetic field lines. This sets up an ambipolar field that in turn accelerates the ions. The thruster is in essence electrothermal, but the thrust is generated by the diamagnetic force of the electrons on the magnets of the thruster.

3

Magnetic Nozzles

Introduction

This chapter introduces the main object of study of this thesis, the magnetic nozzle, in more detail. Magnetic nozzles are in essence a convergence-divergence of the magnetic field of the thruster produced by an additional magnet. This convergence-divergence of the magnetic field has essentially the same effect as a conventional nozzle: it results in a sonic point at the throat (where the magnetic field has it's peak value). The plasma further expands along the divergent part where electron thermal energy is converted into ion kinetic energy, increasing the thrust. The rest of this chapter will discuss the 2D model of the EP^2 group and it's implementation, DiMagNo. It will also discuss the expected performance based on the model and present some generalised model results.

3.1. 2D Magnetic nozzle model

This section presents more in-depth the DiMagNO model and the plasma fluid model describing the expansion of the plume [1]. The magnetic nozzle model propagates a current-free fully ionised plasma jet with radius R that is injected with sonic velocity at the nozzle throat and accelerated supersonically along the nozzle. The assumed length ordering is $\lambda_D \ll \ell_e \ll R_V \ll \lambda_c$ i.e. a collision-less, quasi-neutral plasma with fully magnetised electrons. Furthermore the plasma is assumed current-free and induced fields are assumed to be negligible, $\beta_0 \ll 1$, electrons are isothermal $T_e = \text{const.}$, ion pressure is neglected as $T_i \ll T_e$ and so is electron inertia except for azimuthal motion. Lastly axi-symmetry is assumed $\partial/\partial\theta = 0$.

Under these assumptions the plasma fluid equations can be reduced to three differential equations and one algebraic equation for the ion dynamics and four algebraic equations for the electron dynamics.[1] The differential equations for u_{zi}, u_{ri} and n are:

$$u_{ri}\frac{\partial \ln n}{\partial r} + u_{zi}\frac{\partial \ln n}{\partial z} + \frac{\partial u_{ri}}{\partial r} + \frac{\partial u_{zi}}{\partial z} = -\frac{u_{ri}}{r} \tag{3.1}$$

$$u_{ri}\frac{\partial u_{ri}}{\partial r} + u_{zi}\frac{\partial u_{ri}}{\partial z} + c_s^2\frac{\partial \ln n}{\partial r} = -(u_{\theta e} - u_{\theta i})\Omega_i \cos\alpha + \frac{u_{\theta i}^2}{r} \tag{3.2}$$

$$u_{ri}\frac{\partial u_{zi}}{\partial r} + u_{zi}\frac{\partial u_{zi}}{\partial z} + c_s^2\frac{\partial \ln n}{\partial z} = (u_{\theta e} - u_{\theta i})\Omega_i \sin\alpha \tag{3.3}$$

They have to be coupled to the algebraic equation for $u_{\theta i}$ and $\mathbf{u}_e$. The conservation of the ion angular momentum along an ion stream-tube ψ_i is:

$$D_i(\psi_i) = r m_i u_{\theta i} + e\psi \tag{3.4}$$

The conservation of the electron Bernoulli function H_e along the magnetic streamline ψ and $u_{\theta e}$:

$$H_e(\psi) = T_e \ln n - e\phi \tag{3.5}$$

$$u_{\theta e} = -\frac{r}{e}\frac{dH_e}{d\psi} \tag{3.6}$$

The ratio of electron to magnetic flux along a streamline:

$$G_e(\psi) = nu_{\parallel e}/B \tag{3.7}$$

And lastly the equation defining the parallel part of the electron velocity $\tilde{u}_e$ to be parallel to the magnetic field direction $\hat{b}$:

$$\mathbf{u_e} = u_{\parallel e}\hat{b} \tag{3.8}$$

These eight equations are a closed system that can be solved for the four variables $\mathbf{u}_i, \mathbf{u}_e, n, \phi$ which are non-dimensionalised with T_e, c_s, R, n_0, with $n_0 = n(0,0)$ and $c_s = \sqrt{T_e/m_i}$ the ion sound speed. Solving the algebraic equations is straightforward, however the differential equations are solved with the method of characteristics.

3.1.1. Method of characteristics

The method of characteristics applied to the problem of an expanding plasma in a magnetic nozzle makes use of the fact that expansion of a supersonic fluid is a hyperbolic problem, where the characteristic lines are the Mach-lines. This method is often applied to the expansion in conventional nozzles [85]. Consider a fully hyperbolic set of n partial differential equations (PDE) L_i of n unknowns f_j in two variables x_1, x_2 with the following structure:

$$L_i \equiv v_{ijk}\partial_{x_k}f_j + c_i = 0 \tag{3.9}$$

where $i, j = 1 \ldots n$ and $k = 1, 2$. The coefficients v_{ijk} and c_i can depend on x_1, x_2 and f_j. Any non-trivial combination of the equations in 3.9 is a compatibility solution $\mathcal{L}(\sigma) \equiv \sigma_i L_i$. It is then possible to find n independent vectors that each reduces $\mathcal{L}$ to a one-directional differential operator along the characteristic lines.[31]

$$\sigma_i v_{ijk} = \mu_j \tau_k \quad \text{for: } j = 1 \ldots n, \quad \text{and: } k = 1, 2 \tag{3.10}$$

where τ is a vector tangent to the local direction of the characteristic line associated with that particular σ. Let $(x_1(s), x_2(s))$ be a parametrisation of that line by the parameter s such that:

$$dx_1 = \tau_1 ds; \quad dx_2 = \tau_2 ds \tag{3.11}$$

With the variable s, the compatibility equation of that characteristic can be reduced to:

$$\mu_j \partial_s f_j + \sigma_i c_i = 0 \tag{3.12}$$

which has only derivatives along the direction of s. The resulting n compatibility equations from 3.12 can be propagated along the characteristics to calculate the evolution of the variables f_j in the region of influence of the initial condition [85].

3.1.2. DiMagNo code

The DiMagNo model is implemented in object-oriented modular MATLAB code to be easily reusable and extensible. The code consists of three parts: pre-processing where the plasma characteristics, magnetic field, simulation parameters and initial conditions are defined, simulation where the initial points are propagated and the differential equations integrated to calculate the variables $n, \mathbf{u}_i, \mathbf{u}_e, \phi, c_s$ and post-processing where derived variables are calculated and interactive exploration of the data-set is possible.

When integrating the particular case of the magnetic nozzle there are three characteristics, which slightly complicates the process. The characteristic lines are the Mach-lines $\tau = (u_{zi}\sqrt{M^2-1} \mp u_{ri}, u_{zi} \pm u_{ri}\sqrt{M^2-1})$ and the ion stream lines. To account for all three characteristics the DiMagNo code propagates the Mach-lines of two adjacent grid points on the integration front and defines a new point at their intersection. It then propagates the solution backwards along the ion stream-line to the previous front interpolating the plasma parameter values at the intersection. Making use of the symmetry of the problem the z-axis ($r = 0$) is chosen as the lower boundary while the plasma-vacuum edge ($r = R_V$), defined by the magnetic stream-tube of the top-most initial point is the upper plasma boundary. Only every second integration front has points on the plasma boundary (outer point) and the axis (axis-point) the intermediate fronts without these points are referred to as sub-fronts. Any magnitude A is integrated using $\partial A/\partial s = (A_i - A_f)/\Delta s$.

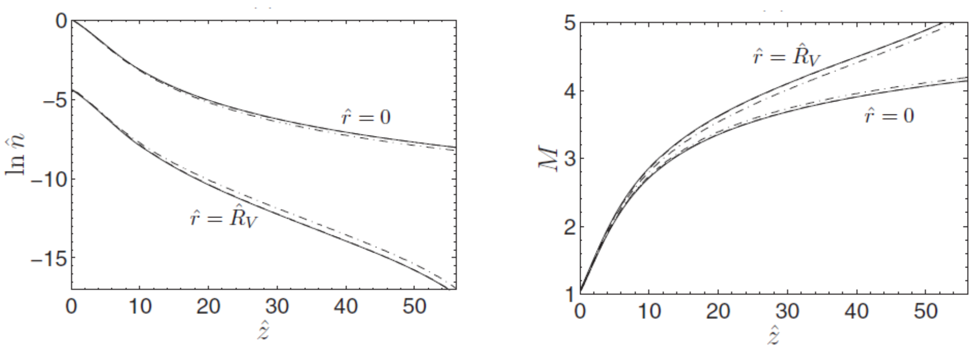

(a) Axial density profile.

(b) Ion velocity profile.

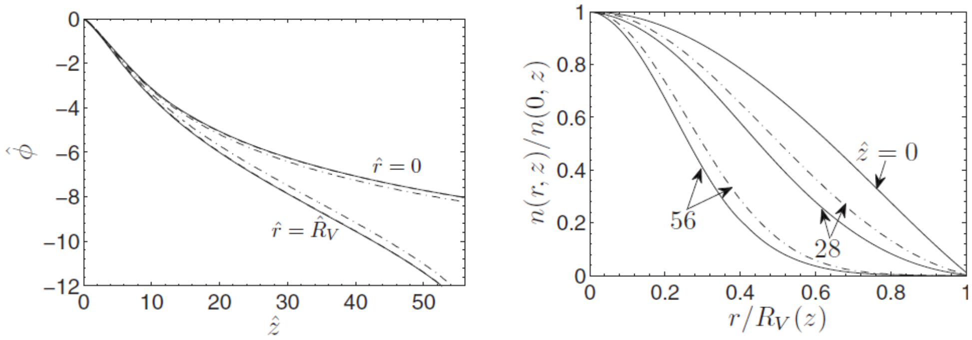

(c) Electric potential profile.

(d) Radial density profile.

Figure 3.1: Axial plasma response of a non-uniform plasma [$\sigma = 0.99$]. Solid, dashed and dashed-dotted lines are for $\hat{\Omega}_{i0} = 0.1, 10, 100$ respectively. From ref. [1]

3.2. Plasma response

Simulations of the DiMagNo code predict the plasma response of the magnetic nozzle. The plasma response is described mainly in terms of the ion Mach number $M = \tilde{u}_i/c_s$, the plasma density n and the electric potential ϕ. But other quantities such as current densities and derived quantities like thrust and power can be calculated too.

Simulations for a plasma that is non-uniform and sonic at the throat and for varying degrees of initial ion magnetisation, quantified by Ω_{i0} show the following behaviour. There is a gentle increase of M which is in agreement with the isothermal model, as opposed to the more rapid acceleration under adiabatic conditions. The down-stream radial non-uniformity for both M and ϕ are mild considering the expansion ratio of 10^3. Ion mass flux tends to concentrate axially downstream which is both beneficial for detachment, divergence and thrust in general. These trends can be observed in figure 3.1.

One of the main improvements over previous theories of this magnetic nozzle model is the relinquishment of the local current ambipolarity (LCA) condition $\mathbf{j} = 0$ in favor of a globally current free condition $\nabla \cdot \mathbf{j}$. This allows the electron and ion streamlines to separate with non-negligible effects on the plasma response. Firstly this allows for the axial concentration of ions favourable to the thrust. Furthermore the radial charge separation results in a radial component of the ambipolar field which applies an $\mathbf{E} \times \mathbf{B}$ drift on the ions resulting in a ion azimuthal current density $j_{\theta i}$. This swirl current has a non-negligible negative contribution to the thrust. Lastly as electron stream-tubes diverge more than ion stream-tubes, while carrying equal total current, their respective current densities deviate creating longitudinal currents into the plasma. The currents are positive on axis while negative along the plume edge to satisfy the global current free condition.

3.3. Propulsive performance

The propulsive performance of a thruster is quantified by the amount of thrust, the thrust efficiency and the specific impulse of the thruster. The thrust is the axial force on the thruster which is the sum of three contributions, two of which originate in the chamber while the third is exclusively related to the magnetic nozzle. The thrust in the chamber is the difference between the pressure force and the electric force in the sheath of the back-wall. The third contribution to the thrust is the magnetic force between the azimuthal plasma current and the thruster coils. The total force can then be written as:

$$F = F_p - F_e + F_m \tag{3.13}$$

and where note that the contribution of the chamber is: $F_{ch} = F_p - F_e$.

The total momentum flux equation for all three species (electrons, ions and neutrals) is [3]:

$$\nabla \cdot \overline{\overline{M}} = e(n_e - n_i)\nabla\phi - en_e\mathbf{u}_e \times \mathbf{B} \tag{3.14}$$

where the momentum tensor is: $\overline{\overline{\mathbf{M}}} = \sum\limits_{\alpha=i,e,n} \left(m_\alpha n_\alpha \mathbf{u}_\alpha \mathbf{u}_\alpha + p_\alpha \bar{\bar{I}}\right)$. The axial momentum flow across any radial cross-section of the plasma beam is given by:

$$F_z(z) = 2\pi \int_0^{R_V(z)} drrM_{zz}(z,r) \tag{3.15}$$

Ignoring drag on the side-wall, assuming sufficient magnetic shielding, the pressure term is given by evaluating equation 3.15 at the back-wall. The electric term is given by the first term on the right hand side (RHS) of equation 3.14, which taken over a radial section is just:

$$\pi\epsilon_0 \int_0^R drr\left(\frac{d\phi}{dz}\right)^2 \tag{3.16}$$

to be evaluated at the back-wall. This force is the attraction between the positive charge in the sheath and the negative charge on the back-wall and gives a negative contribution to the thrust. The contribution of the electric force with respect to the pressure force is about a factor 0.38 and can considerably reduce the thrust generated in the chamber.[3]

The magnetic contribution is given by the second term on the RHS of equation 3.14. We then find:

$$2\pi \int_0^{L_n} dz \int_0^{R_V(z)} drr(-j_\theta)B_r \tag{3.17}$$

From this equation it is also immediately apparent why the magnetic contribution is confined to the magnetic nozzle; only in the divergent field is the radial component of the magnetic field non-zero.

If we define a factor $\kappa_F = F_m/F_{ch}$, which depends on the nozzle length L_n but is only weakly dependent on T_e, we can write the total thrust as:

$$F(T_e, L_n) \simeq F_{ch}(T_e)\,[1 + \kappa_F(L_n)] \tag{3.18}$$

This shows that for a given T_e the thrust increases over the nozzle, depending only on the nozzle length. Experiments have shown a value of κ_F of $0.4 - 0.7$ agreeing with numerical simulations. [3]

The global efficiency of a thruster is given by the ratio of beam power to total power $\eta = F^2/2\dot{m}P_T$. However an alternative definition based on the plasma beam properties is the internal efficiency: $\eta_i = P_{zi}/P_T$, where:

$$P_{zi} = \pi \int_0^{R_V(L_n)} drrnm_i u_{zi}^3(L_n, r) \tag{3.19}$$

P_{zi} is the ion axial kinetic energy at L_n, the end of the nozzle.

The internal efficiency is the product of the chamber, conversion and divergence efficiencies: $\eta_i = \eta_{ch}\eta_{con}\eta_{div}$, with:

$$\eta_{ch} = \frac{P_b}{P_T} = 1 - \epsilon_{ion} - \epsilon_{wall} \qquad \eta_{con} = \frac{P_i}{P_b} \qquad \eta_{div} = \frac{P_{zi}}{P_i} \tag{3.20}$$

The chamber efficiency is the ratio of the beam power, i.e the power through the chamber exit plane, over the total supplied power. This solely depends on the power spend on ionising and the losses to the wall. The conversion efficiency is the ratio between the ion power in the beam and the beam power, it illustrates the distribution of energy over the ion and electron populations in the beam. Over the magnetic nozzle the electron energy is converted into ion energy, the extent of this conversion is given by this efficiency. Lastly the divergence efficiency is the ratio between ion axial kinetic energy and the total ion energy in the beam. It is a measure of the losses due to beam divergence as only the purely axial momentum of the ions contributes to the thrust.

There is no source of energy in the magnetic nozzle, there is only a conversion electron energy to ion kinetic energy. We can therefore write:

$$P_b = P_e(z) + P_i(z) = \text{const.} \tag{3.21}$$

The ion and electron power in the nozzle are given by:

$$P_i(z) = \pi \int_0^{R_V(z)} drrm_i u_i^2 u_{zi} \tag{3.22}$$

$$P_e(z) \simeq \pi \int_0^{R_V(z)} drr\,(5T_e n u_{ze} + 2q_{ze}) \tag{3.23}$$

Here it is assumed that the contribution of the neutrals is negligible and that $m_e u_{\theta e}^2 \ll 2T_e$. The last assumption is also a prerequisite for the magnetic nozzle model and therefore satisfied for the domain of the simulations. As with the thrust we can define an expansion factor κ_P almost independent of T_e:

$$\kappa_P = \frac{P_i(z)}{P_{i0}} - 1 \tag{3.24}$$

where $P_{i0} = P_i(0)$ the energy of the sonic flow at the throat. The factor kappa happens to grows roughly as the square of the local r-averaged Mach number M.[3] The parametric dependence of the beam power can now be written as:

$$P_b(T_e, L_n) = P_e(T_e) + P_{i0}(T_e)\,[1 + \kappa_P(L_n)] \tag{3.25}$$

It can be shown that at the throat only a fraction of the beam power, about one-fifteenth, is deposited on the sonic ion flow. Quantitative estimates of the efficiencies are as follows. The conversion efficiency is independent of T_e and is about 44%. This value is for the (un-physical) case of an isothermal plasma which in fact is the worst case scenario. However experiments hint at a polytropic thermodynamic relation for electrons which could improve this number [33, 42, 49]. Chamber efficiency is due to ionisation losses which are unavoidable but can be reduced to about 10% in the high ionisation regime, i.e. at high $T_e \approx 20\ eV$. Losses to the wall for an unshielded back-wall result in a total chamber efficiency of 60% but can be improved to 80% by magnetic shielding. Plume or divergence efficiency is determined by the magnetic nozzle and its divergence. The isothermal model predicts values of 70-90% depending on the nozzle conditions [1]. Including non-isothermal electron thermodynamics results in efficiencies of 60-80% for $\gamma_e = 1 - 1.3$, with a higher polytropic index being favourable to the efficiency [56]. The total maximum internal efficiency is somewhat below 30% which is meagre as an upper estimate. However as both plume divergence and electron thermodynamics in the plume are not well understood this number can be considered a first estimate.

Summary

This chapter discussed the magnetic nozzle concept in greater detail. First the 2D magnetic nozzle was introduced, including the fluid equations and the analytical equations for the electrons needed to close the system. This system is solved by the DiMagNo code using the method of characteristics. The model produces a plasma response with a decrease of the plasma density and potential decreasing downstream resulting in a gently increasing Mach number, up to $M = 4 - 5$ far downstream. The model also predicts an axial concentration of the ions which is beneficial for thrust. The advantage of this model over earlier 1D, and 2D model is the use of a global current free assumption over local current ambipolarity assumption. This includes separation of electron and ion streamlines and resulting radial ambipolar fields, azimuthal $\mathbf{E} \times \mathbf{B}$ drifts and longitudinal currents into the model.

Furthermore it was explained how the model calculates the performance of the magnetic nozzle. This can be broken down into three efficiencies: the chamber efficiency, the ratio of absorbed power to power at the exit; the conversion efficiency, a measure of the conversion of electron to ion energy in the nozzle; and the divergence efficiency, the ratio of axial ion power to total ion power. Also important are the expansion factor for thrust that is a measure of the thrust gain in the nozzle.

4

Plasma Diagnostics

Introduction

There are many diagnostic methods available to study plasmas. In general a distinction can be made between intrusive and non-intrusive methods. Intrusive methods probe the plasma with (electrostatic) probes, whose physical presence perturbs the plasma locally and possibly globally. Using physical models the local perturbation is related to the parameters of the bulk plasma. Invasive diagnostics are generally cheap, simple and can be manufactured in-house. The main disadvantages of invasive techniques are the possibility of globally perturbing the plasma and the difficulty in interpreting the measurements which relies heavy on physical models.

Non-intrusive methods study the plasma by means of the electromagnetic spectrum. This can either be passive diagnostics, collecting radiation naturally emitted by the plasma or active diagnostics, probing the plasma with EM-waves. Depending on the diagnostic this is can be done in the microwave, infra-red or VIS-UV range. Generally non-invasive techniques do not perturb the plasma, however they are also more expensive, complex and require expertise to operate.

Each diagnostic can only measure one or two different plasma parameters and characterisation of a plasma usually requires an array of diagnostics. Due to their complexity and cost most non-invasive techniques are out of the scope of this thesis and main measurements are limited to electrostatic probe measurements. An exception is optical emission spectroscopy which consists of a relatively cheap and simple set-up available at the electric propulsion laboratory. A thorough review of several diagnostic techniques has been presented in the literature review preceding this thesis, this chapter will therefore only focus on the key points.

4.1. Langmuir probe

The Langmuir probe (LP) is the first plasma diagnostic ever developed and is named after the father of plasma physics Irving Langmuir. It consists of a single conductor immersed in the plasma in series with a variable voltage source and an ampere meter. The conductor can be of varying geometry, such as planar, cylindrical or spherical, with cylindrical being the most common for practical reasons. To have a closed circuit the vacuum chamber functions as a second electrode.

By varying the bias potential applied to the probe, the current drawn from the plasma varies as well. The resulting I-V characteristic can be processed to derive several plasma parameters. Plasma density and electron temperature can usually readily be extracted. The plasma potential and the electron energy distribution function (EEDF) in theory can be recovered as well, however due to the noisy nature of the data these results are not always meaningful as these parameters are dependent on the first and second derivative of the I-V curve.

The I-V curve has a distinct shape and can be divided into three parts. For voltages well below the floating potential $V < \phi_f$ the probe is in the ion collection regime as it collects mostly ion current. Up to the plasma potential ϕ_p the curve is exponential due to the Boltzmann distributed electron population and the probe is said to be in the electron-retardation regime. Above the plasma potential $V > \phi_p$ the collected electron current theoretically saturates to the random electron flux, the electron collection regime. However in reality the electron current never saturates due to an expanding sheath and the presence of a magnetic field.

The collected current is the sum of the ion and electron currents $I = I_e + I_i$ where the electron current is given by [48]

$$I_e = \begin{cases} I_{es} \exp\left(\frac{V-\phi_p}{T_e}\right) & \text{for} \quad V < \phi_p \\ I_{es} & \text{for} \quad V > \phi_p \end{cases} \tag{4.1}$$

where the electron saturation current is:

$$I_{es} = \frac{1}{4} enA \sqrt{\frac{8eT_e}{\pi m_e}} \tag{4.2}$$

From equation 4.1 it can be seen that the exponential part is proportional to T_e. The electron temperature can generally be recovered from the inverse of the slope of a log-plot of I_e. Although I_{es} is proportional to n the electron current generally does not saturate and it is difficult to relate I_{es} to n especially in the presence of magnetic fields. The plasma potential ϕ_p can be estimated by the inflection point of the I-V which is usually found by finding the maximum of the first derivative. The electron energy distribution is given by [48]:

$$g_e(V) = \frac{2m_e}{e^2 A} \left[\frac{2e(\phi_p - V)}{m_e}\right]^{1/2} \frac{d^2 I_e}{dV^2} \tag{4.3}$$

Since the plasma density usually cannot be properly extracted from the electron saturation current, this parameter is usually derived from an analysis of the ion collection regime. However the relationship between the plasma density and the electron saturation current is not as straightforward as in the case of the electron saturation current. Furthermore the behaviour of the ion saturation current is heavily dependent on the probe geometry, plasma density and electron and ion temperatures. Several models of the ion collection of electrostatic probes have been developed with different accuracy and applicability. Below the planar approximation, Bernstein-Rabinowitz-Laframboise theory, Allen-Boyd-Reynolds theory and the orbital motion limited theory are discussed.

4.1.1. Planar approximation

The most simple case is the one developed for planar probes but is equally valid for cylindrical probes (with radius a) in the case of a thin-sheath, i.e. the sheath width s is much smaller than the probe radius. As the sheath width is usually of the order of several Debye lengths the general criterion is $\lambda_D \ll a$.

Assuming Boltzmann distributed electrons with temperature T_e and ballistic ions initially at rest in the bulk plasma, $T_i = 0$ and an electric potential profile $\phi(x)$. The sheath edge is defined at $x = 0$ where $\phi = 0$ and $\phi' \sim 0$. Using conservation of energy for ions and the Boltzmann relation for electrons yields:

$$n_i = n_{is} \left(1 - \frac{2e\phi}{m_i u_s^2}\right) \tag{4.4}$$

$$n_e = n_{es} \exp\left(\frac{\phi}{T_e}\right) \tag{4.5}$$

where the subscript s denotes the values at the sheath edge. Using this to solve Poisson's equation yields the Bohm sheath criterion $u_s \geq u_B = \sqrt{eT_e/m_i}$ for the sheath solution to be stable. Ions thus approach the probe with the Bohm velocity u_B. The ion saturation current in this approach is given by:

$$I_{is} = -0.61 Aenu_B \tag{4.6}$$

The factor 0.61 follows from the relation between the density at the sheath edge and the bulk density. Since the kinetic energy of ions initially at rest in the bulk plasma is completely gained from the potential drop, the potential in the bulk plasma is: $\phi_0 = m_i u_B^2/2 = T_e/2$. Using this in the Boltzmann relation $n = n_0 \exp(-\phi/T_e)$ yields $n_{is} \approx 0.61 n_0$. In this model the ion current saturates to a constant value.

However in practice due to the sheath expanding with increasing bias potential the collected current keeps increasing and the ion saturation current is nearly linear. Therefore it is common practice to fit a straight line to the $I - V$ curve in the ion collection regime, extrapolate this to V_f and insert this into equation 4.6 to solve for n. It is however necessary to first measure the electron temperature to calculate u_B.

4.1.2. Orbital Motion Limited theory

For more tenuous plasmas where $\lambda_D \gg a$ the orbital motion limited (OML) theory is applicable. This approach for a cylindrical probe takes into account the angular momentum of the ions approaching the probe and allows for orbiting motion. Starting from the conservation of energy and angular momentum with $-v_r, v_\theta$ the radial and azimuthal velocity of the ions at the sheath $r = s$ and the primes denoting the corresponding values at the probe $r = a$:

$$\frac{1}{2}m_i\left({v'}_r^2 + {v'}_\theta^2\right) = \frac{1}{2}m_i\left(v_r^2 + v_\theta^2\right) + e\left|\phi - V\right| \tag{4.7}$$

$$av'_\theta = sv_\theta \tag{4.8}$$

For an ion to reach the probe $v_r < 0$ and $v_r'^2 > 0$. Solving for $v_r'^2 = 0$ yields:

$$v_{\theta 0} = \left(\frac{v_r^2 + 2e\left|\phi - V\right|/m}{s^2/a^2 - 1}\right)^{1/2} \tag{4.9}$$

Particles will therefore only reach the probe if $|v_\theta| \leq v_{\theta 0}$ is satisfied. The total current to the probe can be found by integrating the radial flux at the sheath:

$$I = 2\pi sLen \int_0^\infty v_r \mathrm{d}v_r \int_{-v_{\theta 0}}^{+v_{\theta 0}} \mathrm{d}v_\theta f(v_r, v_\theta) \tag{4.10}$$

which for a Maxwellian distribution yields the following expression [60]:

$$2\pi aLen\sqrt{\frac{eT_i}{2\pi m_i}}\left[\frac{2}{\sqrt{\pi}}\sqrt{\frac{|\phi - V|}{T_e}} + \exp\left(\frac{|\phi - V|}{T_e}\right)\mathrm{erf}\left(\sqrt{\frac{|\phi - V|}{T_e}}\right)\right] \tag{4.11}$$

For large (negative) voltages as is the case in the ion collection regime $T_e \ll |\phi - V|$ and in the cold ion limit $T_i \rightarrow 0$ this can be simplified to:

$$I_{is} = -\frac{enA}{\pi}\sqrt{\frac{2e|\phi - V|}{m_i}} \tag{4.12}$$

which is the expression for the OML ion current. For the regime $\lambda_D \gg a$, plotting the measured $I^2 - V$ in the ion collection region should yield a straight line. By equating a linear fit with the square of equation 4.12 both n and ϕ can be recovered.

4.1.3. Bernstein-Rabinowitz-Laframboise theory

The downside of either of the above theories is that they are only valid in the limits of an infinitely small or large sheath. They do not cover the cases where $\lambda_D \sim a$. Furthermore, the planar approximation does not take orbital motion into account while the OML theory is not self-consistent i.e. it does not solve for the electric potential. A more complete theory that mitigates these short-comings is Bernstein-Rabinowitz-Laframboise (BRL) theory [46]. This theory has been developed for stationary, collision-less plasmas without magnetic fields and Maxwellian ions at rest or flowing parallel to the cylindrical probe. It uses the constants of motion - the energy E and angular momentum J - to express the ion motion in the r, θ plane:

$$E = \frac{1}{2}m_i(v_r^2 + v_\theta^2) + e\phi(r) \tag{4.13}$$

$$J = m_i v_\theta r \tag{4.14}$$

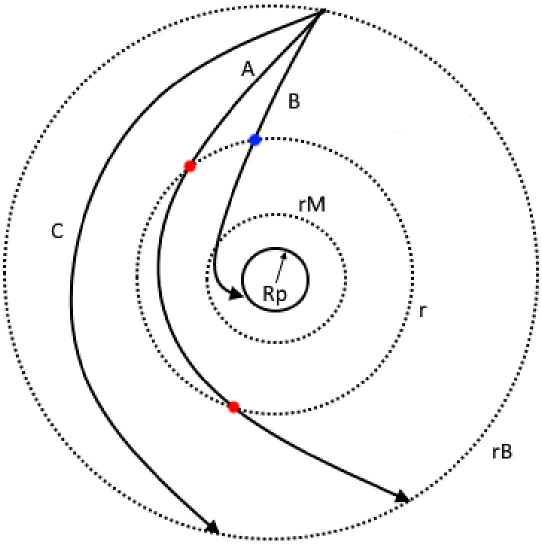

Figure 4.1: Particle trajectories A,B,C orbiting a cylindrical probe. Rp: probe radius, rB: boundary condition, rM: absorption radius

Solving for the kinetic energy yields:

$$\frac{1}{2}m_i v_r^2 = E - \left[e\phi(r) + \frac{J^2}{2m_i r^2}\right] \tag{4.15}$$

The second term on the RHS can be regarded as an effective potential $U(r)$. Ions with an energy E that move in this potential see a potential barrier due to their angular momentum. The first necessary (but insufficient) condition for ions to reach the probe is $E - U(r) \geq 0$. For a fixed E and a given radius r there is a largest J_1^2 such that for $J^2 < J_1^2$ all particles are collected. In the same way there is a largest J_2^2 such that for $J > J_2^2$ particles no longer reach that particular r as they have been deflected by a potential barrier at a different radius $r' > r$. The proper condition is thus $E \geq U(r')$ for all $r' \geq r$, i.e. the energy of the particle has to exceed the potential energy not just at r but at all larger radii. Particles that approach the probe from the boundary condition trace three different trajectories. (A) Particles cross the radius r, orbit the probe and cross the radius r a second time. Incoming particles have a distribution $f_{v_r<0}$ while the outgoing particles have $f_{v_r>0}$. Due to the symmetry of the central force field of the probe these distributions are equal and the total distribution crossing r is $f = 2f_{v_r<0}$. This corresponds to the case $J_1^2 < J^2 \leq J_2^2$. (B) Incoming particles cross r, strike the probe and are collected. The outgoing distribution is zero is this case and the total distribution is $f = f_{v_r<0}$, corresponding to the case $0 < J^2 \leq J_1^2$. (C) Particles approach the probe but are deflected at a larger radius r', their total distribution at r is therefore simply zero, corresponding to the case $J^2 > J_2^2$. From this analysis it follows that the total distribution can be expressed as an integer multiple of the incoming distribution $f = Kf_{v_r<0}$ with $K = 0, 1, 2$. The three particle trajectories are visualized in figure 4.1.

The particle density profile can be calculated from:

$$N(r) = \int\limits_{v_\theta=-\infty}^{v_\theta=\infty} \int\limits_{v_r=-\infty}^{v_r=\infty} \hat{f}(E,J)\frac{\partial(v_r, v_\theta)}{\partial(E,J)} dE dJ \tag{4.16}$$

The notation $\hat{f}$ signifies the reduced distribution function $\int_{-\infty}^{\infty} f(E,J,v_z)dv_z$. It is obvious that azimuthal velocity distribution is symmetric, the Maxwellian distribution function is not dependent on J and the previous discussion showed that $f(E) = f_{v_r<0}K(J^2)$, therefore it follows that:

$$N(r) = \frac{2}{M^2 r} \int\limits_{v_\theta=0}^{v_\theta=\infty} \int\limits_{v_r=-\infty}^{v_r=0} \hat{f}_{v_r<0}(E)K(J^2)\left[\frac{2}{M}\left(E - e\phi(r)\right) - \frac{J^2}{M^2 r^2}\right]^{-\frac{1}{2}} \tag{4.17}$$

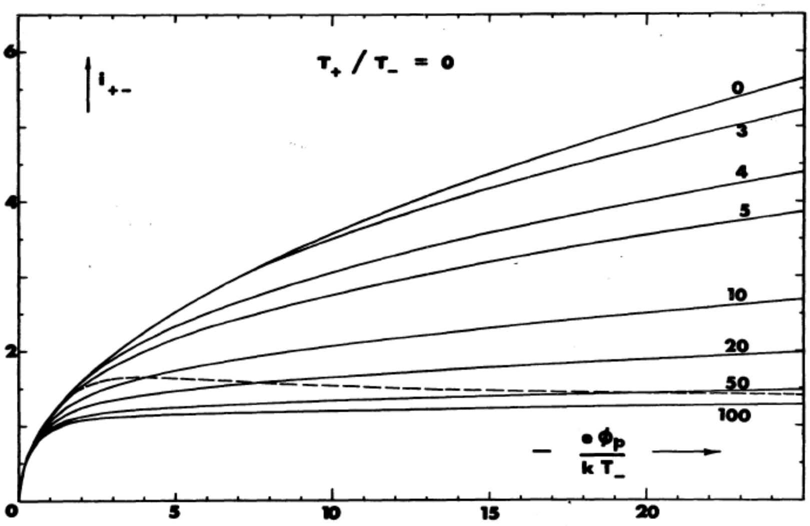

Figure 4.2: Normalise $I - V$ curves from Bernstein-Rabinowitz-Laframboise theory. [46]

Because $K(J^2) = K_n = 2, 1, 0$ (depending on the value of J^2 w.r.t. J_1^2, J_2^2) integration over v_θ leaves a sum of integrals:

$$N(r) = \frac{2}{M} \int\limits_{E=0}^{E=\infty} dE \hat{f}_{v_r<0}(E) \sum_{n=1}^{2} K_n(J^2) \arcsin\left[\frac{J^2}{2Mr^2(E - e\phi(r))}\right]^{\frac{1}{2}} \Bigg|_{J=J_{n-1}(E)}^{J=J_n(E)} \tag{4.18}$$

defining $J_0 = 0$. When expanding the sum it becomes apparent that it can be rewritten as:

$$N(r) = \frac{2}{M} \int\limits_{E=0}^{E=\infty} dE \hat{f}_{v_r<0}(E) \sum_{n=0}^{2} Q_n \arcsin\left[\frac{J_n^2}{2Mr^2(E - e\phi(r))}\right]^{\frac{1}{2}} \tag{4.19}$$

Here a new factor $Q_n = 2, -1, -1$ is introduced, for $n = 0, 1, 2$. Laframboise solved this numerically with an iterative scheme. The bias potential ϕ_0 and the probe radius a are known a priori. The crux is to find the values of J_1, J_2. The scheme is as follows: (i) solve Poisson's equation for ϕ, ϕ' and ϕ''. (ii) Find J_1, J_2 and calculate $N(r)$ for electrons and ions, which can be used to again solve Poisson's equation. This is repeated until sufficient accuracy is achieved. The collected current can be calculated from [46]:

$$I = \frac{4\pi e}{m_i^2} \int\limits_{E=0}^{E=\infty} \hat{f}_{v_r<0}(E) J_1(E) dE \tag{4.20}$$

As the probe radius and bias potential are known a priori, the current I can be calculated for different V and a. Laframboise generated a set of (normalised) $I - V$ curves for different values of the probe parameter $\xi = a/\lambda_D$ here shown in figure 4.2.

4.1.4. Iterative solution scheme

The curves of Laframboise have been generated in 1966 and are only available in graphical form. To improve their applicability Chen parametrised these curves to be able to recalculate them on demand.[20] The normalised current and potential are $i = I_i/nj_r$ and $\zeta = |\phi - V|/T_e$ where $j_r = \sqrt{eT_e/2\pi m_i}$. The parametrisation is given by:

$$\frac{1}{i^4} = \frac{1}{A\zeta^B} + \frac{1}{C\zeta^D} \tag{4.21}$$

Table 4.1: Coefficients for fitting parameters for $\xi < 3$

	a	b	c	d	f
A	1.12	0.00034	6.87	0.145	110
B	0.50	0.008	1.50	0.180	0.80
C	1.07	0.95	1.01	–	–
D	0.05	1.54	0.30	1.135	0.370

Table 4.2: Coefficients for fitting parameters for $\xi > 3$

	a	b	c	d	f	g
A	1.142	19.027	3.000	1.433	4.164	0.252
B	0.530	0.970	3.000	1.110	2.120	0.350
C	0.000	1.000	3.000	1.950	1.270	0.035
D	0.000	2.650	2.960	0.376	1.940	0.234

Where the fitting parameters $A, B, C, D(\xi)$ are functions of the probe parameter. To improve fitting two different regimes are defined: $\xi < 3$ and $\xi > 3$. The fitting parameters for $\xi < 3$ are given by:

$$A = a + \frac{1}{\frac{1}{b\xi^c} - \frac{1}{d \ln \xi^f}} \tag{4.22}$$

$$B, D = a + b\xi^c \exp(-d\xi^f) \tag{4.23}$$

$$C = a + b\xi^{-c} \tag{4.24}$$

The values of the coefficients a, b, c, d, f are given in table 4.1.

The fitting parameters for $\xi > 3$ are given in by the equations below and the corresponding coefficients in table 4.2.

$$A, B, D = a + b(\xi - c)^d \exp[-f(\xi - g)^g] \tag{4.25}$$

$$C = a + b \exp[-c \ln(\xi - d)] + f(1 - g \ln \xi) \tag{4.26}$$

In this approach a distinction is made between the plasma potential for electrons ϕ_e and that for ions ϕ_i. Physically they should have the same value and this at first seems a rather murky practice. Chen notes that some discrepancy between ϕ_e and ϕ_i is to be expected due to the difficulty of calculating i for $\zeta \approx 0$ and the fact that his fits perform the worst around this point. Furthermore in reality there is dependency on T_i, while the curves used here are only for $T_i = 0$. Discrepancies between ϕ_e and ϕ_i can sometimes be of the order of several T_e but without this distinction the method seems not to work.

The $I_{i,th} - V$ curves can be calculated for a priori known values of T_e, n and ϕ_i, ϕ_e. However these are precisely the plasma parameters to be determined. The solution is an iterative scheme where for an initial estimate of T_e, n, ϕ_i, ϕ_e, the theoretical ion current saturation curve $I_{i,th}$ is generated as follows:

$$I_{i,th} = e \cdot n \cdot i \cdot A \cdot \sqrt{\frac{eT_e}{2\pi m_e}} \tag{4.27}$$

The mean of the relative difference ε_i is minimised while varying ϕ_i and n.

$$\varepsilon_i = \frac{1}{n} \sum^{n} \frac{|I - I_{i,th}|}{|I|} \tag{4.28}$$

The best fit is then subtracted from the total current to get the electron current $I_e = I - I_{i,th}$. A theoretical electron current $I_{e,th}$ is generated from eq. 4.1 using the values for T_e, ϕ_e. The mean of the relative difference of the logarithm of both the measured and theoretical electrons currents ε_e is minimised by varying T_e, ϕ_e.

$$\varepsilon_e = \frac{1}{n}\sum^{n} \frac{|\ln I_e - \ln I_{e,th}|}{|\ln I_e|} \tag{4.29}$$

This new value of T_e is then used to recalculate the ion saturation current. This whole process is repeated several times. Then the sum of both relative differences is minimised by varying all four parameters simultaneously, yielding the best fit for n, T_e.

The algorithm presented in this section has been implemented in MATLAB; the code is provided digitally. A list of digital attachments can be found in appendix D.

4.1.5. Allen-Boyd-Reynolds theory

An alternative theory to BRL theory is Allen-Boyd-Reynolds (ABR) theory, initially developed for spherical probes and later adapted to cylindrical probes by Chen.[4, 21] ABR theory assumes cold ions, $T_i = 0$ which means orbital motion is ignored and ions only radially approach the probe. The method solves Poisson's equation from $r = \infty$ where $\phi = 0$ to $r = a$ the probe radius. Poisson's equation in cylindrical coordinates is given by:

$$\frac{1}{r}\frac{\partial}{\partial r}\left(r\frac{\partial \phi}{\partial r}\right) = \frac{e}{\epsilon_0}(n_e - n_i) \tag{4.30}$$

Assuming Maxwellian electrons $n_e = n_0 e^{\phi/T_e}$ let I be the total current of ions to the probe. The ion flux per unit length is then:

$$\Gamma_i = n_i v_i = \frac{I}{2\pi r} \tag{4.31}$$

where $v_i\sqrt{-e\phi/m_i}$ the ion velocity. Using this to find an expression for n_i and putting this together with n_e into equation 4.30 and substituting $\zeta = -\phi/T_e$ and the sound speed $c_s = \sqrt{eT_e/m_i}$ yields:

$$T_e\frac{1}{r}\frac{\partial}{\partial r}\left(r\frac{\partial \zeta}{\partial r}\right) = -\frac{e}{\epsilon_0}\left[\frac{I}{2\pi r}\frac{(2\zeta)^{-1/2}}{c_s} - n_0 e^{-\zeta}\right] \tag{4.32}$$

This can be rewritten using the Debye length $\lambda_D = \sqrt{\epsilon_0 T_e/n_0 e}$ and $\xi = r/\lambda$ and the normalised current:

$$i = \frac{I}{2\pi T_e}\left(\frac{m_i}{2\epsilon_0 n_0}\right)^{1/2} \tag{4.33}$$

to:

$$\frac{\partial}{\partial \xi}\left(\xi\frac{\partial \zeta}{\partial \xi}\right) = \iota\zeta^{-1/2} - \xi e^{-\zeta} \tag{4.34}$$

For each assumed normalised current i (requiring T_e to be measured a priori) this equation can be integrated from $r = \infty$ to an arbitrarily small radius. The normalised potential at the probe radius $\zeta(a) = \eta_p$ is the probe potential corresponding to that particular ι. Calculating a family of curves $\xi - \zeta$ can be used to yield a $i - \eta_p$ characteristic for a probe of radius a by cross-plotting. To expedite post-processing Chen has parametrised these curves with an empirical formula to be able to generate such characteristics in real time. The method is similar to that described for BRL theory in the previous chapter. The parametrisation is given by:

$$i\xi_p = \left[\left(A\zeta^B\right)^4 + \left(C\zeta^D\right)^4\right]^{1/4} \tag{4.35}$$

The parameters $ABCD(\xi)$ are given by:

$$A, C = a\xi^b + c\xi^d \tag{4.36}$$

$$B, D = a + b\ln\xi + c(\ln\xi)^2 \tag{4.37}$$

The coefficients a, b, c, d are given in table 4.3.

Table 4.3: Coefficients for fitting parameters for ABR theoery

	a	b	c	d
A	0.864	1.500	0.269	2.050
B	0.479	-0.030	-0.010	–
C	1.008	1.700	0.336	2.050
D	0.384	-0.150	0.013	–

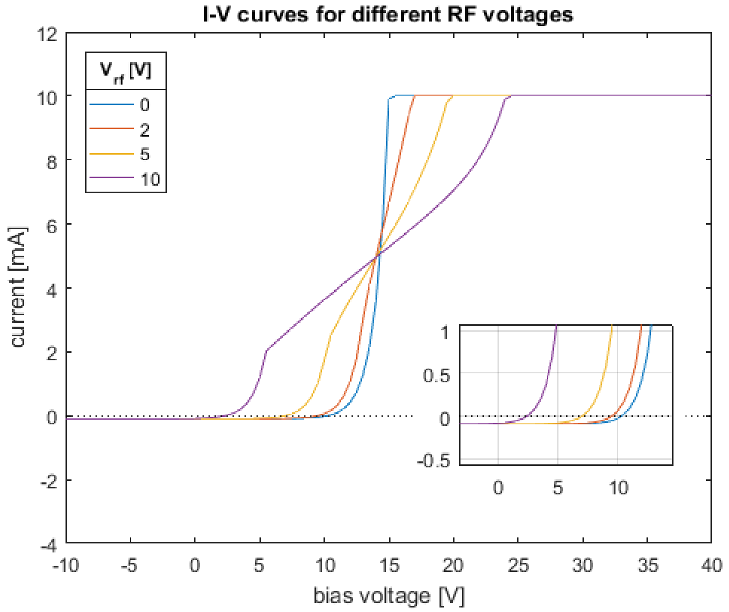

Figure 4.3: $I - V$ curves under the influence of RF fluctuations. Ion and electron saturation as in eq. 4.6 and 4.1. Calculations based on [10]

4.2. RF-Compensated probe

The plasma thruster is powered by a high powered RF antenna to ionise and heat the plasma. The downside of this is the presence of RF fluctuations in the plasma, that can propagate downstream. Although these fluctuations will quickly decrease with distance in the near plume region they may significantly alter the plasma response of the Langmuir probe. The effect of the RF fluctuations on the local plasma potential can be modelled as:

$$\phi(\mathbf{r}) = \phi_{dc}(\mathbf{r}) + V_{rf}(\mathbf{r}) \sin(\omega_{rf} t) \tag{4.38}$$

For the helicon thruster the RF frequency f is of the order of tens of MHz and therefore much faster than the sampling frequency of the measurement. The measured $I - V$ curve is therefore time-averaged. However since the current is not a linear function of $V - \phi$ this time-averaged measurement is not representative of the real $I - V$ curve. In general the slope of the exponential part (in a log-plot) will be less steep than the real curve. As T_e is the inverse of this slope, this will yield a falsely high value of the electron temperature. Another feature of Langmuir $I - V$ curves in RF plasmas is a shift of the floating potential to a more negative value and the plasma potential to a more positive value. The effect of the RF fluctuations can be clearly seen in figure 4.3.

Several attempts have been made to correct for Langmuir probe measurements in RF plasmas, the most successful being the RF-compensated probe of Sudit and Chen [76]. The RF-compensated Langmuir probe (RFCLP) is a regular Langmuir probe augmented with RF-chokes and an capacitively coupled auxiliary electrode. The chokes increase the impedance at the RF frequency and its first harmonic, and the auxiliary electrode helps the probe tip to follow the RF fluctuations.

The RFCLP can be modelled as in figure 4.4. Here $Z_{ck}(\omega)$ is the impedance of the chokes and $Z_{sh}(\omega) = R_{sh} \parallel C_{sh}(\omega)$ the impedance of the sheath at the tip. V_s is the plasma potential ϕ from eq.

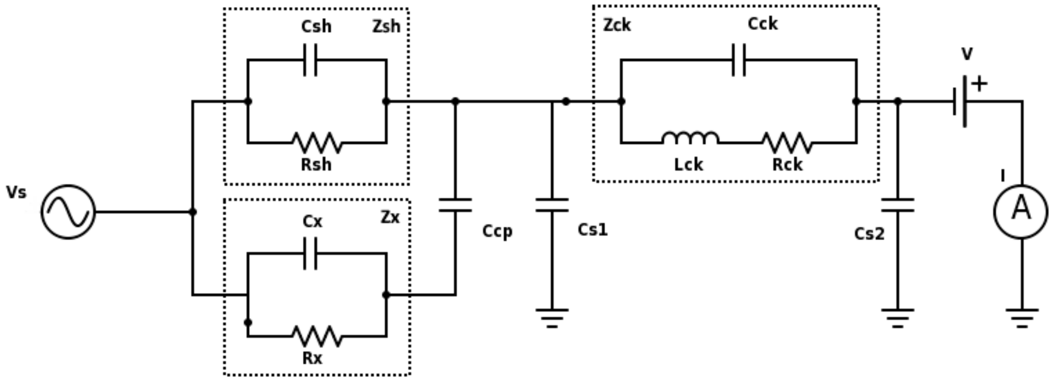

Figure 4.4: Electric model of the RF compensated Langmuir probe. [76]

4.38, V_p the potential at the probe tip and V the bias potential. Z_{sh} and Z_{ck} effectively form a voltage divider. To prevent the RF fluctuations from influencing the exponential part of the curve, $V_p - V_s \sim |V_{rf}|$ has to be kept within much less than the electron temperature T_e:

$$\frac{Z_{ck}}{Z_{ck} + Z_{sh}} |V_{rf}| \ll T_e \tag{4.39}$$

However in reality there is always a stray capacitance C_{s1} of the order of 1 pF that will short out high frequency signals; the effective impedance as seen from the tip is therefore $Z_{eff} = Z_{ck} \parallel Z_{s1}$. Since this impedance will always be smaller than Z_{ck} an auxiliary electrode is added that is coupled through a capacitance C_{cp} so as to not affect the DC component. This auxiliary electrode has a much larger surface area than the probe tip, and thus a low sheath impedance Z_x as this scales with A^{-1}. The total sheath impedance $Z_{sh} \parallel Z_x$ about a factor $1 + R_A$ smaller than Z_{sh}, with R_A the ratio of areas of the tip and electrode. Based on this analysis the following condition has to be satisfied for the probe to filter the RF fluctuations:

$$Z_{eff} \gg \frac{Z_{sh}}{1 + R_A} \left(\frac{V_{rf}}{T_e} - 1 \right) \tag{4.40}$$

Sudit and Chen also derive approximate expressions for C_{sh} and R_{sh} under the assumption of a planar sheath and $\omega_{pi} \gg \omega_{rf}$ meaning that the sheath can equilibrate at each phase of the RF cycle. The ion plasma frequency is given by:

$$\omega_{pi} = \sqrt{\frac{e^2 n}{\epsilon_0 m_i}} \tag{4.41}$$

For an RF frequency of 13.56 MHz the minimum plasma density therefore has to be of the order of $10^{18}\ m^{-3}$, while for 27.12 MHz this is almost $10^{19}\ m^{-3}$. Provided this condition is met, the sheath capacitance and resistance, evaluated at the floating potential are given by [76]

$$R_{sh} = \frac{m_i^{1/2}}{0.61 \cdot e^{3/2} \cdot A} \cdot \frac{T_e^{1/2}}{n} \tag{4.42}$$

$$C_{sh} = \frac{\epsilon_0^{1/2} e^{1/2} A}{2^{7/4}} \left(\frac{n}{T_e} \right)^{1/2} \left(\frac{V_f - V_s}{T_e} \right)^{-3/4} \tag{4.43}$$

In the planar sheath the difference between floating and plasma potential is about $5.2 T_e$. The last part of the expression for C_{sh} can be replaced by a factor for $5.2^{-3/4}$. The total impedance is the parallel combination of the capacitance at the RF frequency and the resistance. It has to be noted that resistive part scales with n^{-1} while the capacitive part scales with $n^{-1/2}$ and impedance is resistance dominated for densities over $10^{16}\ m^{-3}$.

4.2.1. Probe design

For the electric propulsion lab a RFCLP has been developed, operating at 13.56 MHz. The probe consists of four chokes in series, two resonant at the RF frequency and two at the corresponding first

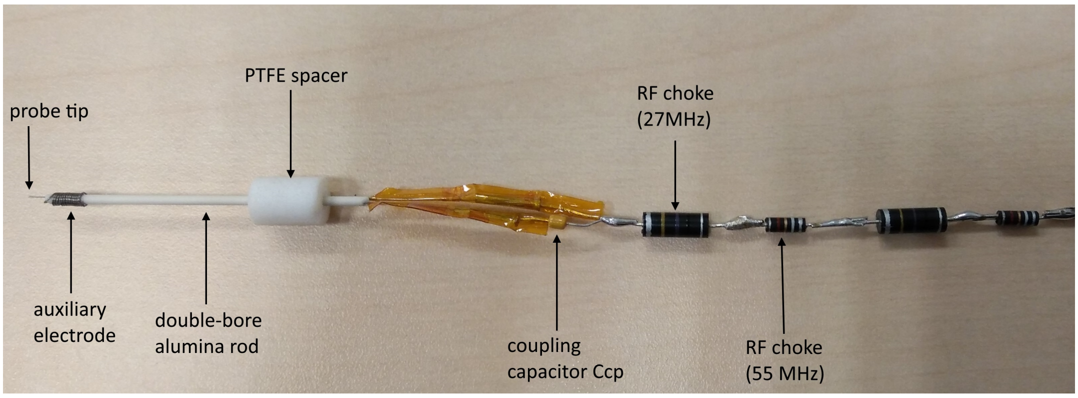

(a) RF compensated Langmuir probe.

(b) RFCLP circuit. (c) Close-up of RFCLP tip.

Figure 4.5: Images of the RFCLP developed at the electric propulsion lab of UC3M.

Table 4.4: Values of the RFCLP chokes

f [MHz]	ω [rad]	L [μH]	R [Ω]	C [pF]
13	$8.2 \cdot 10^7$	100	8.0	1.5
27	$1.7 \cdot 10^8$	47	2.11	0.74
55	$3.5 \cdot 10^8$	6.8	2.7	1.02

harmonic. One end of this circuit is crimped to a tungsten rod of 0.127 mm radius, which forms the probe tip. To this same end a 22 nF capacitor was soldered, of which the other end was crimped to a tungsten wire of similar diameter. Both the tungsten rod and wire were inserted in a 1.6 mm outer diameter, 0.4 mm inner diameter, double bore alumina rod; the tungsten rod protruding about 3 mm. The tungsten wire extending several centimetres, is tightly wound around the alumina rod to form a cylindrical auxiliary electrode. The whole circuit is placed inside a 11.4 mm outer diameter, 7.4 mm inner diameter alumina tube. The smaller alumina rod is matched to the larger tube by means of a customised PTFE spacer and sealed with zirconium-dioxide paste. The other end of the circuit is soldered to a (pin) connector with which the probe can be wired to the measurement equipment. Photos of the circuit and the probe are shown in figure 4.5.

To asses the functionality of the probe the value of Z_{sh} can be calculated using equations 4.42 and 4.43. The value of Z_{ck} as a function of th frequency has been determine experimentally and is shown in figure 4.6. The values for the chokes are given in table 4.4. From 4.40, V_{rf} is calculated and plotted as a function of n, T_e. The condition 'much less than ($\ll$)' is defined as a difference of at least one order of magnitude.

From figure 4.6 it can be seen that the choke impedance around the RF frequency is about 10^5 Ω although it can be argued that the response for the 13.56 MHz probe deviates from the theoretical curve. However since $Z_{eff} = Z_{ck} \parallel Z_{s1}$ where the latter is about 10^4 Ω this impedance is dominated by the stray capacitance, i.e. $Z_{eff} \approx Z_{s1}$. Note that all frequency dependent values are evaluated at the RF frequency.

Plots of the maximum magnitude of V_{rf} that can be filtered by the probe as a function of plasma

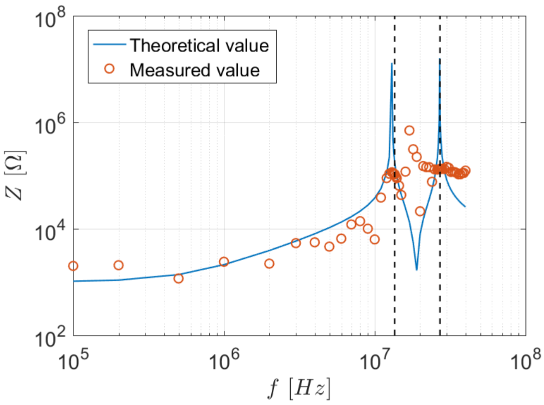

Figure 4.6: Characterisation of 13.56 MHz probe.

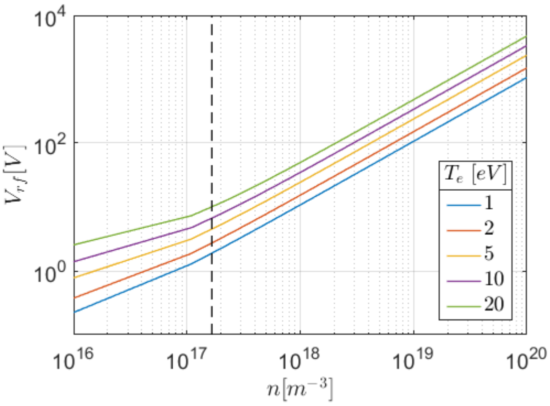

Figure 4.7: Maximum RF potential that can be filtered by the RFCLP as a function of n and T_e. Dotted lines denote $\omega_{pi} = \omega$. Note that since $\omega_{pi} \propto \sqrt{n}$ the density has to be 2 orders higher to satisfy $\omega_{pi} \gg \omega$.

density are given in figure 4.7. It is clear that the probes work better in hotter and denser plasmas. For the worst case of $10^{18}\ m^{-3}$ and $1eV$ the probe can filter about 2.5 V however for higher densities, temperatures this quickly increase to several tens of Volts. Based on figure 4.3 RF potentials of much more than 10 V are not to be expected as otherwise the $I - V$ curve would be deformed too much. It is possible to estimate V_{rf} by measuring an $I - V$ curve with an emissive probe and taking the first derivative. According to [83], in the presence of an RF component there should appear two maxima, where the distance between them is equal to $2V_{rf}$. This method can be used to verify whether the RFCLPs are well equipped to filter the present RF signal.

4.3. Emissive probe

Emissive probes (EPs) make use of the fact that a material like tungsten, when sufficiently heated, will emit (half-)Maxwellian electrons with a temperature T_w equal to that of the probe. When the bias potential of the probe passes through the plasma potential the measured current suddenly increases as the emitted electrons are now also collected. At bias potentials below the plasma potential the emitted electron current shows up as an effective ion current. The measured effect is not affected by plasma flow as it is directly dependent on only the plasma potential This makes it a preferred diagnostic for ϕ. The emission current of an EP, as a function of the bias voltage V is:

$$I_{em} = \begin{cases} I_{em0} & \text{for} \quad V < \phi_p \\ I_{em0} \exp\left(\frac{V-\phi_p}{T_w}\right) & \text{for} \quad V \geq \phi_p \end{cases} \tag{4.44}$$

where the temperature limited emission current I_{em0} is given by:

$$I_{em0} = \mathcal{A} T_w^2 S \exp\left(\frac{-\Phi_w}{T_w}\right) \tag{4.45}$$

Here $\mathcal{A}$ = 3.0 A m^{-2}K^{-2} the Richardson-Dushman constant for tungsten, T_w the probe temperature, and $\Phi_w = 2.63$ eV the work function of thoriated tungsten, S is the surface area of the probe. Note that T_w is in electron-Volt [41]. The exponential region in the IV-curve of emissive probes is dependent on $T_w \ll T_e$ while that of Langmuir probes depends on T_e. As in most plasmas $T_w \ll T_e$ the emissive probe is very sensitive to the plasma potential, yielding a more accurate measurement [69].

Emissive probes consist of a thin wire connected in series with a DC current source for heating. In between the two leads of this circuit is a voltage divider with resistors of equal magnitude. The midpoint between these resistors has the same potential as the midpoint of the thin. For the *floating point method* the voltage is directly measured at this point. For the *inflection point in the limit of zero emission* method the whole heating circuit is connected to a variable voltage source and current meter in series to be able measure an $I - V$ curve. However in the latter case the bias voltage in the $I - V$

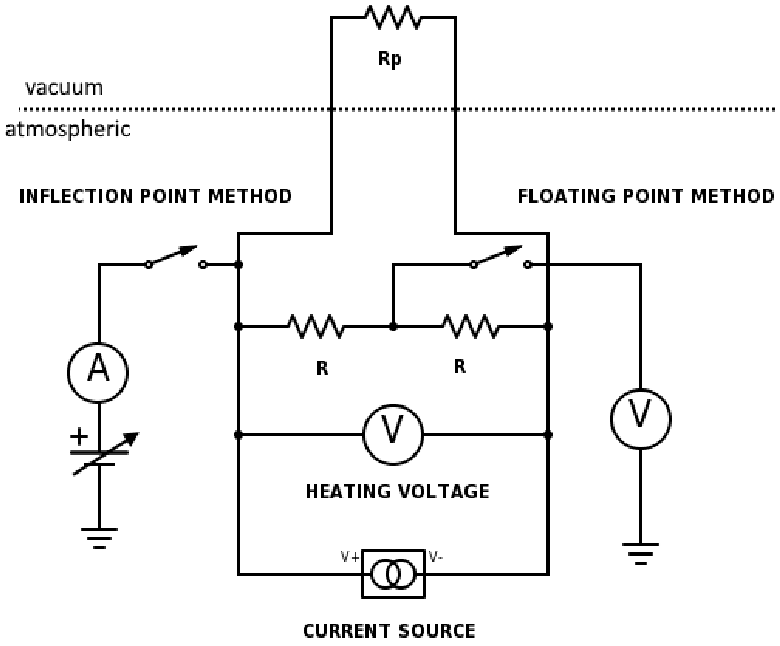

Figure 4.8: Schematic of emissive probe setup for both the *floating point method* and *inflection point in the limit of zero emission method*.

plot has to be shifted by half the heating voltage. A schematic of the setup is shown in figure 4.8. The *floating point with large emission method* is based on the fact that as emission is increased the floating potential of the emissive probe will approach the plasma potential [69]. For increasing probe temperature the floating potential will sharply increase but at a certain temperature suddenly plateau near the plasma potential. The most accurate way to estimate ϕ from a $\phi_f - T_w$ plot is by linear fitting both regions with their intersection defining the plasma potential. A less accurate way is choosing the saturation value as the plasma potential. Both numerical and experimental work have shown that for this method an emissive probe will always float $1 - 2\ T_e$ below the actual plasma potential [70]. For an accurate absolute measurement this has to be corrected for.

In the *inflection point in the limit of zero emission method* $I - V$ curves are taken for different probe temperatures to find the inflection point. Extrapolating these points to the limit of zero emission, i.e. $T_w = 0$, will yield the plasma potential. This is similar to the inflection point method for a regular Langmuir probe. Finding the inflection point has a large uncertainty due to noise being magnified in the first derivative. However since the *inflection point in the limit of zero emission* uses multiple data points this greatly reduces the error. The estimated error for the floating point method is about $0.1\ T_e$ in estimating the floating point plus a systematic error of $\sim T_e$ or, if is this is corrected for, an extra error ΔT_e, the uncertainty in T_e. The inflection point method has an error of about $0.1\ T_e$ plus the uncertainty in the heating voltage ΔV_H [70].

Emissive probe measurements in magnetised plasmas can be affected by the magnetic field. Electrons emitted perpendicular to the field can become trapped in gyro-orbits around the probe contributing to the space-charge and changing the characteristics of the probe. Experimental research has shown that the orientation of the probe with respect to the magnetic field lines is of greater influence than the magnetic field strength especially when parallel to the field $|\theta| < 15°$. However, sufficiently increasing the probe temperature will mitigate the effect of the magnetic field [38]. For a more in-depth treatment of emissive probes the reader is referred to the recent and excellent review of Sheehan [69].

4.3.1. Probe design

The emissive probe developed at the electric propulsion lab of UC3M consists of a alumina double bore rod of 1.6 mm outer diameter, 0.4 mm inner diameter. A 50 μm diameter thoriated tungsten (0.5%) wire folded and both ends inserted in the bores of the alumina rod. Thoriated tungsten is chosen because

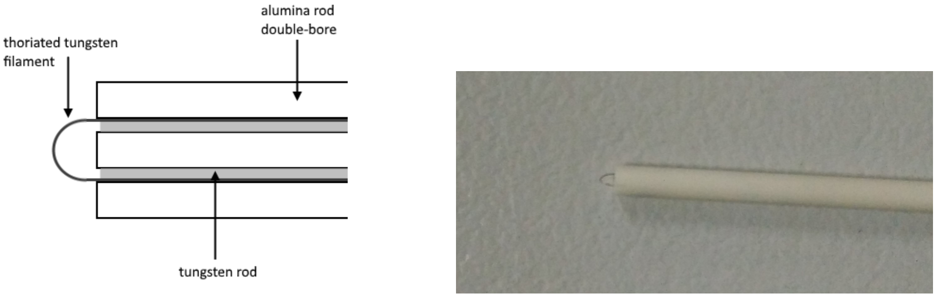

(a) Schematic cross-section of probe tip.

(b) Close-up of probe tip.

Figure 4.9: Emissive probe design.

it has an increased electron emission with respect to regular tungsten up to a factor 10^3 [69]. The fold forms a 1 mm half-loop protruding on one side of the alumina. Two 0.254 mm diameter tungsten wires are inserted into the alumina to pressure fit the thoriated tungsten wire. The protruding sides of both wires are crimped together to a copper wire to be connected to the vacuum feed-through. On the atmospheric side both leads are connected to a DC current source. Between the leads two 100kΩ resistors are connected in series and the midpoint is connected to a cable with a banana plug that fits the measurement equipment. An schematic cross-section of the emissive probe tip and an actual photo can be seen in figure 4.9

4.4. Faraday probe

Faraday probes (LPs) are an extension of planar Langmuir probes. Planar probes have the disadvantage of end-effects; the electric field is neither homogeneous nor strictly perpendicular to the collection area near the ends of the plane. Faraday probes mitigate this problem by adding a guard-ring biased at the same potential as the collector that does not contribute to the measured current. This forces a planar field over the collector. Faraday probes are usually not used to measure $I-V$ curves but instead are kept constant at a sufficiently negative voltage to ensure ion collection and are swept through the plasma (plume) to measure the spatial distribution of ion current density and the beam divergence. When the probe is operated in a Cartesian coordinate system the effective collection surface has to be corrected by a factor $cos\theta$, with $\theta = \tan^{-1}(r/z)$. If the density is known, the magnitude of the ion velocity can be derived from the current density:

$$j = enu_i \tag{4.46}$$

This is an interesting quantity to measure for several reasons: i) knowing the density and a cosine correction, the ion velocity u_i can be calculated. ii) knowing also T_e it is possible to calculate the thrust $F(z)$ up to a given $z = const.$:

$$F(z) = 2\pi \int_0^{R_V} drr[m_i u_{zi}^2(r) + T_e]n(r) \tag{4.47}$$

iii) Integrating a radial current profile yields the total beam current. Comparing this value at the thruster exit plane to the propellant mass flow rate can be used to estimate the propellant utilisation efficiency η_u of the thruster.

$$\eta_u = \frac{\dot{m}_i}{\dot{m}} = \frac{m_i}{e} \cdot \frac{2\pi \int_0^{R_V} drrj(r)}{\dot{m}} \tag{4.48}$$

It has to be noted that the above equation only accounts for singly charged ions.

iv) From the radial ion current density profile the divergence half-angle δ of the plume can be calculated. There are two ways to do define δ. The 95% divergence half-angle which is defined by the half-angle of the cone that contains 95% of the total beam current and is found by numerically solving equation 4.49 for $R_{0.95}$. Usually, for far-field measurements

$$\frac{2\pi \int_0^{R_{0.95}} j(r)rdr}{2\pi \int_0^{R_V} j(r)rdr} = 0.95 \tag{4.49}$$

From $R_{0.95}$ the divergence angle $\delta_{0.95} = \tan^{-1}(R_{0.95}/z)$ can then be found. The second definition sets the cosine of the divergence angle equal to a momentum weighted average of the current density which is approximated with the ratio of axial current to total current [40, p.23]:

$$\langle\cos(\delta)\rangle = \frac{2\pi \int_0^{R_V} j(r)\cos(\theta)rdr}{2\pi \int_0^{R_V} j(r)rdr} \tag{4.50}$$

where $\cos(\theta) = z/\sqrt{r^2 + z^2}$. Usually the latter definition gives a slightly smaller value for the divergence angle but is closer related to the axial momentum, and therefore the thrust.

Since the probe is always facing in the axial direction the effective collection surface is dependent on the radial position. On the centre line the probe surface is perpendicular to the ion beam but far off-axis it become more and more tangential. The effective area facing the thruster is decreased with a factor $\cos(\theta)$. The current density $j(r) = j_z(r)\cos^{-1}\theta$, where $j_z = I/A$, the measured current over the probe area. The factor $\cos^{-1}\theta$ is unity on-axis and increases to about a factor 3.5 in the wings of the plume, depending on the axial position.

Facility background pressure can influence Faraday probe measurements. High velocity ions have charge exchange (CEX) collisions with the cold background gas resulting in slow ions and fast neutrals. This population of slow ions will still be collected by the probe due to its negative potential overestimating the beam current, especially far off-axis where the beam pressure and background pressure are of similar magnitude. One way to mitigate this is to shield the probe with a collimator or a magnetic field allowing only high energy ions to reach the collector, but this adds complexity to the probe design. Moreover some CEX ions due collisions with beam neutrals are to be expected and these would also be filtered by shielded probes. Research on the influence of the background pressure on Faraday probe measurements showed that at each angular position θ the measured current density as a function of the background pressure is a linear relationship, which can easily be extrapolated to zero background pressure. The extrapolated current density profile is representative of that in true vacuum. [6]. Note that because both the contributions of CEX and the cosine correction are both largest off-axis the current density might be overestimated even more.

4.4.1. Probe design

The Faraday probe is made of a collector and guard ring both conducting, but electrically isolated from each other. The gap between the two should be small enough to ensure a flat electric field. Conventional design criteria mention a gap of less than 5-10 Debeye lengths which, depending on the plasma density, is of the order of less than 100 micron. However recent work by Brown and Gallimore showed that this criterion can be relaxed when using a geometric correction factor that accounts for collection of ions in the gap. Fast ions in the gap are slowed down when striking the dielectric baseplate and are then collected by the side-walls of either collector or guard ring. By comparing probes with different collection areas and gap widths and by varying the differential potential between collector and guard ring, their correction factor was proven to accurately model this effect. [13]

The effective collection area is the collector area A_C plus a gap correction factor κ_G. The correction factor is the gap area $\pi(R_{GR}^2 - R_C^2)$ with R_{GR} the inner radius of the guard ring, multiplied by the ratio of the side-wall surface area of the collector to the sum of the surface areas of both the collector and guard ring side-wall surface areas, which are $2\pi R_C h_C$ and $2\pi R_{GR} h_{GR}$ respectively, with h the height. Correction factor is then:

$$\kappa_G = \pi(R_{GR}^2 - R_C^2)\left(\frac{2\pi r_c h_c}{2\pi r_c h_c + 2\pi R_{GR} h_{GR}}\right) = \pi(R_{GR}^2 - R_C^2)\left(\frac{R_c}{R_c + R_{GR}}\right) \tag{4.51}$$

where the second equality holds in the case $h_C = h_{GR}$ as it the case for our probe. The effective collection area is given by:

$$A_{eff} = A_c + \kappa_G = A_c\left(\frac{R_{GR}}{R_C}\right) \tag{4.52}$$

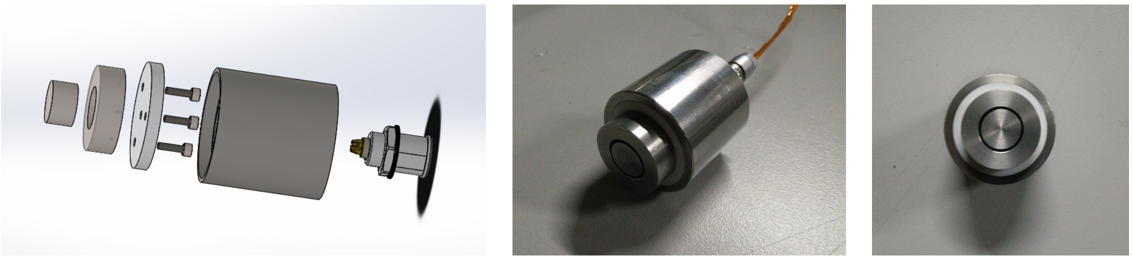
(a) CAD design exploded view (b) Front view (c) Top view.

Figure 4.10: Faraday probe design.

Where again the second equality only holds for $h_C = h_{GR}$; when the collector and guard ring have the same height the collection area is effectively increased by the ratio of the guard ring inner radius to collector radius.

The collector has a radius of 5 mm and is made of stainless steel. The guard ring, also made of stainless steel has an inner radius of 5.5 mm and an outer radius of 10 mm. The gap width is therefore 0.5 mm. The aforementioned effective area is therefore 10% larger than the collector area.

Both the guard ring and collector have tapped holes to mount them to a Macor disc. The disc is pressure fit to the stainless steel cylindrical sleeve which will be grounded. The sleeve houses a 4 pin connector: one lead is connected to the bolt fastening the collector, another to one of the bolts of the guard ring. The other two leads are connected to an platinum RTD sensor embedded in the guard ring. This sensor monitors the temperature of the guard ring which is assumed to be equal to that of the collector. A CAD drawing and a photo of the Faraday probe are shown in figure 4.10

The temperature of the probe doesn't give any relevant information about the plasma but is installed as a safety measure. The power flux to the probe can be estimated from the ion energy flux density: $\frac{1}{2} n m_i u_i^3$ which at the throat where $M = 1$, is roughly $10^{-16} \cdot n T_e^{3/2}$. As an upper estimate a $10 eV$, $10^{20}\ m^{-3}$ plasma would give a power flux of about $3 \cdot 10^5\ W/m^{-2}$. Assuming purely radiative losses this would result in a temperature of about $1800\ K$ or a little over $1500°C$ which is above the melting temperature of steel. Although this is a very optimistic upper estimate and although the plasma density and therefore power flux density dramatically decrease downstream, even for more reasonable plasma conditions of $10^{18}\ m^{-3}$ the temperature could increase up to $300°C$.

Summary

In this chapter presented the theory behind the plasma diagnostics used in this study. The most important diagnostic is the Langmuir probe which is used to measure the plasma density, electron temperature and plasma potential. Several theories used to infer the plasma density from the current-voltage characteristic have been discussed. The leading Langmuir probe theories used in this work are the BRL and ABR theories. The former takes into account the angular momentum of the ions, and ignoring collisions, tends to over-predict the density while the latter ignores angular momentum and generally under-predicts the density. Parametrisations of both theories are used in this study as it greatly speeds up the post-processing of Langmuir probe data. A post-processing scheme has been discussed that iteratively fits the ion-saturation and electron-retardation parts of the $I - V$ characteristic. The theory of RF fluctuations on Langmuir probe measurements has been discussed and and RF-compensated probe that aims to mitigate these effects, was introduced. Then Emissive probes were introduced, including their capabilities, underlying theory. Emissive probe measurements in this study are conducted using the *floating potential in the limit of large emission*. This allows for fast plasma potential measurements yielding a value that floats about 1 T_e below the actual plasma potential. Faraday probes were introduced alongside a discussion of the various parameters that can be derived from the resulting ion current density profiles. FP measurements are used to infer the plume divergence, total current (and hence utilisation efficiency) and estimates of the ion velocity and thrust when combined with Langmuir probe measurements. Also the design of the Faraday probe used in this study was presented as well as a short analysis on the effects of the spacing between the guard-ring and collector.

5

Experimental Setup

Introduction

This chapter presents the experimental setup used in this study. Firstly the helicon plasma thruster prototype is discussed that is the source of the plasma and generates the magnetic nozzle. An overview is given of its characteristics and dimensions and the nominal configuration used in this study. The RF system and antenna powering the thruster are also discussed. Then the vacuum facility is introduced, its dimensions and pumping capacity followed by an overview of the probe positioning system and its capabilities, how the system is aligned and the operating software. Then the setups for each diagnostic are discussed in the order Langmuir probe, Faraday probe and emissive probe .

5.1. HPT05 prototype

The magnetic nozzle that is the object of this study is generated by helicon plasma thruster prototype HPT05 developed by EP^2 and SENER. It is designed as a flexible testing platform for different geometries, magnetic configurations, antennas, frequencies and gases. The goal is to verify the existing models, understand the loss mechanisms and optimise its performance.[59] The relevant design parameters consist of the chamber length L[1], mass flow $\dot{m}$, RF power P, magnetic field strength B and RF frequency f. Currently the facility has the option to fuel the thruster with either Argon or Xenon, although in the future other propellants will be added.

The chamber consists of a quartz tube and is lined by three water-cooled electromagnets: two solenoids for the axial magnetic field in the chamber and another solenoid for the nozzle which can be operated separately from the chamber solenoids. An optional annular permanent magnet can be placed at the back wall for magnetic screening. In between the chamber magnets sits a 75 mm half-helical antenna. The back-wall consists of an alumina injector plate housing the annular magnet. An overview of the design parameters and ranges are shown in table 5.1.

Table 5.1: Design parameters for the HPT-05 prototype.

Variable	Nominal value	Operating range
Chamber diameter	30 mm	–
Chamber length	150 mm	0.0 - 150
Mass flow	1.5 mg/s	0.1 - 2.0
Power	1.0 kW	0.5 - 1.5
Magnetic field	400 G	0.0 - 800
RF frequency	13.56 MHz	13.56 or 27.12
Antenna	75 mm half-helical	–
Propellant	Argon	Argon or Xenon

---

[1] The chamber length can be varied by varying the position of the injector plate inside the chamber.

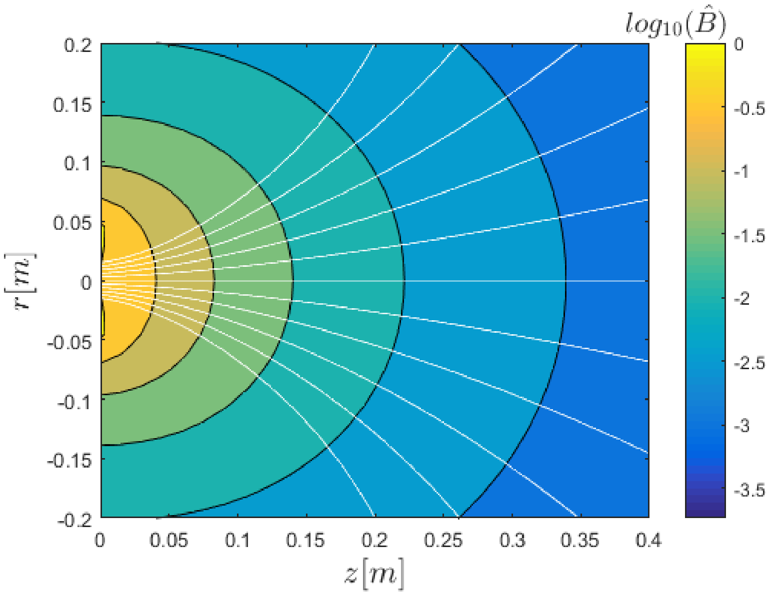

Figure 5.1: Magnetic field in the plume for the nominal configuration.

5.1.1. Nominal configuration

The nominal configuration used in this study deviates slightly from the nominal design values. The rationale for this is that this configuration was found to produce a stable plasma with a denser, brighter plume. The nominal value of the RF power is 500 W which is the highest value allowing stable continuous operation over a long period of time (> 1 hour) at the nominal magnetic configuration. The nominal magnetic configuration is specified in terms of the current and polarity of the magnetic field coils, which are part of the intellectual property of SENER and UC3M. The magnetic field in the plume is simulated with a simple code which calculates the magnetic field from the stream function of a superposition of current loops that represent the magnetic coils of the HPT-05. A map of the magnetic field in normalised quantities is shown in figure 5.1. The magnetic field lines originate from the thruster exit (at $z = 0$) with the outer most from r = ±15 mm. The nominal magnetic field strength at the center of the exit plane is $B_0 = 560$ G. The nominal propellant is Argon at a flow rate of 50 sccm, or 1 mg/s. The chamber dimensions are 15 mm radius and 150 mm length. The RF driving frequency is 13.56 MHz. The antenna is specified in section 5.1.2.

5.1.2. RF-system

The HPT-05 prototype was designed with a custom made RF-circuit and half-helical antenna made by SENER. However this circuit was not functional for most of the duration of the test campaign and therefore the thruster is operated with a commercial off-the-shelf (CoTS) RF-system and a custom made, double loop antenna. The RF-system consists of a Seren IPS HR2001 RF generator, a Seren IPS AT20 matching network and a Seren IPS MC2 automatic matching network controller.

A discontinuity in impedance along an RF-circuit can lead to part of the wave being reflected. Therefore the matching network ensures that the impedance of the antenna + thruster is matched to that of the RF generator to maximise the forward power and minimise the reflected power. The matching network consists basically of a parallel (the load) and a series (the tune) variable capacitor which can be tuned to adjust the impedance. The matching network used in this set-up is designed for capacitively coupled loads which means the matching network has a series inductor. The HPT is inductively coupled. The result is that the matching point is near the limits of the matching network, with a tune at 3% and the load at 97%. Due to this, the auto-matching function of the matching network is not available and matching is done by hand. During start-up the system heats up and there is a drift in impedance that has to be corrected for. After the system is thermally stable the matching point is stable too, untill the power is increased. Then the matching point has to be re-adjusted to minimise the reflected power until it is stable again. Over the range of nominal operating conditions, 200-900 W, the matching point only varies a few percent.

The antenna consists of a copper rod as the signal line and copper tube 16 mm diameter and 6 mm thickness as the return line in a coaxial configuration. An image of the custom loop antenna is shown in figure 5.2. The signal line is connected through a LewVac FHP5 high power feed-through to the matching network, while the return line (tube) is connected to the vacuum chamber wall. On the atmospheric side the matching network and amplifier are grounded to the vacuum chamber. After disconnecting and reconnecting the thruster for modifications the matching point of the RF-system and antenna were checked with a Rohde & Schwarz Vector Network Analyser. If the matching point was found to be 'off' it was reconfigured by adjusting the tune and the load of the matching network.

Figure 5.2: Photos of the antenna used in this study.

During the test-campaign several improvements where made to the connections which helped reduce arcing, radiation at the atmospheric side and unstable impedance. Operation was completely halted for several weeks to investigate and mitigate ambient radiation on the atmospheric side. Large electric fields where indeed measured outside the vacuum chamber. To mitigate this and provide a safe working environment a Faraday cage made of 2 mm thick aluminium plates was manufactured to house the RF equipment and shield the feed-through connection. The Faraday cage was bolted to the vacuum chamber and in this way grounded. The RF-equipment was grounded by bolting copper straps to both the equipment and the Faraday cage. The electric field measurements where again performed after installation of the Faraday cage and were found to be reduced to below critical levels.

5.2. Vacuum Chamber

The vacuum facility of the electric propulsion lab consists of a customized Oerlikon cylindrical vacuum chamber, 3.5 m long with a 1.5 m diameter. It is optimized for testing low-mid power electric thrusters up to 2 kW. It has two full-diameter access doors, multiple viewports for DN250CF flanges or quartz windows. The chamber is evacuated by a Leyvac LV80 (80 L/h) drypump, two MAGW2.200iP (2000 L/s each) turbomolecular pumps and three Leyvac 140 T-V cryopanels (30.000 L/s Xenon combined). The minimum pressure achievable is of the order of 10^{-7} mbar and 10^{-5} mbar with a 20 sccm Xenon flow which can be maintained continuously for five days. Before thruster operation the vacuum has to be below $5{\cdot}10^{-7}$ mbar , after turning on the gas feed the pressure increases nominally to $2.5{\cdot}10^{-5}$ mbar. The antenna is only powered on if the background pressure is less than $5{\cdot}10^{-5}$ mbar. Two photos of the outside and inside of the vacuum facility are shown in figure 5.3.

5.3. Probe Positioning System

To properly assess the plasma parameters in the plume it is essential to perform spatially resolved measurements. To move the probes with respect to the plume a 3-DOF probe positioning mechanism has been developed. The design of this system has been the topic of the internship for the Space Engineering master track. Detailed design of custom pieces, manufacturing, assembly, integration with the different probes and development of the operating software were done during this thesis. The system consists of three translational stages in a Cartesian configuration of a $1500 \times 925 \times 770\ mm^3$ measurement volume. The translational stages use steel-reinforced polyurethane belts and are driven by vacuum-rated stepper motors. All bearings in the system are passive linear bearings avoiding the

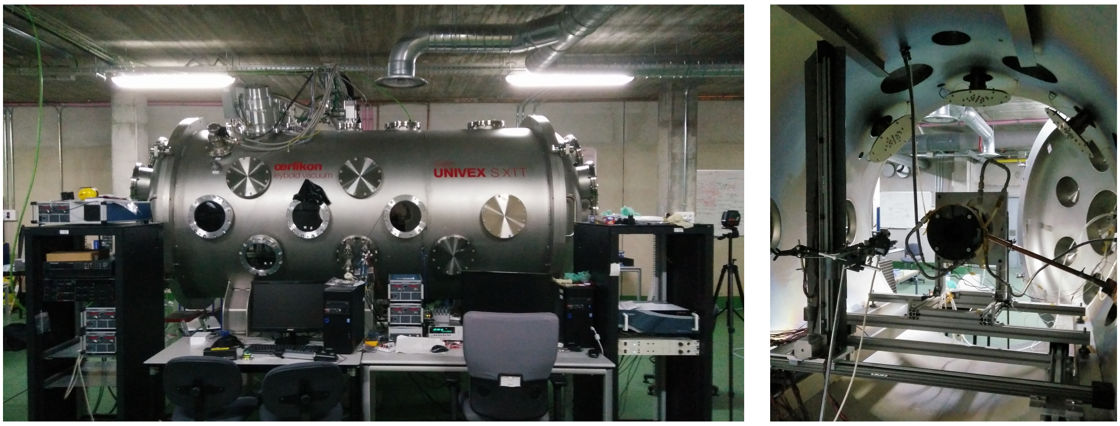

(a)

(b)

Figure 5.3: Vacuum facility of the EP2 plasma propulsion lab.

need for lubricants that would complicate vacuum operations. The stepper motors are driven by two Arun Microelectronics SMD210 stepper motor drivers which can be remotely operated from a PC. The stepper motors have 200 steps per revolution and turn at a minimum speed of 10 Hz which in a loaded system can be comfortably increased up to 60 Hz. With a transmission of 70 mm/rev for the Z and X axis and 54 mm/rev for the Y axis this results in speeds from 3.5 mm/s up to 21 mm/s (2.7 to 16 mm/s). It takes the system little over a minute to traverse any axis. The resolution of the system is 0.35 and 0.27 mm respectively which is of the order of the precision which is about 0.3 mm. For reliable results measurements should be conducted with a resolution of no less than 1-2 mm. The total accuracy of the positioning system is largely dependent on the alignment of the system to the thruster. The face of the vertical Y-stage facing the thruster plume is covered with a grounded 2 mm expanded graphite plate to shield the belt and probe cabling from the ion beam. Whether this relatively large grounded structure will perturb the plasma upstream has to be investigated. Mounted on the vertical stage is a aluminium extension with on the far side an aluminium block that is machined to fit one RF-compensated Langmuir probe, one Faraday probe, and any combination of three emissive and simple Langmuir probes. A picture of the probe positioning system and the probe interface can be seen in figure 5.4. Note that the horizontal extension is not yet installed in these pictures. The probe mount and the graphite wall are isolated from the base of the system and the chamber by the plastic bearings of the X-axis and the probe platform is therefor floating.

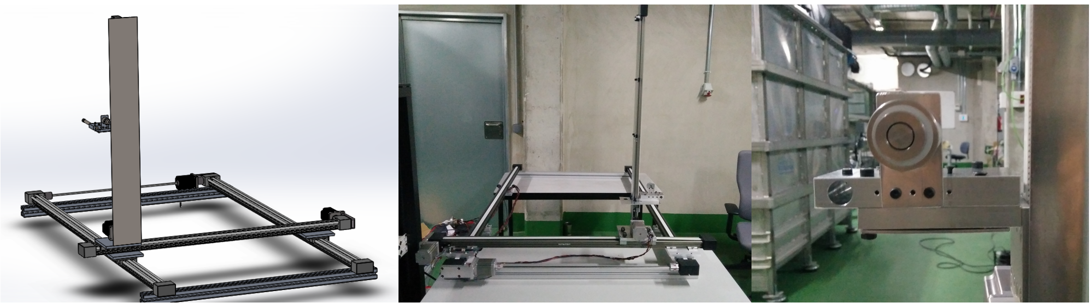

(a) CAD drawing.

(b) Probe positiniong system.

(c) Close-up of probe interface with Faraday probe installed.

Figure 5.4: Probe positioning system.

5.3.1. System alignment

The probe positioning system has to be aligned to the thruster to ensure accuracy in the position of the probe. For alignment the thruster is aligned along the axis of the vacuum chamber using a plane laser. Similarly the probe positioning system is aligned along the same axis as well as in the plane perpendicular to it. Both the thruster and the positioning system can be adjusted at the corners of their support using threaded feet. After alignment to the chamber the positioning system is clamped to the chamber. Whenever the thruster is removed for maintenance or improvements it is realigned with the chamber. After realignment the cross-hair of the plane laser is aligned along the axis of the thruster. The positioning system is then remotely positioned such that the centre of the Faraday probe is in the cross-hair, and the internal X,Y position of the stepper motors is noted. The Langmuir probe is then positioned on axis and incrementally moved towards the thruster until it is at the exit plane, noting the internal Z position of the stepper motor. The noted values for Z,X,Y are inserted into the settings file of the LabVIEW program from which it calculates the system zero. This zero is defined as the centre of the thruster exit plane. The offset between the probes is also stored in the program to account for the fact that the X,Y coordinates are aligned with the Faraday probe while for the Z coordinate this has been done with the Langmuir probe. Using the offset of the system and the probe offsets the program automatically operates with the correct reference frame of the probe in use (with respect to the system zero). Alignment of yaw and pitch of the thruster is for now done by visually leading to a small misalignment which is noticeable in the measurements. Here there is some room for improvement. Not including the yaw and pitch misalignment the absolute error in the position is estimated to be 1 mm in all three dimensions, for measurements up to 500 mm downstream.

5.4. Automated Probe Scanner Software

Many measurements have to be taken to generate a spatial profile of sufficient resolution. Consider then that such measurements have to be repeated for different probes and different thruster settings and one quickly realises that manually taking measurements would be a Sisyphean task. Therefore a LabVIEW program has been developed that integrates the remote control of the probe positioning system as well as that of the Keithley and DAQ measurements. A schematic of the integrated set-up of PC, Keithley, DAQ and motor drivers that facilitates this remote control is shown in figure 5.5.

The program allows the user to either move the system to a manually or upload a pre-programmed path. When uploading a pre-programmed path the system performs a measurement at each coordinate along the path. When taking measurements the data (either single measurements or an $I - V$ sweep) are stored in a file labelled with the date and time of measurement and the corresponding coordinate of position to later be easily accessible for post-processing. A screenshot of the UI of the program can be seen in figure 5.7.

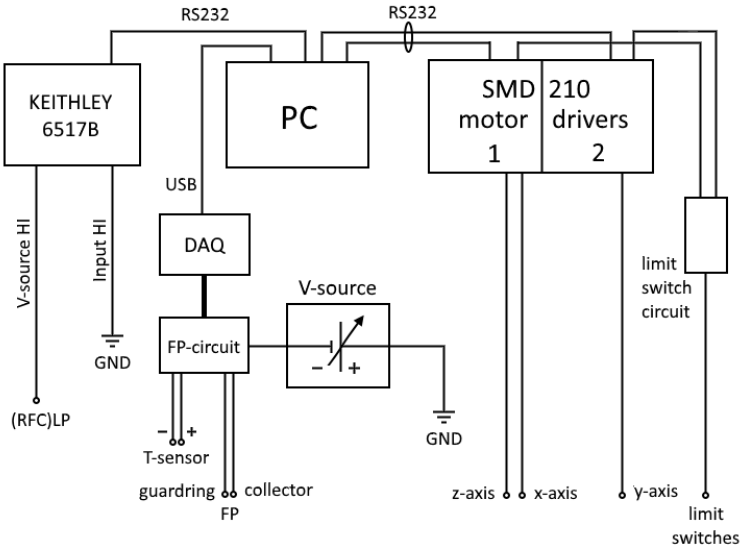

Figure 5.5: Schematic overview of integrated measurement set-up.

5.5. (RF-compensated) Langmuir probe setup

The electrostatic probe set-up consists of the Langmuir probe, RF-compensated Langmuir probe, emissive probe and Faraday probe designs detailed in chapter 4. All probes are mounted on the probe positioning system described in the next section. IV sweeps are conducted with a Keithley 6517B electro-meter in the forced voltage measure current (FVMI) mode which internally connects the voltage source and current meter in series. The sweeps take about 30 seconds to complete. The 6517B has a sensitivity ranging from the mA to the pA range and the measurement resolution ranges from 3.5 to 6.5 digits, where a lower resolution results in a faster measurement. The voltage source can deliver up to 1 W in either a ±100 V or ± 1000 V range, limiting the maximum current to 10 mA or 1 mA respectively. Voltage sweeps can be performed between any two voltages within the selected range with a resolution of 5 mV and 50 mV respectively. A time delay can be programmed before the measurement is taken at each step. The Keithley further allows to program median filters of a given rank and running or repeating averaging filters with a given window. The Keithley is connected to the PC through a RS-232 cable and can be remotely operated.

5.6. Faraday probe set-up

The Faraday probe measurements are conducted with a National Instruments NI-9220 DAQ. It can handle input voltages $\pm 10\ V$ and has a 16-bit resolution. The collector (COL), the guard-ring (GR) and both leads of the RTD sensor (T+,T-) of the Faraday probe are connected to a multipin feed-through on the vacuum side. On the atmospheric side the corresponding pins are connected to a custom made circuit, hereafter referred to as the FP-circuit.

The circuit consists of a variable measuring resistor R_m and a Wheatstone bridge for the temperature sensor. The collector is connected in series with a variable resistor to the negative output of a variable voltage source, whose positive output is grounded to the chamber. Another wire coming from the negative voltage source output bypasses the R_m and is connected to the guard-ring. This way both collector and guard-ring are kept at the same (negative) voltage with respect to the chamber. The current through the measurement resistor produces a differential voltage which is measured with the DAQ. The variable resistor is chosen such that the maximum voltage drop over the resistor is $0.1V$ (preventing the collector bias to deviate too much from the guard-ring bias. The DAQ has 16 bit with a range from $\pm 10\ V$.

The temperature sensor is a platinum RTD with a base resistance of $R_0 = 100\Omega$ at $0°C$ and for $T \geq 0°C$ changes resistance with temperature as:

$$R(T) = R_0(AT^2 + BT + 1) \tag{5.1}$$

where $A = 3.908 \cdot 10^{-3}$ and $B = -5.775 \cdot 10^{-7}$. The resistor is connected in a Wheatstone bridge with two resistances of 16 kΩ and one of 100 Ω. The source voltage for the bridge is a 9V-battery. Both the source voltage and the bridge voltage are measured with the DAQ. The bridge voltage in a Wheatstone bridge is given by:

$$V_B = \left(\frac{R_2}{R_1 + R_2} - \frac{R_x}{R_x + R_3}\right) \tag{5.2}$$

where in our case $R_1 = R_3 = 16\ k\Omega$ and $R_2 = R_0 = 100\Omega$ and $R_x = R(T)$. Since all other resistances are known, the RTD resistance can then be inferred from the ratio of the source and bridge voltages.

$$R(T) = \frac{R_1}{\left(\frac{R_2}{R_2+R_1} - \left(\frac{V_B}{V_S}\right)\right)^{-1} - 1} \tag{5.3}$$

Knowing $R(T)$ the temperature can then be found from the inverse of the quadratic equation 5.1. The whole measurement circuit of the RTD sensor is also connected to the output of the voltage source such that it is at the same voltage as the collector and guard ring. This allows to use one common line(GND) pin of the DAQ for the whole circuit, which is connected through a 1 MΩ resistor. A diagram of the circuit for the Faraday probe can be seen in figure 5.6.

During measurements it was found that switching the measuring resistor proved rather cumbersome and that the accuracy was only sufficient near the axis. Radially outward the density drops quickly and the collected current is too small to produce a voltage with a sufficient signal-to-noise ratio. The set-up

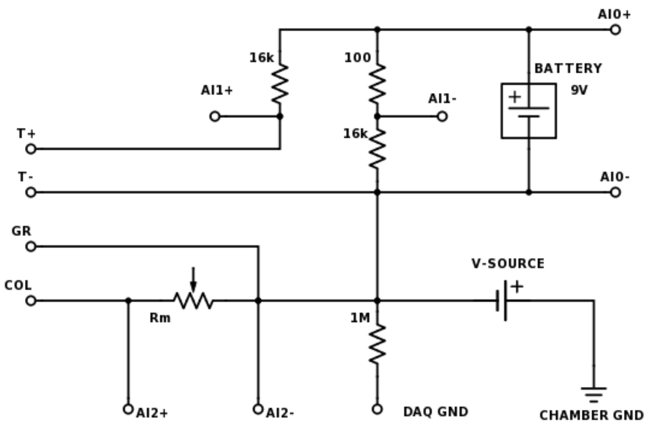

Figure 5.6: Circuit diagram for Faraday probe circuit. AIx+ and AIx- are the positive and negative analog inputs of channel x of the DAQ.

was modified to use the Keithley to in the FVMI configuration (similar to the LP set-up). The collector was connected through the Keithley and kept at a fixed -30 V while the Keithley measured the current. The guard ring was connected to a separate voltage supply also at -30V. This has the advantage of the Keithley automatically adjusting its sensitivity such that accuracy is maintained both on axis and in the wings of the plume. In earlier measurements the previously described set-up using the DAQ was used while later measurements use the Keithley set-up. Each case will be mentioned accordingly when the results are presented in later chapters.

5.7. Emissive probe set-up

For the emissive probe measurements the Keithly is not connected in FVMI mode and the EP probe is connected to the input HI while the input LO is grounded to the chamber. The emissive probe is heated by a BK precision PVS60085MR current source with up to 5 A. The leads of the emissive probe are connected to high gauge wire to be able to withstand the high currents. Both leads each use two pin pins of the multi-pin for the same reason. On the atmospheric side two 100 kΩ resistors are placed in series between the positive and negative lead of the probe. From the midpoint between them a cable terminating a banana plug is soldered that can be connected to the Keithley. In the floating point method the probe is fed a heating current of 0.8 A, having an estimated temperature of 1600 K. Its floating potential is measured by the Keithley. The Emissive probe can be operated automatically and remotely using the LabVIEW program.

Summary

This chapter introduced all the equipment and the overall measurement setup in detail. Firstly the specifics of the HPT05 prototype were discussed. In this study the thruster is mainly operated in one specific configuration, were only the RF power is sometimes varied. The nominal configuration is 500 W RF power at 13.56 Hz, 50 sccm Argon and a magnetic field of 560 G at the exit plane. The thruster resides in a vacuum chamber which is at $2.5 \cdot 10^{-5}$ mbar during operation at 50 sccm. Four different diagnostic probes are mounted on a probe positioning system that has three degrees of freedom and is aligned with the thruster. Its translational accuracy is ±0.3 mm and the error due to misalignment in yaw and pitch are estimated smaller than 1 mm. The $I - V$ curves of the (RF-compensated) Langmuir probe are obtained with the Keithley sweeping from ±100 V in steps of 1V. The Faraday probe is biased at -30 V and the current is measured either directly with the Keithley or through a measurement resistor using the NI-9220 DAQ. The emissive probe is heated to 1600 K using 0.8 A. This potential is measured using the Keithley. Both the positioning system as well as the Keithley and the DAQ are connected to a PC and integrated using a LabVIEW program. This allows for fast, automated line measurements using any probe and along any dimension. The program automatically operates from the reference frame of the probe in use.

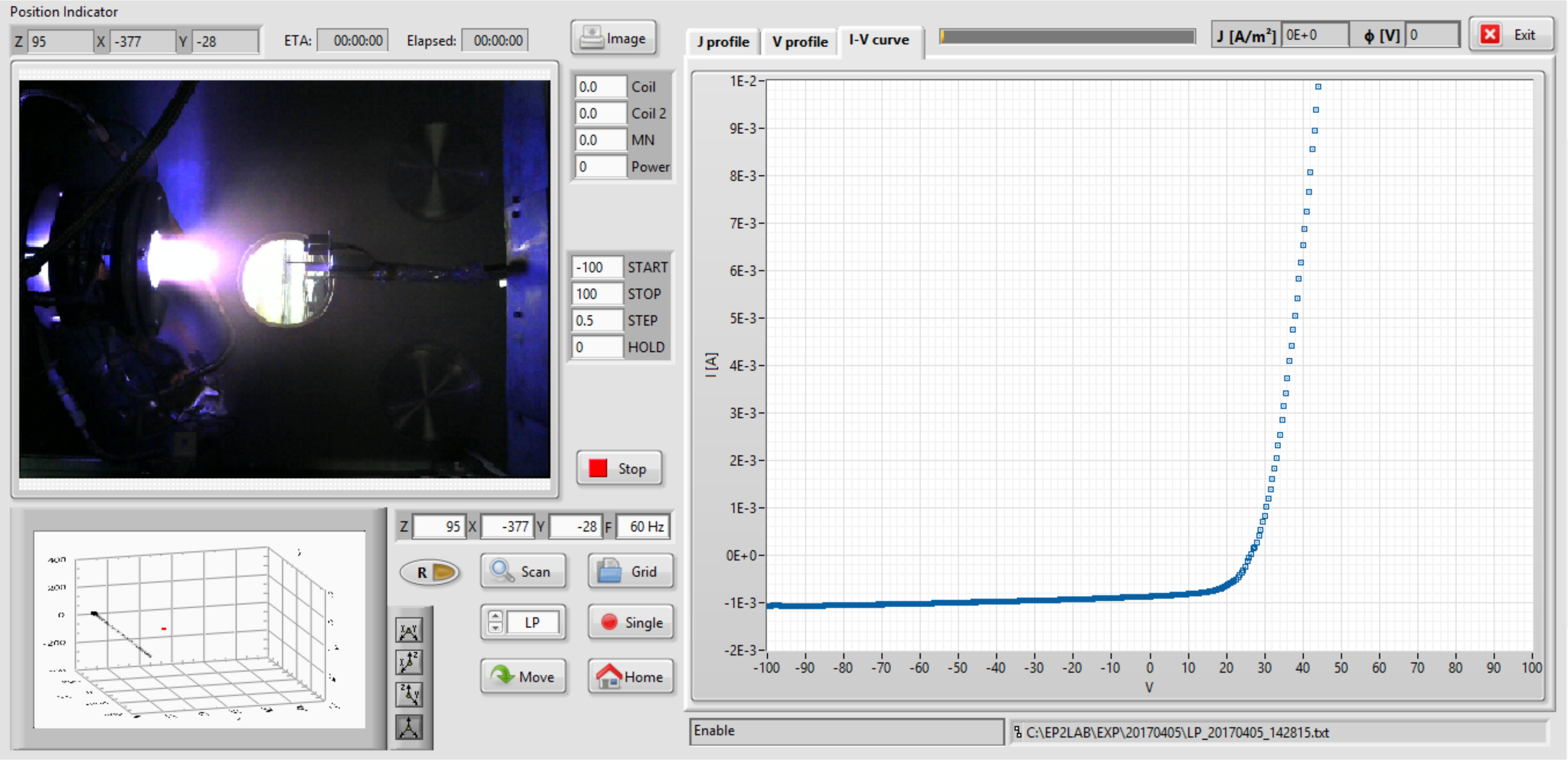

Position Indicator
Z 95 X -377 Y -28
ETA: 00:00:00
Elapsed: 00:00:00
Coil 0.0
Coil 2 0.0
MN 0.0
Power 0
START -100
STOP 100
STEP 0.5
HOLD 0
Z 95 X -377 Y -28 F 60 Hz
J [A/m²] 0E+0
ϕ [V] 0
Enable
C:\EP2LAB\EXP\20170405\LP_20170405_142815.txt

Figure 5.7: Screenshot of LabVIEW program UI.

6

Operational and Measurement Procedures

Introduction

All experiments have been conducted according to a predefined test plan. To ensure uniformity and to allow for reproducibility a series of procedures have been developed that help standardise and guide the experiments. In this chapter these procedures, both operational and experimental are defined. In particular this chapter explains the test plans. It furthermore presents the operational procedures for the thruster and the measurement equipment and the way the raw data are managed.

6.1. Test Plans

This section will present the test-plans that define the experiments that substantiate this report. Two different plans have been defined containing each a series of measurements. The first test plan consists of 5 experiments that aim to characterise the LP, RFCLP and EP probes, validate the implementation of Chen's post-processing method and establish the repeatability of measurements. The second test plan consists of series of 7 experiments to characterise the plume in terms of spatially resolved plasma parameters, current density profiles and derived quantities. The paragraphs that follow provide more detailed information on each experiment stating the objective, a description of the test and the hypothesis. Tables 6.16 and 6.17 at the end of this chapter profice a summary of all tests.

6.1.1. D1 - Evaluation of iterative post-processing

The goal of the first test is to evaluate the implementation of Chen's iterative post-processing scheme (IPS). If the iterative scheme is found to be an improvement on the alternative, the planar approximation, it will be used to process all subsequent $I-V$-curve measurements. There are two criteria by which to judge this method. Firstly it should adequately predict the plasma parameters n, T_e. Ideally the results would be calibrated to a known plasma source or a validated diagnostic. Since neither option is available we will compare the result to the planar approximation assuming the latter gives a correct value. As a pass criterion we choose a maximum disagreement of 10% between the two methods.

Secondly the fit of the iterative method should be an improvement on the planar approximation to be of added value. The second criterion therefore should be that the fitting error of the ϵ_{IPS} to be smaller than the error of the planar approximation fit ϵ_{PA}. There is also a more qualitative criterion for an improved fit. Subtracting the fitted ion current from the total current results in the electron current which is assumed to be Maxwellian. A 'better' fit of the ion current would therefore result in a electron current that is linear over a larger domain in a semi-log plot.

To make a more solid comparison the measurements should be taken under different circumstances. Since it is difficult to provide a plasma with a priori known properties instead $I-V$ curves can be measured at different axial positions. The density and potential and possibly the electron temperature are expected to decrease downstream. Axial measurements also ensure that the probe is aligned with the flow avoiding interference due to the plasma flow. The closest measurement possible without the probes visibly interfering with the plasma is at $z = 20$ mm. Measurements are taken up to 200 mm provide a range of plasma parameters. The axial resolution is limited to 20 mm to limit the measurement time; a single $I - V$ curve takes about 30 seconds to measure. Repeating the axial scans at different RF-power further increases the diversity of plasma parameters, therefore measurements are taken at 500, W, 650 W and 800 W. The other justification for this range of settings is to prevent taking redundant measurements. This data will also be used for characterisation of the plume. The details are summarised in table 6.1.

Table 6.1: T.D1 - Evaluation of iterative post-processing algorithm

Objective	Evaluate the iterative post-processing scheme
Hypothesis	Method 'better' fits the $I - V$-curve and adequately predicts plasma parameters.
Test	Compare fitting and resulting parameters to planar approximation.
Criterion	Agreement of n, T_e within 10%, fitting error $\epsilon_{IPS} < \epsilon_{PA}$
Thruster Settings	
RF-power	500, 650, 800 [W]
Magnetic Configuration	nominal
Mass-flow rate	Argon 50 [sccm]
Diagnostic Settings	
Probe	simple Langmuir (r: 0.127, L:0.2 [mm])
Position	Axial: x, y(0,0), z(20:20:200) [mm]
Voltage	-100:0.5:100 [V]

6.1.2. D2 - Hysteresis of $I - V$ curves

Theoretically the direction of the voltage sweep should not be of influence on the $I - V$ characteristic. However due to the near instantaneous switching on of the voltage at the start of the curve some transient effects could occur. This can be easily verified by comparing two $I - V$ curves taken at the same operating point but swept from positive to negative voltage and vice versa. The data for this experiment were taken during a short test-campaign of SENER testing their half-helical antenna and custom RF-system. The operating power was only 300 W and because of that the magnetic field was slightly lower than in the nominal configuration used in most of the other experiments. However, since the the exact operating point for this experiment is irrelevant this is not further specified. This test can be repeated for any operating point. The $I - V$ curve was taken on-axis (to align with the flow) and at $z = 40$ mm. The axial position is also not crucial for this experiment, and is chosen arbitrarily. The details are summarised in table 6.2.

Table 6.2: T.D2 - $I - V$ curve hysteresis

Objective	Assess hysteresis due to the direction of the voltage sweep.
Hypothesis	$I - V$ curve is insensitive to sweep direction.
Test	Compare $I - V$ curves and resulting plasma parameters for both directions
Criterion	$I - V$ curve data points and resulting plasma parameters are within 10%
Thruster Settings	
RF-power	300 [W]
Magnetic Configuration	sub-nominal
Mass-flow rate	Argon 50 [sccm]
Diagnostic Settings	
Probe	simple Langmuir (r: 0.127, L: 0.2 [mm])
Position	(z, x, y) = (40,0,0) [mm]
Voltage	-100:0.5:100 [V] AND 100:-0.5:-100 [V]

6.1.3. D3 - Repeatability of $I - V$ curve measurements

To quantify the repeatability of the $I - V$ curve measurements a series of 10 curves are taken with the simple LP at the same operating point and position. For a stable plasma and a precise setup the plasma parameters derived from the $I - V$ curves should be of similar value with a small spread. A sample of 10 measurements should be sufficient to derive a standard deviation. From the sample a 95% confidence interval can be determined. The limits of the 95% divided by the mean give a sense of the relative error in these measurements. These samples can be taken at an arbitrary operating point, in this case on axis, at 50 mm downstream, with 500 W RF power and a magnetic configuration slightly deviating from the nominal one. The magnetic field is not crucial for this measurement.The details of this test are summarised in table 6.4.

Table 6.3: T.D3 - Repeatability of $I - V$ curve measurements

Objective	Assess repeatability of $I - V$ curve measurements
Hypothesis	Variation in plasma parameters of consecutive $I - V$ measurements is small.
Test	Determine plasma parameters from a sample of 10 $I - V$ curves.
Criterion	Resulting plasma parameters are within 10% of the mean.
Thruster Settings	
RF-power	500 [W]
Magnetic Configuration	super-nominal
Mass-flow rate	Argon 50 [sccm]
Diagnostic Settings	
Probe	simple Langmuir (r: 0.127, L: 0.2 [mm])
Position	(z, x, y) = (50,0,0) [mm]
Voltage	-100:0.5:100 [V]

6.1.4. D4 - Verification of the RF-compensated Langmuir Probe

To verify the RF-compensated Langmuir probe it is compared to the simple Langmuir probe. The electron retardation region of the $I - V$ curve is expected to differ from that of the Langmuir probe. However the ion saturation part should be unaffected by the electronics of the RFCLP and therefore be equal to that of the LP. To allow for a variation in the plasma and a measurement uncertainty as a pass criterion we let the ion-saturation curves of the RFCLP and LP differ a maximum of 5%. To provide a range of different plasma conditions and to avoid redundant measurement we repeat the measurements specified in experiment D1 with the RFCLP. The details are summarised in table 6.4.

Table 6.4: T.D4 - Verification of RFCLP

Objective	Verification of RF-compensated Langmuir probe.
Hypothesis	RFCLP produces an ion current profile similar to the LP profile.
Test	Cross-compare the RFCLP to the simple LP.
Pass Criterion	Ion-saturation currents agree within 5%
Thruster Settings	
RF-power	500, 650, 800 [W]
Magnetic Configuration	nominal
Mass-flow rate	Argon 50 [sccm]
Diagnostic Settings	
Probe	LP, RFCLP (r: 0.127, L: 0.2 [mm])
Position	Axial: x, y(0,0), z(20:20:200) [mm]
Voltage	-100:0.5:100 [V]

6.1.5. D5 - Identification of Emissive probe saturation regime

To use the emissive probe in the floating point method the heating current at which the probe potential saturates has to be identified. For this purpose the emissive probe is positioned 20 mm downstream of the centre of the thruster exit plane. The floating potential is then measured for different values of the heating current.

The heating current is increased from 0.1 A when the probe starts glowing visibly, up to 0.8 A. The upper limit is chosen since at this current the wire burned up during a previous measurement. The probe potential versus heating current is measured twice, first at 0.1 A intervals and then repeated with a higher, 0.02 A resolution, where the curve is found to increase. Operating conditions are the nominal magnetic configuration and 500 W of RF power.

It is expected that increasing the heating current will increase the floating potential of the probe up to a certain point where it almost saturates, only marginally increasing with the heating current. This graph has a distinct knee and the saturated part approaches a horizontal asymptote. The saturation heating current is defined as the heating current about 0.1 A past the knee point. The details are summarised in table 6.5.

Table 6.5: T.D5 - Identification of EP saturation regime

Objective	Identification of EP saturation regime.
Hypothesis	EP floating potential saturates for sufficiently high heating current
Test	Measure EP floating potential vs. heating current.
Pass Criterion	The curve has a distinct knee and a horizontal asymptote .
Thruster Settings	
RF-power	500 [W]
Magnetic Configuration	nominal
Mass-flow rate	Argon 50 [sccm]
Diagnostic Settings	
Probe	EP (r: 50 [μm])
Position	(z, x, y) = (20,0,0) [mm]
Current	0.1:0.1:0.8 [A] and 0.1:0.02:0.8 [A]

6.1.6. T1 - Characterisation of plasma parameters in the near plume

To measure the spatial variation of plasma parameters in the near plume, Langmuir probe measurements are taken in axial and radial directions. From the Langmuir[1] probe the plasma density, electron temperature and plasma potential can then be inferred. The measurements are taken at 500 W and nominal magnetic configuration.

Along the axial dimension measurements are taken from 20 mm to 200 mm downstream in 20 mm intervals. The lower boundary of 20 mm is the closest the probe can approach the thruster without visibly altering the plasma. The upper boundary is about twice the length of visible plume. Earlier exploratory measurements showed that LP measurements beyond 200 mm could not be processed properly. The 20 mm interval is chosen to limit the acquisition time, while still providing a reasonable resolution.

Similarly radial measurements are taken at 5 different axial positions, from z = 40 mm to z = 200 mm in 40 mm intervals. The radial spacing is ±50 mm in 5 mm steps at z = 40 mm, ±100 mm in 10 mm steps at z = 80 mm and ±150 mm in 15 mm steps at z = 120 mm and above. These ranges are chosen because the plume is divergent and upstream its radial dimension is smaller, while it increases downstream.

The intervals are adapted to trade-off resolution an acquisition time. Beyond z = 120 mm the radial range is not extended past ±150 mm as the plasma density there is expected to be too low to be measured accurately. As this experiment is exploratory and aims to characterise the plume there is no clear hypothesis to be tested. The profile will later be compared to the magnetic nozzle model but there is no a priori quantitative pass criterion.

---

[1] It will be shown in section 7.4 the RFCLP does not produce correct results.

Both the plasma density and the plasma potential are expected to decrease downstream. Both parameters are related via the Boltzmann equation:

$$n(\phi) = n_0 \exp\left(-\frac{\phi - \phi_0}{T_e}\right) \tag{6.1}$$

An isothermal plasma a plot of $\ln n$ vs. ϕ should yield a straight line. The electron temperature is expected to decrease downstream with a polytropic exponent of about $\gamma_e = 1.1 - 1.3$ [56]. In radial direction the plasma density is expected to be axi-symmetric, peaking on the centre-line and decreasing in the radial direction. The plasma potential is expected to peak on the centre and slightly decrease in radial direction. The Electron temperature is expected to be roughly constant over the radial direction. The details of the test are summarised in table 6.6.

Table 6.6: T.T1 - Characterisation of plasma parameters in the near plume

Objective	Explore spatial variation of plasma parameters in the near plume.
Hypothesis	Evolution of plasma parameters follows the predictions of DiMagNo model.
Test	Measure $I - V$ curves along axial and radial direction.
Pass Criterion	Simulation and measurement agree within the measurement error.
Thruster Settings	
RF-power	500 [W]
Magnetic Configuration	nominal
Mass-flow rate	Argon 50 [sccm]
Diagnostic Settings	
Probe	LP (r: 0.127, L: 0.2 [mm])
Position	axial: x, y(0,0), z(20:20:200) [mm] radial: z, y(40,0), x(-50:5:+50) radial: z, y(80,0), x(-100:10:+100) radial: z, y(120,0), x(-150:15:+150) radial: z, y(160,0), x(-150:15:+150) radial: z, y(200,0), x(-150:15:+150)
Voltage	-100:0.5:100 [V]

6.1.7. T2 - Effect of the RF power on the spatial distribution of n, T_e, ϕ

The effect of the RF power on the spatial distribution of the plasma parameters in the plume needs to be assessed. Increasing the RF power is expected to mainly increase the plasma density in the source. In the DiMagNo model the expansion is independent of the plasma density. The spatial variation of the plasma density is therefore expected to be independent of the RF-power.

There are no models yet predicting the effect of the RF power on the electron temperature. Preliminary measurements indicate that the temperature at the source is independent of the RF power (see appendix A) and therefore it is expected that the electron temperature in the plume is also independent of the RF power.

To investigate this effect the axial profile and the radial profile at z = 40 mm are repeated for 650 W and 800 W. These power levels are chosen to sample the interval of 500 W, below which the discharge is unstable for the nominal magnetic configuration and 800 W, above which the antenna starts to overheat. The details of the test are summarised in table 6.7.

6.1.8. T3 - Effect of RF-power on the plume divergence

The plume divergence is important parameter for the performance of the thruster, reflective of the ratio of axial momentum to total momentum in the plume. The relevant quantity is the divergence half-angle (either 95% mass cone or momentum weighted average as discussed in section 4.4) which can be calculated from radial ion current density profiles.

To concurrently investigate the effect of the RF-power on the divergence angle the measurements is repeated at different RF-power. Faraday probe measurements are fast and can therefore be taken

Table 6.7: T.T2 - Effect of RF-power on plasma parameters in the near plume

Objective	Explore effect of P on spatial variation of plasma parameters in the near plume
Hypothesis	Relative variation of plasma parameters is independent of P
Test	Measure $I - V$ curves along axial and radial direction for different P
Pass Criterion	
Thruster Settings	
RF-power	500, 650, 800 [W]
Magnetic Configuration	nominal
Mass-flow rate	Argon 50 [sccm]
Diagnostic Settings	
Probe	LP (r: 0.127, L: 0.2 [mm])
Position	axial: x, y(0,0), z(20:20:200) [mm]
	radial: z, y(40,0), x(-50:5:+50)
Voltage	-100:0.5:100 [V]

at a higher resolution. Radial profiles are taken from ±400 mm in 5 mm intervals. The gradients in the profile are higher near the centre and lower in the wings. To save time the resolution is 5 mm between ±150 mm and 10 mm elsewhere. Due to its size the probe perturbs the plasma when closer than 100 mm downstream.

To be able to compare LP and FP data the profiles are taken at 120 mm downstream from 500 W to 900 W in 100 W steps. The probe bias is chosen to be at -30 V to ensure that practically all electrons are repelled. This value is based on LP measurements from which is was found that for this bias the probe is always in the ion saturation regime.

Similar to the reasoning behind the hypothesis of T.T2 the divergence angle is expected to be independent of the plasma density and hence the RF-power. As a pass criterion the divergence half-angle has to be independent of P within the measurement uncertainty. Details of the test are summarised in table 6.8.

Table 6.8: T.T3 - Effect of RF-power on plume divergence

Objective	Effect of RF-power on plume divergence
Hypothesis	Plume divergence is independent of RF-power
Test	Measure radial ion density profile for different P
Pass Criterion	Divergence half-angle is independent of P within the error
Thruster Settings	
RF-power	500:100:900 [W]
Magnetic Configuration	nominal
Mass-flow rate	Argon 50 [sccm]
Diagnostic Settings	
Probe	FP (r: 5 [mm])
Position	radial: z, y(120,0), x(-400:10:150:5:+150:10:+400) [mm]
Bias	-30 [V]

6.1.9. T4 - Downstream evolution of the plume divergence

To study how the plume evolves downstream the plume divergence is calculated from ion current density profiles taken at different axial positions. The measurement is taken at nominal magnetic field, mass flow rate and 500 W RF power. The radial spacing of the profiles is similar the same as in T.T3 and the profiles are taken at 120, 160 and 200 mm downstream to allow for comparison with radial Langmuir probe measurements from T.T1.

At 120 mm downstream the ions are not expected to follow the fields lines anymore and the plume divergence is expected to be constant downstream. The pass criterion in similar with T.T3 is that the divergence half-angle is independent of the axial position within the measurement uncertainty. Details of the test are summarised in table 6.9.

Table 6.9: T.T4 - Downstream evolution of the plume divergence

Objective	Downstream evolution of the plume divergence.
Hypothesis	Plume divergence is independent of axial position.
Test	Measure radial ion density profiles at different axial position.
Pass Criterion	Divergence half-angle is independent of z within the error.
Thruster Settings	
RF-power	500 [W]
Magnetic Configuration	nominal
Mass-flow rate	Argon 50 [sccm]
Diagnostic Settings	
Probe	FP (r: 5 [mm])
Position	radial: z(120), y(0), x(-400:10:150:5:+150:10:+400) [mm] radial: z(160), y(0), x(-400:10:150:5:+150:10:+400) [mm] radial: z(200), y(0), x(-400:10:150:5:+150:10:+400) [mm]
Bias	-30 [V]

6.1.10. T5 - Effect of RF-power on the utilisation efficiency

The utilisation efficiency is a parameter of interest indicative of the thruster's performance. It is proportional to the total current ejected by the thruster. The total current can easily be calculated from radial ion current density profiles. It is dependent on the ion velocity and the density. The ion velocity profile is expected to be independent from the RF-power. However the density is expected to scale with the square root of P, for constant T_e (at the source).[15] It is there fore expected that the utilisation efficiency also scales with the square root of P. As a pass criterion we then require that the data $\eta_u(P)$ can be fit with $a \cdot (P-b)^{-1/2}$, with a, b fitting parameters. For this test the same radial ion current density profiles as those of T.T4 are used, to avoid redundant measurements. Details of the test are summarised in table 6.10.

Table 6.10: T.T5 - Effect of RF-power on plume divergence

Objective	Effect of RF-power on the utilisation efficiency
Hypothesis	Utilisation efficiency scale with square root of RF power
Test	Measure radial ion density profile for different P
Pass Criterion	Data points $\eta_u(P)$ can be fitted with $a(P-b)^{-1/2}$
Thruster Settings	
RF-power	500:100:900 [W]
Magnetic Configuration	nominal
Mass-flow rate	Argon 50 [sccm]
Diagnostic Settings	
Probe	FP (r: 5 [mm])
Position	radial: z, y(120,0), x(-400:10:150:5:+150:10:+400) [mm]
Bias	-30 [V]

6.1.11. T6 - Estimation of ion Mach number in the near plume

The ion Mach number can be estimated from the ratio of the ion current density and the plasma density and scaling it with the local ion sound speed which is ∝ $\sqrt{T_e}$. Therefore an axial density profile and an axial current density profile are measured within a short time frame. The profiles is taken from z = 50 mm to 200 mm in steps of 20 mm. The resolution is limited by the acquisition time of the LP. While the closest distance is limited by the FP. At z < 50 mm the bulky FP visibly perturbs the plasma.

The Mach number downstream from the throat and therefore expected to be larger than 1. The DiMagNo model predicts a Mach number of 4-5 far downstream. The Mach number is therefore expected to range between 1-5 and increase downstream. The details of the test settings are shown in table 6.11.

Table 6.11: T.T6 - Estimation of Mach number in the near plume

Objective	Estimation of the Mach number in the near plume.
Hypothesis	Mach number larger than 1 and increasing downstream
Test	Combine radial and axial ion density and plasma density profiles.
Pass Criterion	Mach number $1 < M < 5$ and monotonically increasing downstream.
Thruster Settings	
RF-power	500 [W]
Magnetic Configuration	nominal
Mass-flow rate	Argon 50 [sccm]
Diagnostic Settings	
Probe	FP (r: 5 [mm])
Position	axial: x, y(0,0), z(50:10:200)
	radial: z(120), y(0), x(-400:10:150:5:+150:10:+400) [mm]
	radial: z(160), y(0), x(-400:10:150:5:+150:10:+400) [mm]
	radial: z(200), y(0), x(-400:10:150:5:+150:10:+400) [mm]
Bias	-30 [V]
Probe	LP (r: 0.127, L: 0.2 [mm])
Position	axial: x, y(0,0), z(20:20:200) [mm]
	radial: z, y(120,0), x(-150:15:+150)
	radial: z, y(160,0), x(-150:15:+150)
	radial: z, y(200,0), x(-150:15:+150)
Voltage	-100:0.5:100 [V]

6.1.12. T7 - Estimation of total thrust and thrust efficiency

The thrust and thrust efficiency can be estimated by combining radial ion current density and plasma density profiles. The local thrust density is given by:

$$f(z,r) = m_i n u_{zi}^2 + n T_e = m_i \frac{J_z^2(z,r)}{e^2 n(z,r)} + n(z,r) T_e \tag{6.2}$$

Integrating this expression over the radial direction yields the total thrust at a particular z. The efficiency can be calculated using equation 1.5. As with T.T5 the quantities will be calculated from radial profiles used in T.T1 and T.T4. At this stage it is very difficult to predict a number for the thrust efficiency, but based on other thrusters in literature and considering the early stages of development an efficiency $\leq 1\%$ would be reasonable. Furthermore the thrust (efficiency) is expected to increase downstream since the plasma has been able to expand more. An efficiency of more than 10% is extremely unlikely and would indicate a problem with the measurement or method. Therefore $\eta < 10\%$ is chosen as the pass criterion. The details of the test settings are shown in table 6.12.

Table 6.12: T.T7 - Estimation of thrust and thrust efficiency

Objective	Estimation of thrust and thrust efficiency.
Hypothesis	Thrust (efficiency) increases downstream,
Test	Combine radial and axial ion density and plasma density profiles.
Pass Criterion	Thrust efficiency $\eta < 10\%$
Thruster Settings	
RF-power	500 [W]
Magnetic Configuration	nominal
Mass-flow rate	Argon 50 [sccm]
Diagnostic Settings	
Probe	FP (r: 5 [mm])
Position	radial: z(120), y(0), x(-400:10:150:5:+150:10:+400) [mm] radial: z(160), y(0), x(-400:10:150:5:+150:10:+400) [mm] radial: z(200), y(0), x(-400:10:150:5:+150:10:+400) [mm]
Bias	-30 [V]
Probe	LP (r: 0.127, L: 0.2 [mm])
Position	radial: z, y(120,0), x(-150:15:+150) radial: z, y(160,0), x(-150:15:+150) radial: z, y(200,0), x(-150:15:+150)
Voltage	-100:0.5:100 [V]

6.2. Keithley 6517B Operation

The Keithley is completely remotely controlled. All $I - V$ curve measurements conducted with the Keithley are subject to the following settings given in table 6.13 and are referred to as procedure K1. The Keithley is synchronised with the line cycles of the power grid. NPLC 'on' signifies that the integration time of the Keithley is expressed in number of power line cycles, for the Spanish electrical grid with 50 Hz this results in an integration (i.e. measurement) time of 20 ms. Usually the $I - V$ sweeps are conducted from a negative to a positive value. However if necessary this order can be reversed. When the collected current exceeds 10 mA the Keithley saturates and automatically ends the voltage sweep. The upper and lower boundary for the sweeps have been set at ±100 V. The lower limit was chosen such that a sufficiently long interval of ion saturation regime was present in the $I - V$-curve. The upper limit includes the 'knee'/inflection point of the electron saturation region if the total current does not exceed 10 mA. The resolution of 0.5 V was chosen to limit the measurement time; $I - V$ sweeps with these settings take about 30 seconds per sweep.

Table 6.13: K1 - Keithley Settings

Setting	Value
set NPLC	AUTO
Resolution	5.5
Range	AUTO
Reference	OFF
Median filter	OFF
Averaging filter	OFF
Start voltage	-100 V
Stop voltage	+100 V
Voltage step	0.5 V

6.3. Thruster Operation

Thruster ignition and operation precedes any experiment. Thruster operation consists of start-up (T0) and stability check of the thruster (T1), described below. Due to heating of the antenna feed-through there is a thermal drift of the balance load which needs to be adjusted for during operation. Usually it takes a minimum of 10 minutes for the system to stabilise during which the temperature of the feed-through and the forward/reverse power are monitored and the balancing load is adjusted accordingly. The procedure of changing settings and shutting of the thruster are either straightforward or do not impact results and are not mentioned in detail.

The stability check is a set of tasks to qualitatively and quantitatively check the stability of the thruster. During stable operation the plume divergence, brightness and colour should not visibly change. An increase in reflected power signifies a change is plasma resistance and should not happen after the system is thermally stable. After increasing the power it can take several minutes before the system is thermally stable again. When necessary the matching network can be manually adjusted to reduce the reflected power.

Table 6.14: P.T0 - Thruster Start-up

#	System		Task
0	Vacuum	0.1	Ensure pressure $\leq 5 \cdot 10^{-7}\ mbar$.
1	Water-cooling	1.1	Open main valve
		1.2	Open valve for magnetic coils
		1.3	Open valve for RF amplifier
		1.4	Open valve for Matching Network
2	Mass-flow	2.1	Open Argon supply valve
		2.2	Set mass-flow level to desired value
		2.3	Start mass-flow
		2.4	Ensure pressure $\leq 5 \cdot 10^{-5}\ mbar$.
3	RF-system	3.1	Turn on RF amplifier
		3.2	Turn on Matching Network
		3.3	Adjust Tune and Load capacitors
		3.4	Start RF power
		3.5	Increase RF power until thruster ignites
		3.5	Set RF power to desired value
4	Magnets	4.1	Turn on DC power supplies for all coils
		4.2	Set current for coil 1, 2 and MN coil
		4.3	Apply current to MN coil
		4.4	Apply current to coil 1 and 2
5	Verification	5.1	Visual inspection for stable operation: brightness, colour, stability, divergence
		5.2	Monitor forward and reverse power
		5.3	Adjust load, RF power and coil current until thruster is stable at the required settings

Table 6.15: P.T1 - Thruster Stability Check

#	System		Task
1	Visual check	1.1	Visual inspection of plume (see P.T0 - 5.1)
2	Power check	2.1	Check forward power
		2.2	Check reverse power
		2.3	Adjust Tune and Load capacitor until P_{rev} is $< 5\%$ of P_{fwd}

6.4. Data Management

All data is stored in text files by the LabVIEW program and written to a standard folder `C:\EP2LAB\EXP\YYYYMMDD` which is generated on the day of measurement. All data files are then manually assessed by cross-checking with lab-notes taken during experiment and the selected data files are then uploaded to a Google drive shared folder for back-up. This way the files are also accessible for post-processing, to all users subscribed to the folder.

The format of the Langmuir probe data is a text file with the name `LP_YYYYMMDD_HHmmss.txt`, where the first part is the date in year, month, day and the second part the time of measurement in hours, minutes, seconds. For RFCLP measurements the file name start with `RF` instead of `LP`. The text file consists of four header lines, the first line noting the data and time, the second line noting the thruster settings: RF power, coil 1 current, coil 2 current and MN coil current and the third line noting the axial, transversal and vertical position in mm. The body of the file consists of two columns: the voltage in V and the current in A.

The Faraday probe files are named `FP_YYYYMMDD_HHmmss.txt` with a similar header except for the line with the line denoting the position. For the DAQ setup the body of the file consists of six columns given by the z, x, y coordinates in [mm], the temperature of the probe in , the current density and its uncertainty, both in A/m^2]. For the Keithley setup there is 5 columns, z, x, y the current in A and the bias voltage in V.

The format of the emissive probe is similar to the format of the Keithley setup Faraday probe. The format of the name is `EP_YYYYMMDD_HHmmss.txt` and the body consists of four columns: the z, x, y coordinates in mm and the plasma potential in $[V]$ Example data files are shown in appendix C.

A list of all raw data files used in this study can be found in appendix B.

Summary

In this chapter the operational and measurements procedures were discussed. First the data management system was explained including the structure of the raw data files. Then operational protocols for igniting the thruster and maintaining stable operation were presented as well as the operational settings for the Keithley. The remainder of the chapter was dedicated to presenting the different experiments that form the core of this study. The experiments are divided into two groups: experiments related to characterising the probe diagnostics and experiments related to characterising the plume and thruster performance. Each experiment was described in detail including the objective, hypothesis, test, pass criterion and the test settings as well as a justification for these settings.

Table 6.16: Summary of tests for validation of diagnostics

#	Objective	Test	Hypothesis
T.D1	Assessment of validity and applicability of Chen's post-processing method for $I-V$ curves.	Measure $I-V$ curves with LP and process the data with both PA and BRL theory comparing the results.	$I-V$ curves can be processed by BRL theory and results agree with PA within less than 10%.
T.D2	Assessment of hysteresis in the direction of the voltage sweep.	Measure $I-V$ curves with LP sweeping from negative to positive voltage and vice versa.	Average relative difference of the resulting $I-V$-curves and the inferred plasma parameters are < 5%.
T.D3	Assessment of the repeatability of $I-V$ curve measurements.	Determine the mean and standard deviation of the plasma parameters from a sample of $I-V$ curves.	Error of $I-V$ curve derived parameters is defined by their 95% confidence interval
T.D4	Assessment of RFCLP for measuring plasma density, potential and electron temperature.	Compare LP and RFCLP $I-V$-curves and resulting plasma density.	Ion saturation current and plasma density of both probes agree within 5%.
T.D5	Identify emissive probe saturation regime.	Measure (plasma) potential with the EP as a function of heating current.	Plot of ϕ vs. I_H shows saturation at high current.

Table 6.17: Summary of tests for thruster characterisation.

#	Objective	Test	Hypothesis
T.T1	Spatial distribution of plasma parameters (n, T_e, ϕ) in the near plume.	Measure $I-V$ curves with LP along radial and axial dimensions.	Evolution of plasma parameters follows the predictions of DiMagNo model.
T.T2	Effect of the RF power on the spatial distribution of n, T_e, ϕ.	Measure $I-V$ curves along axial and radial dimension, for different RF-power.	Relative spatial variation of the plasma parameters is independent of P.
T.T3	Effect of RF-power on the plume divergence.	Measure radial ion current density profiles at different P	Divergence angle is independent of P
T.T4	Downstream evolution of the divergence angle.	Measure ion current density profiles at different axial positions.	Divergence angle is constant downstream.
T.T5	Effect of RF-power on the utilisation efficiency.	Measure ion current density profiles at different RF power.	Utilisation efficiency increases proportional $\sqrt{P}$
T.T6	Estimate ion Mach number in the near plume.	Measure radial current density and plasma ion density profiles (at same coordinates)	Ion Mach number increases downstream from 1 to to no more than 4-5.
T.T7	Estimate total thrust and thrust efficiency.	Measure radial current density and plasma ion density profiles	Thrust efficiency of $\eta < 1\%$

7

Characterisation of Probe Diagnostics

Introduction

This chapter presents the characterisation and testing of the Langmuir probe diagnostics, both simple and RF-compensated, as well as the emissive probe. The results here are an investigation of the applicability of the probes, their particularities and short-comings. First the application of the $I-V$ curve post-processing is presented including an evaluation of the iterative post-processing scheme based on Chen's parametrisation of BRL theory. Furthermore an analysis of hysteresis due to the direction of the sweep is given. The RF-compensated probe results are compared to the simple probe and an attempt is made to verify both probes within the limits of this study followed by an error estimation. Lastly the characterisation of the emissive probe is presented along with some preliminary measurements.

7.1. Langmuir probe I-V curve fitting

The $I - V$ characteristics produced by Langmuir probes need to be processed to extract information about the plasma parameters. In general plasma density can be extracted from either the ion-saturation current or the electron saturation current at the plasma potential. However in the case of a helicon plasma the electron saturation can be affected by the magnetic field. Furthermore for this method the plasma potential is needed which has a large uncertainty when measured from the inflection point of the $I - V$ curve. Plasma density is therefore primarily inferred from the ion-saturation current. There are several models relating the ion-saturation current to the plasma density, each with different underlying assumption. The models used in this study are the planar approximation, Bernstein-Rabinowitz-Laframboise , Allen-Boyd-Reynolds and although mostly avoided, Orbital Motion Limited theory. A more in-depth description of these models is found in section 4.1. Applying these models, a theoretical ion-current is generated which is then subtracted from the total measured current yielding the electron current. Fitting the electron current with a straight line in a semi-log plot then yields the electron temperature. The plasma potential is found by identifying the extremum in the first derivative dI/dV. These procedures have been implemented in MATLAB to expedite the post-processing of the $I - V$ curves.

7.1.1. Evaluation of iterative BRL fitting algorithm

The iterative post-processing scheme of section 4.1.4 has been implemented in MATLAB code (see appendix D for a list of electronically submitted files). However it has to be verified whether this method produces similar results to other methods. The results are primarily compared to the planar approximation which is valid for the case $\lambda_D \ll a$. It predicts a constant ion saturation current. In practice the ion current grows linearly with the applied voltage. Because the sheath width increases with increasing voltage the effective collection area increases as well. Post-processing using this method is straightforward and the details are mentioned in section 4.1.1.

The hypothesis is that the iterative scheme, based on BRL theory better approximates the plasma parameters n, T_e, ϕ than the planar approximation. To quantify 'better', the quality of the fit expressed as the relative mean error over the fitting interval is used. Also the range of the fitting interval is of importance; if the fit is only representative of the data over a very small interval it is obviously not a good fit. Therefore the threshold for the width of the interval of an acceptable fit is set at 30 V. The functional behaviour of the ion current is assessed qualitatively. BRL theory predicts a sub-linear ion current approaching a straight line in a $I^2 - V$ plot, while the planar approximation predicts straight line in an $I - V$ plot. Another qualitative assessment of the ion-current fit is how it affects the electron current. The electron current is assumed to be Maxwellian, and a $\ln(I) - V$ plot should produce a straight line. However, since the current is the sum of both the electron and ion current and since the electron current saturates around the plasma potential these plots are rarely straight over a large interval, if at all. Subtracting the ion current from the total current yields the electron current I_e, and a $\ln(I_e) - V$ plot is linear over a larger range. A 'better' fit of the ion current is therefore one that recovers the linear behaviour of the electron current in the semi-log plot.

To compare both methods a set of $I - V$ curves was analysed with both methods and the fits and the results were compared. The curves consist of the axial scans from 20 to 200 mm downstream of the thruster exit plane taken at 500 W, 650 W and 800 W. This data-set was chosen as it should provide a wide range of plasma parameters which would make the analysis more robust. The advantage of choosing axial measurements is that the probes are be aligned with both the magnetic field and the ion velocity vector. Otherwise this would complicate the measurements if not outright invalidate the underlying theory. Details of the test can be found in section 6.1.1 of the previous chapter.

7.1.2. Results

While processing the data sets, several things became apparent. Firstly both methods do not fit well for all curves. The densities encountered varied from about 10^{18} m^{-3} near the thruster exit to $5{\cdot}10^{15}$ m^{-3} farther downstream, while plasma temperatures where around 3-5 eV. Resulting Debye lengths varied between 0.02 - 0.04 mm which translates to a probe parameter $2.1 < \xi < 6.4$. The ion current becomes more linear at lower densities (smaller ξ) while becoming more and more quadratic for higher densities. Figure 7.1 shows the fitting of the ion current with the planar approximation for two extreme cases $n = 10^{17}$ m^{-3} and $n = 10^{18}$ m^{-3}.

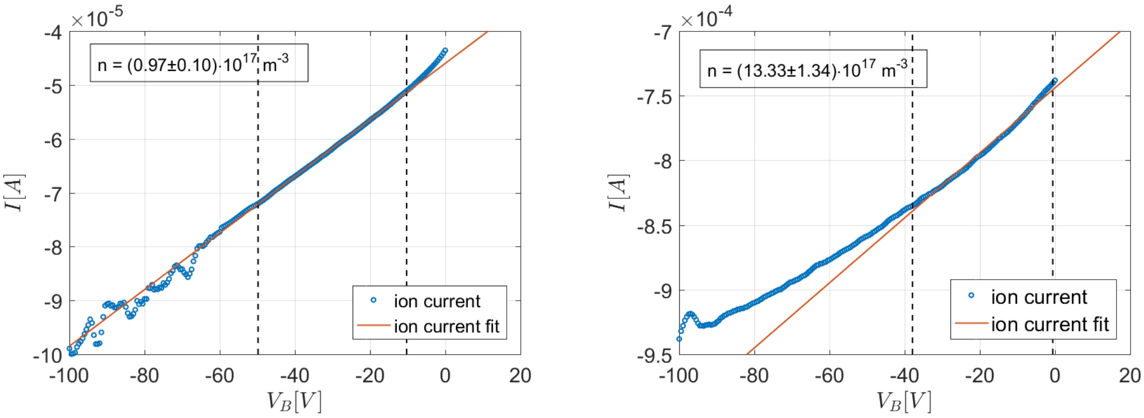

(a) P = 500 W, z = 200 mm.

(b) P = 650 W, z = 40 mm.

Figure 7.1: Fit of ion-saturation current with planar approximation at a low and high plasma density.

Note that both graphs are $I - V$ plots. The dotted lines demarcate the fitting interval. The resulting densities according to the planar approximation are shown in the top of the figures; the reported error is solely due to the error in the fit and should not be taken as the total error. The first plot with a density of 10^{17} m^{-3} clearly shows the linear behaviour predicted, and the planar approximation is a good fit. In the second plot the ion saturation current is not at all linear. It could be argued that the plot appears slightly more linear between -40 to -80 V. This indeed produces a lower relative error, 0.1% vs. 0.3%. However the fit shown in the figure produces a more linear electron current. The resulting density would only change 0.7% while the resulting temperature is 14% higher. This behaviour is seen in general and therefore when fitting the planar approximation to non-linear curves the interval closer to the right of the curve is chosen. This difference in the quality of the fit depending on the density is also present when fitting the BRL theory. Plots for the same cases but now using BRL theory are shown in figure 7.2.

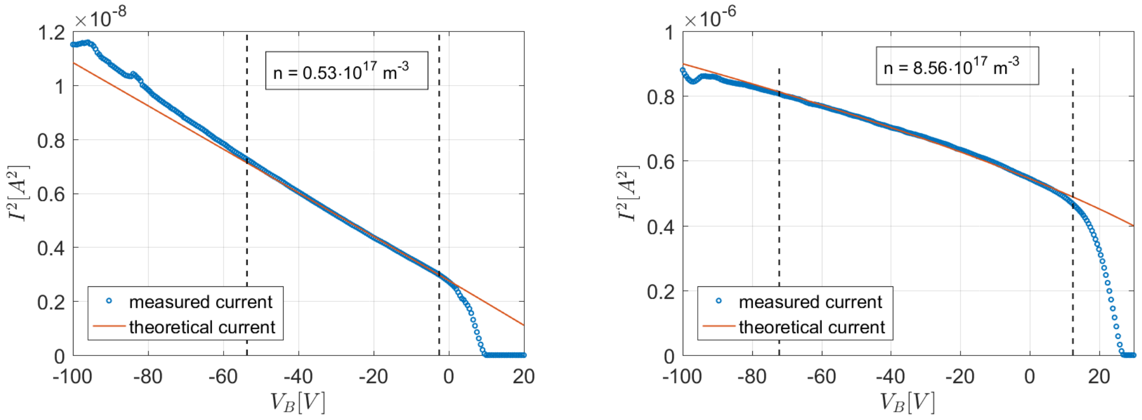

(a) P = 500 W, z = 200 mm.

(b) P = 650 W, z = 40 mm.

Figure 7.2: Fit of ion-saturation current with BRL theory at a low and high plasma density.

Note that the figures now show $I^2 - V$ plots. The first plot, for lower density is a reasonable fit, however that in the second plot is clearly a better fit. It shows that BRL theory apparently forms a better fit at higher densities. This is further substantiated by the impossibility to fit BRL theory to curves of even lower densities which were encountered during radial density profile measurements, where densities drop below 10^{16} m^{-3}. The second plot shows a functional behaviour that's neither linear nor exactly quadratic and cannot be well explained by either the planar approximation or OML theory, showing the added value of using BRL theory.

It can further be seen that the fit in the first plot is a near-perfect straight line in the $I^2 - V$ plot, which is characteristic of OML theory. Fitting this curve with OML theory yielded a density of $(5.1 \pm 0.3) \cdot 10^{16}$ m^{-3} in agreement with the 5.3·10^{16} m^{-3} of BRL theory. Both methods yielded the same electron temperature of 3.0 eV OML theory is generally avoided in this study since BRL theory provides the same functionality and has a more sound theoretical basis.

A good fit of the ion current when subtracted from the total current yields a straight line in the resulting $\ln(I_e) - V$. This can be clearly seen in figure 7.3. The total current as given by the solid line is not linear in this plot and only spans a short range up to the floating potential. The electron current as represented by the circles is linear over a range of roughly 25 V allowing for a very good fit represented by the dashed-dotted line. Although subtracting the ion current in almost all cases improves the electron current fit it is not always as ideal as shown here.

Regardless of the type of fitting the plasma potential is determined from the Langmuir probe measurement by finding the minimum of the negative of the first derivative $-dI/dV$. Although the raw current is smoothed with a moving average filter with a span of 5, the derivative still shows considerable noise. However this usually occurs in the electron saturation region, after the inflection point. In most cases the derivative shows a clear peak signifying the inflection point of the $I - V$ curve, as can be seen in figure 7.4a. The extremum is chosen by inspection and the algorithm then finds the closest value of the voltage, which is limited by the resolution of $0.5\ V$. In some cases there is only a slope on the left side of the extremum followed by noise. In this case where there is no real peak the location of first minimum before the noise is chosen as the plasma potential. An example of this is shown in figure 7.4b Lastly at very high densities it can occur that the collected current exceeds the Keithley's allowed maximum before the inflection point is reached, in this case the plasma potential cannot be obtained.

Taking the above observations into consideration the $I - V$ curves for three RF powers and several downstream on-axis positions have been processed with both BRL theory and the planar approximation. Since their differences are only in the plasma density and electron temperature the focus is on these parameters. Figure 7.5a shows the ratio of the density as obtained by the planar approximation to that obtained by BRL theory, while figure 7.5b shows the same ratio for electron temperature.

From figure 7.5a it can be seen that the planar approximation overestimates (or BRL theory underestimates) the plasma density with almost a factor 2, with a large spread where the 95% confidence interval is (1.3-2.5). There seems to be a trend where the ratio grows roughly linearly up to 80 mm downstream, and then levels off. However this behaviour could not be correlated to any other param-

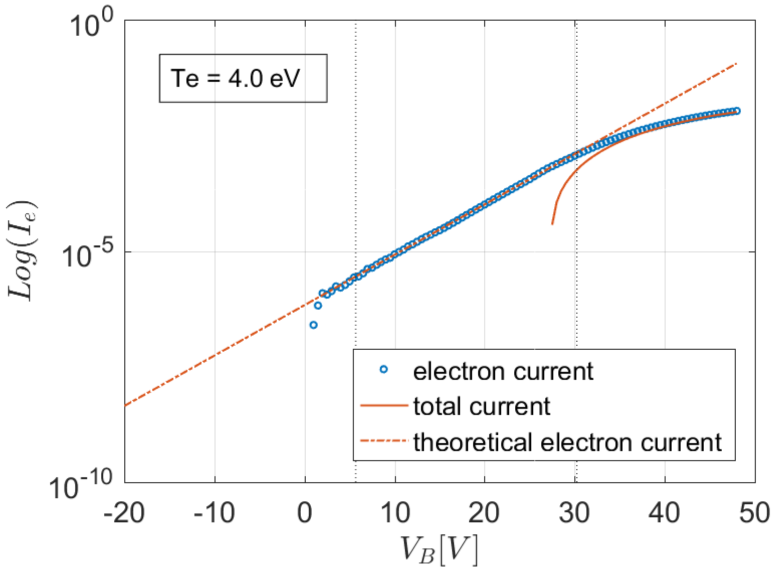

Figure 7.3: Semi-log plot of electron retardation region to find the electron temperature. (P = 500 W, z = 200 mm)

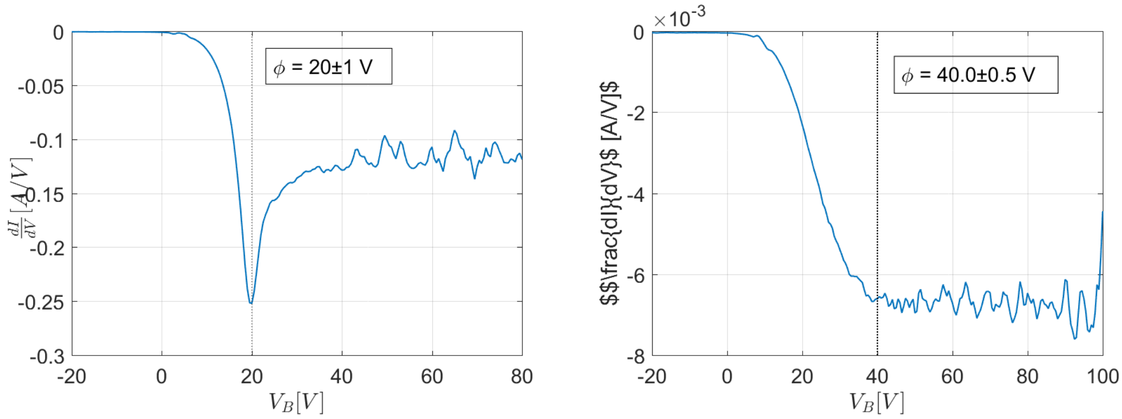

(a) dI/dV curve with clear minimum. (P = 500 W, z = 40 mm) (b) Non-ideal dI/dV curve.

Figure 7.4: Determining plasma potential from dI/dV curves.

eter and it would be far-fetched to infer any functional dependence. Figure 7.5b shows that the results for T_e obtained with both methods are similar.

To assess the quality of the fit in a more quantitative manner the difference in fitting error $\Delta\epsilon$ is presented for both the ion-saturation region as well as the electron retardation region. In all cases the errors $\epsilon_i, \epsilon_e \leq 1\%$. Recall that ϵ_i, ϵ_e where defined in equations 4.28 and 4.29 in section 4.1.4. More precisely the difference is the error from obtained from fitting BRL theory minus that obtained by the planar approximation. When this value is below zero it means that the BRL fit is better than the planar approximation. The plot of $\Delta\epsilon_i$ is shown in figure 7.6a while that of $\Delta\epsilon_i$ is shown in plot 7.6b.

It can be seen for both errors that farther downstream, at lower densities the planar approximation is a better fit. Approaching the thruster, i.e. for increasing density the ion fit obtained with BRL theory improves markedly for the case of 500 W and partially for the case of 800 W. For the case of 500 W and 800 W the electron fitting with BRL theory becomes the better fit already about 150 mm downstream. This means that the functional form of the subtracted ion current here is closer to the real current. It has to be noted that these fitting errors are sensitive to random noise on the $I-V$. Furthermore for the planar approximation at high densities large portions of the ion-saturation current had to be ignored due to lack of linearity which leads to an underestimation of its ion-fit error close to the thruster.

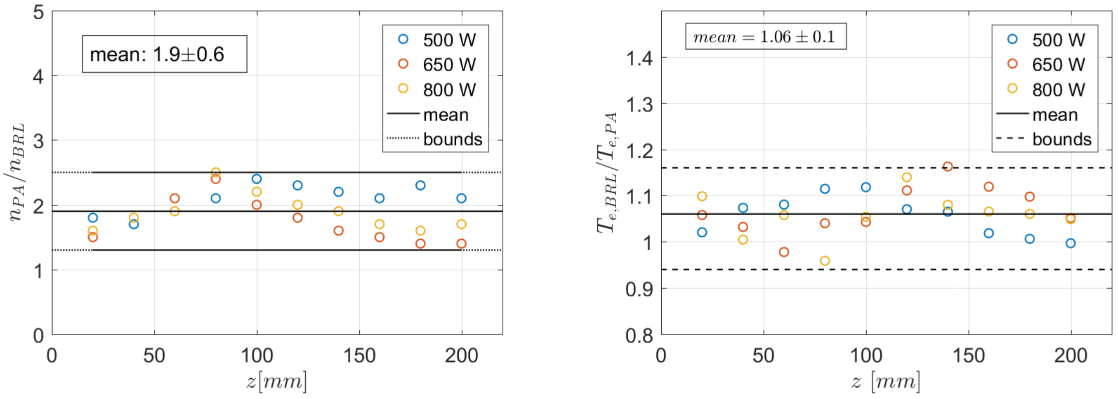

(a) Ratio of plasma densities.

(b) Ratio of electron temperatures.

Figure 7.5: Comparison of plasma parameters as obtained with planar approximation and BRL theory.

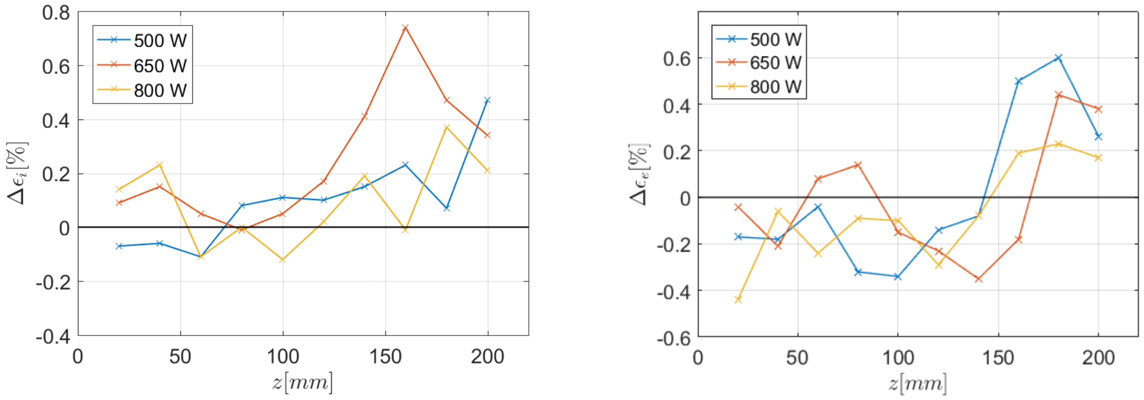

(a) Ion-saturion region.

(b) Electron retardation region.

Figure 7.6: Difference in fitting error between BRL theory and planar approximation.

The iterative BRL fitting scheme uses four fitting parameters, next to the density n and temperature T_e it has a different parameter for the ion plasma potential ϕ_i and the electron plasma potential ϕ_e. In theory these should be the same however comparing both values for the data sets under consideration showed that the difference $|\phi_e - \phi_i|$ ranges anywhere from 5 V downstream up to 35 V close to the throat due the ion potential ϕ_i increasing. The electron potential ϕ_e roughly follows the plasma potential ϕ differing a few Volts. Their ratio being unity near the thruster and deviating by 15-20% downstream.

7.1.3. Discussion

In the previous part of this section the results of applying both planar approximation and BRL theory, to measured $I - V$ curves were presented. The comparison of both methods was done in a plasma whose plasma parameters are unknown. This is therefore only a relative comparison. Furthermore it has to be noted that neither of the two theories compared here take into account magnetic fields, flow or collisions. However the collision mean free path is of the order of the vacuum chamber, ions are weakly or un-magnetised and the probe is approximately aligned with the flow for axial measurements. In a first approximation they can be ignored when analysing the ion saturation current.

It was found that depending on the axial position, i.e. on the density, both theories where more or less applicable. When assessing the quality of the fit it was found that in general the fit of the ion-saturation current improves when the density increases and is on par with, or in some cases better than the planar approximation. Here better is defined as $\epsilon_{BRL} < \epsilon_{PA}$, while at lower densities the opposite is the case. The fit of the electron retardation regime is better for BRL theory over a larger range of densities indicating that the subtracted theoretical ion current better approximates the real ion current. Qualitatively it was also determined that at lower densities the ion current was clearly linear (in accord with planar approximation) while becoming sub-linear at lower densities. This agrees generally with the trend of the fitting errors.

The fact that the ion saturation current is linear at lower densities is surprising. The probe parameter varied $2.1 < \xi < 6.4$ over the data set. Generally the planar approximation is valid for $\xi \gg 1$ while the opposite limit $\xi \rightarrow 0$ is the limit of OML theory. BRL theory should be valid for any ξ. It is equally surprising that BRL theory does not perform well at lower densities. One explanation could be that charge exchange collisions in the sheath destroy the orbital motion of ions orbiting the probe, which then get absorbed, adding to the collected current. This behaviour was analysed by Sternovsky for stationary low density plasma of 10^{13} m^{-3} and a background pressure of $5 \cdot 10^{-4}$ mbar yielding a so-called charge exchange current that is linear with the bias potential [74, 75]. These values differ from those of the HPT05 (10^{17} m^{-3}, $2.5 \cdot 10^{-5}$ mbar). However the neutral pressure near the source is higher than the facility pressure. Using the ideal gas law and the neutral density calculated below, the neutral pressure is about $2 \cdot 10^{-2}$ mbar at the source exit. According to [75] the charge exchange current is only a weak function of the plasma density, is linear in the pressure $I_{cx} \propto p$ and increases slightly with T_e. Similar behaviour was seen in a plasma of 10^{15} m^{-3} and $5 \cdot 10^{-2}$ mbar. The charge exchange cross-section of argon is given by the empirical formula from [64]:

$$\sigma_{cx} = 6.30 \cdot 10^{-18} \cdot \left(\frac{m_i}{E_i}\right)^{0.14} \cdot \Phi_i^{-1.07} \tag{7.1}$$

where $m_i = 39.95$ is the argon mass in atomic mass units, E_i is the ion energy which is between 2-27.4 eV based on a Mach number of 1-3.7 (see section 9.3) and a T_e of 4 eV. Φ_i = 15.76 eV, the ionisation energy of argon. This results in a cross-section of $3.5\text{-}5 \cdot 10^{-19}$ m^2. The neutral density at the thruster exit, neglecting ionisation, is given by:

$$n_n = \frac{4\dot{m}}{m_i A c_n} \tag{7.2}$$

where $\dot{m}$ is the mass flow rate of 1 mg/s, m_i the ion mass in kg, A the thruster exit area and $c_n = \sqrt{8k_B T_n / \pi m_i}$ the mean speed of the neutrals which is about 400 m/s at room temperature. For a thruster radius of 0.015 m this results in a density of $2 \cdot 10^{20}$ m^{-3}. This is only a valid approximation if the ionisation degree is low, say $\lesssim$1%. This is not unlikely with plasma densities <10^{18} m^{-3}. The charge exchange collision mean free path is calculated from $\lambda_{cx} = (n_n \sigma_{cx})^{-1}$. Since the neutrals expand downstream the density is assumed one order lower at z = 200 where M = 3.7 and σ_{cx} = $3.5 \cdot 10^{-18}$ m^2. The mean free path at is then between 0.01 m at the exit and 0.15 m downstream (z = 200 mm). This is much larger than the Debye length which at a density of 10^{16}-10^{17} m^{-3} is about 0.1-1 mm. The ratio $R_\lambda = \lambda_{cx}/\lambda_D$ is then of the order of 10^1-10^3. Sternovsky found that the contribution of the charge exchange current to the total current for ratios of $R_\lambda \sim 10^3$ still equalled 15%. It is not straightforward to translate the results one-one-one to the case of the HPT05, but charge exchange collisions could possibly explain the linear ion current at lower densities.

Another possibility could be that the ion velocity effects the collected current. In reality the probe is never perfectly aligned to the flow. This might explain why the effect becomes more pronounced downstream. However this argument is contradicted by the fact that radial density measurements, where the probe is at an angle of up to 16° to the flow, do not show this behaviour.

Chen also notes that for partially ionised plasmas (or fully ionised plasmas expanding into a background of similar density) collision-less probe theories are inadequate for the regime $3 < \xi < 100$, leading up to errors in the density up to a factor 2. He states that the real value of the density is bracketed by the value as found by BRL theory and that found by Allen-Boyd-Reynolds (ABR) theory. The latter theory ignores orbital motion and therefore generally overestimates the collected current and thus underestimates the density. While BRL theory ignores collisions, that in reality would destroy some of the angular momentum thereby underestimating the collected current and overestimating the density. He found that the geometric mean of the densities as found by ABR and BRL theory agrees with the density as found by microwave interferometry (MWI), a more accurate diagnostic [20]. A comparison of density measurements to Faraday probe measurements, which is presented later, indicated that the density as measured by BRL theory indeed is an overestimation. The MWI measurements [27] confirming the accuracy of the geometric mean of both theories, were performed on an $400-800\ W$ RF inductively coupled plasma (ICP) with an electron temperature of $3\ eV$ densities between 10^{16-17} m^{-3}. Since this is similar to the plasma of the HPT05, this approach is adopted for processing further LP data.

Overall it can be concluded that the iterative BRL fitting algorithm provides a better fit of both the ion current and the electron current at higher densities (high 10^{17} to 10^{18} m^{-3}). The values of the electron temperature it produces are similar to those obtained from the planar approximation. However the densities it measures are roughly a factor 2 smaller with a considerable spread.

The fitting algorithm was based on an excel sheet developed by Chen similar to the aforementioned excel program for ABR theory [24]. In the end it was found that the MATLAB program does not provide a significant benefit over the available excel sheets. What is gained in processing speed is offset by the quirks of the `fminsearch` function that sometimes seems to get stuck in local optima and sometimes diverges from an better solution to an obviously worse solution. The excel sheet also offers more control over the process than the MATLAB program which runs sequentially and has to be re-run to change or correct a fit. The original BRL excel file was only valid for $\xi < 3$ this was modified to automatically adopt the correct parametrisation depending on the value of ξ.

All density measurements reported in the rest of the report are the geometric mean of both methods or by means of the floating potential method discussed above. Temperature measurements of BRL and ABR theories sometimes differ slightly and in therefore their arithmetic mean is used. The processing of Allen-Boyd-Reynolds theory is done with an excel sheet developed by Chen and uses a parametrisation of ABR theory similar to that of BRL theory.[23]

7.2. Error estimation

For the interpretation of the results to be meaningful they have to include error bars. Langmuir probes are not known for their accuracy and error estimations vary wildly, depending on the plasma conditions and the method used, often no error is mentioned at all. In this section an error analysis for the Langmuir probe measurements is presented.

It is important to make a clear distinction between the types of errors and error sources. Errors are either systematic or random. Systematic errors can lead to an offset or a multiplier that lead to values that are consistently larger or smaller than the actual value and affect the accuracy of the measurements. Random errors are unpredictable changes caused by fluctuations in the system, equipment or the environmental conditions and affect the precision of the measurements. The uncertainty in the measurements can come from several sources such as innate fluctuations of the plasma, thermal drift of the equipment, specifically the RF system, limited accuracy of the (measurement) equipment, limitation and uncertainties of the models and deviation from the assumptions of the models.

These error sources can be broken down for the case of the Langmuir probes. Firstly the uncertainty in the equipment. The $I - V$ curves are measured with the Keithley 6517B which provides both the voltage as well as measures the current. The accuracy of the Keithley is about 0.1% for measuring current, while the accuracy of the internal voltage source is 0.15% [44]. The probe area is the product of the length and the radius of the tungsten wire. The length is measured with a caliper with an accuracy of 0.05 mm or 2.5%, while the uncertainty in the radius comes from the manufacturer and is 7.6 μm or 3%. Furthermore the end of the rod is not perfectly planar, but pointy leading to a 5% uncertainty in the probe area.

The assumptions of the models with respect to the collected ion current are a collision-less, un-magnetised, stationary plasma. However Laframboise [46] specifically mentions that a probe aligned with the flow is equivalent to a probe in a stationary plasma; something that is valid for all theories under consideration. However for radial measurements this is not the case, further of axis the ion flow impinging the probe at an angle will influence the collected current. While the electrons are magnetised $\ell_e \leq R_p$, at fields of <1 kG and $T_e \sim 4$ eV the ion Larmor radius is much larger than the probe radius $R_p \ll 10^{-2}$ m < ℓ_i and the ions can be considered un-magnetised. In reality collisions are always present, but for the low background pressures 2.5·10^{-5} mbar should be insignificant. However as was mentioned in the previous section, it could be that charge exchange collisions effect the probe current more than a simple estimate of the mean-free-path would indicate. The linear form of the ion current at densities where the planar approximation is not valid ($\xi = \mathcal{O}(1)$) is possibly related to this. Although this behaviour has also been observed by Chen, this is still an open question. In general the planar approximation is not valid for the densities observed so far: $n < 10^{18}$ m^{-3}. And neither is

OML theory which requires $n \ll 10^{16}$ m^{-3}. Both BRL theory and ABR theory are valid for all values of ξ, but consistently either over- or underestimate the density as has been discussed. Results obtained from the geometric mean of ABR and BRL theory are therefore bracketed between the separate values which are the absolute error bounds. A plot of the axial density at 500 W is shown in figure 7.7a

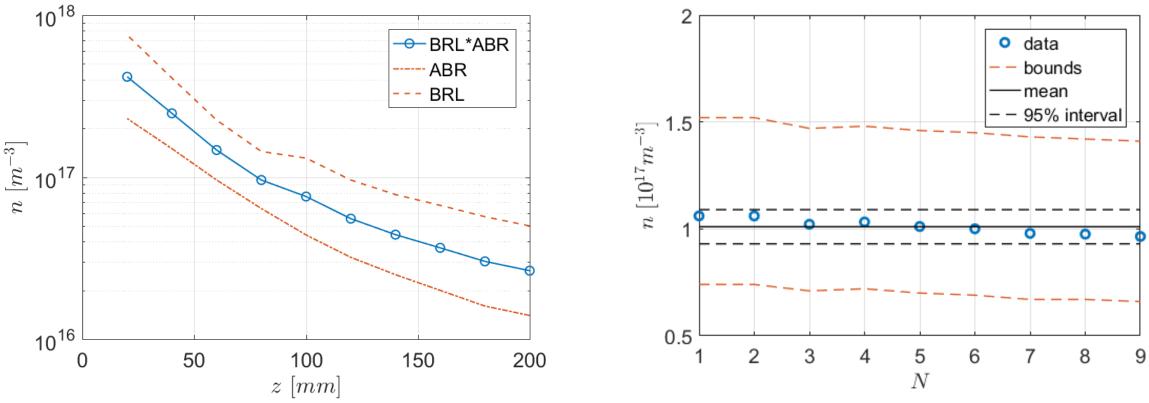

(a) Error bounds of the plasma density as obtained from the geometric mean of BRL and ABR theory

(b) Repeatability of plasma density.

Figure 7.7: Error estimation and repeatability of plasma density measurements.

The uncertainty in the probe area dominates that of the Keithley and is approximately 10%, however this is small in comparison to the aforementioned error bounds, which ranges between 30-80% and is generally closer to the lower boundary. The 10% error is therefore ignored and it is assumed that the real density is anywhere in between the error bounds as set by both theories. Differences in electron temperature between ABR and BRL theory are on average less than 0.2 eV or $< 5\%$. And their arithmetic mean is chosen as the value of T_e. Therefore, in further measurements the error in electron temperature is set to 5%.

7.2.1. Stability of the Plasma

To assess the effect of the stability of the plasma, 10 consecutive $I-V$ curves were measured according to the test plan of section 6.1.4 It provides a measure of the repeatability of the Langmuir probe measurements. One measurement turned out to be too erroneous to process; the remaining 9 measurements span a period of little under 6 minutes. The result for the plasma density is plotted in figure 7.7b. The plasma density shown is the geometric mean of BRL and ABR theory while the bounds are given by their distinct values. The 95%-confidence interval represents the range $\bar{x} \pm t^{*}S$ within which a single measurement lies with 95% certainty. Here $\bar{x} = \sum x_i/N$ is the mean value of the variable in question and S the standard error calculated from:

$$S = \sqrt{\frac{1}{N-1}\sum_{i=1}^{N}(x_i - \bar{x})^2} \tag{7.3}$$

where N is the number of measurements and x_i the outcome of the i^{th} measurement. The value t^{*} is the upper critical value of the t-distribution for a chosen level of certainty e.g. 90%-95%-99%; it is dependent on the degrees of freedom, in this case[1] $df = N-1$ and for $N = 9$, $df = 2.306$. This approach is based on the t-distribution which is an approximation for the normal-distribution when the standard deviation σ is unknown.

The result for the density is determined to be $(101 \pm 8) \cdot 10^{15}$ m^{-3}, which translates to a a relative error of 8%. Similarly the result for the electron temperature is $4.06 \pm 0.08\ eV$, a relative error of 2% shown in figure 7.8a. Taking a closer look at figure 7.7b shows that the density seems to be monotonically decreasing, instead of varying randomly around the mean; likewise the electron temperature seems

---

[1] Since it is only dependent on one statistical variable, the mean.

to increase. It could be that this is caused due to the thermal drift of the RF-system impedance which slowly decreases the power coupled to the plasma. However the forward and reflected power were maintained constant during this measurement. In any case it is clear that the variation in plasma density and electron temperature are smaller than the errors estimated in the previous section.

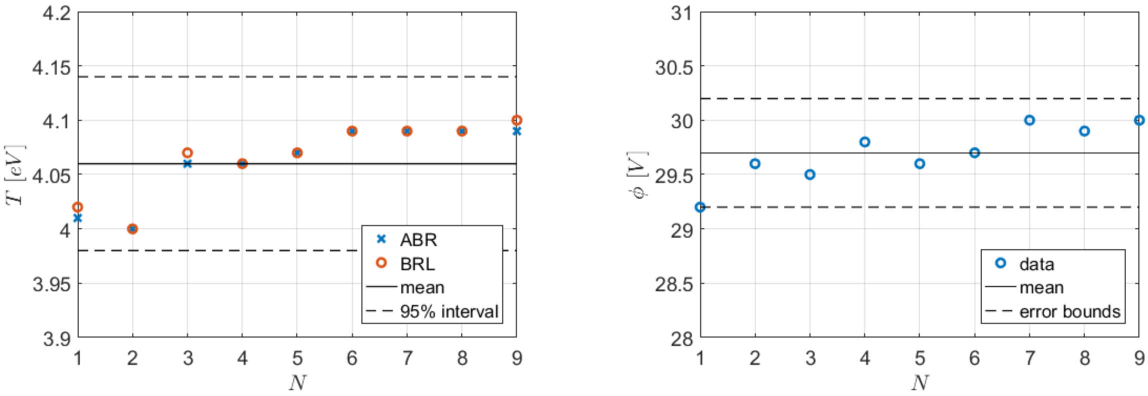

(a) Electron Temperature

(b) Plasma Potential

Figure 7.8: Repeatability of $I-V$ curve measurements.

The plasma potential as measured by the inflection point of the $I-V$ curve is not a very accurate measure for the potential due to amplification of noise when taking the derivative. The inflection point is also only an approximation of the plasma potential. These measurements have to be corroborated with emissive probe measurements. However the LP data is easily accessible and gives a good first estimation of the potential. As was mentioned before the value of V closest to the optimum of the first derivative is the value extracted. This reduces the resolution to that of the voltage sweep, 0.5 V. However since the peak is selected manually an error of 1 V is not uncommon. Noise and possible broadening of the peak hinder the identification of the plasma potential even more. The repeatability of the plasma potential at fixed operating conditions are shown in figure 7.8b. The resulting value is $29 \pm 3\ V$. The error in the plasma potential results from noise, peak broadening, finite resolution and operator errors all which are not dependent on the value of the variable. For plasma potential the absolute error of $3V$ is used. In exceptional cases where the value cannot be unambiguously obtained within this error a larger error may be used.

To summarise, the plasma density reported is the geometric mean of the values obtained from BRL and ABR theory, which independently give the upper (BRL) and lower (ABR) values. They are effectively the error bounds for the absolute value of the density and are roughly between 30-80%. Any innate variation in the plasma density of 8% is relatively small compared to these values. But for a relative comparison this 8% is used as the measurement uncertainty in the plasma density.

For the electron temperature a 5% error was found based on the differences between values found when the subtracted ion current was either obtained from ABR or BRL theory.

The plasma potential in general is reported with a $3\ V$ absolute error.

7.3. Hysteresis and direction of voltage sweep

The voltage sweep for the $I-V$ curve is usually conducted from a negative potential to a positive potential. This is done for practical reasons as it is not a priori known, at what positive voltage the Keithley saturates. However in principle the sweep can also be conducted from a positive to a negative voltage. To assess whether there is a distinction between the two cases, i.e. whether there is some kind of hysteresis, two $I-V$ curves taken sequentially taken at the same operating settings were compared. Both sweeps were performed from ±100 V to ∓100 V in steps of 0.5 V. The details of the test can be found in 6.1.2. Note that these measurements were taken with the helical antenna as opposed to the loop antenna used in most of the experiments.

Both $I-V$ curves are plotted together in figure 7.9. The left figure shows the ion-saturation region, while the right figure shows the semi-log plot of the electron retardation region. In general the two curves seem to align reasonably well, but the plot from negative to positive voltage (forward) shows a deviation close to -100 V. When the voltage sweep is started it switches from 0 to -100 V almost instantly and this tail is probably a transient effect caused by the sudden increase in voltage. In general the first 10 V of the forward sweep can be ignored to mitigate this effect. Curiously this effect does not happen in the electron saturation current of the reverse sweep. One explanation could be that electrons are much faster than ions and are indifferent to the near-instant increase in voltage at the on-set of the sweep. Looking at the electron saturation current it can be seen that the floating potential is slightly lower for the forward sweep.

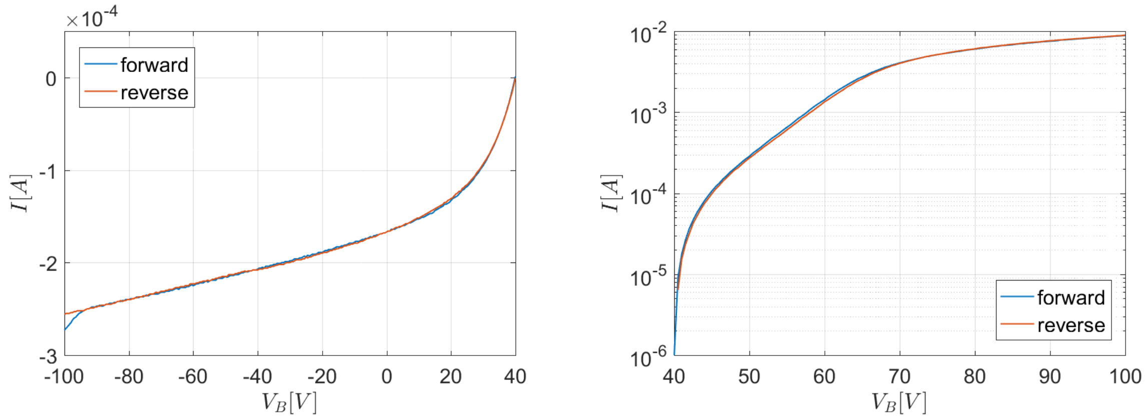

(a) Ion-saturation region

(b) Semi-log plot of electron retardation region

Figure 7.9: Hysteresis of $I - V$ curve measurements.

To quantitatively assess how well the curves match the relative difference is plotted in figure 7.10. On average the curves differ 1.50% in either direction, if the values between 39 V to 42 V around the floating potential are ignored. As the current here goes to zero the relative difference blows up and artificially increases the average. In the electron retardation region the difference can go up to 10%, however since only the logarithm is of interest, the relative difference for the logarithm of the current is 0.5%. Ignoring the tail effect in the ion saturation region the average difference is also 0.5%. It can be concluded that the curves agree within the a priori defined 10% difference and for all practical purposes are closer to 0.5%. Lastly the resulting plasma parameters are compared. The plasma density for the forward sweep was 5.7 (3.0-10.7) $\cdot 10^{16}$ m^{-3} while that of the reverse sweep was 5.5 (2.9-10.6) $\cdot 10^{16}$ m^{-3}. The value in parenthesis are the boundaries defined by the distinct values found from ABR and BRL theory. The electron temperatures found were 7.9±0.4 eV and 8.2±0.4 eV for the forward and reverse sweep respectively. Plasma potentials are 65±3 V and 66±3 V and floating potential 39.9±0.01 V and 40.0±0.01 V. It is clear that all values agree within their error and most certainly within 10%. It is therefore concluded that there is no hysteresis and the direction of the voltage sweep does not significantly affect the $I - V$ curve measurements.

7.4. Evaluation of RF-compensated Langmuir probe

The RF-compensated probe ideally would be tested in an RF plasma with a priori known plasma parameters. In the absence of such a method the RF-compensated probe and the simple Langmuir probe are cross-compared. According to theory, in the ion saturation region this probe should (when scaled for probe area), produce the same results as the simple Langmuir probe. Furthermore under the assumption of a Maxwellian plasma, its IV-curve should have an exponential region, although with a steeper slope than that of the simple LP and a shifted floating potential. The same axial profiles taken with the LP were repeated with the RF-compensated probe. The results of these profiles taken at 500 W, 650 W and 800 W are compared. This provides are range of different conditions that allow for assessment of the RFCLP's behaviour. The exact details of the experiment can be found in section 6.1.4.

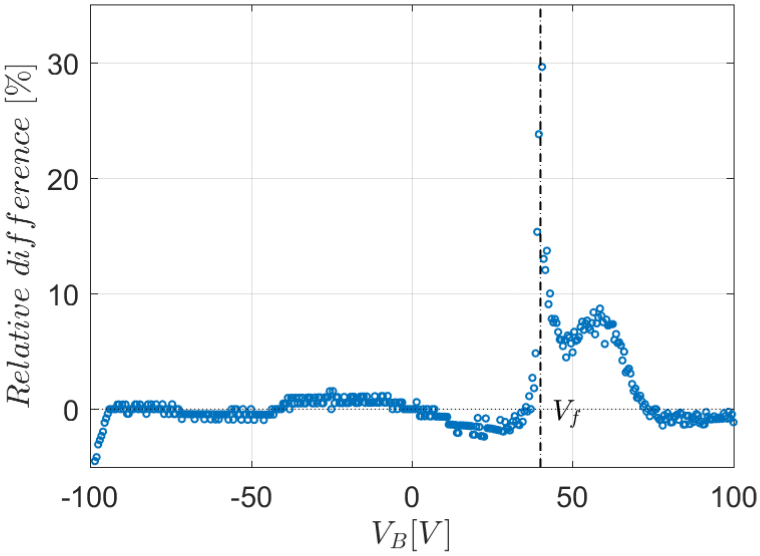

Figure 7.10: Relative difference of reverse sweep with respect to forward sweep.

7.4.1. Results

Firstly a comparison of LP and RFCLP $I-V$ curves, is shown in figure 7.11. The curves shown are for the case of 650 W RF power and at 20 mm downstream. From the left plot two things are apparent. Firstly as expected the floating potential of the $I-V$ curve of the RF-compensated probes is shifted to a more positive value. Secondly the ion current of both probes do not agree at all. Calculating the relative difference between the two curves, it varies almost linearly over the ion-saturation region. And the ion-current of the RFCLP is between 20% (at V_B = -100 V) to 35% (at V_B = 10V) lower than that of the LP. The relative difference in ion-currents has been calculated for all $I-V$ curves under consideration but shows produced no tangible results. However, it is observed that a) the RFCLP ion-current is always lower than the LP ion-current, b) in all cases the relative difference is roughly linear over the ion-collection region with a smaller difference at more negative voltages and c) the absolute values as well as the range of the relative difference differ per $I-V$ curve.

In the right plot the semi-log plot of the electron-collection region is shown. Here two things are can be seen. Firstly the RFCLP curve is translated to the right with respect to the LP, which is due to the more positive floating potential. Furthermore the RFCLP curve has overall a more steeper slope, signifying a lower electron temperature. All of the aforementioned features are present to a greater or lesser degree in all of the compared $I-V$ curves.

When processing the curves it became apparent that at higher densities the ion saturation current gave a remarkably straight line in the I^2-V plot much more so than previous simple Langmuir plots did, which implies OML theory. While at lower densities a similar straight line could be fitted in the $I^{4/3}-V$ plot which hinted a Chen's floating point method [26]. Of the 10 measurements from 20 to 200 mm downstream the first five could be fitted very well with OML theory (also seen in [25]) although the fit degraded slightly downstream. The second five measurements could be fitted well with the floating point method where the fit improved downstream. However when combining the resulting densities the results of both theories did not agree well, that is to say they showed to different trends that did not connect well when switching from one theory to the other. It would also be difficult to compare these results to the results of the LP which where processed with ABR/BRL theory. Therefore OML theory and the floating point method where discarded as viable post-processing methods despite their remarkable fit.

The axial density profiles as measured with both probes for the cases of 500 W, 650 W and 800 W are plotted in figures 7.12a, 7.12b and 7.12c. The dashed dotted lines represent the upper and lower boundaries (from BRL, ABR theory). For the case of 500 W it is immediately apparent that both densities do not agree very well with each other. For the other two cases, at least nearer to the thruster the measurements seem to agree quite well, but deviate a little further downstream. In all cases, both

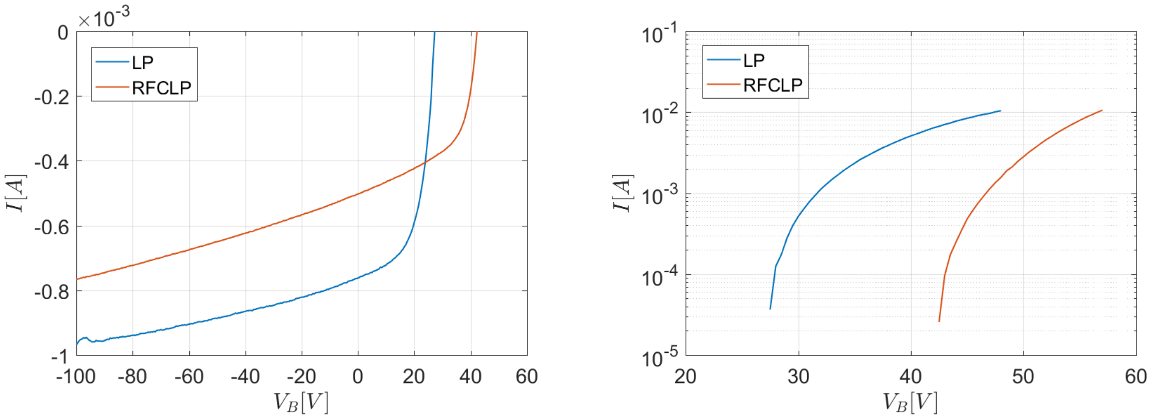

(a) Ion-collection region

(b) Electron-collection region

Figure 7.11: Comparison of $I - V$ curves for simple and RF-compensated Langmuir probes. (P = 650 W, z = 20 mm)

curves agree within each others upper and lower boundaries. To quantify this the relative difference between the simple and RF-compensated probe measurements as a function of the axial position, for all three cases is plotted in figure 7.12d. From this figure it is apparent that the density profiles deviate 20-40% for the 500 W case and 10-30% for the other two cases and that the curves are in better agreement near the thruster exit, and worse downstream.

In the same way figures 7.13a, 7.13b and 7.14a show the comparison of the axial electron temperature profiles as measured with both probes. Comparing these three plots, several things become apparent. Firstly in all three cases the temperature as measured by the RFCLP drops markedly near the throat of the thruster (20-40 mm). Furthermore in the 650 W and 800 W case the electron temperature as measured with the RFCLP is lower than that measured by the LP, while for the 500 W case the temperatures downstream agree within the measurement uncertainty.

Lastly the plasma potential profiles for both probes are compared, for all three cases as shown in 7.14b, 7.15a and 7.15b. Curiously enough the behaviour of the plasma potential is rather opposite to that of the electron temperature. In all cases there is a clear deviation between both probes near the thruster, around 20-60 mm. In the cases of 650 W and 800 W downstream both measurements agree within the measurement uncertainty, while in the case of 500 W both measurements do not agree at all.

7.4.2. Discussion

In the previous section the comparison of the simple Langmuir probe to the RF-compensated probe was presented. However first it has to be noted that everywhere except maybe at z = 20 mm, the plasma density is not high enough to satisfy the assumption that $\omega_{pi} \gg \omega$. This is the underlying assumption that guarantees that the Debye sheath comes to equilibrium in each phase of the oscillation. For the RF-frequency of 13.56 MHz this means that $n \gg 10^{17}$ m^{-3} has to be satisfied which is clearly not the case except perhaps at the exit plane. Despite this, several observations are discussed and where possible, explained.

Concerning the differences of the $I - V$ curves of both probes, part of the behaviour was as expected while part of it was not. The RF-compensated curves do in some cases show a positive shift of the floating potential and a steeper slope of the electron-retardation region, meaning that the RF-compensating probe is indeed, at least partially, correcting the effect of the RF-oscillations. However, since the ions should be unaffected by the RF-oscillations and the compensating electronics the ion-saturation current as measured by both probes should be the same. However this was found not to be the case. Furthermore the difference was not a constant factor (i.e. independent of bias potential) so a difference in probe area can be ruled out. It is is not clear why both ion-saturation currents differ so markedly (10-40%); in all cases the RFCLP measures a lower ion-current.

When comparing the measured density for both probes, all measurements seem to agree within the rather lenient measurement uncertainties; the case of 500 W barely so, while the other two cases seem to agree rather well. Quantitatively this agreement for the 650 W and 800 W cases is still a

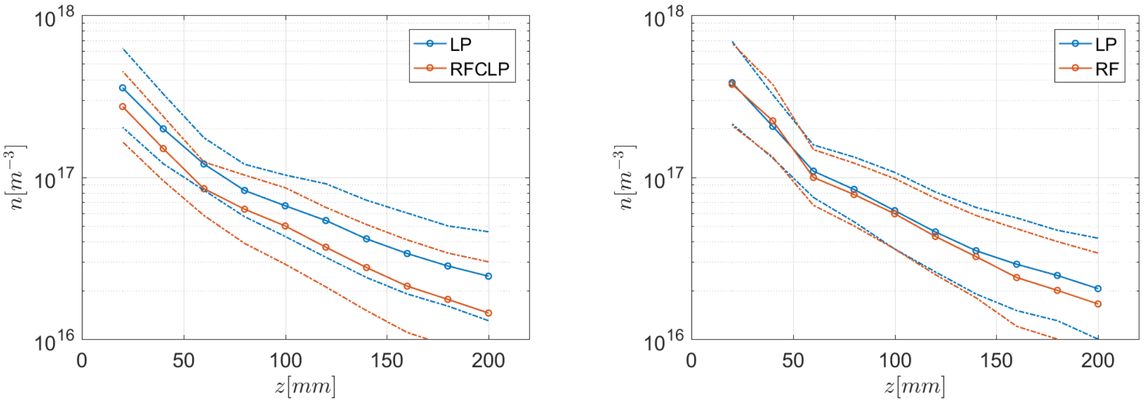

(a) 500 W RF power

(b) 650 W RF power

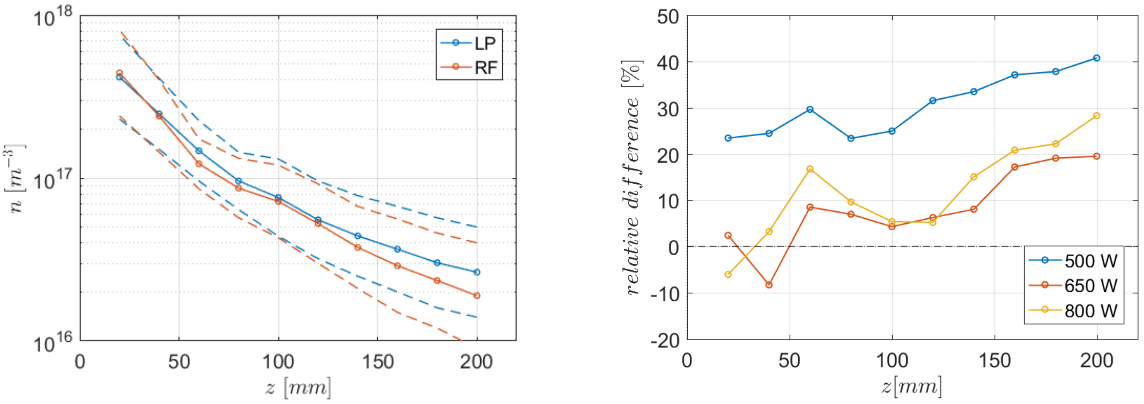

(c) 800 W RF power

(d) Relative difference of LP w.r.t. RFCLP.

Figure 7.12: Comparison of axial density profiles for simple and RF-compensated Langmuir probes.

10-30% difference, with the values deviating more, farther downstream. Correlating the difference in measured ion-current and the difference in the measured density proved unsuccessful. Here the effect of the lower electron temperature measured by the RFCLP is taken into account. Extracting the density from the fitted ion-saturation current requires the electron temperature to be known, since $I_i \propto n\sqrt{T_e}$. As the RFCLP (in the 650 W and 800 W cases) measured a lower electron temperature, for equal the ion-saturation currents this would yield a higher density. A lower measured ion-current and a lower measured electron temperature have opposite effects and thus compensate each other, at least to a certain extent.

Figure 7.16a shows a plot of the mean of the relative difference of the ion-saturation current of both probes, plotted as a function of the axial position. There is no a priori expected functional dependence but this plot was chosen to visualise the behaviour. The cases for higher power, show similar behaviour with a dip in the relative difference around 100 mm downstream, while the 500 W case shows a more constant but significantly larger difference in ion current over the plume. Figure 7.12d is re-plotted next to it for easy comparison. When discarding the first two points (20 mm ,40 mm) in figure 7.16b both plots show a somewhat similar trend, however no hard conclusions can be drawn other than that the relative difference in density is to a certain degree a reflection of a similar difference in the ion-saturation current. The fact that the ion density as measured by both probes is similar (<10% difference) for z = 20-40 mm, despite the difference in ion saturation current can be explained by the difference in T_e. It seems that close to the thruster the probe is able to filter the RF fluctuations yielding a lower T_e. This lower T_e then yields a higher density despite the lower ion saturation current.

The measured electron temperature in all three cases markedly differs close to the thruster and for the higher power cases also further downstream. It is important to recall that the maximum amplitude of the plasma potential oscillations that can be shielded by the probe is dependent on the density. Figure

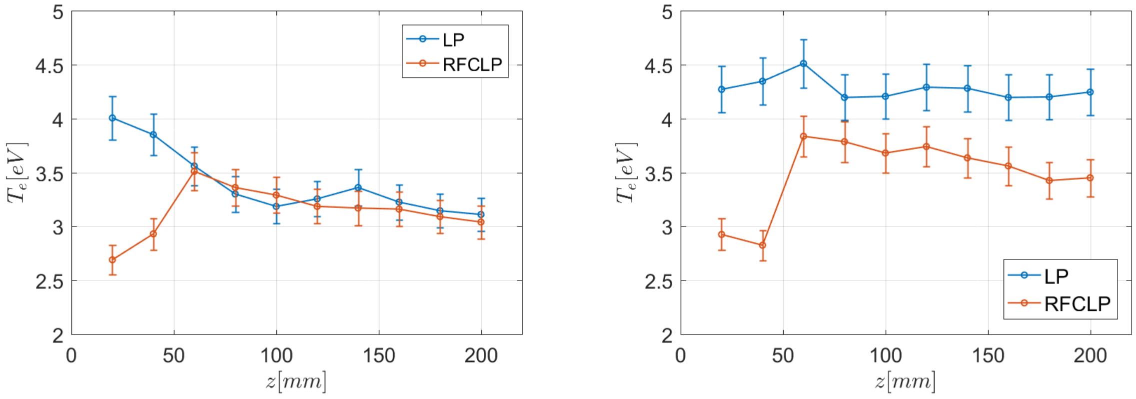

(a) 500 W RF power

(b) 650 W RF power

Figure 7.13: Comparison of axial electron temperature profiles for simple and RF-compensated Langmuir probes.

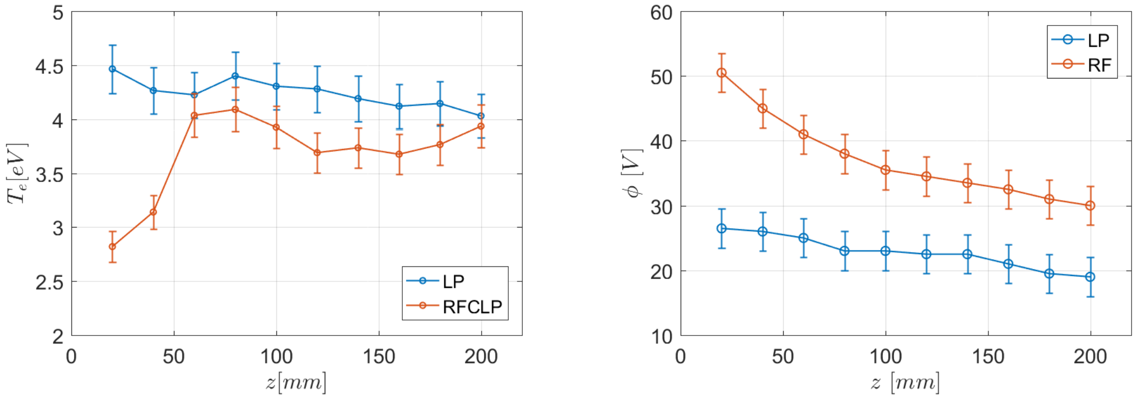

(a) Electron temperature at 800 W RF power

(b) Plasma potential at 500 W RF power

Figure 7.14: Comparison of axial plasma parameter profiles for simple and RF-compensated Langmuir probes.

4.7 in section 4.2 shows this dependence and from this figure it is clear that only for densities of 10^{17} m^{-3} and higher, does the probe shield oscillations of the order of the electron temperature. Furthermore it is important to note that the amplitude of the oscillations decrease further downstream as the inverse square of the distance to the antenna and that it is larger for higher RF power. The reason that the electron temperature is markedly lower only very close to the thruster could be that only here the density is high enough to filter the oscillations. Further downstream the amplitude of the oscillations decreases but so does the ability to filter. Without knowing the amplitude of the plasma potential oscillations it is impossible to assess whether the RFCLP filters all or only part of the oscillations. The fact that T_e for the 500 W case downstream is the same for both probes could mean that the RF field here is too small to actually perturb the $I - V$ curve, while at 650 W and 800 W they do.

Lastly the plasma potential profiles pose another problem. The plasma potential as measured with the RFCLP should in principle be lower than the LP instead of higher as shown in figures 7.14b to 7.15b. However since the magnetic field perturbs the electron saturation region this is not exactly straightforward. Judging from only the 650 W and 800 W cases it could also be that close to the source the RFCLP is perturbing the plasma too much due to the large secondary electrode. The area ratio being 24, the secondary electrode extracts significantly more current from the plasma. However the 500 W case does not corroborate this idea since the plasma potential is higher as measured with the RFCLP over the whole plume.

In any case the 500 W case in general should raise some doubts as both the plasma density as well as the plasma potential differ greatly for both probes. It could be that the plasma conditions have

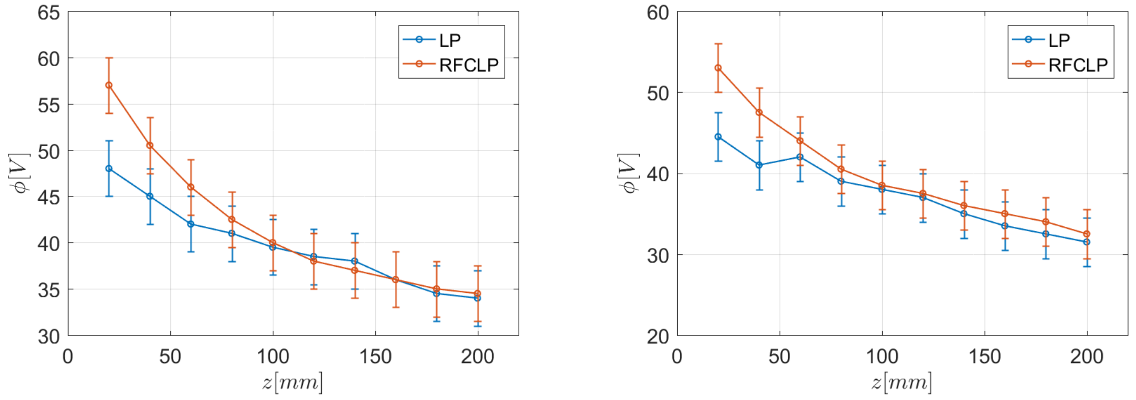

(a) 650 W RF power

(b) 800 W RF power

Figure 7.15: Comparison of axial plasma potential profiles for simple and RF-compensated Langmuir probes.

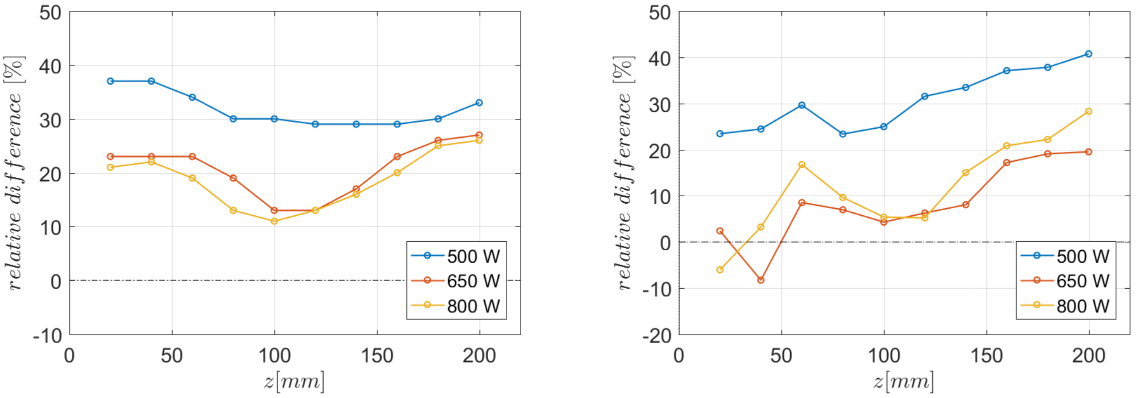

(a) Relative difference in ion-saturation current

(b) Relative difference in plasma density

Figure 7.16: Side-to-side comparison of relative difference in ion saturation current and in resulting plasma density for LP and RFCLP at different RF powers.

been different during these measurements. However there were no significant differences in chamber pressure, RF power, magnetic field during the measurements which were taken over a 17 min interval with 4 min between both measurements.

To summarise the comparison on the RFCLP has so far proven to be inconclusive. Therefore all further experiments are performed with the simple LP. It is important to note that one of the main assumptions, namely $\omega \ll \omega_{pi}$ is not satisfied in any of the measurements except near the exit plane. This clearly hinders the interpretation of the measurements as the theoretical framework need no longer apply. Furthermore the 500 W case seems to deviate strongly from the other two cases and it is recommended that it is repeated to verify the behaviour. It is also difficult to assess whether the probe is actually capable of filtering the oscillations, since their amplitude is not known a priori. One way to verify this is by measuring $I - V$ curves with an emissive probe. The first derivative should show two peaks with the difference between them equal to two times the amplitude of the RF-oscillations. Furthermore measuring the plasma potential with the emissive probe can be used to verify whether the potential as measured by the LP or RFCLP gives the correct value.

7.5. Emissive Probe Characterisation

Currently the emissive probe is used with the method of floating potential in the limit of large emission. For this method the required value of the heating current needs to be established. Furthermore an estimate of the probe temperature is given. All results presented in this section are from measurements taken at 500 W and using the nominal configuration. Figure 7.17a shows an image of the very luminescent emissive probe at 0.8 A heating current. The thruster is operating at 500 W but the plasma emission is completely overshadowed by the incandescence of the EP.

7.5.1. Saturation Regime

As discussed in section 4.3 when the heating current is increased the probe emission current increases. When the probe emission current is increased sufficiently, the floating potential of the EP approaches the plasma potential. A single measurement of the probe potential is then sufficient to measure the plasma potential. This method allows for fast mapping of the plasma potential in the plume. To investigate this saturation regime the probe potential is measured at the centre of the thruster exit plane as a function of the heating current. The potential is expected to stay relatively constant at low heating current, then sharply increase and then level off to a value near the plasma potential. Measurements were taken from 0.1 to 0.8 A. The upper limit was chosen because during previous measurements the wire burned above 0.8 A. Fortunately the potential saturated around 0.8 A of heating current. Between 0.1 and 0.4 A the resolution was 0.1 A, after 0.4 A the resolution was increased to 0.05 A and from 5.0 A increased further to 0.02. This resolution was manually adjusted based on a previous preliminary measurement at low resolution. The results are shown in figure 7.17a. The expected behaviour is clearly reflected in this plot. The potential starts increasing after 0.4 and levels off around 0.7-0.8 A.

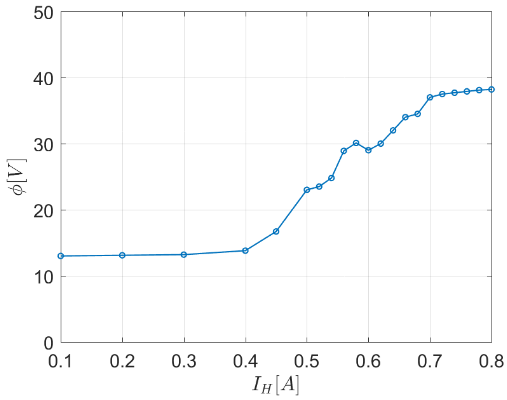

(a) Probe potential as a function of heating current.

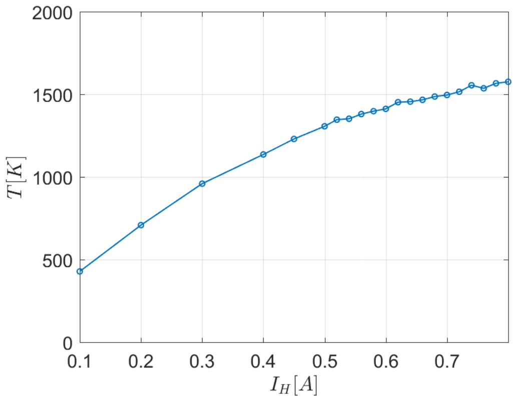

(b) Probe temperature as a function of heating current.

7.5.2. Probe Temperature

It is not necessary to know the emissive probe temperature to perform the plasma potential measurements. However, it is of interest for verification purposes and to calculate the emission current using Richardson-Dushman. Ideally the probe temperature is measured directly with an infrared thermometer, however the glass of the vacuum chamber is opaque in the spectral region used by this thermometer. Another way would be to acquire the spectral distribution using the spectrometer and fitting a Planck curve. It is even easier to measure the probe temperature indirectly. Since the probe wire is heated with a simple current source that displays both the current and the voltage, the probe resistance as a function of the heating current can be calculated. Furthermore the ratio $R(T)/R_{300K}$ as a function of temperature is for (Thoriated-)Tungsten is tabulated in [43]. Fitting this data with a second order polynomial $T = ax^2 + bx + c$, with $x = R(T)/R_{300K}$ yielded coefficients $a = -1.6519$, $b = 203.55$ and $c = 126.18$. The calculated resistance was divided by its value at room temperature: 1.4Ω and the corresponding temperature was calculated using the polynomial. The resulting curve is shown in figure 7.17b. It can be seen that the probe temperature at 0.8 A reaches 1600 K. This method introduces a small error since the room temperature is not at 300K but 293K and R_{300K} includes the resistance of the leads.

Lastly, the emitted current density using Richardson-Dushman's law (eq. 4.45) is calculated for both Tungsten and Thoriated-Tungsten, based on the aforementioned temperature calculation. This calculation does not take into account the formation of space-charge and only calculates the theoretical emission current density. The results are presented in figure 7.17b.

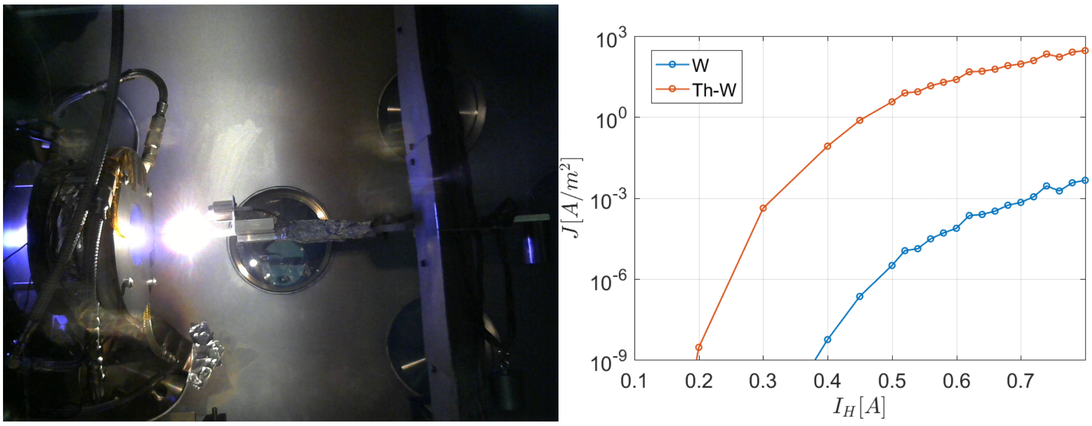

(a) Image of highly luminescent emissive probe at 0.8 A heating current.

(b) Emission current density according to Richard-Duschman as a function of heating current.

7.5.3. Preliminary Comparison of LP and EP plasma potential measurements

As a first test of the emissive probe, two axial and two radial plasma potential profiles were acquired. The axial profile was taken in tandem with axial Langmuir probe measurements allowing for a preliminary comparison. The axial plasma potential profiles were measured with the emissive probe at a heating current of 0.8 A. The measurements are taken from 200 to 20 mm downstream in 5 mm intervals. The EP measurements take less than 30 seconds while the same data taken with a Langmuir probes would take over 20 minutes with a lower spatial resolution. This already shows the main advantage over LP based plasma potential measurements. The Langmuir probe measurements taken concurrently with these curves turned out to be particularly noisy. The results, presented in figure 7.17a are by no means conclusive but serve as a preliminary comparison. Both curves for the EP are taken 6 minutes apart and they differ by less than 2.5%. Emissive probe measurements using the method of floating point in the limit of large emission usually float about $1T_e$ below the real plasma potential.

To provide this correction for the plasma potential, the temperature as measured with the Langmuir probe was extrapolated over the full range of z = 20 to z = 200 mm. The temperature was fitted with a polytropic cooling law (to be discussed in section 8.2 of chapter 8) while the normalised density profile was fitted with $\sim z^{-1}$ the combination of both yielded an approximation for $T_e(z)$. The corrected curves is plotted in green with a 7.5% errorbar (5% in T_e 2.5% in ϕ).

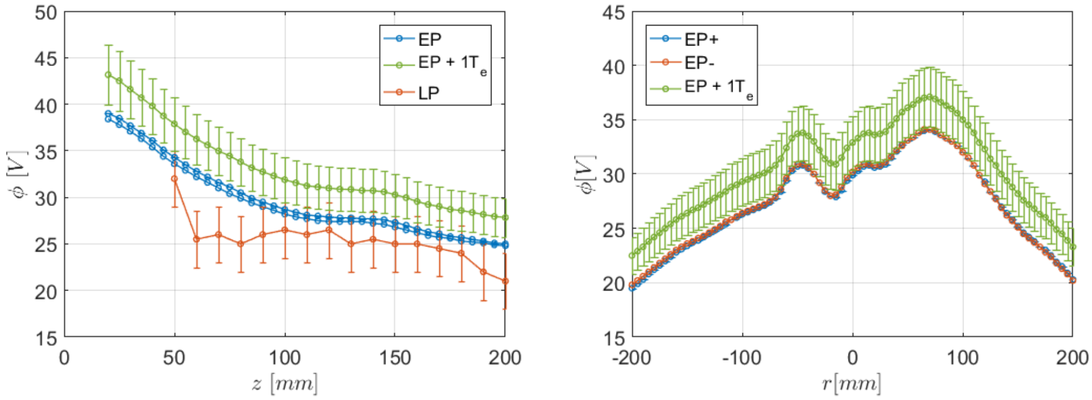

(a) Axial plasma potential profiles taken with both EP and LP.

(b) EP radial plasma potential profiles at z = 80 mm.

7.5.4. Radial plasma potential profile

Two consecutive (within 2 min) radial plasma potential profiles were obtained at z = 80 mm, taken in opposite direction i.e from -200 to +200 (EP+ and EP-) and vice versa in 5 mm intervals. The results are shown in figure 7.17b. Both measurements agreed within less than 2%. The temperature T_e was obtained from the axial LP measurement at z = 80 mm and assumed constant over the radial direction (a reasonable assumption as will become clear in in section 8.2 with perhaps a ±1 V error). The corrected curves is plotted in green with a 7.5% errorbar (5% in T_e 2.5% in ϕ).

7.5.5. Discussion

In this section the plasma potential was measured as a function of the heating current. It was found that 0.8 A is a sufficient heating current for the method of *floating potential in the limit of large emission*. However since the required emission current scales with the plasma density, the saturation heating current might shift to a higher value for denser plasmas. As such, this curve needs to be repeated for measurements at higher RF power.

Furthermore the temperature of the probe was estimated with indirect measurements of the resistance as a function of the heating current as plotted in 7.17b. It can be seen that the probe temperature approaches 1600 K at 0.8 A heating current. Using this relation the Richardson-Dushman current density for both pure tungsten and the thoriated tungsten was plotted. The emission of Th-W greatly outperforms that of pure Tungsten, and the current density is roughly five orders higher at 0.8 A of heating current. This clearly shows the benefit of using Th-W over pure W for emissive probes.

The two axial and radial plasma potential profiles as measured with the emissive show a smooth profile, with high resolution (5 mm) and short measurement time; about 40 data points per minute compared to 2 points per minute with the LP. Temperature measurements are necessary to provide a correction for the absolute value of the potential. However for relative measurements this is not necessary. In both cases two profiles where measured which agreed within 2.5% (axial) and 2% (radial) implying a small random error and an insensitivity to the direction of the sweep in case of the radial profile.

When comparing the LP and EP measurements in the axial profile it can be seen that the LP underestimates the plasma potential by >5 V, has a larger random error and does not provide a smooth profile. Furthermore in the comparison between LP and RFCLP it was found that the RFCLP plasma potential increased more than the LP plasma potential which seems to agree better with the EP measurements. Unfortunately no data was taken with the EP and RFCLP concurrently, so no conclusions can be drawn. The comparison between LP and EP is not conclusive either, in part because the LP data in this case was particularly noisy. However it can be concluded from these preliminary results that the emissive probe is an improvement over the Langmuir probe for plasma potential measurements in both accuracy and speed.

Summary

In this chapter plasma probe measurements have been discussed in great detail. An evaluation of a MATLAB based post-processing algorithm based on Chen's iterative scheme has been presented. It was found that this method provided similar or better results in comparison to the planar approximation which was found to fit the data rather poorly. However Chen's implementation in Excel in the end proved more flexible in processing the data. All Langmuir probe data in this report are processed with Excel sheets based on Allen-Boyd-Reynolds theory and Bernstein-Rabinowitz-Laframboise theory. The latter Excel sheet has been modified to take into account both the cases $\xi > 3$ and $\xi < 3$. From literature it was found that under similar conditions as in this work the geometric mean of the densities as found from both theories agreed well with independent micro-wave interferometry measurements. This empirical approach was therefore adopted.

An error estimation was performed for all plasma parameters. The uncertainty of the plasma density is in large part due to the fact that both ABR and BRL theories are valid, but produce results differing up to 30-80% from their geometrical mean. The values from the separate theories (ABR, BRL) were taken as the upper and lower boundaries. It has to be noted that uncertainties in plasma density inferred from LP measurements, of the order of 50% are not uncommon [66].The repeatability of the plasma density measurements was of the order of 10%. For the electron temperature an uncertainty of 5% was found by comparing the differences between the results of both theories. The uncertainty in the plasma potential is largely due to a badly defined peak in dI/dV and operator error in selecting the maximum; it was estimated to be 3 V. The stability of the plasma was assessed by repeating a single measurement multiple times over a time span of 6 minutes and the plasma was found to be stable within the measurement uncertainty Possible hysteresis in the $I - V$ curves based on the direction of the voltage sweep was found to be non-existent.

A comparison of simple and RF-compensated Langmuir probe measurements for three different RF powers and at several axial positions downstream of the thruster were inconclusive. Most importantly one of the main assumptions underlying the theory of RF-compensation was not satisfied. Furthermore there were unexplained differences in measured ion-current that to some extent correlated with differences in plasma density between the two probes. Electron temperatures differ markedly mostly near the thruster, but it can not be concluded that the RFCLP values are the correct value. It is necessary to measure the amplitude of the plasma oscillations before any real conclusions can be drawn. Theoretically, downstream any shielding should be non-existent (max$(V_{rf}) < 1V$) due to the low density. The plasma potential for the RFCLP deviated from the LP measurement close to the thruster. This also remains unexplained and should be further investigated by comparison to emissive probe measurements.

Lastly a characterisation of the emissive probe was presented along with some preliminary measurements. The emissive probe was shown to be working, providing plasma potential measurements at 40 samples per minute with high accuracy outperforming the Langmuir probe. For a 500 W operating point the necessary heating current for the floating point method was found to be 0.8 A corresponding to an estimated probe temperature of 1600 K. Furthermore it was shown that thoriated tungsten is a big improvement over pure tungsten in terms of emission current.

8

Plasma Parameters in the near-Plume

Introduction

In this chapter the measurements of plasma parameters in the near plume region (up to 200 mm downstream) are presented. Many important phenomena such as plume formation and magnetic thrust generation happen in this region. It also provides sufficient information to compare the results to the DiMagNo simulation. Further downstream the plasma density drops and different diagnostic and post-processing methods are needed, something the findings of section 7.1 substantiated. Considering the current capabilities of the lab and the time constraints of this study, the focus is on the near-plume.

All measurements have been taken with the Langmuir probe. Plasma Potential measurements with the emissive probe are pending. All measurements presented here are for the case of the nominal magnetic field as discussed with 560 G at the centre of the exit plane and a mass flow rate of 50 sccm as detailed in 6.1.6 and 6.1.7. The axial and radial evolution of the plasma density, electron temperature and plasma potential are presented, discussed and the results for three different RF powers are compared.

8.1. Plasma Density

The main figures of merit for any thruster are the thrust and I_{sp}. The advantage of a HPT is a high thrust density compared to other electric thrusters. This is due to the inherently high plasma density of helicon source. The density is therefore a very important plasma parameter. Note that plasma density is the number density, defined as the number of ions/electrons per cubic meter. This section presents the results on the axial and radial evolution of the plasma density in the plume as measured with the simple Langmuir probe.

8.1.1. Axial evolution

Firstly the downstream axial evolution[1] of the plasma density is investigated for 500 W, 650 W and 800 W. The results are plotted in figure 8.1a

The difference in density between the 500 W and 650 W case is between 5-20% while the difference between wit the 800 W case is up to 25%. This is larger than the 10% repeatability found in the previous chapter. In all three cases the density decays rapidly downstream. To compare the trend of the axial evolution all three curves are normalised with their respective maximum values and the axial dimension is normalised with the thruster radius of 15 mm. A semi-log plot of the normalised profiles are shown in figure 8.1b. From this plot it becomes clear that the axial evolution is independent of the total RF power, only downstream there seems to be a small difference between the three cases. The semi-log plot shows that the density decays with z^{-1}. After 10 thruster radii the density is reduced by about one order of magnitude.

---

[1] Axial evolution is defined as the on-axis downstream evolution.

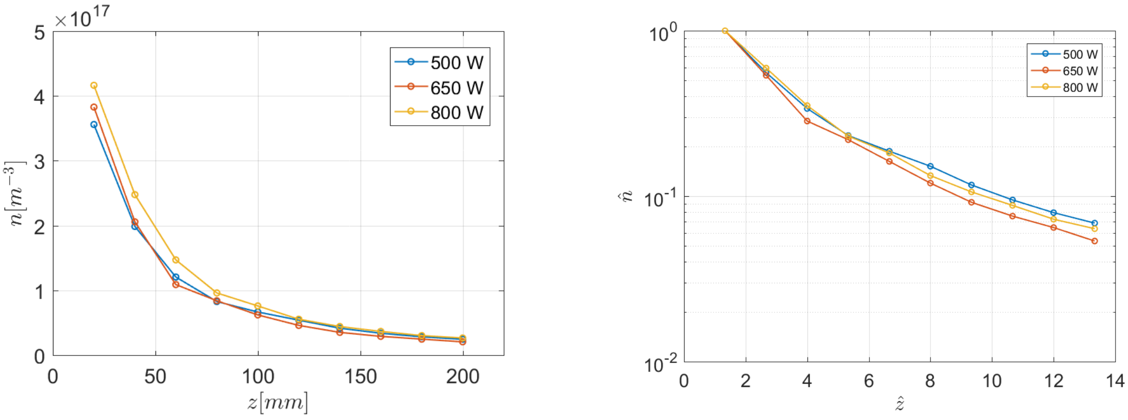

(a) Axial density profile at different RF power.

(b) Normalised log plot of axial density profiles

8.1.2. Radial evolution

Similar to the axial evolution the radial evolution of the plasma density has been measured. Profiles are obtained at z = 40 mm downstream, to 50 mm on either side of the centre line with a resolution of 5 mm for the cases of 500 W, 650 W and 800 W at the same conditions are mentioned before. The resulting profiles are plotted in figure 8.1a. From this plot it can be seen that the plasma density increases with the RF power which is expected. However the relationship between the source density and the input parameters is a separate investigation, part of which is introduced in appendix A. In this section, and this report in general the focus is on the relative evolution of the plasma parameters. From figure 8.1a it can furthermore be seen that for all three powers there is roughly flat front near the centre line, with an asymmetry on the left side that becomes more pronounced with increasing power. To better assess how the RF power influences the radial evolution, all three curves are normalised with their centre value and the radial dimension is normalised by the thruster radius. The resulting figure is shown in figure 8.1b on a semi-log plot. Apart from the 'defect' on the left side of the 800 W case the curves reduce to the same general profile indicating that the radial evolution is not dependent on the RF power. Another asymmetric 'defect' can be seen on the right wing where the density is higher that the preceding exponential decay predicts around +2.3 thruster radii. This 'defect'[2] is present for all three powers indicating that it is a structural characteristic of the plasma.

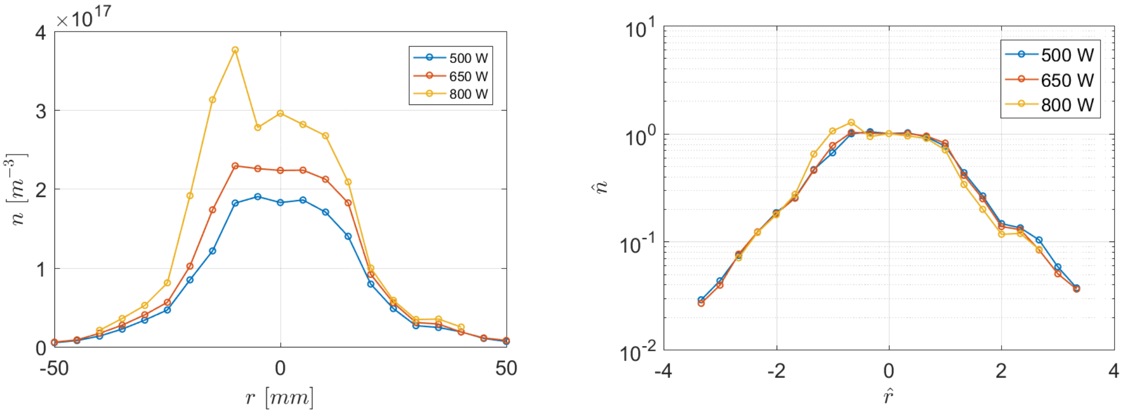

(a) Linear scale.

(b) Normalised, logarithmic scale.

Figure 8.1: Radial density profiles as function of RF power.

For the 500 W case several radial density profiles have been measured at different axial positions, from 40 to 200 mm in 40 mm intervals. Measuring closer to the thruster would perturb the plasma too

---

[2] Defect is used here to denote the deviation from the expected axi-symmetry

much. Due to the expanding nature of the plume the maximum width of the profile was chosen smaller, close to the thruster than downstream, but with a smaller resolution. Downstream the measured profile spanned a larger diameter of the plasma but the resolution was increased to keep measurement time within a reasonable limit. The measurement points are given in table 8.1.

z [mm]	r [mm]	step [mm]
40	± 50	5
80	± 100	10
120	± 150	15
160	± 150	15
200	± 150	15

Table 8.1: Radial density profile grid spacing

When processing the data it was found that not all data points could be processed since the ion saturation region of $I - V$ curves in these cases were linear and didn't fit the model. Similar to the discussion in chapter 7 at these densities the planar approximation is not valid and it is not clear what model is applicable to interpret this data. The measurements that could be processed are shown in figure 8.2 in both linear and a semi-log plot.

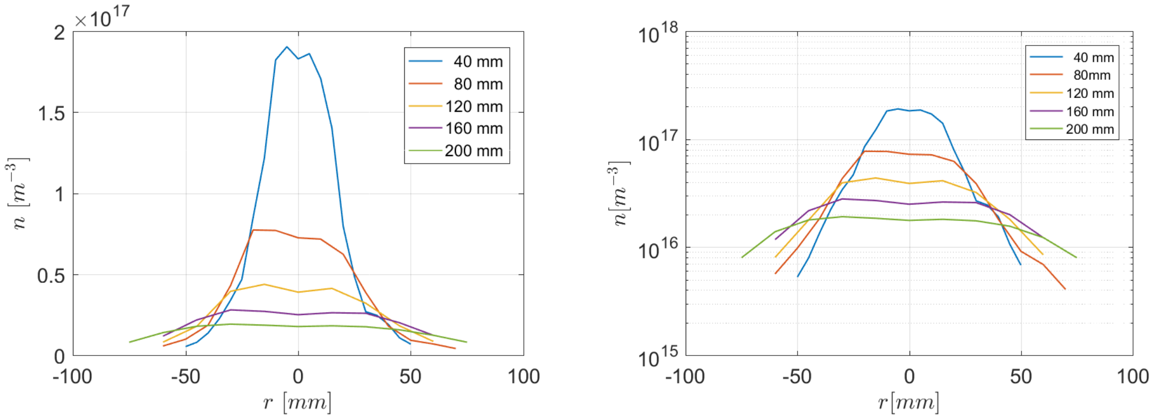

(a) Linear scale

(b) Semi-log scale.

Figure 8.2: Radial density profiles at different axial positions for P = 500 W.

From the linear plot two things become evident. In general the front is relatively flat with two small peaks off-centre. Furthermore the profile is slightly asymmetric with a higher density on the left side of the profile. Both the asymmetry and the small peaks decrease downstream. Par-axially the density decays quickly in the axial direction, as discussed in the previous section. Near the edges the plasma density increases; the plasma expands radially from the axis towards the wings of the plume. In each profile the density near the centre is roughly of the same order of magnitude while radially it decays quickly. From the semi-log plot it becomes clear that the radial evolution of the plasma is exponential, since the behaviour far off-axis is linear the semi-log plot. From the semi-log plot it is also clear that there is another asymmetry off-axis on the right side of the profile. For the profile at z = 40 mm and r = +30 mm the density is slightly higher than the exponential decay of the preceding points would predict. This 'defect' then migrates radially to +60 mm at z = 80 mm. At z = 120 and z = 160 there are no data points beyond r = +60. The fact it is measured at both z = 40 and z = 80 implies that it is actually present in the plasma and also persists over time as there are more than 10 minutes between both measurements.

To better visualise the plume the profiles were interpolated onto a finer grid with 1 mm resolution and off-axis the profiles are extended by extrapolating the exponential behaviour up to $r = \pm 80$ mm. In this way a contour plot of the plasma density in the near plume region can be made. Figure 8.3 shows this plot in both linear and log-scale superimposed on a photo of the plume. The photo was taken and scaled by using the size of the bore of the MN coil. Its inside diameter is about 90 mm, which results in a scaling factor of about 3 pixels per mm. Using this factor the image iss cropped to an area corresponding to $0 < z < 200$ mm and $-80 < r < 80$ mm. The photo is taken in the mid-plane (i.e. from the side) while the density profile is a transversal cross-section (i.e. as seen from the top). When there is axi-symmetry these should coincide, however in reality the plume is not fully axi-symmetric as was obvious from the radial profiles. Furthermore the emission of the plasma is not only dependent on the density of the ions but also that of the neutrals as well as the plasma density. However the approximate correlation is illustrative of the plume.

Although this is an approximation it nicely visualises the plume in terms of density. Since the curves beyond z = 80 mm do not extend far enough radially to include the aforementioned 'defect' the exponential extrapolation might omit this bump. However since this bump already migrated 30 mm radially from z = 40 to z = 80 mm it is not unlikely that this 'defect' at z = 120 mm is already outside of the ±80 mm range. In the linear plot the strong decay in axial direction is more emphasised while in the semi-log plot the divergence of the expansion can be clearly seen.

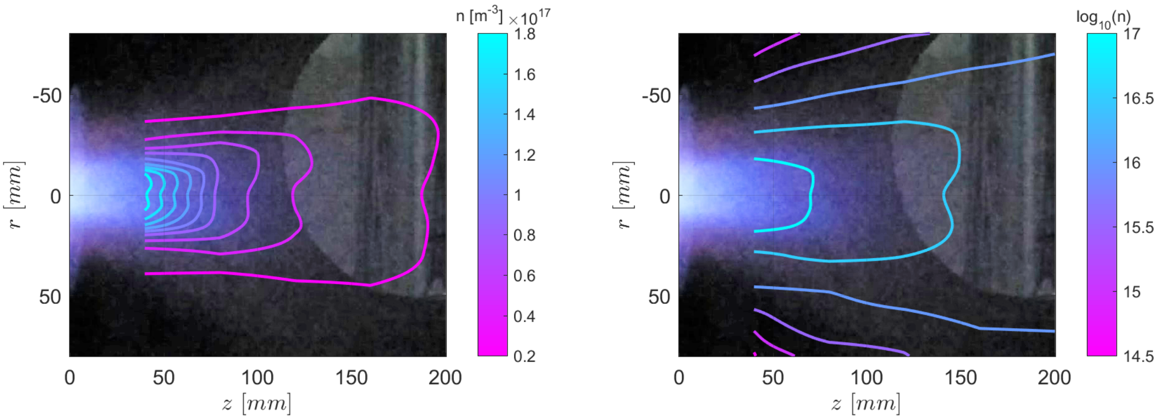

(a) Linear plot.

(b) Semi-log plot.

Figure 8.3: Contour plot of plasma density in the near plume. P = 500 W.

8.1.3. Discussion

In this section the axial and radial evolution of the plasma density were presented for three different levels of RF power. Comparing normalised profiles in both dimensions it became clear that, bar some defects, the spatial distribution of the plasma density is independent of the RF power. The shape of the plume therefore is independent of the magnitude of the plasma density. This finding is in line with the DiMagNo model that uses a normalised plasma density. According to the DiMagNo model the plume expansion is dictated mainly by the temperature and the magnetic field. Repeating these measurements for different magnetic nozzle strengths should be the next step to corroborate this. The low overall plasma density $n < 10^{18}\ m^{-3}$ implies that the thruster is not operating in a helicon mode, but is still in an inductive mode. At 800 W as spike can be seen slightly left off-centre of the radial profile. It is not clear what causes this and why it occurs only on one side. Density peaks off-centre have been observed in helicon thrusters and are attributed to electrons moving along the edge of the magnetic nozzle. [19, 68, 78] However this is always symmetric, which here is clearly not the case.

On top of that there is the 'defect' in the right wing of the radial profile. Clearly the axi-symmetric assumption of the DiMagNo model does not hold up. This could either be due to a misalignment of the thruster with respect to the measurement system or due to an asymmetry in the plasma production in the source. The latter is probable considering the irregular shape of the antenna. The fact that recent measurements (not presented in this work) with a half-helical antenna, show a single, symmetric peak corroborate this.

8.2. Electron temperature

8.2.1. Axial evolution

The axial temperature profile is presented in figure 8.4a. From this figure it can be seen that the temperature is similar for 650 W and 800 W while the 500 W case is about 5-10% lower than in the other two cases. Furthermore in the 500 W case the temperature decreases over the axial direction, while in the other two cases the plasma has a constant temperature of about 4.2 eV.

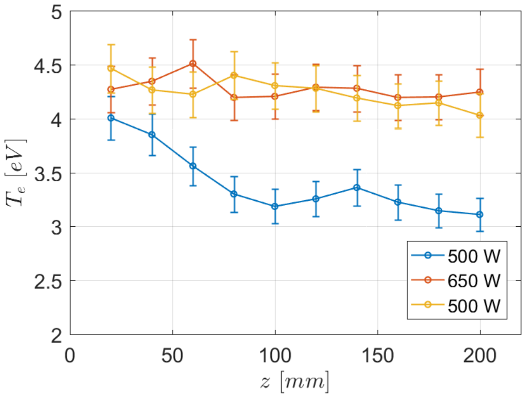

(a) Axial evolution of electron temperature for different RF power.

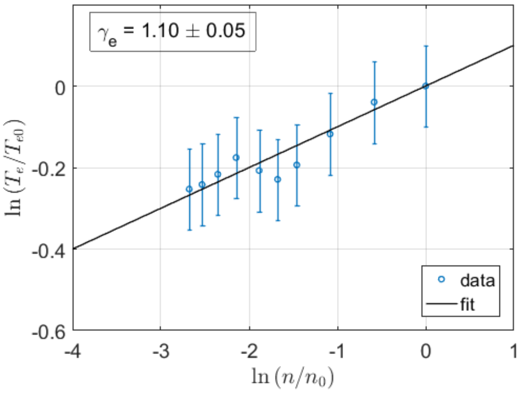

(b) Fit of polytropic cooling law for P = 500W.

Since the 500 W case clearly shows signs of cooling the polytropic coefficient γ_e can be calculated. The polytropic cooling law can be formulated as:

$$\left(\frac{T_e}{T_{e0}}\right) = \left(\frac{n_e}{n_{e0}}\right)^{\gamma_e - 1} \tag{8.1}$$

There the 0-subscript denotes a value for normalisation, usually $n_{e0} = n_e(0)$. In this case however, the values of T_e, n_e at z = 20 mm are used for normalisation. The logarithm of the normalised temperature is plotted as a function of the logarithm of the normalised density in figure 8.4b and fitted with a straight line. The fitting yielded a value $a = 0.10 \pm 0.05$ which results in a polytropic coefficient of $\gamma_e = 1.10 \pm 0.05$.

8.2.2. Radial Evolution

Also of interest is the radial evolution of the electron temperature First three radial plots taken at z = 40 mm for 500 W, 650 W and 800 W and shown in figure 8.4a. Error bars are only shown here for single points to avoid cluttering, they are approximately independent of the radial position. From this plot it can be seen that there is an asymmetry in the temperature profile, where the temperature differs about ±1.1 eV from the average of 3.7 eV, higher on left side and lower on the right side. This asymmetry is present for all three power levels and therefore independent of them. Furthermore, since these measurements have been taken during different tests, it means that this asymmetry is structurally part of the plasma.

The same data points as used for the density profiles were processed to find the electron temperature and are shown in figure 8.4b. Error bars are only shown here for single points to avoid cluttering, they are approximately independent of the radial position. From this plot it becomes apparent that the temperature increases downstream, compliant with the axial evolution discussed before. The asymmetry mentioned before is also present for z = 80 mm and then relaxes downstream where the temperature evens out over the radial dimension.

8.2.3. Discussion

The two main findings from the spatial distribution of the temperature are the following: firstly there is a clear asymmetry of the temperature in the radial direction. It is not clear what causes this asymmetry but it could be related to the sub-optimally shaped antenna. For the loop-antenna that is asymmetric and irregular an asymmetric radiation profile can be expected that could be responsible for most of the observed asymmetries. Repeating these measurements with the half-helical antenna could provide

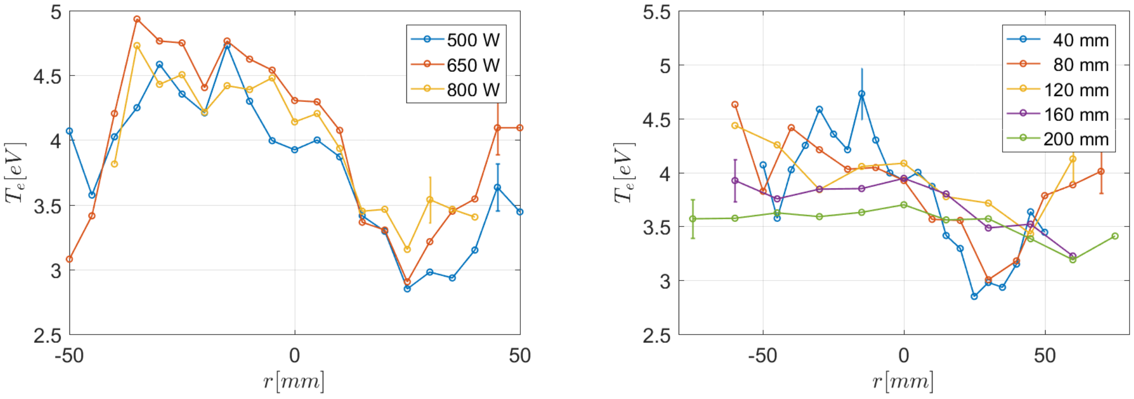

(a) Radial evolution of electron temperature at z = 40 mm for different RF power.

(b) Radial evolution of electron temperature at different axial position and P = 500 W.

insight on this issue. The other main point is the observed polytropic cooling at 500 W while at 650 W and 800 W the plasma seems isothermal in the axial direction. The assumption of isothermal electrons leads to an un-physical situation where the potential can decrease indefinitely. In reality even at higher power the electrons should experience cooling downstream. However, it could be that the rate of cooling is so low that cannot be measured within the uncertainty of these measurements. The estimated polytropic coefficient of $\gamma_e = 1.10 \pm 0.05$ is in line with measurements on other helicon devices as well as moderate cooling rates assumed in the extension of the magnetic nozzle model [42, 49, 56]. Kinetic modelling of electron cooling is in it's early stages, but could provide future predictions that could be compared to these measurements [53].

8.3. Plasma Potential

8.3.1. Axial evolution

The axial evolution of the plasma potential as measured with the Langmuir probe is shown in figure 8.4a. Two things can be seen from this plot, firstly the results for 800 W and 650 W seem to agree within the error. Secondly the 500 W case has a remarkably lower plasma potential over the full range of the axial dimension. To better compare the three curves a normalised plot is shown in 8.4b. Here $\hat{\phi} = \phi - \phi_0$ with $\phi_0 = \phi(1.33)$ and $\hat{z} = z/R$ where the thruster radius R = 15 mm. From this second plot it becomes clear that the 650 W and 800 W cases show a similar axial progression, within the error bars, while for the 500 W case the potential decreases more slowly, this is compliant with the observed cooling.

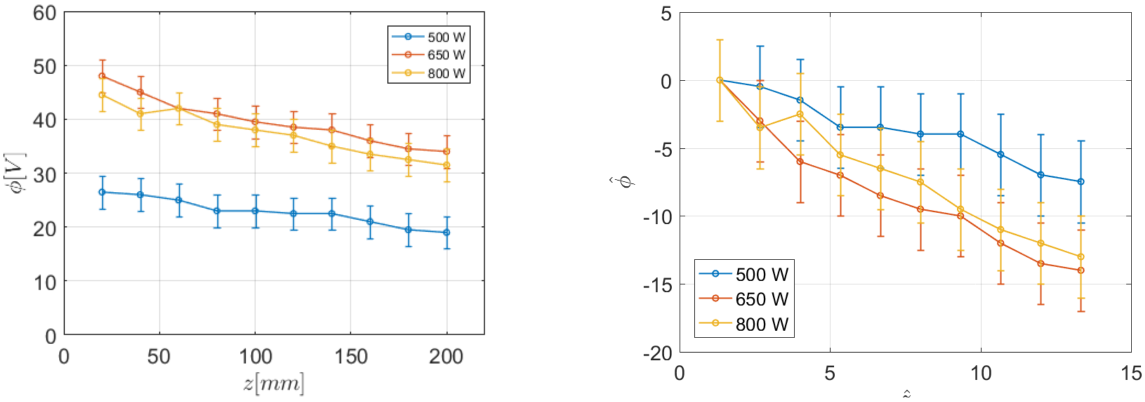

(a) Real values.

(b) Normalised

Figure 8.4: Axial evolution of plasma potential for different RF power.

8.3.2. Radial evolution of the plasma potential

The radial evolution of the plasma potential for the 500 W, 650 W and 800 W case are plotted in figure 8.5a. This plot differs from the preceding plots of the temperature and density in that it compares the three cases at z = 80 mm instead. This was done since the 500 W case at z = 40 was too noisy to allow for a good comparison. The radial profile is relatively flat but asymmetric, linearly increasing from about 36 V to the left of the centre line to about 44 V to the right of the centre line. Surprisingly the potential is the same for all three RF powers, including the 500 W case. This contradicts the axial measurements discussed before and shown in figure 8.4a. It seems that the thruster was operating at different conditions than during the radial measurements taken afterwards. This may also explain the large difference between the LP and RF-compensated probes, in density and potential along the axial direction discussed in the previous chapter.

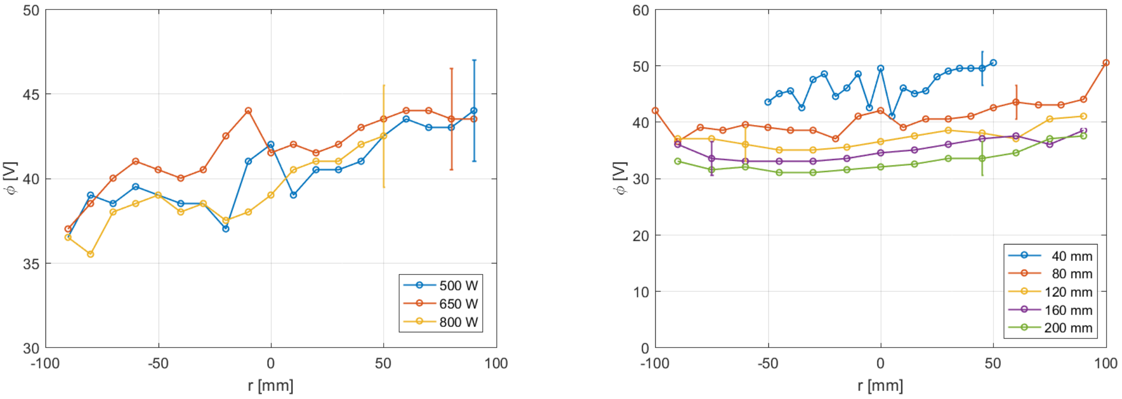

(a) For different RF power at z = 80 mm.

(b) For different axial position at 50 W.

Figure 8.5: Radial evolution of plasma potential

The radial profiles for the 500 W case have been measured at the same axial positions as for the other parameters specified in table 8.1. The results are plotted in figure 8.5b. The same asymmetry as discussed before can be seen to propagate over the axial direction. The plasma potential also seems to be slightly higher at the edges.

8.3.3. Discussion

In this last section the plasma potential profiles in axial and radial dimension have been measured with the Langmuir probe. As the Langmuir probe was already employed for density and temperature measurements, processing the $I - V$ curves to obtain plasma potential measurements was of minimal effort. However in the light of chapter 7.5 these results are of mediocre quality and should be repeated with the emissive probe in the future.

The axial profiles for the 650 W and 800 W case seem to be independent of the power and follow the same dependence. The 500 W case differs in two respects, firstly it is absolute value about 10-20 V below the plasma potential of the other two cases. It is not yet clear what could cause this behaviour. Secondly it decreases at a slower rate compliant with the observed cooling. The axial evolution of the density and the plasma potential are related through the Boltzmann equation:

$$n(\phi) = n_0 \exp\left(-\frac{\phi - \phi_0}{T_e}\right) \tag{8.2}$$

For an isothermal plasma, plotting $\ln(n/n_0)$ vs. $-\hat{\phi}/T_e$ should yield a straight line with a slope of -1. In this case a logarithm base 10 is used, and a straight line with slope $-\ln(10)$ to accommodate the nomenclature of Merino [57]. This plot is shown for the data of 500 W, 650 W, and 800 W in figure 8.6a side by side with the theoretical plots from Merino. For $\gamma_e = 1.1$ there is an asymptotic increase to $-\hat{\phi}/T_e = 11$ at $\log_{10}(n/n_0) \to -\infty$ as $n \to 0$, shown in figure 8.6b. The lines of $\gamma_e = 1$ and $\gamma_e = 1.1$ with respect to the data points cannot clearly be distinguished over this range of densities. Only for the last two points do the error bars contain the isothermal line but not the polytropic line. However

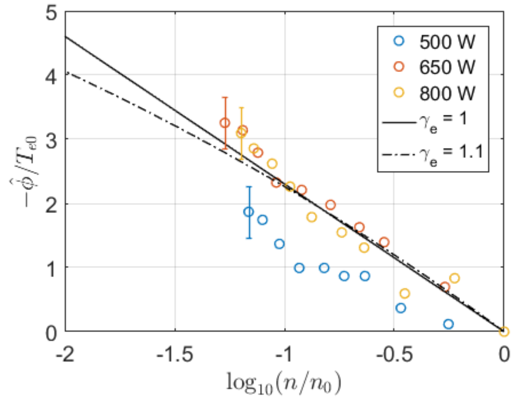

(a) Normalised plasma potential as a function of the normalised density for different RF power.

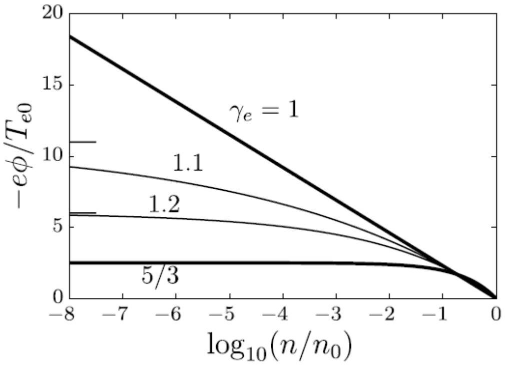

(b) Ambipolar electric potential ϕ as a function of plasma density n, for different values of γ_e. [56]

this is not convincing enough to draw a hard conclusion about the electron thermodynamics. The model predictions are shown for a larger range of densities and the isothermal and polytropic solutions only properly diverge (more than the measurement uncertainty) past $\log_{10}(n/n_0) = 2$. Data further downstream would be needed to better capture the non-linear behaviour of the polytropic case, since only here the two curves really diverge. It is evident that the data points of the 500 W case do not follow the isothermal line but neither does it follow the polytropic prediction for $\gamma_e = 1.1$. This plot is sensitive to the normalisation constant T_{e0} and extending the measurements up to the throat could help to improve the plots as well.

When looking at the radial profiles of the plasma potential two observations can be made. Firstly the plasma potential is not uniform over the radial direction but slightly skewed, lower on the left side and higher on the right side. This is probably related to the asymmetry of the antenna as already discussed in the sections on density and temperature. Furthermore it seems to increase at the edges which is contrary to the model predictions. This would naturally confine the ions which is favourable. However it is small compared to the measurement uncertainty so no conclusions can be drawn.

Further investigations using an emissive probe are needed, which would allow for faster measurements over a larger range. This might uncover larger structures in the potential profile that could explain this unexpected behaviour. The preliminary results of chapter 7.5 already provide some insight. The EP radial profile shown in figure 7.17b over a larger range, r = ±200 mm shows a trend that somewhat agrees with the LP measurements presented here; the asymmetry where the left side of the profile has, on average, a lower value than the right side is seen here as well. However past r = ±70 mm the plasma potential starts decreasing to a value at ±200 mm about 10 V below the centre value. This is the expected behaviour for an expanding plume where as the results from the LP are not.

Summary

In this chapter the spatial distribution of the plasma parameters was presented. The shape of the plume as represented by the axial and radial density profiles has been found to be independent of the RF power and thus the magnitude of the plasma density. The plasma density decreases downstream with z^{-1}. The low ($< 10^{18}\ m^{-3}$) peak value of the density indicates that the thruster still operates in an inductive mode rather than helicon mode. The radial profiles have a relatively flat front around the centre line and decrease exponentially in the radial direction. There were in general clear asymmetries in the radial direction, that directly contradict the axi-symmetric assumption of the magnetic nozzle model. This is expected to be due to the sub-optimal shape of the antenna but needs further investigation. Axial electron temperature measurements showed a isothermal behaviour for higher power levels but electron cooling with a polytropic coefficient of $\gamma_e = 1.10 \pm 0.05$. Radially there was a large asymmetry in the temperature, with fluctuations about ±1 eV around the centre value. Also possibly related to the antenna shape. Over the full range electron temperatures were within 2.5-4.5 eV. Plasma potential measurements in axial direction were compliant with electron temperature measurements, where the decrease of the potential was slower for the 500 W case. A semi-log plot of normalised density vs.

normalised potential corroborated the isothermality of the 650 W and 800W case. Radial profiles again showed asymmetry, as well as slightly higher values of potential near the edges. However preliminary measurements with the emissive probe contradict this behaviour.

9

Characterisation of Propulsive Properties

Introduction

This chapter focuses on the propulsive properties of the thruster as inferred from the plume measurements. Consecutively it covers the plume divergence, ion velocity profile, utilisation efficiency and provides an estimate of the total thrust and thrust efficiency. Without a thrust balance all such measurements are only indirect measurements with a large error margin and therefore only serve as an order of magnitude estimation. Most of these results come from Faraday probe measurements, sometimes augmented with the results of the Langmuir probe.

9.1. Divergence

Plume divergence is an important parameter for any thruster. It is a measure of the ratio between axial to total ion momentum. The narrower the divergence the more the accelerated ions contribute to thrust. Plume divergence can be inferred from Faraday probe measurements. It is either defined as the half-angle of the cone containing 95% of the ion flux or the momentum weighted average of the ion current as was explained in section 4.4. There is one caveat for our setup: it operates in Cartesian coordinates with the probe surface always facing the axial direction. For near-plume measurement this is not unusual. However, most (far-)plume measurements, use polar coordinates where the probe always faces the thruster exit. This means that in this case it is necessary to do a cosine correction to get the effective area perpendicular to the beam. This section presents Faraday probe measurements obtained at different RF powers and different downstream positions and calculate the plume divergence.

The first set of measurements are taken with the Faraday probe using the NI-DAQ ADC setup described in section 5.6. The measurements were taken using a $1\ k\Omega$ resistor. Both collector and guard-ring were biased to -30 V to ensure that the probe is in the ion-collection regime. The maximum voltage across the resistor was 2 V, meaning that guard-ring and collector differed by max 2V near the peak of the profile. The DAQ averages a 100 samples, obtaining a mean value and the standard deviation.

Measurement uncertainties include the uncertainty in the collector area, the standard error in the measurement and a 1% error in the resistor value. The resulting relative uncertainty is the sum of these relative errors and are calculated by the LabVIEW program and saved in the raw data file. The error in the cosine correction is added later and is about 0.5% on average. The relative error over the full measurement domain is between 2% near the centre line and up to 80% near the wings. The mean is 17% and the median value 5%. The current density profile at z = 200 mm for 800 W is plotted together with the relative error as a function in figure 9.1. Here it can be seen that indeed over centre of the profile the error is reasonable (<10%) but in the wings the relative error increases sharply. However, since j here is very low compared compared to the centre values the impact of the error is partially mitigated. Integrating over $j \pm \Delta j$ gives an upper and lower value for the total current I_t which results in a relative error of 9-16% and in the same way a 1° error for δ and $\delta_{0.95}$.

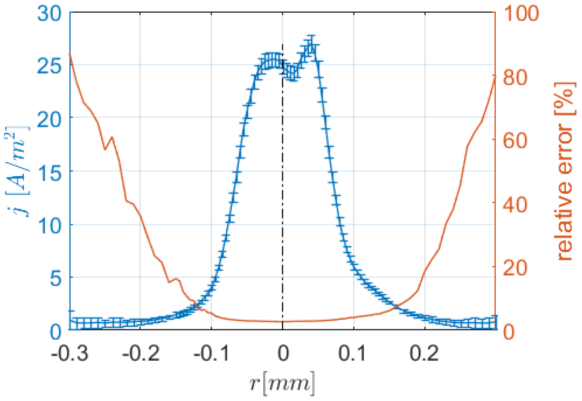

Figure 9.1: Current density profile at 800 W including relative error.

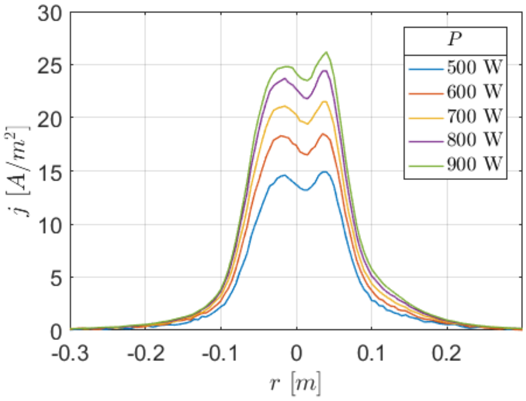

Figure 9.2: Radial ion current density profiles at z = 200 for different RF power.

9.1.1. Influence of RF power

This section presents the results of the test outlined in section 6.1.9. The measurements were taken at z = 200 mm downstream from -300 < r < 300 mm with a 5 mm step size from 0 to 150 mm and a 10 mm step size above 150 mm. The profiles for five different power levels from 500 to 900 W are compared. All current density profiles take into account an effective area 10% larger than the actual collector area as discussed in section 4.4. The current density profiles are plotted in figure 9.2. Measurement uncertainties are omitted to avoid clutter and are of comparable magnitude to those in figure 9.1. From this several things are evident. Firstly there is a double peak, more pronounced compared to the small peaks in the plasma density profile of the previous chapter. It can furthermore be seen that the profile is not centred, this is most likely due to misalignment of thruster and measurement system. The centre of the curve is displaced about 10 mm to the right, at z = 200 mm this means a yaw misalignment a little under 3°.

The same data is plotted on a semi-log scale in figure 9.3. Here it can be seen that in the wings of the curve, the signal-to-noise ratio (SNR) decreases significantly. This is due to the fixed value of the measurement resistor; at low current current density the measured voltage becomes of the order of the noise. This observation led to the second setup using the Keithley for FP measurements. The Keithley auto-adjusts it's sensitivity resulting in a high SNR over the full range of the curve. Furthermore the voltage drop over the Keithley is negligible and the guard-ring and collector are really at the same bias. Due to this noise the integration boundaries are chosen to be ±205 mm as up until here the noise is tolerable. This integration boundary encloses a 45° cone as well as the magnetic flux lines originating from the edge of the plasma column at the exit plane. Compared to the full integration domain this omits 5-7% of the beam current. Both the total current and the beam divergence are therefore slightly underestimated.

To better compare the curves, they are scaled with their maximum value and plotted in figure 9.4. After normalisation all curves effectively reduce to one and the same curve. This is compliant with similar findings for the plasma density profiles. It implies again that the shape of the plume is independent of the power, i.e. of the source density. The plume divergence calculated for all five curves should therefore be the same. The calculated divergence angles, both the 95% angle as well as the arc-cosine of the momentum weighted average of the current density are given in table 9.1. Uncertainties in integrated current follow from integrating the results for the lower and upper values of j given by its uncertainty. Although not within the specified measurement uncertainty the divergence angle is clearly independent of the RF power as expected. It is also evident that the divergence angle as found by equating its cosine to the momentum weighted current density provides a more favourable value of 24° compared to the 95% half-angle of 39°.

9.1.2. Axial evolution

Near the thruster the plasma tends to follow the magnetic field lines, however further downstream the plasma is expected to detach, here the plume divergence should be no longer dominated by the magnetic nozzle. In first approximation the expansion can be regarded as conical and the divergence

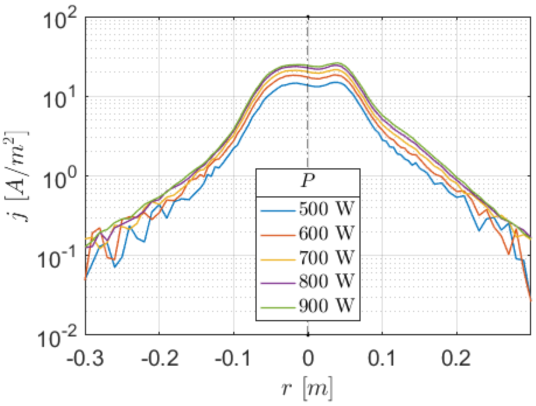

Figure 9.3: Semi-log plot of radial ion Current density profiles at different RF power.

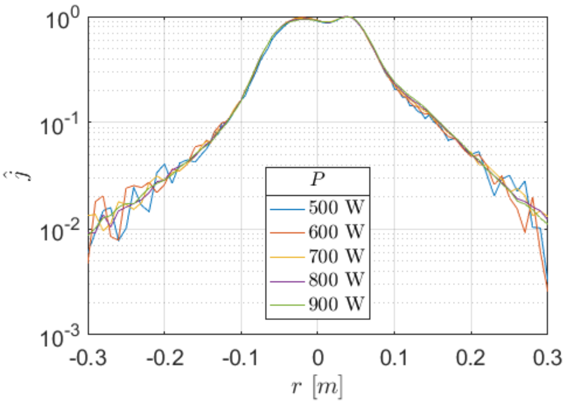

Figure 9.4: Semi-log plot of normalised radial ion current density profiles at different RF power.

P [W]	$\delta_{0.95}[°]$	$\delta[°]$	$I[mA]$	$\eta_u[\%]$
500	39±1	23±1	342±64	10±2
600	39±1	23±1	443±77	12±2
700	39±1	24±1	519±88	14±2
800	39±1	24±1	591±98	16±3
900	39±1	24±1	637±102	18±3

Table 9.1: Divergence half-angle for different RF power.

half angle should be constant along the axial direction. To verify this, three current density profiles were measured at different downstream positions: 120 mm, 160 mm and 200 mm at 500 W RF power as outlined in section6.1.9. These measurements were taken using the Keithley.

The uncertainty in the Keithley is of the order of 0.1% which is a random error while the uncertainty in the collection area is 2% and is a systematic error. Due to the higher accuracy the random error due to the cosine correction, $\Delta\theta/\theta$, which is of the order of <0.4%, now cannot be ignored. The total relative error is about 2.5%. When using this to calculate the upper and lower boundaries of the integrated values the resulting relative error is about 2.5%. Repeating this calculation for the divergence angles results in an relative error less than 2% which is unlikely. Instead the error is propagated in equations 4.49 and 4.50. With a 2% error in the integrated values that yields a relative error of approximately 5% for both $\delta_{0.95}$ and δ respectively.

The resulting curve is shown in figure 9.5. This plot shows clearly that peak current density decreases downstream. Figure 9.6 shows a semi-log plot of the same data but normalised with the respective centre values and plotted as a function of angular position. From this last plot it becomes evident that the shape of the profile is conserved downstream. This means that the divergence remains constant over the range z = 120-200 mm. This is verified by calculating the divergence half angles.

When calculating the total current at different positions a problem is encountered that is inherent to Faraday probe measurements in Cartesian geometry. To include all current emitted into the hemisphere θ ±90° the integration boundary would need to be $r = \pm\infty$ which is clearly impossible. With finite integration boundaries, the solid angle is dependent on the the ratio between the integration boundary and the axial position. This necessitates a dynamic integration range that changes with the axial position. This problem has been encountered in literature before and has not been definitely solved. The best solution so far is e-folding where the integration is continued until the integrand value reaches e^{-k} times the peak value. It is similar to conventions in for example collision theory where the mean free path for decay of a beam is defined as the distance over which the uncollided flux decreases by 1/e from its initial value [67]. Here $k = 4$ is chosen which means that the curve is integrated until j is about 1% of the centre value. This method proved to be a good choice as in this case the total current at three sections remained constant. For larger k the integration boundary exceeded the measurement domain, for smaller values the integrated current and divergence angle would be underestimated.

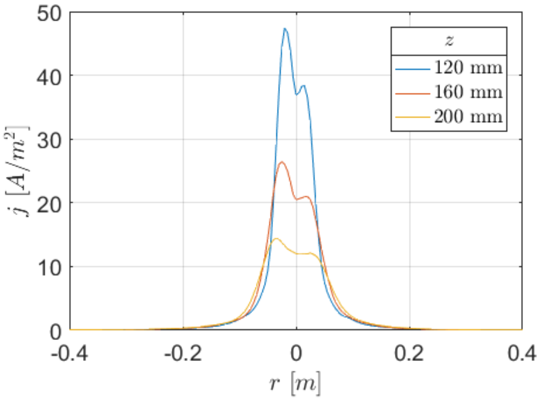

Figure 9.5: Ion current density profile as a function of radial position at different axial positions and P = 500 W.

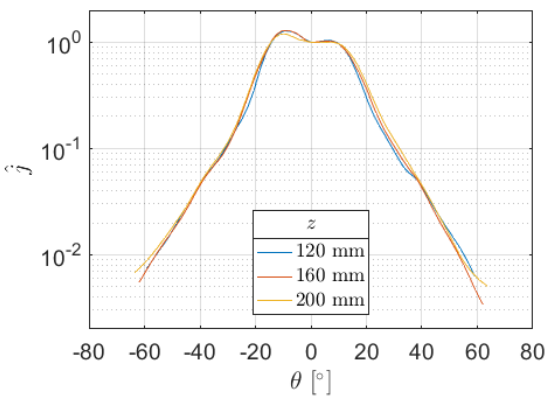

Figure 9.6: Normalised ion current density profile as a function of angular position at different axial positions and P = 500 W.

The beam divergence half-angle has been calculated (with both methods) for all three down stream positions and are are given in table 9.2. As mentioned before the total current is indeed constant within the uncertainty as are both values of the divergence half-angle.

$z[mm]$	$\delta_{0.95}[°]$	$\delta[°]$	$I[mA]$
120	44±2	24±1	307±8
160	42±2	23±1	313±8
200	44±2	24±1	305±8

Table 9.2: Divergence half-angle at different downstream positions

9.1.3. Effect of the magnetic nozzle

The divergence angle is found to be independent of the RF power, compliant with the results of section 8.1 which showed that the plasma density distribution in the plume was also independent of the RF power. According to the DiMagNo model the magnetic field, that of the magnetic nozzle particularly, dictate the shape of the plume. It is therefore of interest to investigate the effect of the magnetic nozzle on the plume divergence. Turning on and off the magnetic nozzle coil has a visible effect on the shape of the plume as can be seen in figure 9.7. The plume clearly becomes more convergent near the thruster.


(a) Magnetic Nozzle OFF

(b) Magnetic Nozzle ON.

Figure 9.7: Images of thruster plume at 500W with magnetic nozzle ON and OFF.

To further investigate this effect two current density profiles taken 200 mm downstream, at 650 W are compared. For both profiles also the total current and the divergence angle were calculated. The two profiles can be seen in figure 9.8a. Clearly the current density profile without the magnetic nozzle is broader and has a much lower magnitude on axis but higher on the wings. Total current was found to be 339±8 mA with the Mn and 391±9 mA without. The 95% divergence angle was 56±1° without MN and 52±1° with while the momentum weighted divergence half-angle is 34±1° without magnetic nozzle, and 27±1° with.

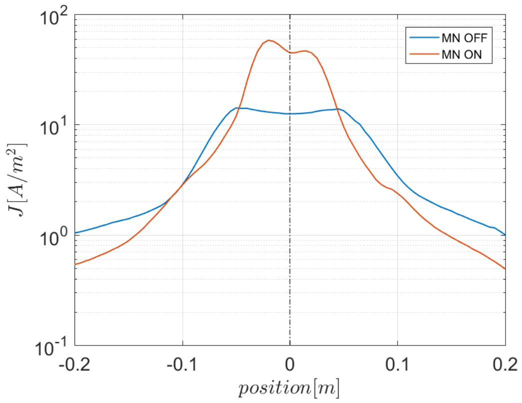

(a) Effect of magnetic nozzle on plume divergence at P = 650 W.

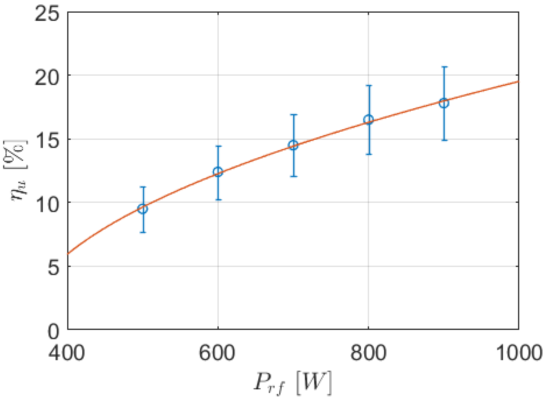

(b) Utilisation efficiency as a function of RF power.

9.1.4. Discussion

In this section the results on the divergence angle as measured by the Faraday probe were presented. The effect of the RF power, the evolution downstream and the effect of the magnetic nozzle were investigated. Normalising the current density profiles taken at different RF power resulted in a single profile, indicating a constant divergence angle. This is corroborated by calculating the divergence angles according to both definitions. Both divergence angles are independent of the RF power within the measurement uncertainty. This result is compliant with the plasma density measurements of chapter 8. It further confirms the idea that the shape of the plume is independent of the magnitude of the density. Taking measurements at three different axial positions, and calculating the divergence angle shows that in this case too the divergence angle remains constant. At least downstream the plasma seems to expands conically. Near the exit plane the plasma is expected to follow the magnetic field lines, however further downstream the ions are expected to detach from the field lines resulting in a freely expanding plume.[55] The fact that the plume divergence is constant downstream supports this. The caveat is that these measurements have been taken in a Cartesian system. Far-plume measurements using polar coordinates should be used to further confirm these findings as well as near-plume measurements in the region $z < 120$ mm. For the latter a smaller Faraday probe is required that would perturb the plasma less. The magnetic nozzle clearly has an effect on the plume divergence as can be seen from 9.7. Turning the magnetic nozzle on decreases the 95% divergence angle by 4° and the momentum weighted divergence angle by 7°. The total current is 13% lower with the magnetic nozzle off against expectations. The total current is a function of the source and should be independent of the nozzle. The calculated 95% divergence half-angle without the nozzle is close to integration boundary (59°). It could be that without the nozzle the plume is more divergent than these 59° and a significant portion of the plasma is outside of the measurement domain. To verify this the measurement domain should extend further than ±200 mm radially. While measurements in polar coordinates would circumvent this issue completely. Further experiments will need to measure the plume divergence at different magnetic nozzle strengths to investigate this dependence more in depth.

9.2. Utilisation efficiency

Another important figure of merit is the utilisation efficiency, a measure of the fraction of the mass flow rate that leaves the thruster as ions. This figure can be found by calculating the integrated beam current and dividing it by the electron charge and the mass flow rate. Following the test plan of section 6.1.10 the current density profiles at different RF power presented in the previous section have been processed in this way. The resulting utilisation efficiencies are listed in table 9.1 and plotted in figure 9.8b. The current density is proportional to the plasma density and the ion velocity. The magnetic nozzle model predicts that the evolution of the Mach number (for constant temperature) is independent of the initial density at the source and should therefore be independent of the RF power. The total current as a function of RF power should therefore have the same dependency on P as the plasma density. Based on [15] for a constant electron temperature in the source it is expected that $n \propto P^{-1/2}$ and a similar functional dependence is expected here. The data in figure 9.8b have been fitted with a function the form $y = a(x-b)^{1/2}$ which is evidently a good fit. The parameters are $a = 0.7589\ W^{-1/2}$ and $b = 338.9\ W$. At the maximum operational power of 1 kW a utilisation efficiency of about 20% is predicted. However it has to be noted that $\eta_u \propto \dot{m}^{-1}$. If the mass flow exceeds the ionisation rate the excess mass cannot be ionised. For a given power and magnetic field the utilisation efficiency is expected to increase with the mass flow rate up to a certain point and then saturate. Therefore it could very well be that the mass flow rate of the HPT05 can be lowered without diminishing the total current thus increasing η_u. Hence these measurements need to be repeated for different mass flow rates to verify this.

9.3. Ion Mach profile

The exhaust velocity of an electric thruster is proportional to the ion velocity. As the exhaust velocity is proportional to the I_{sp} it is an important figure of merit. Due to the expansion in the magnetic nozzle the ions are accelerated to several times the sound speed. To investigate this acceleration in the axial direction indirect measurements of the ion velocity have been conducted according to the test plan of section 6.1.11. By combining axial Langmuir probe and Faraday probe measurements the Mach number is estimated. Since $J = enu_i$ and $c_s = \sqrt{T_e/m_i}$, M is calculated from:

$$M = \frac{J}{n\sqrt{T_e/m_i}} \tag{9.1}$$

LP and FP measurements have been conducted for the case of 500 W, and the nominal magnetic configuration. Measurements were taken from 50 to 200 mm downstream in 10 mm intervals. The resulting Mach profile is shown in figure 9.8 The Mach number starts at little over M = 4 at z = 50 mm and almost linearly decreases to little under M = 2 at 200 mm downstream.

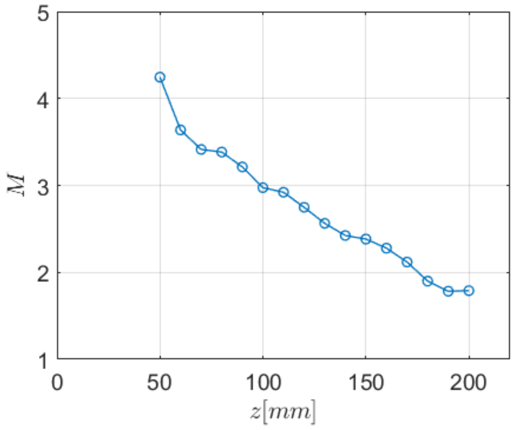

Figure 9.8: Axial evolution of ion Mach number based on combined FP and LP measurements.

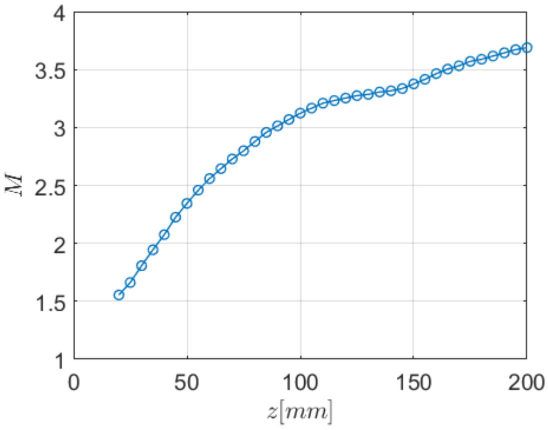

Figure 9.9: Axial evolution of ion Mach number based on EP measurements.

9.3.1. Discussion

The resulting Mach profile is rather remarkable. The ion Mach number is supersonic in all measurements, but seems to decrease downstream. This is the case for both the axial and the radial profiles.

This trend is contrary to all expectations. An expanding plasma, is necessarily accelerated downstream by virtue of mass conservation. As discussed in section 9.1.2 the total current is constant downstream; since the density drops downstream the velocity necessarily must increase. The main reason that deceleration is unlikely is the fact that the plasma potential decreases monotonically downstream, this potential drop goes hand in hand with the acceleration of the ions.

The example axial plasma potential obtained with the emissive probe and shown in figure 7.17a was taken during the same experiment as the Langmuir and Faraday probe data. This figure clearly shows a potential drop of about $5T_e$ from z = 20 to z = 200. Assuming M = 1 at the throat, by conservation of energy this should translate to an ion Mach number of about 4 at z = 200. It could be that either the current density is underestimated or that the density is overestimated. The former seems unlikely because of the conservation of current downstream. Density measurements are prone to uncertainty as discussed before, as the models are elaborate and based on many assumptions. The Langmuir probe data used in figure 9.8 was also processed with the planar approximation, but this yielded the same trend $\propto z^{-1}$ so it's unlikely that it's due to the use of a particular ion collection theory.

Of the combined curves, the axial current density profile scales approximately $\propto z^{-1.6}$ while the density profile scales with $\propto z^{-1}$. This means that the Mach number will scale $\propto z^{-0.6}$ (ignoring the drop in the temperature which would worsen this trend) which is the trend observed in 9.8. However based on both DiMagNo and 1D solutions of the expansion the Mach number is expected to approximately scale $\propto z^p$ with $0 < p < 1$. According to the DiMagNo model the density is expected to scale $\propto z^{-q}$ with $q \geq 2$, if this was the case the Mach number would scale as expected with $0 < p < 1$. Therefore main cause seems to be they density measurement. Instead of calculating the velocity from the ion current density and the plasma density it can also be calculated from the plasma potential using conservation of energy: $m_i u_i^2 = m_i u_{i0}^2 - 2e\phi$. There is one caveat: u_{i0} is unknown. As the resulting Mach profile is linear between 20<z<60 mm, u_{i0} was chosen such that the linear extrapolation of these points resulted in M = 1 at z = 0. This is a solid assumption based on [5]. To calculate the local sound speed the temperature as measured with the Langmuir probe was extrapolated over the range of 20 to 200 mm using a power law fit. The resulting Mach profile is plotted in figure 9.9. This Mach profile increases from M = 1 up to M = 3.7 agreeing with the expected trend. At z = 200 the electron temperature is 2.8 eV corresponding to an ion acoustic speed of 2582 m/s. The ion velocity at M = 3.7 is therefore 9528 m/s corresponding to an I_{sp} a little short of 1000 s. This value for the I_{sp} should not be given to much importance. The real I_{sp} reflects the average axial ion velocity of the whole plume while here the on-axis value is used. Only a thrust balance measurement can give a trustworthy estimate of the I_{sp}.

9.4. Ratio of ion to magnetic flux

Another interesting quantity related to the axial ion current density is the ratio of ion flux to magnetic flux:

$$\frac{J}{B} = \frac{enu_i}{B} \propto enu_i R_V^2 \tag{9.2}$$

The second equality follows from the fact that the total magnetic flux $B(z)R_V^2(z)$ is constant. In a 1D model this ratio is constant, however in 2D models and in reality this does not necessarily have to be the case. Using the magnetic field calculated from a superposition of current loops representing the HPT-05 electromagnets; and the measured axial ion current density the axial evolution of this quantity is calculated. The result is shown in figure 9.10. It has to be noted that this quantity is only reported for a single line, which is a 1D approximation to a 2D situation. However since the global shape of the radial ion density profile is preserved downstream this does give a valid qualitative result. In figure 9.10 the ratio increases downstream. This means that the magnetic flux expands faster than the ion flux, i.e. the ion current does not follow the magnetic field lines. This plot implies that the ions detach from the magnetic field lines which is beneficial from both the propulsive and lifetime perspective; it limits the divergence and makes sure plasma does not return to impinge on the spacecraft. This measurement could be improved by measuring the magnetic field with a Hall probe instead of using the calculated magnetic field.

9.5. Estimates of Thrust and Efficiency

The most important figure of merit is the thrust produced by the thruster. The direct way of measuring thrust would be by means of a thrust balance. Indirectly it could be measured with a momentum flux

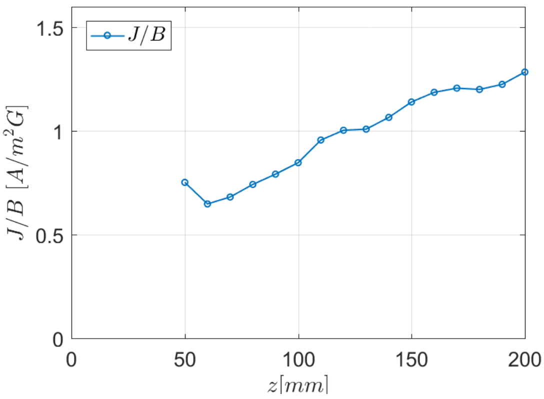

Figure 9.10: Axial evolution of ratio of ion flux to magnetic flux.

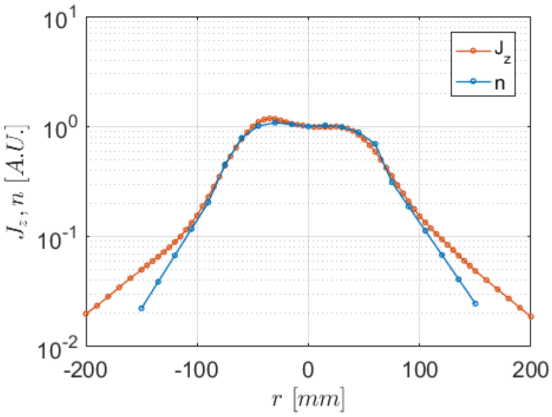

Figure 9.11: Comparison of normalised radial profiles of ion density n and axial ion current density J_z at z = 200 mm and P = 500 W

sensor. However the thrust can also be estimated by combining Faraday and Langmuir probe measurements as detailed in the test plan of section 6.1.12. The axial momentum flow and hence the thrust across a radial section downstream is given by [3]:

$$F_z(z) = 2\pi \int_0^{R_V(z)} drrM_{zz}(z,r) = 2\pi \int_0^{R_V(z)} drr\left(m_i n u_{zi}^2 + nT_e\right) \tag{9.3}$$

M_{zz} is the axial component of the momentum flux tensor defined in section 3.3. Since the contribution of the neutrals is negligible and because $T_i \ll T_e$, $n_i = n_e = n$ and $m_e \ll m_i$ it is possible to write: $M_{zz} = m_i n u_{zi}^2 + nT_e$ which results in the second equality of the above the equation. Measurements of n and j_z (j without cosine correction) can be used to calculate the local ion momentum flux:

$$m_i n u_{zi}^2 = \frac{m_i}{n(r,z)}\left(\frac{J_z(r,z)}{e}\right)^2 \tag{9.4}$$

Using this together with the measurement of T_e the thrust density f can be calculated as follows:

$$f(z,r) = \frac{m_i}{n(z,r)}\left(\frac{J(z,r)}{e}\right)^2 + en(z,r)T_e(z,r) \tag{9.5}$$

Numerically integrating f over a measured radial profile gives an estimate of the thrust. Although the contribution of the electron pressure should be small downstream, it cannot be ignored as in the measurements it is anywhere between 20-50% of the total momentum flux. As was the case with the radial Mach profile, Langmuir probe data is only available up to ±60 mm. Since it is proportional to J_z^2 and n^{-1} which have similar shape the radial ion momentum flux profile also has this shape. Its magnitude is largest on-axis and exponentially decreases downstream. However off-axis radial sections are larger than those close to the centre line which enhances their contribution. To assess how the calculated thrust scales with the integrated area the following procedure was used. For the radial section at z = 120 mm, the density profile was extended up to ±150 mm in radial direction and the local T_e was replaced everywhere with the mean of the measurements between ±60. Comparing the results of using the local vs. the average temperature over the r = ±60 mm section only differed about 0.7% showing that this is a reasonable approximation.

In the previous section it was found that the downstream plasma density as measured by the Langmuir probe was overestimated. For one case an axial plasma density is inferred by combining the inferred ion velocity from EP measurements and a the ion current density from Faraday probe measurements using $J = nu_i$. The resulting axial density profile decreases faster downstream than the that measured with the LP and is found to agree well with the theory as will be shown in the next chapter. Unfortunately this measurement is not possible for radial profiles.

To somehow take into account this correction, the magnitude of the radial plasma density profile used in this calculation is scaled with the ratio between the axial density profile obtained with the LP and that obtained with EP and FP combined. This assumes that the shape of the radial density profile is correct. This assumption is substantiated by the similarity of the normalised density and axial current density profiles shown in figure 9.11. Up until ±100 mm they have the same shape, while beyond this point they deviate. This could be due to a higher ion velocity in the wings or due to the effect of facility background pressure effects on the ion current density measurement as explained in [6]. Since it is not clear which is the case the profile is only integrated up to r = ±100 mm. The uncertainty in this measurement is given by:

$$|\Delta_f| = \frac{J_z^2}{n}\left(2\left|\frac{\Delta_{J_z}}{J_z}\right| + \left|\frac{\Delta_n}{n}\right|\right) + nT_e\left(\left|\frac{\Delta_n}{n}\right| + \left|\frac{\Delta_{T_e}}{T_e}\right|\right) \tag{9.6}$$

Here the uncertainty due to using the average temperature and extrapolating the density profile with an exponential function were ignored. The error is dominated by a 50% error in n. The the relative value of Δ_f/f is about 60% over the whole domain. Since the error is constant, the integrated value F also has an error of 60%. At z = 200 mm and integrating from ±100 the thrust was found to be 1.0±0.6 mN. The thrust efficiency is calculated from equation 1.5 with a mass flow rate of 1 mg/s and 500 W power yielding η = 0.10±0.06%. It is a very meagre result compared to thrust efficiency from literature of 0.6-17% (see table 2.1) as measured with a thrust balance. Considering the large error not much importance can be given to this number. It has to be noted that the thruster is in an early stage and not optimised in any shape or form. The measurement is also indirect and draws on quite a few assumptions. If anything it should be viewed with suspicion. It shows that the HPT05 is clearly not yet in a the range of other thrusters. For a proper thrust measurement a thrust balance or at least a momentum flux sensor as used in [81], should be used.

9.6. Replicability & Reproducibility

Replicability is paramount to scientific research; if findings cannot be replicated, they are either random or erroneous. Replicability refers to the ability to replicate a study including experiments, yielding the same results. Reproducibility refers to the ability to reproduce the outcome of the analysis using the original data set. The latter is obviously less convincing that the former however it is used to verify results up to a certain extent when replicating an experiment is not straightforward due to for example cost or time constraints.

In the context of this study reproducibility and replicability can be understood in the following manner. The raw data files listed in appendix B are available and analysis can be reproduced using the MATLAB and excel files listed in appendix D or similar methods using the same underlying theory (BRL/ABR). This should yield the same results. Replicability in the case of the magnetic nozzle can be checked on several levels. Ideally these experiments would need to be replicated in a different thruster with a similar configuration. At a lower level the measurements can be replicated using the HPT05 in a different diagnostic facility. However at the lowest level the measurements of this test campaign should be replicated in the EP^2 test facility. It has to be stressed however that the current test-campaign is the first set of measurements obtained. Although initially planned, within the time limit of this study it has not been possible repeat the experiments. Despite this, some comments on the replicability of the results can be made.

First of all based on current experiments the thruster seems to be stable when operating at a particular operating point. That is to say, as long as the discharge is not interrupted and the antenna system is in thermal equilibrium the plasma is stable. This is substantiated by several observations. First of all by the analysis of the Langmuir probe measurements presented in section 7.2.1 and furthermore by the repeatability of the emissive probe measurements shown in figures 7.17a and 7.17b of section 7.5. Repeated measurements show only a 2% variation on average. A similar comparison of two consecutive Faraday probe measurements is shown in figure 9.12. The measurements are taken at 650 W and at z = 160 mm. One profile is measured by sweeping the probe from right to left, while the opposite is obtained in the opposite direction. Clearly the profiles are very similar, with a mean relative error of 2% and a peak value of 5%. Processing both curves yielded 433±1 mA and 432±1 mA respectively for the total current. The divergence half angles were and $\delta_{0.95}$ = 42±2° and δ = 23±1° for both profiles. Clearly the integrated parameters are repeatable. It has to be noted that both experiments were taken

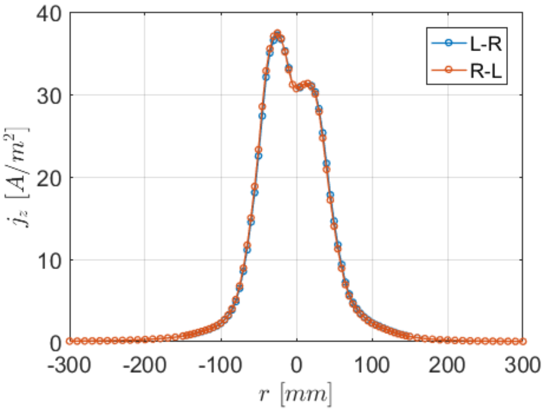

Figure 9.12: Radial profile of axial ion current density measured by sweeping the FP both from left to right and vice versa.

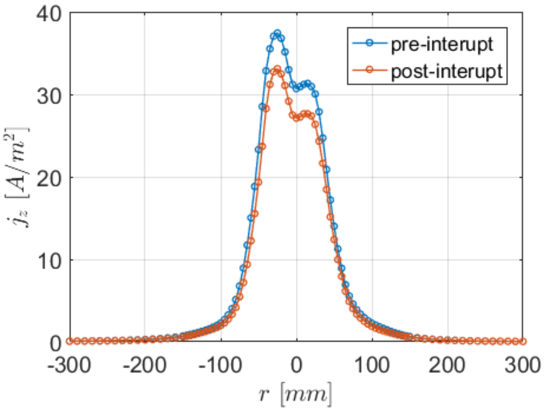

Figure 9.13: Comparison of radial profiles of axial ion current density before and after losing the discharge.

over a 7 min time period (due to the inherent measurement time) further indicating that the plasma can be considered stable.

Recent work on the thruster, not included in this report, employed a high speed camera to analyse plasma stability. Preliminary results of this study indicated that both random and periodic variations up to 20 kHz are absent in the plasma. Based on the above arguments it is therefore concluded that the thruster in steady operation produces a stable plasma and results and trends obtained from single discharge (i.e. without losing the discharge) are consistent. Therefore care is taken to ensure that all results presented in this work, per result, are obtained from a single discharge.

To be able to discuss the replicability of the results between to different discharges (on the same or different date), two radial Faraday probe measurements obtained directly before and after losing a discharge, are compared in figure 9.13. Clearly the profile obtained after restarting the thruster has a lower overall magnitude than the other profile. The relative error between the profiles has a mean of 13% and peaks at about 20%. For this profile the total current and divergence angles have been calculated as well resulting in: 372±1 mA, 42±2° and 23±1°. After reigniting the discharge has a 14% lower total current (and therefore 14% lower utilisation efficiency). However the divergence half-angles are, within the measurement uncertainty, identical to those of the discharge before it was lost. This leads to two conclusions. Firstly the shape of the plasma in this case in the form of the divergence is uncoupled from the total current or magnitude of the plasma density. Something which was already substantiated by the investigation of the effect of the RF-power on the divergence and plasma density profiles. Secondly separate discharges do not produce an identical plasma in terms of total current and plasma density and by extension neither in terms of plasma potential. For the electron temperature this has to be investigated. Lastly it is concluded that the trends in terms of relative values identified in this work are valid but that the absolute values of total current, plasma density and plasma potential differ per discharge. It is therefore paramount that the replicability of the HPT05 plasma is properly investigated in a future test-campaign.

Summary

In this chapter several propulsive figures of merit were studied and discussed. Firstly the plume divergence was investigated. It was found that the plume divergence is independent from the RF power further substantiating the idea that the shape of the plume independent of the total density. Furthermore it was shown that the plume divergence is constant, at least downstream of z = 120 mm. This indicates that the plume divergence is no longer dictated by the shape of the magnetic field, i.e. the plasma detaches from the field lines. Lastly it was shown that the magnetic nozzle reduces the plume divergence with about 7°. By measuring the total current it was shown that the total current is constant over the axial direction as expected. Furthermore from the total current the utilisation efficiency was calculated for different RF power. The utilisation frequency scales with the square root of the RF power.. By combining Langmuir probe and Faraday probe data the axial ion Mach profile was calculated. It was found that the resulting curve showed a decelerating plasma contradicting basic physics and 1D-model and DiMagNo predictions as well as plasma potential measurements. Based on these findings it is suspected that the Langmuir probe density measurements overestimate the density downstream. A Mach profile calculated from emissive probe data results in a Mach profile that shows the expected trend resulting in a Mach number of 3.7 at $z = 200$. The ratio of the ion flux to magnetic flux was found to increase downstream which indicates that the magnetic flux expands faster than the ion flux this further substantiates the idea of ion detachment. By combining LP and FP measurements an estimation of the thrust was obtained, resulting in a low preliminary value of the thrust efficiency. Lastly the stability of the plasma and the replicability of the discharge was discussed. It was concluded that separate discharges do not produce an identical plasma in terms of total current and plasma density and by extension neither in terms of plasma potential. But the trends in terms of relative values identified in this work are valid nonetheless.

10

Comparison with Theory and Literature

Introduction

In this chapter, the results reported in the previous chapters are put in perspective. First the results are compared to the results of similar thrusters found in literature. In the second part of this chapter the results are compared against simulations of the DiMagNo model.

10.1. Comparison to results from literature

Research on magnetic nozzles and helicon thrusters has been done since the 90's, although most early efforts were numerical in nature. Most experimental work dates from the mid-00's or later and the amount of relevant thruster experiments is sparse. Furthermore comparison is difficult as the type of plasma source, its specifications, the diagnostics used and the pursued objectives vary among the different experiments. Nonetheless several relevant studies have been identified that use similar devices and that produced results of the same type as in this study. The similarities and differences between the setups are discussed and the results are compared.

10.1.1. Chi-Kung helicon reactor at ANU

The Chi-Kung helicon reactor is a device operated at the Australian National University. A relatively recent work by Boswell [11] studied the evolution of the electron temperature in a magnetic nozzle. The device used is a helicon source with 137 mm diameter and 310 mm length. The magnetic field is a weak magnetic mirror with peaks of 150 G at the throat and 20 cm upstream. The device uses a 200 mm long Nagoya-III antenna powered by a 13.56 MHz RF signal at 250 W. The reported source pressure is 0.3 mTorr of argon which translates to 47 mg/s using equation 7.2 and the ideal gas law (assuming neutrals at room temperature). Resulting plasma densities are of the order of 10^{16} m^{-3}. A planar Langmuir probe is used to measure the $I - V$ curves from which the EEDF is inferred, which in turn is used to calculate density, electron temperature and plasma potential.

The main differences with the setup used in this project is the source tube diameter and the small volume of the vacuum chamber. This is only 320 mm wide and 300 mm long. With these dimensions the plasma cannot fully expand and is bound to interact with the walls of the chamber in a way that will perturb the near-plume. The background pressure (without mass flow) is also of th order of 10^{-6} mbar, one order higher than in the case of the HPT05, increasing collisions. Boswell reports a plasma density that drops about one order of magnitude over the first 200 mm. Their results are plotted together with both the LP and EP+FP results obtained in this work, in figure 10.1a. The densities have been normalised with the value at z = 50 mm and z has been translated by 50 mm and normalised with the respective thruster radii. It can be seen that the density profile of [11] decreases much faster than in the case of the HPT05. One explanation could be that the low magnetic field strength used in the Chi-Kung results in a less focused plume with a lower on axis density.

The EEDF determined in [11] showed the presence of two electron populations of 4.5 eV and 9.5 eV respectively. Usually the cold population dominates the behaviour of the plasma. Both temperatures were used to normalise the plasma potential profile and the results plotted together with normalised

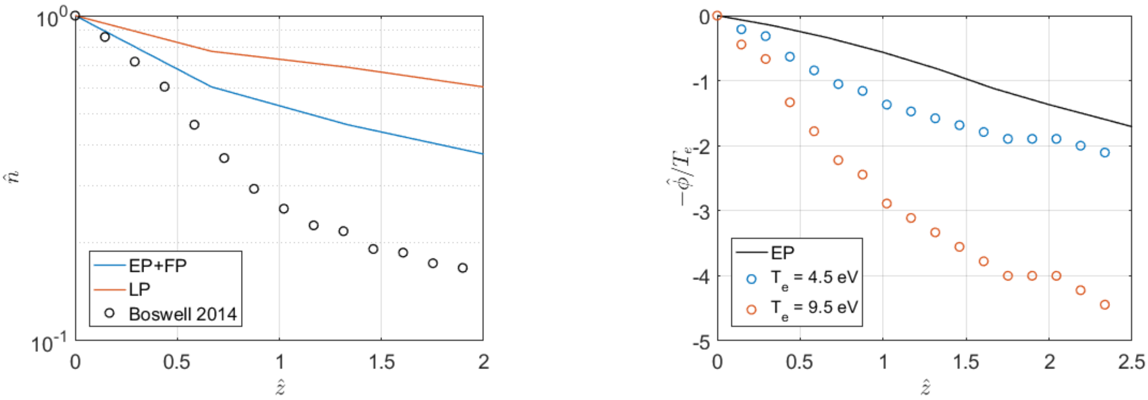

(a) Normalised plasma density.

(b) Normalised plasma potential.

Figure 10.1: Comparison of axial evolution of plasma parameters with results from [11]

EP profile of section 7.5 in figure 10.1b. As was expected from comparison of the plasma density profiles, the plasma potential of the Chi-Kung decreases more rapidly regardless of the dominant electron temperature. In general the results of this study do not compare well with those of the HPT05. This is attributed to the difference in magnetic field strength, thruster radius and the very small vacuum chamber used in [11]. Due to the latter, interactions with the wall are expected to perturb the plasma.

10.1.2. mini-Helicon experiment at MIT

The mHTX thruster is a device developed at MIT which was cancelled in 2008, despite (doubtful) claims of an efficiency up to 17%. The device consists of a 20 mm radius, 200 mm length tube, using a half helical antenna at 13.56 MHz. The RF power is in the range 0.6-1 kW and the magnetic field ranges from 1-2 kG. The propellant was argon with mass flow rates up to 1 mg/s. Despite the significantly higher magnetic field, this thruster is quite similar to the HPT05. The vacuum facility used was large enough to avoid interference with the walls and was able to reach pressures less than 10^{-6} mbar. Most research on this thruster involves thrust balance and spectroscopy but one master thesis rapport [73] involved Langmuir and Mach probes. Measurements were taken at a fixed positions, on-axis, 42 mm downstream. This study reports plasma densities increasing from $1{\cdot}10^{17}$ to $9{\cdot}10^{17}$ m^{-3} when increasing the RF in the range 600-1000 W. Although there are not enough data points to confidently assess the trend but it seems to be scaling roughly with P^k, with $k \leq 1$. Electron temperatures are in the range 2.4 - 4.4 eV and decrease with mass flow rate while it is found independent of P. The the density increases with the mass flow rate up to 1 mg/s where it levels off. The Mach number is found independent of the power and to increase with the mass flow rate. With 1 mg/s, M = 2.1 at z = 42 mm, similar to that of the HPT05 (see figure 9.9. Ion velocities are in the range 2400-3200 m/s. Overall the magnitudes reported in this study at z = 42 mm agree well with those of the HPT05 at the same position. This is partially expected due to the similarity between the thrusters. Because of the higher magnetic field a higher efficiency is expected for the mHTX. The author does indeed report an efficiency on the order of 17% and I_{sp}'s of 1200-2200 s. However it is not very clear how these are calculated and they rely heavily on assumptions such as full ionisation (>95%), which are poorly substantiated. Therefore these numbers are to be regarded with suspicion.

10.1.3. VASIMR VX-200i

The VASIMR is a high power EP device that uses ICRH as its main power coupling mechanism However, its plasma source consists of a 32 kW helicon source. Several experiments have been conducted without the ICRH stage, using only the helicon source. The caveat here is that the ICRH stage cannot be removed and that plasma leaves the helicon and passes through the axial magnetic field of the ICRH stage. It is not clear if plasma column remains colinear after leaving the helicon source or whether it partially expands. Magnetic fields, when using only the helicon source are about 1700G [51]. The thruster is operated with 25 mg/s of argon. Facility background pressure during operation was $2{\cdot}10^{-5}$

mbar. Results are reported poorly but some axial profiles of n, ϕ, T_e could be obtained. Plasma density drops linearly from 8·10^{19} to 2·10^{19} m^{-3} over 0-400 mm and then decreases linearly to close to zero at z = 1 m. Results are not plotted in logarithmic scales so proper scaling cannot be inferred in this second region. Plasma potential drops from 18 V to 10 V over 0-400 mm and then stays nearly constant at 10 V. According to the study the plasma potential and density follow the Boltzmann relation up to 500 mm downstream, using the local electron temperature. The electron temperature drops from 8 eV to little 2 eV over 0-200 mm and then slowly decreases to about 1.4 eV downstream. Combining their data for T_e and n and fitting eq. 8.1 results in two distinct values for γ_e. Over the first region up to 200 mm, $\gamma_e \approx 2$ while downstream $\gamma_e = 1.15$. This means that the first part of the expansion is adiabatic while downstream it is polytropic with an exponent close to that found for the HPT05 at 500 W. While adiabatic behaviour is not expected for the HPT05, Sheehan [71] did expect this for the VASIMR. He performed a different analysis of the same data but his results were not conclusive. Overall it can be concluded that the VASIMR cannot be properly compared to the HPT05.

10.1.4. HPT-I at Tohoku University

10.1.5. sub:comparison:Takahashi

The HPT-I experiment at Tohoku University in Japan takes place in a large 600 mm diameter, 1400 mm length vacuum chamber with a base pressure (without mass flow) of 2.7·10^{-6} mbar. The thruster has a 64 mm diameter and a 200 mm length, about twice as wide as the HPT05. It operates with a mass flow rate of 0.75 mg/s and uses a water-cooled double turn loop antenna. The antenna is powered with a 1 kW, 13.56 MHz RF signal. The magnetic field is generated by a single solenoid with a variable peak magnitude up to 750 G. Both $\dot{m}$,P as well as B are in the range of the HPT05, and even the type of antenna used is similar. The main differences are the increased radius and the higher facility pressure. Overall the HPT-I and the HPT05 are comparable devices. The study of [80] focuses on the diamagnetic-induced momentum in the MN and reports the axial evolution of the plasma density. The 14 A case of [80] corresponds to a magnetic field of about 500 G at the thruster exit, comparable to the field of the HPT05 at the same position (560 G).This data is therefore compared to the results of the HPT05. Measurements are taken using a planar Langmuir probe.

The reported peak density in the source is about 1·10^{18} m^{-3}. Plasma density at z = 50 was 1·10^{17} m^{-3} similar to the combined EP+FP measurement at 500 W which yielded 9.3·10^{16} m^{-3}. Densities are normalised with $n(z = 50mm)$ and compared in figure 10.2. The LP measurements of the HPT05 agree well with the results of Takahashi. The EP+FP measurement agrees only up to z = 60 mm, but decreases twice as fast downstream. For a better comparison measurements up to the throat are needed.

Takahashi et al. estimate a charge exchange mean free path λ_{cx} of 5-10 cm. They point to this as one of the reasons for increased downstream ion density. The resulting slow ions are more magnetised than the original fast ions and this results in less cross-field diffusion. Similar λ_{cx} have been calculated for the HPT05. Two different devices showing this behaviour, that contradicts the model (see section 10.2), indicate that the Langmuir probe measurements are in fact correct but that the local density is increased due to charge exchange. The fact that both measurements only start to deviate at 5 cm downstream, i.e. of the order of λ_{cx} further substantiates this conclusion. The combined FP+EP measurement is less sensitive to the slow charge exchange ions as their contribution to the ion current density as measured with the FP is much lower. This method therefore yields a plasma density that is representative of the fast ions. This also explains its agreement with the model which does not account for charge exchange.

In the study of [82] the azimuthal electron current is studied in the same setup as [80] and the radial evolution of n, T_e an ϕ is reported. The plasma density profile obtained from [82], at z = 50 mm is shown in figure 10.3 together with the profile as measured with the LP at z = 40 mm. The radial position is normalised with the repsective thruster radii and the density with the peak value of the respective curves. The circles and crosses are from ref. [82] for magnetic fields at the thruster exit of 560 G and 80 G respectively, the line shows the result from the LP also at 560 G. Takahashi reports a decrease in density on the centre line for higher magnetic field, resulting in a double peak. This behaviour decreases for lower magnetic fields. However the results from the HPT05 which operates at a higher magnetic field does not show this behaviour at all. The trend of the HPT05, near the centre line agrees well with that of the the low magnetic field case of Takahashi but starts to deviate beyond 2 thruster radii. As the facility pressure in [82] is one order higher then for the HPT05 this could possibly

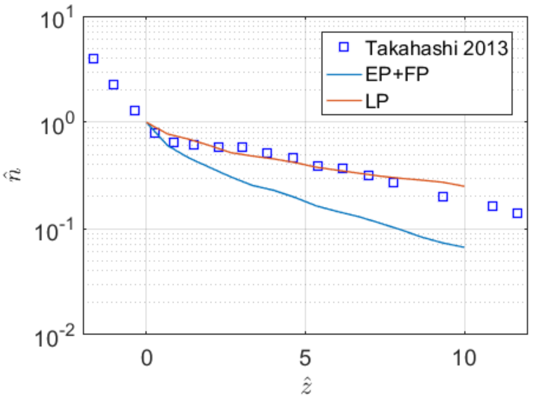

Figure 10.2: Comparison of axial evolution of plasma density to the results of [80].

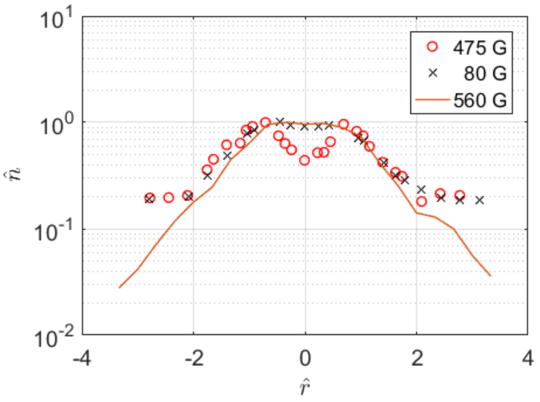

Figure 10.3: Comparison of radial evolution of plasma density to the results of [82].

be due to charge exchange collisions. According to Takahashi the off-axis peaks develop downstream and do no originate in the source. They are attributed to transport of electrons along the nozzle surface; this is a generic feature that is reported in several studies. [19, 68, 78]. It is not clear why this feature is not present in the HPT05. Takahashi further finds electron temperatures of 4 eV off-axis, 6 eV on the centre-line and peaks of 8-9 eV corresponding to the density peaks. The reported radial plasma potential profile is Gaussian with a drop of about 10 V over 2 thruster radii, its width is proportional to the magnetic field strength. None of this behaviour is reproduced in the HPT05.

10.1.6. MN-PD²X at Princeton

Perhaps one of the most interesting experiments on helicon thrusters is the Magnetic Plasma Dynamics and Detachment Experiment (MN-PD²X) [49], conducted by Little at Princeton. It is the only study that reports on the plume divergence in the magnetic nozzle of a helicon thruster. The particular device consists of a 305 mm long, 75 mm wide borosilicate tube and uses a flat spiral antenna mounted on the thruster back wall. It is powered with a 13.56 MHz signal up to 1.5 kW. Magnetic fields strength ranged up to 800 G. The thruster's nominal operating point is at 500 W and up to 2 mg/s of Argon. Facility pressure is $2.7 \cdot 10^{-5}$ mbar at a mass flow rate of 0.5 mg/s.

Little investigated the effect of the source tube length on the plasma profile at the throat. He found that the profile has a flat front whose width decreases with increasing source length. Because the antenna is mounted at the back, increasing the length means that the ionisation source is moved more upstream and the resulting plasma column enters a different, elongated flux tube[1], resulting in a thinner plasma column at the source. However he also found that the profiles decreased exponentially further off-axis. For the HPT05 a similar behaviour is seen at downstream profiles. The exponential decay is a result of Fick's law of diffusion (with an ambipolar cross-field diffusion coefficient).

RF compensated Langmuir probe measurements of the source at 500 W and 0.5 mg/s found plasma densities of 10^{18} m^{-3} and electron temperatures of 7 eV. Comparing both ϕ vs. T_e and $\log_{10} n$ vs. ϕ a polytropic coefficient of γ_e = 1.15±0.03 was found in [49], similar to the γ_e = 1.10 found for the HPT05.

Most relevant for comparison to the work of this thesis report are the plume divergence measurements. In [49] a Faraday probe biased at -30 V was swept through the plume of the MN-PD²X operating at 500 W and 0.5 mg/s. The probe was operated in a polar coordinate system and measurements where taken between 0-95° at $z = 150$ mm and repeated every 25 mm up to 525 mm downstream. This was done for different magnetic field strength ranging from 89 G at the thruster exit plane, up to 310 G in steps of 44 G. From the resulting current density profiles, the 30%, 60% and 90% mass cone half-angles were calculated and converted into z, r coordinates and normalised with the effective radius of the magnetic coil. The resulting points were plotted on top of a map of the field lines to compare the divergence of the ion flux to the magnetic flux. The results for the highest magnetic field (310 G) are shown in figure 10.4a. For comparison similar plots are generated from the current density profiles discussed in section 9.1.2 which are shown in figure 10.4b. However the plotted magnetic field lines

---

[1] See figure 8 of ref. [50]

are chosen to reflect the 30-60-90% magnetic flux lines. The outer magnetic flux lines in both figures originate at the edge of the plasma column at the throat.

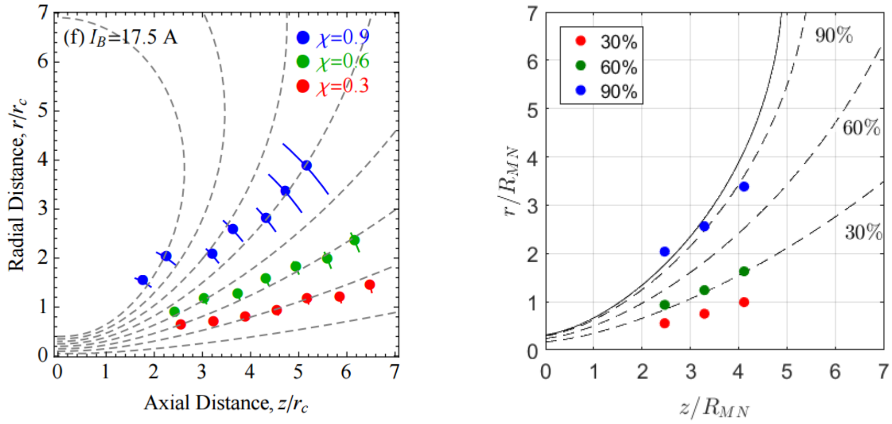

(a) Results from ref. [49] at 310 G at the throat.

(b) Results of HPT05 at 560 G.

Figure 10.4: Comparison of results on ion detachment with ref. [49].

In figure 10.4a it can be seen that the magnetic field lines diverge more than the ion flux and starting from $z/r_c \approx 3$ the ions detach and focus inward. The results of the HPT05 shown in 10.4b show a similar picture. The 60% mass cone coincides with the 30% magnetic field line while the 90% cone lies slightly outside the magnetic flux tube at $z/R_{MN} \approx 2.5$. All three mass cones seem roughly linear and if extrapolated downstream even the 90% flux tube eventually detaches. But as there is no data beyond this point this is speculation.

It seems that the 90% flux tube lies outside the magnetic flux tube up until $z/R_{MN} \approx 2.5$, which can have several explanations. Firstly Under-collimated plumes have been observed in the VASIMR by Olsen [62] when operating with only the helicon. However as mentioned in section 10.1.3 this setup is not comparable to the HPT05. Also these plumes are under-collimated over the whole domain.

Furthermore Little [49] finds that the divergence decreases with the magnetic field. The HPT05 results at 560 G show more divergence than the results of Litte at 310 G. He notes that at a certain magnetic field strength the plume divergence is expected to increase again, due to ion magnetisation. However for this to happen in the HPT05 the magnetic field at the throat should exceed 1.9 kG.[2] This would also not explain an under-collimated plume as the ions streamlines would coincide with the magnetic field lines.

One explanation could be that the electron confinement is reduced due to collisions. This effect is represented by the Hall-parameter $\chi_{He} = \Omega_e/\nu_e$ which is equal to the amount of gyrations an electron can make before it undergoes a collision. A Hall-parameter larger than unity (but in practice larger than 100) indicates good confinement. Here $\nu_e \approx \nu_{ei}$ is dominated by electron ion collisions, which are given by $R_{ei}n$ with $R_{ei} \sim 10^{-12}$. For plasma densities of 10^{17}-10^{18} $\nu_e \sim 10^6$ which results in $\chi_{He} \sim 10^4$ meaning electrons are well confined.

What is also possible, in the light of the charge exchange collisions, is that in the case of the HPT05 the ion current density in the wings is overestimated. Since the true current density here is low, charge exchange has a relatively large contribution in the wings, something observed often in Faraday probe measurements [14]. As mentioned in section 4.4, Azziz developed a method to correct for this behaviour by extrapolating measurements at different facility pressures to the value at hard vacuum. [6, 14] Because the FP in the HPT05 experiments are performed in a Cartesian coordinate system a cosine correction is applied. This correction factor is unity on axis but increases towards the wings. This results in and even higher reported current density off-axis as it enhances the effect of the charge exchange collisions.

Read [67] uses Faraday probes in a Cartesian coordinate system without using a cosine correction he justifies this by his limited measurement domain claiming that the cosine correction would be

---

[2] This translates to $R/\ell_i \sim \mathcal{O}(10)$, see ref. [1].

insignificant. Brown [14] advises to use a Cartesian system only for measurements up to 8 times the thruster radius, which in case of of the HPT05 would be up to z = 120 mm. However this is based on experiments on Hall thrusters. Since the hall thruster radius is relative large due to its annular exhaust, with channel width to thruster radii ratios exceeding a factor 3 not being uncommon this might not be a good rule of thumb for thrusters such as the HPT05 where thruster diameter is equal to its 'channel width'. Omission of the cosine correction and charge exchange collisions have opposite effects on the measured ion current density profile, whether they cancel out cannot be ascertained. Further research is needed, for example by comparing Faraday probe measurements in a polar coordinate system to those of the Cartesian system.

To conclude the results of Little agree well with those of the HPT05. Processing downstream ion current density profiles in the manner of [49] further confirmed ion detachment in the HPT05 plume.

10.2. Comparison to DiMagNo simulations

The DiMagNo code is the implementation of the magnetic nozzle model. It solves the expansion of the plasma in the magnetic nozzle using the method of characteristics as explained in chapter 3. Although many measurements have been conducted on the plasma expansion, the limitations on both the thruster in its current setup as well as the diagnostic prevent a thorough validation of the DiMagNo code. This chapter compares the model simulations and the measurements for several plasma parameters along the axial dimension, but only for the nominal configuration. This allows for a qualitative comparison of the trends and show the limitations of the current setup. It also provides insight on the requirements for future validation experiments.

10.2.1. Simulation setup

Most of the measurement data has been generated for the case of 500 W RF power, 50 sccm Argon and the nominal magnetic configuration. Therefore the simulation is run for this case. The model takes as input the magnetic configuration, plasma parameters at the initial front, a model for the plasma and a thermodynamic model for the electrons. The model for the plasma is straightforward and defines a plasma consisting of a single population of electrons - as opposed to two or more distinct populations with different temperatures - and a population of singly charged ions. The simplest and default thermodynamic model is the isothermal model that assumes a constant electron temperature. From the measurements at 500 W, it was found that the temperature varies in both the radial and axial direction. However for a first comparison the isothermal model is assumed.

The magnetic model is the same model mentioned in section 5.1.1 It models the HPT-05 magnetic solenoids with a series of current loops. The DiMagNo code then uses the analytical solution of the magnetic stream function for a superposition of loops to calculate the local magnetic field.

By default DiMagNo propagates the plasma profile at the nozzle throat. However it is also capable of propagating any downstream profile. As input the profile requires an initial front that specifies the radial distribution of the density, plasma potential and ion velocity. All other quantities such as the electron Bernoulli function H_e, the conservation of electron angular momentum D_e and the electron azimuthal frequency $w_{\theta e}$ are internally calculated using analytical expressions (eq. 3.4-3.6.)

The initial conditions (IC) are taken from radial measurements at $z = 40$. For the density profile the left side of the plot in figure 8.2a in section 8.1 was used. The measured values from $r = -50$ mm to $r = 0$ were interpolated using a spline on an evenly spaced thousand point grid ranging from 0 to 1 (the normalisation factor for the spatial dimension is therefore $r_0 = 50$ mm, the width of the IC.) The density is manually normalised with its centre value before being loaded into the IC. The normalised experimental data points are plotted together with the IC input in figure 10.5a. As discussed in chapter 8 the electron temperature shows an asymmetry around the centre value. However in this isothermal model the temperature has to be constant. Therefore the IC temperature $\hat{T}_e = 1$ over the whole range of $\hat{r}$. The experimental data points are normalised with the centre value $T_{e0} = 3.925\ eV$ eV and plotted together with the IC value in figure 10.5b.

From figure 8.5b in chapter 8 it was found that the plasma potential potential linearly decreases in the radial direction. To provide the plasma potential profile for the IC. The experimental radial potential profile at z = 40 was fitted with a straight line. This line was then translated such that $\hat{\phi}(0) = 0$ and scaled with T_{e0}. The normalised data points are plotted in figure 10.5c together with the resulting IC profile. The magnetic field is internally normalised with the value at the centre of the initial front. The

Mach number at $z = 40$ mm was estimated to be 2.06 from the axial profile of figure 9.9 of section 9.3. Since the initial front is not at the throat, there is bound to be some divergence. Therefore the direction of the velocity was chosen to be parallel to the magnetic field. An approximation which should be valid close to the thruster. The magnitude of the axial and radial components of the normalised (with $c_s = \sqrt{T_{e0}/m_i}$) ion velocity along the IC are plotted in figure 10.5d

The simulation produces normalised quantities which can be scaled back to their original values for comparison to experimental data. From the initial conditions DiMagNo creates an initial front of 200 points that is then propagated downstream. The exit conditions were chosen such that the propagated fronts span the region $40 < z < 200$ mm and $-400 < r < 400$ mm, i.e simulation spans the domain of the experimental data.

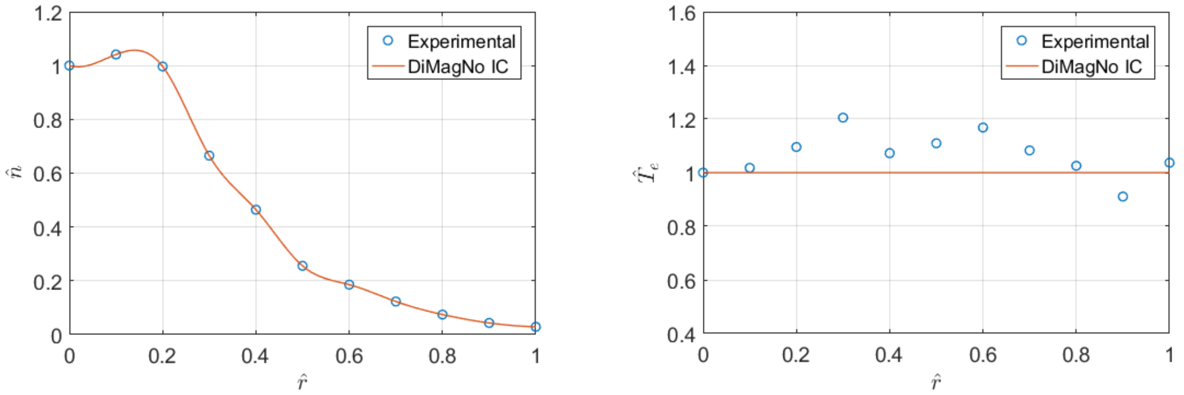

(a) Plasma density.

(b) Electron temperature.

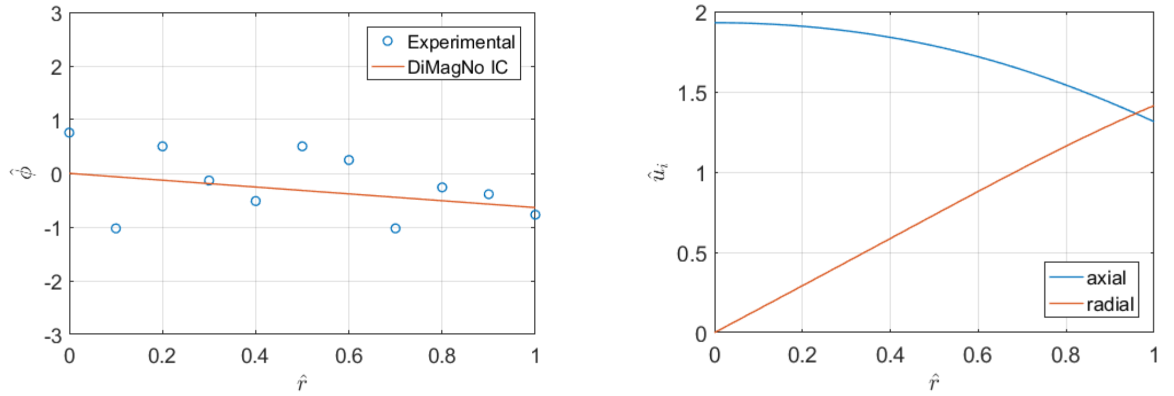

(c) Plasma potential.

(d) Ion velocity.

Figure 10.5: Initial front for the DiMagNo simulation.

10.2.2. Simulation results

In this section the results of the DiMagNo simulation are presented together with the experimental data. Only the axial evolution[3] of the plasma parameters are considered. The output of the DiMagNo simulation takes the form of a set of 2D-arrays, one for each parameter. DiMagNo does not solve the plume expansion on a regular grid, so the axial and radial coordinates are also contained in the output. For each grid point the plasma density, plasma potential, ion velocity (axial and radial components) and the magnetic field (axial and radial components) are available. Combining the ion velocity and the plasma density gives access to the ion current density.

The axial evolution of the plasma density, plasma potential, ion current density and the ion Mach number are plotted together with their experimental values in figure 10.6. All simulation results have

---

[3] On-axis downstream evolution

been scaled back to real quantities. The plasma potential is scaled with $T_{e0} = 3.64$ eV (obtained from axial LP measurements concurrently with the FP and EP measurements used for comparison) and the ion velocity is scaled with the sound speed based on T_{e0} which gives the value of c_s = 2965 ms^{-1}. Since the LP measurements for the radial plasma profile used for the IC and the EP measurements of the axial profile were taken at different dates the absolute value of the plasma potential is not the same. For a proper comparison the plasma potential as measured with the EP is translated such that the potential at z = 50 mm is equal to zero (i.e at z = 50 mm the simulation and measurement are forced to coincide). The plasma density is scaled with a factor n_0 = 1.428·10^{17} m^{-3}.

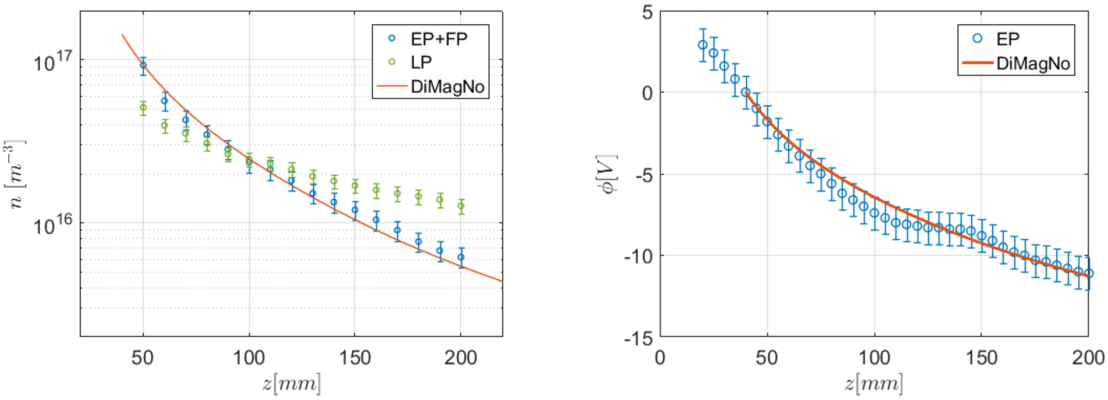

(a) Plasma density.

(b) Plasma potential.

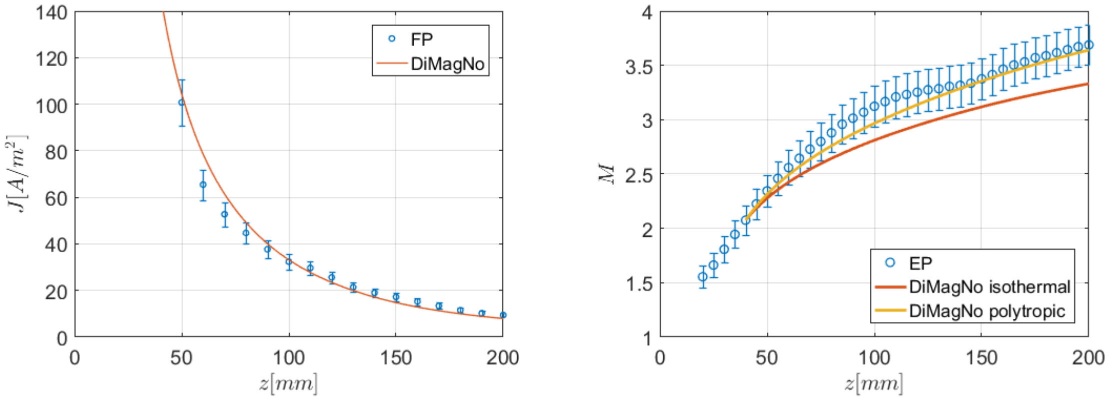

(c) Ion current density.

(d) Ion Mach number.

Figure 10.6: Comparison of measured and simulated plasma parameters as a function of axial position.

10.2.3. Error estimation

To make a meaningful comparison between the model and the measurements error bars are a necessity. In this paragraph the uncertainty in the measured quantities is estimated. The current density as measured with the Keithley has two sources of error, the Keithley itself which has an accuracy of about 0.1% for current measurements and the uncertainty in the surface area of the probe which is 2%. The uncertainty of the Keithley is negligible when summing in quadrature and is ignored in further calculations. This leaves out fluctuations in the plasma which would need to be established by measuring the current density as a function of time and calculating the variance. However from the stability analysis using the Langmuir probes in section 7.2.1 it was found that the fluctuation in the density was 8%. Since the current density is proportional to the density we add both errors and the total error is 10%.

For the plasma potential as measured with the emissive probe no error analysis has yet been performed. However based on fluctuations observed during the characterisation we estimate a (pes-

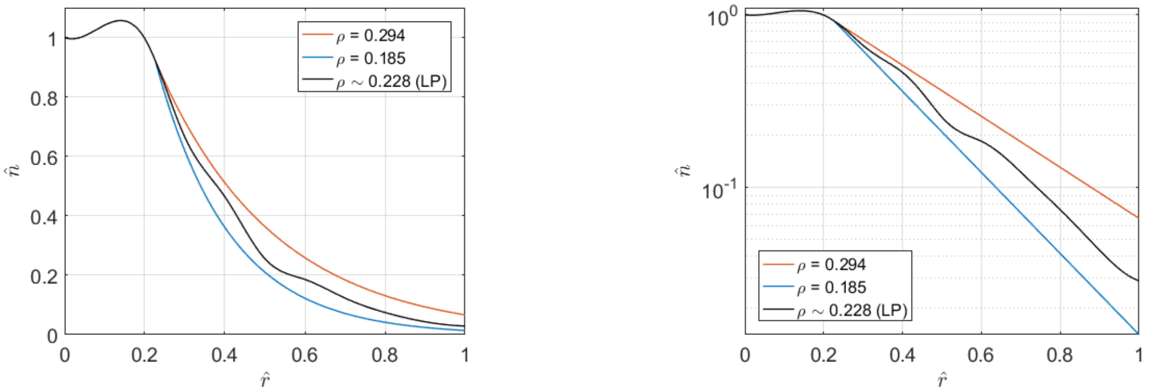

(a) Linear scale.

(b) Logarithmic scale.

Figure 10.7: Normalised radial plasma density profiles with different exponential off-axis decay.

simistic) value of ±1 V. The Keithley has a 0.025% error for voltage measurements but this is negligible. The floating point method has an absolute error of about 1 T_e but since this is a comparison of relative values this can be ignored. The relative error in ϕ based on ±1 V is less than 4%. which is equal to the relative error in u. To get the Mach number u is scaled with the sound speed $c_s \propto \sqrt{T_e}$, since the relative error in T_e is 5% (from section 7.2) this adds an extra 2.5%. The sum of the relative errors for M is less than 12%.

Lastly, the density is an even more compounded measurement, the ratio of J to u. The total relative error therefore is the sum of the relative errors of those quantities, the total error in n is therefore up to 15%. The density as measured with the LP has a 10% error (based on the repeatability).

Note that for all cases these values are only upper estimates and in the plots the error is calculated per point.

10.2.4. Sensitivity Analysis

When validating a model it is important to analyse how variation in the input affects the output of the model. It has been mentioned before that there is an uncertainty in the radial plasma density profile, which might be inflated off-axis due to the presence of charge exchange ions. Furthermore the plasma potential profile used is based on LP measurements which have been shown to deviate from the more accurate plasma potential profiles. Improving the diagnostic setup would of course mitigate this problem, but at a cost. Therefore it is of value to investigate what precision in the inputs is required to be able to validate the model. A full sensitivity analysis is outside the scope of this work. However one example comparison has been performed.

The radial plasma profile can be roughly approximated as a flat front (neglecting the small off-centre peaks) and exponentially decaying wings. For the evolution of the on-axis plasma density the discrepancy between the different measurements and between the measurements and the model, increases downstream. The increase in density has a larger relative effect when the plasma density is lower, similar to the behaviour seen in FP measurements. Therefore it is expected that a similar discrepancy in the radial profile would occur mainly off-axis. To model this the on-axis front up to $\hat{r} = 0.22$ is maintained but the exponential decay past this point is varied. The exponential decay is given by:

$$n(r) = n_0 \exp(-\hat{r}/\rho) \tag{10.1}$$

The original plasma density profile decays with $\rho \sim 0.228$. Two other profiles are generated with $\rho = 0.195$ and $\rho = 0.294$ respectively decaying faster and slower than the original profile. All profiles are plotted together in figure 10.7 in both linear and logarithmic scale. The density at $\hat{r} = 1$ for the profile with $\rho = 0.294$ is 2.3 times that of the original profile while here that of the original profile is 2.1 times that of the profile with $\rho = 0.195$.

Simulations are run with all three plasma profiles and the resulting axial and radial evolution are compared. Figure 10.8 shows the axial evolution of the density profiles up to $z = 200$ mm. Clearly over

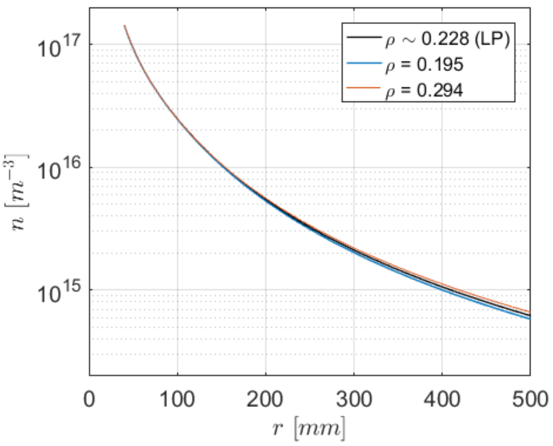

Figure 10.8: Comparison of downstream evolution of simulated on-axis density for different input profiles.

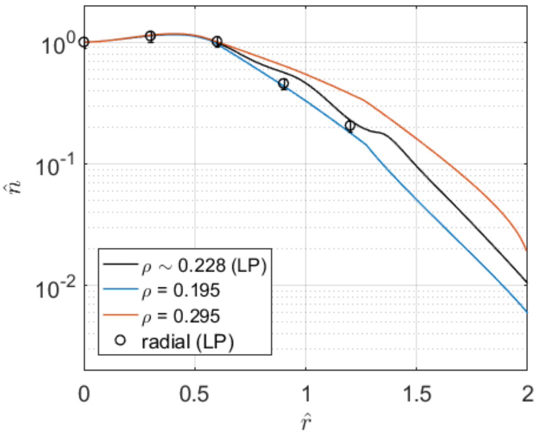

Figure 10.9: Comparison of simulated radial density profiles at $z = 120$ mm, for different input profiles.

a large portion of the domain the profiles are virtually indistinguishable. At $z = 200$ mm the relative differences are only 2% and 7% respectively. In figure 10.9 the simulated radial profiles at $z = 120$ mm are plotted in logarithmic scale. The profiles have been re-normalised with the local on-axis density and the normalisation of the radial dimension is equal to the input profile. Here it can be seen that the ordering of the profiles is conserved. Furthermore the ratio of densities at the edge ($\hat{r} = 2$) are now 1.84 and 1.75 indicating that profiles became slightly more similar. Also plotted is the radial profile at $z = 120$ mm as inferred from Langmuir probe measurements, normalised with their respective on axis density. The error bars shown here are 10% (based on the repeatability of section 7.2.1.) It can be seen That at overall the shape of the simulated radial profile seems to agree with the measured profile. However further off-axis the results seem to agree better with the profile with $\rho = 0.195$.

10.2.5. Discussion

From the plots in 10.5 it can be seen that the initial fronts for the plasma parameters are a reasonable approximation. The density profile is a spline which by definition fits all the data points. The electron temperature deviates by a maximum of 20% from the constant value of 1, while the experimental value of the normalised potential fluctuates by about ±1 around the initial profile. The Mach number varies considerably over the IC but this is defined by the local divergence of the magnetic field. The separation between the magnetic and ion streamlines this close to the thruster exit plane is expected to be less than 1° so this is a valid approximation.[1] Furthermore the radial variation of the plasma parameters at the initial front should not affect the axial evolution too much, since this is mainly dictated by the magnetic field and the electron cooling.

When comparing simulations of the axial evolution of the plasma density with the LP measurements and the combined EP and FP measurements in figure 10.6a, it becomes apparent that the plasma density as measured with the LP does not at all agree with the simulated results. Even when the simulated result is scaled with the LP value at $z = 40$ mm there is no agreement. As mentioned before the LP density is approximately proportional to z^{-1} while the simulated result is proportional to z^{-2}. On the other hand the plasma density as inferred from combining the EP and FP measurements shows a good agreement with the simulated results. This outcome furthermore substantiates the idea that the LP measurements of density are indeed overestimated.

Based on the preliminary sensitivity analysis it can be concluded that the comparison of the evolution of on-axis values is insensitive to modest variations in the radial plasma density profile of the initial front. This increases the credibility of the resulting comparison. It was shown that the radial discrepancy between the different input profiles persists downstream. The measured profile agrees better with the simulations using a reduced off-axis density at the initial profile, however it is not possible to draw any conclusions based on two data points. It is clear however that a sensitivity analysis does provide useful insight into the relationship between model input and output. Extending this analysis to all parameters is therefore warranted.

The second plasma parameter that is compared is the plasma potential. In figure 10.6b it can be seen that upstream near $z = 40$ mm and downstream from $z = 160$ the simulated plasma potential agrees well with the plasma potential as measured with the EP. However between 60-160 mm the measured potential profile shows a fluctuation about the simulated profile. Both curves agree within the measurement uncertainty. There is no reason to distrust the measured plasma potential, but the cause of this behaviour is unclear. The same measurement was repeated twice (see section 7.5) and the same behaviour was observed. This leads to the conclusion that this is a persisting structure in the plasma rather than a transient fluctuation. From other measurements (see chapter 8) it was concluded that the plume is not axi-symmetric. This could affect the downstream evolution of other plasma parameters. The model is axi-symmetric by definition and cannot reproduce such behaviour.

The third simulated parameter is the ion current density, shown in figure 10.6c together with the measured values. The data and the simulation agree well over the full range, although not everywhere within the measurement uncertainty.

The ion Mach number quickly deviates from the measured values. Although the simulation shows a somewhat similar trend it results in a downstream Mach number about 11% lower. Electron cooling, which is not taken into account in the isothermal model, increases the acceleration of ions. To see if this could explain the discrepancy between the isothermal simulation and the measured data, the same simulation was run but now using a polytropic model with $\gamma_e = 1.086$ (found from the polytropic law using the density from the combination of EP and FP). The resulting Mach profile is also plotted in figure 10.6d. Including electron cooling clearly increases the Mach number and improves the fit with the measured profile to agree within the measurement uncertainty. The downstream Mach number at 200 mm is 3.65 and is within 2% of the measured value. This improvement is expected as the ion velocity used in the Mach profile is scaled with the temperature measurements of the Langmuir probe. These measurements showed a decreasing temperature downstream following a polytropic law, leading to a higher Mach number downstream. Including this same polytropic behaviour in the simulation naturally replicates this behaviour. Using a direct measurement of the Mach number, for example using a Mach probe would circumvent the use of the temperature measurement.

Overall the axial evolution of the simulated and measured quantities agree well, except for the Langmuir probe derived plasma density which in the light of the discussion of **??** is possibly due to charge exchange. The agreement of plasma potential and ion current density with the simulated data are the strongest argument for validation of the model as these are based on direct measurement of the plasma parameters in question. The Mach profile and the density profile are indirect measurements based on the aforementioned parameters. It is therefore expected that they would both agree and the compliance among them is reassuring. Although this limited comparison is not enough to validate the model, but it does seem to indicate that the model gives correct predictions. The simulation also provides integrated values such as total current and thrust. Since the initial radial density profile may be incorrect (inflated off-axis density due to charge exchange) there is no guarantee that these values are correct. Despite this it is still interesting to compare these values to the earlier estimates. The thrust as calculated from the simulation and scaled using T_{e0}, r_0, n_0 is 1 mN, exactly the same as the estimation in section 9.5. This perfect agreement seems fortuitous, but encouraging, as it shows that the initial estimate is of the right order of magnitude.

For a proper validation experiment similar comparisons have to be made at different magnetic field configurations to extend the validity of the model over a larger range. A more thorough sensitivity analysis of the model inputs need to be performed to assess whether the diagnostic setup needs to be improved to be able to validate the model. The actions to be taken, ordered by priority, are:

1. Perform a sensitivity analysis of the input parameters on the model outcome.
2. Modify the setup to extend measurements up to the throat such that the normalised ion velocity profile at the throat can be assumed constant and equal to 1. Modifications include mainly reduction in size of the FP and the probe arm to reduce their perturbation of the plasma.
3. Investigate the effect of charge exchange on the plasma density in the plume.
4. Utilise the EP to provide a more accurate plasma potential profile at the throat.
5. Compare the downstream radial evolution of the plasma parameters to the model simulations.

6. Include a Mach probe to provide a more direct measurement of the ion Mach number to compare to the model outcome as well as to verify the assumption of item 1.

All but the last of the aforementioned steps are necessary for a solid validation of the model. The sensitivity analysis has the highest priority as it should indicate what the benefits are of improving the input for the initial front. Investigating the effect of charge exchange is also absolutely necessary since current density measurements are inexplicably overestimated downstream. Measuring the current density profile at the throat, combined with either the assumption $M = 1$ or a measured value of the ion velocity could be used to estimate the plasma density, however a direct measurement would be more robust.

Summary

This chapter presented a comparison of the results of the HPT05 with those of similar thrusters found in literature as well as with the DiMagNo model. Comparison to similar thrusters is not straight forward due to differences in design, mainly in source radius and magnetic fields strength. The most relevant comparisons are with those of Takahashi [80, 82] and Little [49, 50]. It was found that the downstream axial density profiles as inferred from the LP agreed with similar measurements of Takahashi. This similarity concurrent with the deviation from the models point to possibly elevated downstream densities due to charge exchange. Processing downstream ion current density profiles in the manner of [49] in further confirmed ion detachment in the HPT05 plume.

In the second part of this chapter the axial evolution of measured and simulated plasma parameters. The plasma potential and ion current density as measured directly with the emissive and Faraday probe respectively proved to be in good agreement with the model prediction. The plasma density and the Mach profile were calculated from the EP and FP measurements and were also in good agreement. The plasma density as measured with the Langmuir probe did not agree with the model, possibly due to a population of slow charge exchange ions. Furthermore it was shown that including the polytropic model into the simulation improved the fit of the Mach profile as expected. Overall the comparison showed that the model correctly reproduces the axial evolution of the plasma parameters in question for this particular configuration. A sensitivity analysis of the initial front on the simulated results is needed to confirm the merit of improving the diagnostic setup. Future validation experiments should in any case investigate the downstream radial evolution of the plasma parameters and include a range of different (magnetic) configurations.

11

Conclusions & Recommendations

11.1. Conclusions

This section presents the conclusion that can been drawn from this work. Furthermore the research questions posed in chapter 1 will be answered. The conclusions are divided over four sections, dealing with the probe diagnostics, the plume expansion, the propulsive performance and the DiMagNo code.

The main conclusions can be summarised as follows. The plasma density as inferred from the Langmuir probe using current theories was found to deviate from the DiMagNo model but agree with the results of Takahashi [80]. Combining measurements of u_i as inferred from the emissive probe with measurements of j from the Faraday probe yield current density that agrees well with the DiMagNo model. The current working hypothesis is that the LP probe measurements of the density are increased due to charge exchange to which the latter method is less sensitive.

The electron temperature can be measured easily but the effect of the RF-fluctuations are not yet clear. The results on the RFCLP are inconclusive, as one of the assumptions of the underlying theory is not met under the current conditions. The emissive probe can be operated in the floating potential method and provides a more precise and faster alternative to the Langmuir, for measuring the plasma potential.

The plasma expansion is found to be independent of the RF power, and therefore of the magnitude of the density. The shape of the plasma is instead dictated by the shape of the magnetic nozzle. The MN produces a significant improvement in the plume divergence. Furthermore there are signs of downstream ion detachment from the magnetic field lines as well as polytropic cooling of the electrons.

The utilisation efficiency is limited to 20% for the current setup but could be improved by increasing the electron temperature, the magnetic field or changing to a different propellant such as Xenon.

Lastly a comparison of DiMagNo simulations to the measurements indicate a good overall agreement. More rigorous experiments are needed for a full validation.

11.1.1. Langmuir Probe

The Langmuir probe that was developed for the EP^2 propulsion laboratory was applied to the HPT05 prototype plume in order to investigate the plasma density, potential and electron temperature. The plasma density is inferred from the ion saturation current using one of the available theories.

In this study the parametrisation of Bernstein-Rabinowitz-Laframboise theory was implemented in MATLAB to iteratively and concurrently, solve for the plasma density and temperature. While it was found that the implementation was generally successful it was concluded that an (already existing) implementation in excel was more practical and allowed for better control of the process. The excel implementation was modified to also include the case $\xi < 3$. The ion saturation current was also analysed with Allen-Boyd-Reynolds theory as [20] showed that the geometric mean of those theories agreed better with other (microwave interferometry) measurements. Therefore this geometric mean was used for the remainder of the measurements. The BRL theory was compared to the planar approximation and was found that regardless of the theory the axial evolution was similar, however the ordering of the magnitudes of the plasma density was found to be $n_{PA} > n_{BRL} > n_{ABR}$.

In section 10 it was found that, when corroborating plasma density measurements from the Langmuir probe to an inferred plasma density from combining Faraday and Emissive probe measurements, their axial evolution did not agree. The plasma density as measured with the LP was approximately $\propto z^{-1}$ while that of the combined EP and FP measurement was approximately $\propto z^{-2}$. However when comparing the downstream on-axis evolution of the plasma density inferred from the LP to that of [80] it was found that they agreed well. Combining measurements of u_i as inferred from the emissive probe with measurements of j from the Faraday probe yielded current density that agrees well with the DiMagNo model.

As charge exchange mean free path lengths are of the order of centimetres it is suspected that there is a population of slow charge exchange ions present in the plume. Langmuir probe measurements are equally sensitive to the slow and the fast ions in the plume, while the Faraday probe measurements are predominantly sensitive to the fast beam ions. It is therefore hypothesised that charge exchange ions inflate the downstream ion density as inferred from the Langmuir probe resulting in the behaviour seen in both this study as well as [80]. While the combined FP+EP measurement yields the plasma density profile in the absence of charge exchange ions as predicted by the model.

The BRL theory (and also the ABR theory) provided a better fit to the data obtained close to the thruster, while downstream the planar approximation was a better fit. The planar approximation is valid for the case $\lambda_D \ll a$ with a the probe radius. However this is only the case for densities over $10^{18}\ m^{-3}$. The planar approximation is barely valid near the thruster but its condition is not met downstream where the density drops rapidly. Curiously the ion saturation current becomes more linear downstream, which is a hallmark of the planar approximation, precisely contrary to the expectations. One possible explanation is charge exchange collisions in the sheet increasing the ion saturation current. Sternovsky [74, 75] showed that this could play a roll even in plasmas where the charge exchange mean free path was of the order of a thousand times the Debye length. For the HPT05 this ratio is between $10^2 - 10^3$. Based on this work no further conclusions can be drawn but this issue has to be investigated further. The linear ion current at plasma densities where the planar approximation is no longer valid makes it impossible to interpret Langmuir probe data in areas far downstream and in the wing of the plumes.

The electron temperature in general can be easily extracted from the Langmuir probe voltage-current characteristic as it requires no intricate theory and relies only on the assumption that the electrons are Maxwellian. Subtracting the theoretical ion current from the total current, in cases where the theory fits the ion saturation current well, improved the fit of the electron current. In such cases the electron current in a semi-log plot is linear over up to three orders of magnitude. No other means of measuring the electron temperature was available and therefore the error in the absolute value is unknown. However when using the measured electron temperature to scale the DiMagNo results to to real values this resulted in good agreement with other data. There is one issue with the temperature measurements, as they can turn out to be erroneously high due to the RF-fluctuations. This will be discussed in the next section.

The plasma potential could be extracted from the Langmuir probe measurements with varying degrees of success. When the first derivative of the $I - V$ curve is smooth and sharply peaked, it yields good results. However this is not always the case. In general it has a large uncertainty especially compared to Emissive probe measurements.

Lastly the stability of the plasma was assessed by taking a series of consecutive Langmuir probe measurements at a fixed configuration and at a fixed position. The plasma is relatively stable showing a 2% variation in the temperature, an 8% variation in the density and a 10% variation in the plasma potential.

11.1.2. RF-compensated Langmuir Probe

The RF-compensated probe is designed to shield the Langmuir probe from RF-fluctuations that can lead to a higher measured electron temperature than the actual value. The RFCLP was designed to have the same collection area as the simple Langmuir probe such that their collected ion saturation currents should be equal. The $I - V$ curves of both probes as well as the resulting plasma parameters were compared under different plasma conditions. It was found that the ion saturation currents of both probes differed more than expected. The problem with using the RFCLP in the current thruster configuration is that one of the main assumptions, $\omega_{rf} \gg \omega_{pi}$ is not satisfied. Only for densities of $n > 10^{18}$ m^{-3} this condition is met. It ensures that the sheath can equilibrate within the period of the RF fluctuations. The maximum amplitude that can be filtered depends also on the density. Even for the most optimistic case of 10^{18} m^{-3} (near the thruster exit-plane) the maximum filtered RF-potential is theoretically approximately 20 V. However since the amplitude of the fluctuations are unknown no conclusions can be drawn. It is of little value to interpret the probe results when the assumptions of the underlying theory are not valid. The RFCLP should be tested again in a plasma of sufficient density where this condition is met. Densities of this order is expected when the thruster is operating in helicon mode.

Despite the conditions not being met, some observations were made that are of interest for further investigation. Electron temperatures agreed well downstream (within 10%) but the RFCLP measured temperature was significantly lower at <60 mm. It is not clear if this is because the RF-field is too small past this point, or because the density there is too low to filter the RF-fluctuations; it is probably a combination of both. However without knowledge of the amplitude fluctuations of the potential this remains inconclusive. An $I - V$ characteristic of the Emissive probe could provide inside on this.

Furthermore the floating potential as measured with the RFCLP is higher than for the LP closer to the thruster indicating that indeed some part of the fluctuations are effectively shielded. The plasma potential as inferred from the RFCLP, close to the thruster, is higher than that for the LP. This is contrary to the theoretical expectations. However preliminary EP measurements indicate that these values are more correct than those of the LP.

Overall the results on the RFCLP are inconclusive. It needs to be used in a plasma of sufficient density (helicon mode) which means that it is per definition not useful anywhere outside of the throat area. Furthermore the amplitude of the RF-fluctuations needs to be investigated before any meaningful conclusions can be drawn about the efficacy of the RFCLP.

11.1.3. Emissive Probe

From the characterisation of the Emissive probe it was concluded that for the nominal configuration, it is possible to operate it in the floating potential method in the limit of large emission for a heating current of 0.8 A. At higher plasma densities the probe saturates at a higher heating current. Therefore at higher RF power this value has to be reevaluated. The probe temperature was estimated to be 1600 K. It was furthermore shown that Thoriated-Tungsten has a (theoretical) emission current of up to 5 orders of magnitude larger than pure Tungsten, confirming its value as a probe material.

Although no extensive comparison with LP probe measurements was conducted, overall it could be concluded that the emissive probe surpasses the LP plasma potential measurements in speed (40 data points per minute, versus 2 data points per minute) and precision (about 2% random error versus ±3V). Further experiments are needed to confirm a higher accuracy. However theoretically the electron temperature needs to be known to correct the absolute value, which is obtained from LP measurements. For a slowly decreasing electron temperature a single measurement at the throat should be sufficient. For relative measurements such a correction is not necessary at all.

11.1.4. Plume Expansion

The plume expansion was characterised by the Langmuir probe in terms of the plasma density, electron temperature and plasma potential. Firstly the low densities $n < 10^{18}\ m^{-3}$ indicate that this is an inductively coupled plasma and that the thruster is not yet operating in helicon mode. In radial direction there were both defects and a clear asymmetry which are attributed both to the irregular antenna and possible misalignment in yaw angle. Recent measurements, not covered in this study, using a half-helical antenna produced a single central peak, with a slight asymmetry.

It was furthermore concluded that both the radial and axial evolution of the plasma density was independent of the RF power, and therefore independent of the absolute density. This implies the shape of the plasma is mainly determined mainly by the magnetic nozzle. The axial evolution was found to be $\propto z^{-1}$, decreasing slower than expected. As mentioned before this is suspected to be due to charge exchange ions. In radial direction the plasma is relatively constant around the centre line but drops exponentially towards the wings.

The evolution of the electron temperature in axial direction for the nominal configuration (at 500 W) show signs of cooling with a polytropic coefficient of $\gamma_e = 1.10 \pm 0.05$. At higher power (650 W, 800 W) the behaviour is isothermal. This has two possible explanations. Either at higher power the electrons are supplied with more energy from the source offsetting the cooling, or due to the stronger RF-field the temperature measurements are spuriously high obscuring the mild cooling. In radial direction the electron temperature is asymmetric. The profile is reminiscent of a sinus where the temperature peaks

±1 eV on either side of the centre line around a 4 eV mean value. The asymmetry diminishes downstream. The working hypothesis is that this is also due to the irregular shaped antenna. Repeating the measurements for a regular (half-helical) antenna should illuminate this matter.

The axial evolution of the plasma potential is the same at higher power, but decreases more slowly at 500 W. This is compliant with the observed electron cooling. Radial plasma potential profiles show an approximately constant value that decreases downstream. However from EP measurements it was shown the radial profile actually curves down at the wings, which is caused by electrons diverging more than ions, creating a radial ambipolar field.

Ion current density measurements and the inferred plume divergence were found to corroborate the idea that the plume expansion is dictated by the magnetic nozzle as the plume divergence half-angle was independent of the RF power. Furthermore the plume divergence remained constant downstream (> 120 mm) indicating that the ions here no longer follow the magnetic field. This was also substantiated by the measurement of j/B which was found to increase downstream. This means that the magnetic flux expands faster than the ion flux, indicating detachment of ions from the magnetic field lines which is favourable for thrust. Lastly it was shown that the presence of the magnetic nozzle has a big impact on the plume divergence. Switching the nozzle on decrease the divergence half angle with 10%. The plume 95% divergence at full magnetic nozzle strength was around 42-44° while the cosine weighted half-angle was about 23-24°. (The latter method reflects more the average angle of the ion momentum.) Further investigation of the relationship between the nozzle strength and the divergence is warranted.

11.1.5. Performance

Based on the measurements conducted for this study three figures of merit could be inferred for the thruster-magnetic nozzle combination: the thrust efficiency, the utilisation efficiency and the plume divergence. The results of the latter have been discussed in the previous section. The utilisation frequency was found to increase $\propto \sqrt{P}$, the square root of the RF power (and therefore linear in n), with about 20% at 1 kW. This is a meagre result considering that this efficiency in theory could be 100%. However according theory, this efficiency is dependent on the electron temperature and the magnetic field. An efficiency of 100% at the nominal magnetic field strengths are for electron temperatures of over 10 eV, twice the currently measured 3-4 eV. Also recent measurements with Xenon, not included in this work, hint at a utilisation efficiency of around 50%, probably due to its lower ionisation energy.

An attempt was made to estimate the the total thrust by combining the LP density and FP current density measurements. The estimated value of 1.0±0.6 mN corresponding to an efficiency of 0.10±0.06%. Calculations of the DiMagNo code for the thrust also yielded 1 mN. Although 0.1% is a very low value for the efficiency there are two reasons to be optimistic: firstly currently there are large losses in the RF system and the antenna which are included in the total efficiency. These losses are completely due to the current RF architecture and not representative of the thruster's performance. Secondly the thrust scales linearly with the plasma density, and increasing the plasma density by one or two orders of magnitude greatly increases the thrust and thrust efficiency. Operating the thruster in helicon mode is expected to improve this number significantly. Based on the downstream ion velocity an I_{sp} of about 1000 s was estimated. As $F = \dot{m} g_0 I_{sp}$ combining these numbers a value of $\dot{m} = 1$ mg/s is found, consistent with the mass flow rate used in the experiment.

It has to be stressed that both these figures of merit are merely estimates and should do not carry too much weight. Furthermore the HPT05 prototype is a test-platform designed to investigate the physics of the plume and the helicon source. The current configuration should not be treated less as a thruster and more as an experimental setup. Optimisation of the design will happen at a later stage when its internal workings are well understood.

11.1.6. DiMagNo code

Lastly the DiMagNo code simulation was run using the nominal magnetic configuration and normalised measured radial profiles of the density, electron temperature and plasma potential as input. The value of the Mach number was inferred from the measured axial Mach profile. The simulation results were scaled to real quantities and their axial evolution compared to that of the measured quantities.

It was found that the Langmuir probe plasma density did not agree with the model results, while the density inferred by combining EP and FP measurements did agree with the simulation within the measurement uncertainty. The simulation and measurements also agreed for the plasma potential, within the measurement uncertainty. However the plasma potential showed a 'bump' in the plasma potential that is thought to be a structure in the plasma probably related to radial asymmetries for which the model does not account. The measured axial ion current density also agreed overall with the simulated results however, not everywhere within the measurement uncertainty. The Mach profile was inferred from EP measurements and the assumption $M = 1$ at $z = 0$ and using the local temperature to calculate the sound speed, the resulting profile did not agree with the isothermal simulation, but good agreement was found when using a polytropic model for the electrons.

A preliminary sensitivity analysis was performed investigating the effect of the radial density profile on the simulation results. It was shown that for mild off-axis variations of the profile the simulated axial density profile was unaffected. The relative difference between input profiles was roughly conserved over the expansion. This indicates that the simulated radial profiles are sensitive for the input profile. A complete sensitivity analysis of the DiMagNo could should precede further validation experiments.

In general this preliminary comparison indicates that the DiMagNo code accurately predicts the plasma response of the mgnetic nozzle within the limits of the model. The main limitation seems to be the axi-symmetry. For proper validation of the model the comparison should be extended to the radial dimension. It can be concluded that in principle the DiMagNo-model can be validated using electrostatic probes, given some improvements on the setup.

11.2. Recommendations

During this work, both while doing experiments as well as during the processing and writing many areas for improvement were identified. This chapter is considered with the recommendations based on those observations. Some of these recommendations have clear links to the results discussed in other chapters other recommendations are based on personal experience which are nonetheless valuable for future work. The recommendations are divided over several topics: the diagnostics, the prototype, DiMagNo validation experiments and directions for future work.

11.2.1. Electrostatic Probes

Overall the diagnostics used in this study let to meaningful and tangible results, as discussed in in the previous chapter. However some probes didn't work as expected and some did but can be improved. One of the questions that arose during this work is has to do with the presence of charge exchange collisions and their effect on the LP measurement. Can this explain the fact that the ion saturation current becomes more linear downstream, contrary to theoretical expectations? And can this explain the elevated plasma densities found downstream, that deviate from the model?

The main problem with the Langmuir probe was the duration of the voltage sweep using the Keithley. Although the Keithley provides a high accuracy and precision, one LP measurement takes 30 seconds. This in turn limits the spatial resolution, if measurements are to be completed within a reasonable time. It also limits the resolution of the voltage sweep to 0.5 V. Therefore it is proposed to use a setup with a function generator, amplifier and oscilloscope to be able to sweep at a higher frequency and with a higher resolution, reducing the measurement time. Accuracy could then be improved by averaging several $I - V$ curves. The increased voltage resolution allows for obtaining the electron energy distribution function using the Druyvestein formula (eq. 4.3 in chapter 4) which can also yield the electron temperature, and electron density as well as help identify electron populations with distinct temperatures. Another option to improve the measurement speed is the triple-probe that provides plasma density and electron temperature without modulating the probe voltage (i.e without the time-consuming voltage sweep). [8, 34]

The RF-compensated probe did not yield meaningful results, mainly because it was operated in a plasma were the underlying assumptions are not valid. It is also concluded that the probe is only useful for measurements inside or very close to the plasma source. A different, smaller design that could be mounted on the thruster might useful. Firstly the probe has to be tested in a higher plasma density where the condition $\omega_{pi} \gg \omega_{rf}$ is met. Also the the amplitude of the plasma potential oscillations should be investigated by obtaining $I - V$ curves with the emissive probe. The first derivative of such a characteristic should show two maxima, with the distance between them equal to two times the RF amplitude.

The emissive probe was only characterised for one single configuration. It needs to be investigated, if at higher densities, the probe is still in saturation at 0.8 A heating current. It might also be of value to us the inflection point method in the limit of zero emission. This is a more time consuming but more accurate method which can be used to identify the absolute error for the floating potential method. Measuring the plasma potential with the floating potential method as a function of time can help identify better the stability of the plasma. A similar measurment using the Faraday probe can be used for this as well.

The Faraday probe was found to function well. However due to its size it perturbed the plasma when it was positioned to close to the thruster. Furthermore current measurements with the Keithley in the FVMI mode are limited to 10 mA. A FP with a large collector therefore saturates the Keithley when the ion current density is large, i.e. close to the thruster. A new design for a smaller Faraday probe has therefore been proposed. Since the temperature of the FP was found to stay below 120°C a temperature sensor can be excluded allowing for a more compact design.

For the Faraday probe it is of interest to design a positioning system in polar coordinates that allows the probe to sweep along ±90° such that all plasma (in the same plan) ejected from thruster is intercepted by the probe. This will also ensure that the probe is more aligned with the flow direction. Such a system would sweep an arc with a radius of about 400-500 mm giving access to the far plume. These measurements can be used to a) give a better estimate of the total current (and therefore the utilisation efficiency); b) verify the e-folding that is used to provide dynamic integration boundaries needed in a Cartesian system and c) verify the cosine correction that has been used to correct for the angle between the probe and the ion flow.

Lastly the addition of two more probes to the diagnostic assembly would significantly increase the capabilities of the propulsion lab. A Mach-probe would allow for direct measurements of the ion velocity [30]. While a Hall-probe could be used to measure the magnetic field. This could be used to verify the magnetic field model and help locate the throat of the magnetic nozzle.

11.2.2. Other diagnostics

While originally OES was to be included in this work it was later dropped because of insufficient results. However OES can be used to provide information on the source plasma which is otherwise inaccessible to the probes. While it has to be assessed if the plume produces enough light to perform OES here, this could potentially be used for comparison against probe diagnostics. However to provide meaningful absolute results on the plasma density and electron density, more sophisticated models such as a collisional-radiative model need to be developed.[15]

Another interesting diagnostic that is non-intrusive and could be used to provide direct measurements of the electron density is microwave-interferometry. This method has been successfully applied to thruster measurements [65]. A cheap and interesting option could be a design incorporating the network analyser already available in the EP^2 propulsion lab [39].

Probably the most important asset in thruster diagnostics is the ability to measure direct thrust. The development of a thrust balance should therefore have priority for the propulsion laboratory.

Lastly it was found that the vertical degree of freedom was often unused and of little extra benefit. The motor of the vertical stage also needed to provide constant torque to offset gravity. Removing the vertical stage would diminish the obstruction of the plasma plume and free up a stepper motor driver that could be used for other purposes, such as a customised vacuum rated matching network. If for future work a vertical stage is needed, it is recommended to replace the current belt-driven system with a lead-screw system to counteract gravity without needing constant torque. Another useful addition would be translational position sensors. With such sensors the current step-by-step measurements could be done in a continuous motion, speeding up translational sweeps and minimising plasma obstruction.

11.2.3. HPT05 Prototype

The HPT05 prototype and the accompanying magnetic nozzle used in this study generally performed well. Most of the issues regarding thruster originated from the RF architecture, related to arcing between the antenna and the magnetic coils, lossy or bad connections in the feed-through and short circuiting in the antenna feed-line due to overheating. Although not the main concern, these observations were made during the experiments of this study. The general RF architecture needs to be overhauled. One proposed architecture involves installing the matching network on the vacuum side closer to the antenna. A water-cooled antenna could prevent overheating and the accompanying short circuit. Also a more regular (half-helical) antenna is needed as the current irregularly shaped antenna is suspected to produce the observed asymmetries. It was also found that the strength of the magnetic nozzle was insufficient with respect to the axial magnetic field and that in general the magnetic field strength should be increased to be able to operate in helicon mode.

11.2.4. DiMagNo Validation Experiments

To be able to rigorously validate the DiMagNo code proper validation experiments have to be designed. It was shown that in principle this can be done with the current diagnostic setup. One of the main requirements is the ability to measure closer, or preferably up to the thruster exit plane. Also the addition of a Mach probe is needed to compare the simulation to a direct measurement of the ion velocity. Also a different diagnostic or an improve theory for Langmuir probe measurements is needed to provide a correct plasma density measurement. Such a measurement is needed not only for comparison to the simulation but also to provide an accurate radial plasma density profile for the initial front of the simulation. Without such a front comparison of plasma parameters in radial direction is meaningless. Such a radial comparison is paramount to the DiMagNo validation. As a 2D model inclusion of the radial dimension is one of its prime advantages over existing 1D models. Lastly such measurements should be taken over a range of configurations. The most important parameter being the magnetic configuration that mainly determines the plume expansion.

11.2.5. Future Work

Recommendations on future work are in part included in the previous sections and should focus on several directions. Firstly Improving the diagnostic setup with developing a thrust balance as a priority. Designing and carrying out the validation experiments for the DiMagNo code. Improving the helicon plasma thruster prototype with achieving helicon mode as priority. Investigating open questions resulting from this work such as: how does the plume divergence scale with the magnetic nozzle strength, what is the amplitude of the RF induced plasma oscillations and why does the Langmuir probe ion current become linear downstream and what role do charge exchange collisions play? Lastly an interesting venue for future research would be the development of a 3D-magnetic nozzle as has been proposed by the EP^2 group [58].

A

Spectroscopy

Introduction

This appendix presents the preliminary work on optical emission spectroscopy. Due to the limited results obtained and the lack of data at operating conditions corresponding to those of the probe measurements in the main body of this thesis it as decided to include these results in this appendix. The chapter will give a short introduction to the theory behind optical emission spectroscopy, shortly introduce the setup and present some preliminary results on the HPT05 prototype, mainly Argon line identification and measurements of the excitation temperature of the plasma.

A.1. Optical Emission Spectroscopy

Optical emission spectroscopy is a diagnostic method that uses the light emitted by the plasma itself. Light emitted in the VIS-UV range is due to electronic transitions of the atoms and ions in the plasma. The electronic states of an atom are discrete and defined by the corresponding quantum numbers. Transitions between two states p, q have an associated energy $\Delta E = E_q - E_k$. When an electron decays to a lower state the corresponding energy is released in the form of a photon with wavelength $\lambda = hc/\Delta E$, with h Planck's constant and c the speed of light in vacuum. Each atom or ion has a unique set of possible states and corresponding transition lines. States can be populated and depopulated due to collisional or radiative processes. Collision processes can be for instance electron impact (de-)excitation and ionization, radiative recombination and three-body recombination. Radiative processes are absorption, spontaneous emission and stimulated emission.

Absorption and stimulated emission only take place in the presence of a strong radiation density such a laser. For optical emission spectroscopy (OES) only spontaneous emission is relevant. Except the ground state and meta-stable states, all states have a finite lifetime which translates into a probability for spontaneous emission. The intensity of spontaneous emission for a given transition (i, k) is given by:

$$I_{ik} = \frac{hc}{4\pi\lambda} A_{ik} n_i \tag{A.1}$$

where n_i is the population density of state i and A_{ik} the Einstein coefficient for stimulated emission. When all states are in thermal equilibrium the populations of respective states are Boltzmann distributed and therefore:

$$n_i = \frac{N}{Z(T_{exc})} g_k \exp\left(\frac{-E_k}{T_{exc}}\right) \tag{A.2}$$

where N is the total number of particles, Z the partition function and g_k the degeneracy. Combining the last two equations we find:

$$\ln\left(\frac{4\pi\lambda I_{ki}}{g_k hc}\right) = \frac{-E_k}{T_{exc}} + \ln\left(\frac{N}{Q}\right) \tag{A.3}$$

where C is some arbitrary constant. I_{ik} is the measured intensity of a spectral line, and A_{ik}, g_k, λ and E_k can be found in literature. It is evident that the slope of a semi-log plot based on the above equation yields the excitation temperature of the excited states. Whether this temperature is equal to the electron temperature depends on the equilibrium conditions of the plasma.

Another interesting parameter that can be calculated based on OES data is the ion-to-neutral ratio which can be inferred from the ratio of population densities. If the population density n_i of level i of Ar-I is given by:

$$n_i = \frac{N_{Ar}}{Z_{Ar}(T_{Ar}^{exc})} \cdot g_i \cdot \exp\left(-\frac{E_i}{T_{Ar}^{exc}}\right) \tag{A.4}$$

and the population density n_j of level j of Ar-II is given by:

$$n_j = \frac{N_{Ar^+}}{Z_{Ar}(T_{Ar^+}^{exc})} \cdot g_j \cdot \exp\left(-\frac{E_j}{T_{Ar^+}^{exc}}\right) \tag{A.5}$$

than the ratio of densities can be calculated from:

$$\frac{N_{Ar^+}}{N_{Ar}} = \frac{n_j}{n_i}\frac{g_i}{g_j} \cdot \frac{Z_{Ar^+}}{Z_{Ar}} \cdot \exp\left(\frac{E_j}{T_{Ar^+}^{exc}} - \frac{E_j}{T_{Ar}^{exc}}\right) \tag{A.6}$$

A.2. Spectroscopy Setup

Spectroscopy allows measurements inside the thrust chamber where probes cannot be used due to a too high density and RF-field. The spectroscopic measurements can also be used for comparison to the probe measurements. The setup consists of a Ocean Optics HR4000 spectrometer, and a vacuum proof optic fibre. The collecting end of the fibre is fitted with a customised PTFE collimator with a very small collection to ensure a line measurement. The fibre is aligned perpendicular to the axis of the thruster chamber at various positions along the quartz tube, such as the injector plate, at the antenna and near the thruster exit plane. A schematic overview of the OES setup is shown in figure A.1. The HR4000 is capable of measuring in the UV-NIR with a wavelength range of $200 - 1100\ nm$ and a resolution of $\sim 1\ nm$. This rather minimal resolution prevents detailed line analysis such as Doppler-broadening or Doppler shifts and only allows for line identification and simple analysis of line intensity ratios such as Boltzmann plots.

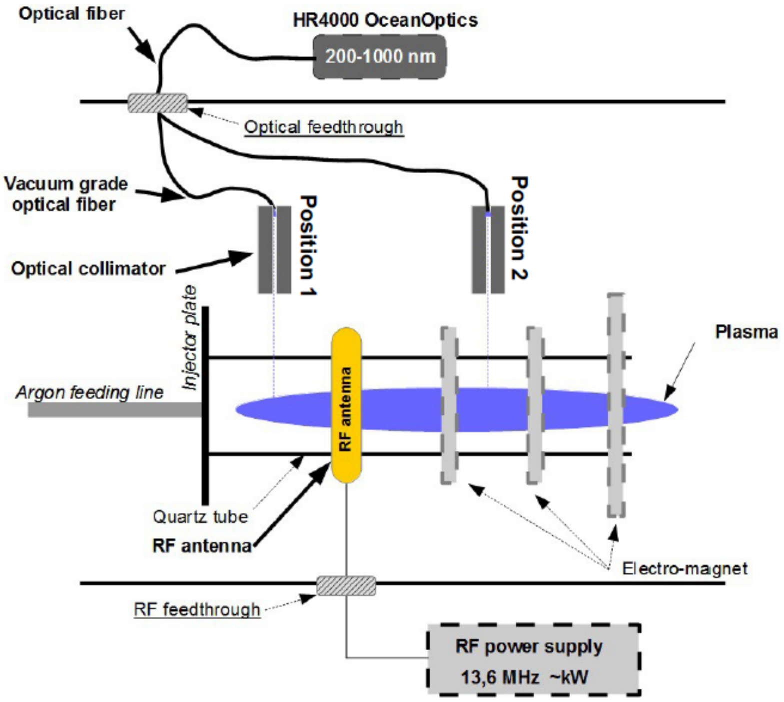

Figure A.1: Schematic overview of the optical emission setup.

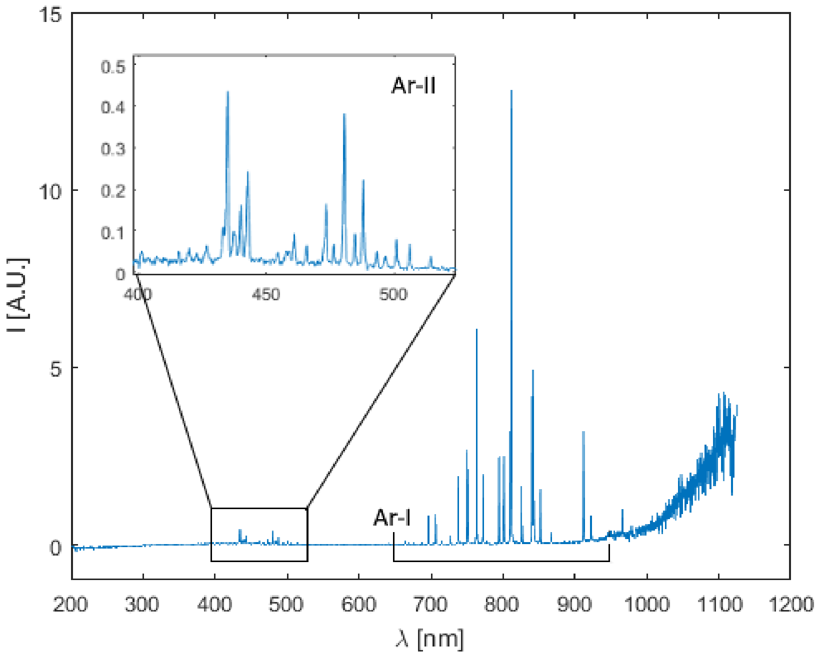

Figure A.2: Argon spectrum of the source, $200 < \lambda < 1100\ nm$

A relative calibration of the spectrometer has been conducted with a Tungsten lamp for the visible region and a Deuterium lamp for the UV region. The resulting relative calibration spectrum was used to correct all measurements.

A LabVIEW program has been developed in cooperation with Dr. Yacine Babou that can track the excitation temperature in real time. It continuously takes averaged measurements with a specified integration time and number of averages. The program then locally subtracts the background from a series of predefined peaks by linear fitting and integrates the peak intensity. These peak intensities are then used to generate a Boltzmann plot and calculate the excitation temperature of both Ar-I and Ar-II. Plots of the peak fitting are available in real-time as to discard any peaks fitted with insufficient accuracy. The Boltzmann plot and excitation temperature are available in real-time as is the time evolution of the excitation temperature. The time resolution is only limited by the collection time which is the product of the number of averages and the integration time and is usually of the order of several seconds. Images of the LabVIEW interface are shown in figures A.11 and A.12 .

A.3. Characterisation of line emission

The plasma inside the source is nearly impossible to access with intrusive diagnostics because these will disproportionally perturb the plasma, except for perhaps flush-mounted wall probes. To acquire information about the plasma inside of the chamber non-intrusive diagnostics are key. Currently EP2 only has access to an OES set-up with limited resolving power. However spectra acquired with this set-up are sufficient to identify the presence of Argon neutrals and ions as well as derive some information about their excited states.

The two main forms of Argon present in the plasma are Ar-I i.e. the neutrals and Ar-II, i.e. the singly ionized ions. Both emit light at different frequencies, Ar-I mostly emits in the near infra-red (>700 nm) while Ar-II mostly emits in the blue part (400-500 nm) of the spectrum. An example spectrum obtained from the HPT-05 is shwown in figure A.2. This also explains the change of color, observed at higher power. At higher power the ion density is expected to increase which means that contribution of Ar-II to the total emission will increase giving the light a more bluish color. Although this change is gradual two distinctly different modes were seen in the plasma which are referred to as pink mode and blue mode and can be seen in figure A.3.

Several Argon lines have been identified in the plasma using the NIST database and are listed in a table as well as shown in a plot of the spectrum in figures A.4 and A.5.[35]

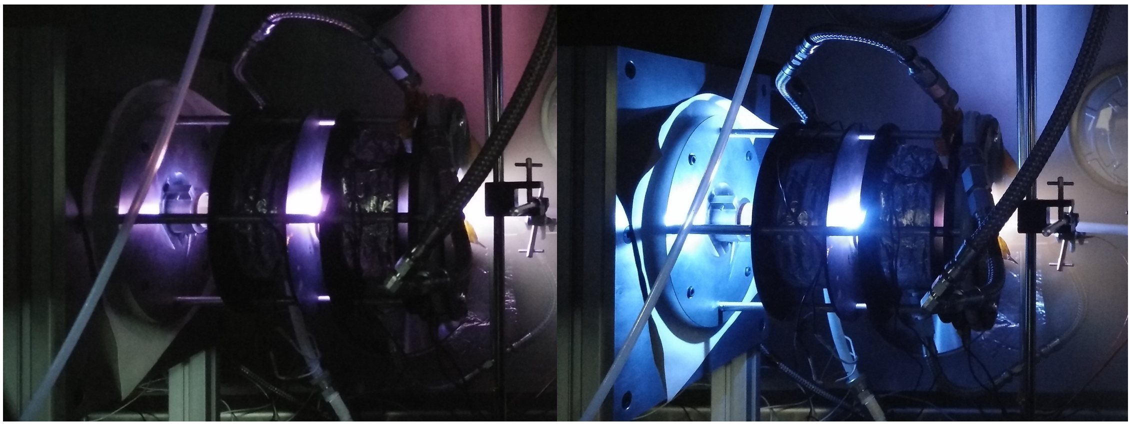

(a) Pink mode (b) Blue mode

Figure A.3: Different modes of operation, classified by color of emission.

Spectral identification of Ar-I and Ar-II is only a minor goal of optical emission spectroscopy. Using a Boltzmann plot the excitation temperature of both species can be inferred as has been explained in section A.1. Another interesting parameter is the ratio of Ar-II to Ar-I emission as this is proportional to their respective densities and as such a qualitative measurement of the ionisation fraction. Both these measurements have been acquired at various RF power. The results are reported in the next section.

The line emission can also be related to the electron temperature and plasma density using a collisional-radiative (CR) model. Developing and implementing the CR model is a time-consuming task as it involves 100-200 collisional reactions that effect all the excited states of Ar-I and Ar-II. Such a model has been developed by Celik for Argon and Xenon plasmas in Hall and Helicon thrusters.[16] Preliminary results of this work predict an electron temperature of 30 eV and density of $10^{-19}\ m^{-3}$ for a 1 kW RF power and a magnetic field of 1800 G. This result contradicts probe measurements on the same device presented in other work and neither agrees well with measurements presented later in this chapter.[73] Celik presented the value of 30 eV as found by comparing simulated and measured spectrum but omits the specifics. The work lacks proper application of the model to the Helicon plasma but provides a good starting point for future work.

A.4. Preliminary Measurements of Source Parameters

In this section some measurements on the excitation temperature and the ratio between Ar-II and Ar-I radiation will be presented. The measurements were obtained at an early stage of the test-campaign when the thruster could only be operated up to 400 W.

The excitation temperature can be calculated using a Boltzmann-plot as explained in section A.1. To study the variation of the excitation temperature of both Ar-I and Ar-II as a function of the RF power, several spectra were obtained at different power. From the raw spectra the background was subtracted and the resulting spectra were scaled with a correction factor based on a calibration with the Tungsten lamp. For both species a series of emission lines were selected that cover a wide range of energy levels. The more distinct the energy-levels of the transitions are, the more accurate the resulting temperature. To isolate each line from the continuum a baseline was fitted from a priori determined fitting limits. This makes it possible to automate the processing of the spectra. The integrated area between a peak in the spectrum and its baseline yields the line intensity I_{ki} in arbitrary units. Figure A.6 shows this process for a single peak.

The value of I_{ki} is then used in equation A.3 and the LHS is plotted against E_q, the resulting data is then fitted with a straight line the slope of which is the inverse of the temperature. An example Boltzmann plot for Ar-I at 375 W operation is shown in figure A.7. The lines used for making the Boltzmann plots of both species are listed in table A.1 including the Einstein coefficient A_{ik}, transition energy E_k and the degeneracy g_k. Note that depending on the spectrum not all lines are necessarily present. The resulting excitation temperatures as a function of RF power are shown in figure A.8. The Ar-II temperature at 1 eV is roughly twice the Ar-I temperature of 0.5 eV. At low temperature the Ar-II

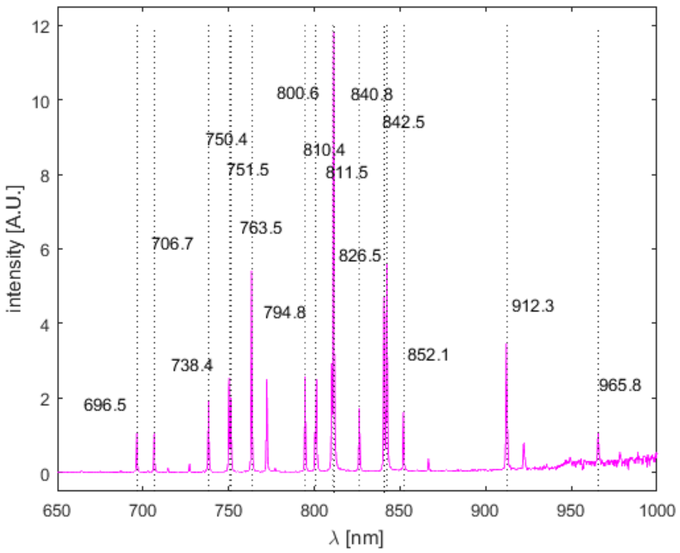

(a) Spectrum

λ [nm]
696.5431
706.7218
738.3980
750.3869
751.4652
763.5106
794.8176
800.6157
810.3693
811.5311
826.4522
840.8210
842.4648
852.1442
912.2967
965.7786

(b) Table of Ar-I lines

Figure A.4: Identification of Ar-I spectral lines.

excitation temperature is slightly higher (although this could be within the uncertainty), but overall both temperatures are constant over the range of RF power. The electron temperature as measured with an LP near the thruster exit plane is plotted for comparison and is also constant over the full range with value of 2.3±0.1 eV.

Without a calibration no absolute measurements of the density are possible however from the current data some relative measurements can be obtained. As explained in A.1 the relative emission of two and Ar-II and Ar-I line can be tracked as a function of the RF power. This ratio of line intensities is equal to the ratio of ion to neutral density as follows from equation A.6. This has been done for the ratio of the emission of the following Ar-II lines: 442.6, 460.9, 487.9, 493.3 and 514.5 nm to the emission of the 763.5 nm Ar-I line. All five ratios as a function of RF power gave equal results and have been averaged and plotted in figure A.9. The error bars are given by twice the standard deviation of the five ratios. It can be seen that from 150 to 350 W the density ratio grows by 2.5 orders of magnitude, then shows a small dip and then a jump in density.

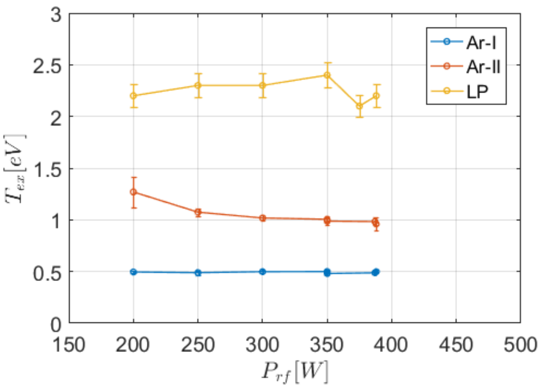

Figure A.8: Example of emission line processing.

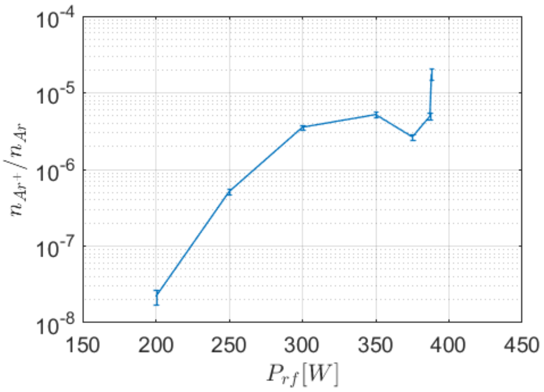

Figure A.9: Density ratio from line emission ratios as a function fo RF power.

Another interesting figure is the total emission of all lines in the blue range, 380-530 nm. All lines in this range are due to Ar$^+$ emission. The line emission is $\propto n$ and $\propto \exp(1/T_{ex})$. However since the temperatures where found to be constant the increase in total emission is driven by an increase in

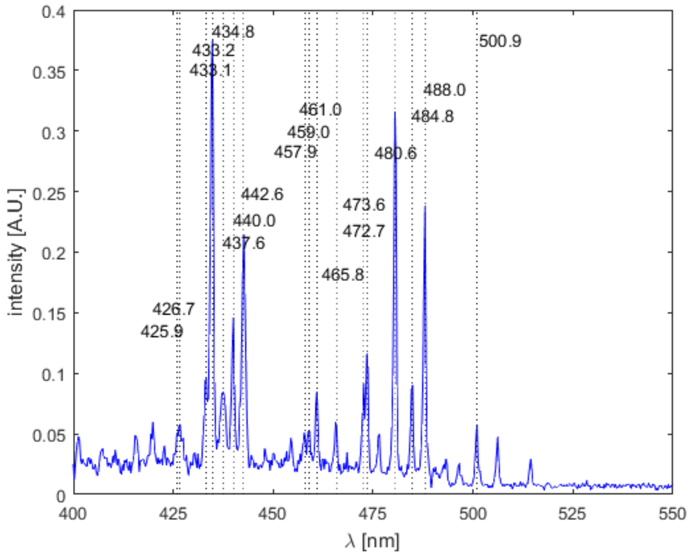

(a) Spectrum

λ [nm]
425.9170
426.6527
433.1200
433.2030
434.8064
437.5954
440.0097
442.6001
457.9350
458.9898
460.9567
465.7901
472.6868
473.5906
480.6020
484,7810
487.9864
500.9334

(b) Table of Ar-II lines

Figure A.5: Identification of Ar-II spectral lines.

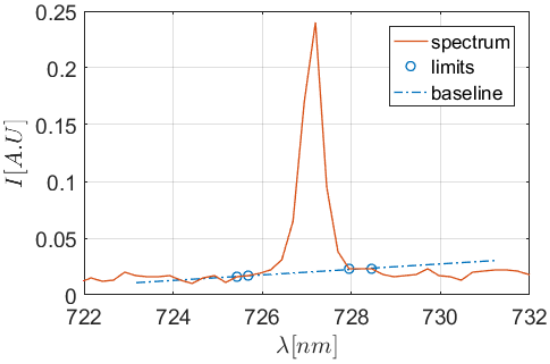

Figure A.6: Example of emission line processing.

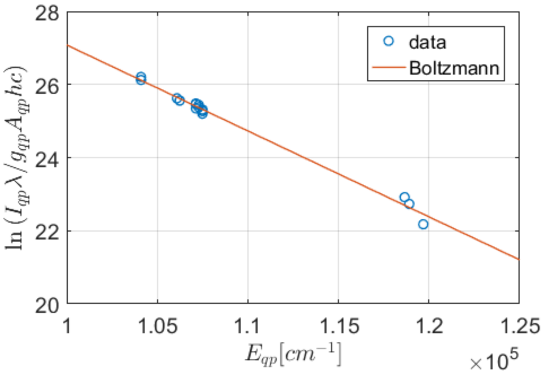

Figure A.7: Boltzmann plot of Ar-I at 375 W RF power.

plasma density. The total blue emission as a function of RF power is plotted in figure A.10 together with Langmuir probe measurements of the plasma density taken at the exit plane. The plasma density here was obtained using BRL theory only and the correct absolute value could be lower. Both measurements are plotted on distinct scales, spanning two orders of magnitude. From this plot it is clear that both trends agree very well with each other and they differ by a constant factor 10^{13}.

A.5. Discussion

It is clear from the previous sections that optical emission spectroscopy can provide valuable information of the source plasma. Without more complex models and a calibration for the density no absolute measurements can be obtained. To relate the excitation temperature to the electron temperature a collisional-radiative model is needed. However both the excitation temperatures as well as the electron temperature are independent of the RF power. This indicates that the energy is spent on ionising rather than heating the plasma. The fact that both the ion-neutral ratio as well as the total blue emission and the LP plasma density increase are compliant with this.

The total blue emission and the Langmuir probe plasma density show the same trend which in-

λ [nm]	A_{ik} [s^{-1}]	E_k [cm^{-1}]	g_k
415.8590	$1.40 \cdot 10^6$	$1.1718 \cdot 10^5$	5
657.2834	$1.93 \cdot 10^6$	$1.1891 \cdot 10^5$	5
687.1289	$2.78 \cdot 10^6$	$1.1865 \cdot 10^5$	3
696.5431	$6.39 \cdot 10^6$	$1.0750 \cdot 10^5$	3
703.0251	$2.67 \cdot 10^6$	$1.1968 \cdot 10^5$	5
706.7218	$3.80 \cdot 10^6$	$1.0729 \cdot 10^5$	5
714.7042	$6.25 \cdot 10^5$	$1.0713 \cdot 10^5$	3
727.2936	$1.83 \cdot 10^6$	$1.0750 \cdot 10^5$	3
738.3980	$8.47 \cdot 10^6$	$1.0729 \cdot 10^5$	5
763.5106	$2.45 \cdot 10^7$	$1.0624 \cdot 10^5$	5
794.8176	$1.86 \cdot 10^7$	$1.0713 \cdot 10^5$	3
826.4522	$1.53 \cdot 10^7$	$1.0750 \cdot 10^5$	3
852.1442	$1.39 \cdot 10^7$	$1.0713 \cdot 10^5$	3
860.5776	$1.04 \cdot 10^6$	$1.1891 \cdot 10^5$	5
866.7944	$2.43 \cdot 10^6$	$1.0609 \cdot 10^5$	3
912.2967	$1.89 \cdot 10^7$	$1.0410 \cdot 10^5$	3
922.4499	$5.03 \cdot 10^6$	$1.0624 \cdot 10^5$	5
965.7786	$5.43 \cdot 10^6$	$1.0410 \cdot 10^5$	3

(a) Ar-I lines.

λ [nm]	A_{ik} [s^{-1}]	E_k [cm^{-1}]	g_k
426.6527	$1.64 \cdot 10^6$	$1.5767 \cdot 10^5$	6
460.9567	$7.89 \cdot 10^7$	$1.7053 \cdot 10^5$	8
476.4864	$6.60 \cdot 10^7$	$1.6024 \cdot 10^5$	4
480.6020	$7.80 \cdot 10^7$	$1.5504 \cdot 10^5$	6
487.9863	$8.23 \cdot 10^6$	$1.5873 \cdot 10^5$	6
493.3209	$1.44 \cdot 10^6$	$1.5535 \cdot 10^5$	4
501.1626	$2.07 \cdot 10^6$	$1.7040 \cdot 10^5$	6
514.5308	$1.06 \cdot 10^6$	$1.5767 \cdot 10^5$	6

(b) Ar-II lines.

Table A.1: Transition line data used for the Boltzmann plots. [35]

dicates that the total blue emission is an indicator of the (relative increase of the) plasma density. However this is only valid because the excitation temperatures are constant. Since the line emission is $\propto \exp(1/T_{ex})$, it is sensitive to the excitation temperature and any changes in T_{ex} would strongly influence the total line emission.

There is furthermore are disagreement between the trends of ion-neutral ratio and the total blue-emission. The former increases almost 3 orders of magnitude while latter increases little under one order of magnitude. The neutral density at the throat assuming room temperature and 50 sccm mass flow is about 10^{20} m^{-3}. Using this to estimate the plasma density from the ion-neutral ratio this yields about $5 \cdot 10^{15}$ m^{-3} at 350 W. This differs from the $7 \cdot 10^{16}$ of the LP measurement, but the latter is an overestimation. Calculating the density using ABR theory and taking the geometric mean will improve the agreement. However doing the same estimate at 200 W would yield a plasma density of $2 \cdot 10^{12}$ m^{-3} which is in no way compatible with the plasma density measurements. One explanation for this is that the assumption of thermal equilibrium is not valid. For the excited states the Boltzmann plot showed a straight line indicating thermal equilibrium, however there is no guarantee that this is valid all the way down to the ground state. The ion neutral density also shows an abrupt increase at 388 W. This could indicate a mode jump. However no conclusion can be based on a single measurement point especially since the there is no information past 388 W. Lastly it has to be noted that these measurements have been taken in a configuration where the antenna was behind the back coil and the line of sight (LOS) was close to the antenna. The thermal equilibrium of the plasma is very different in the part of the plasma strongly affected by the RF radiation then closer to the exit plane. These measurements should be repeated at different positions, i.e. close to the antenna, near the thruster exit plane and if luminous enough in the near-plume. The power scan should be extended to the full range of 100-1000 W. Furthermore the investigation should include the influence of other parameters such as the mass flow rate and magnetic field strength.

Summary

In this chapter the application of optical emission spectroscopy to the HPT05 prototype was discussed. OES can be used to measure the excitation temperature of the neutral and ion species in the plasma source by using a Boltzmann plot. Tracking the ratios of line emission an Ar-II and an Ar-I line are indicative of the ion-neutral ratio. The total intensity in the blue range (380-530 nm) is proportional to

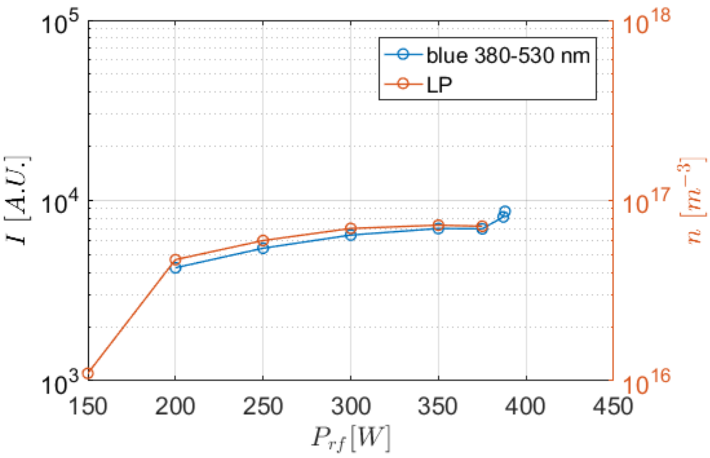

Figure A.10: Total line emission between 380-530 nm as a function of RF power vs. Langmuir probe plasma density.

the plasma density (for constant excitation temperatures). The excitation temperature of Ar and Ar^+ were found to be constant over a range of RF powers (150-400 W) and were 0.5 and 1 eV respectively. This agreed with the electron temperature measurements of the Langmuir probe which were constant over the same range at 2.3±0.1 eV. Ion-neutral ratios where found to gradually increase about 2.5 orders of magnitude and showed an abrupt increase at 388 W, which could indicate a mode jump. For constant excitation temperature the total blue emission is proportional to the density. The total emission increased half an order of magnitude between 200-375 W and agreed very well with concurrent Langmuir probe measurements differing a constant factor of 10^{13}. Repeating the measurements over a larger range of RF powers (up to 1 kW) should provide more insight.

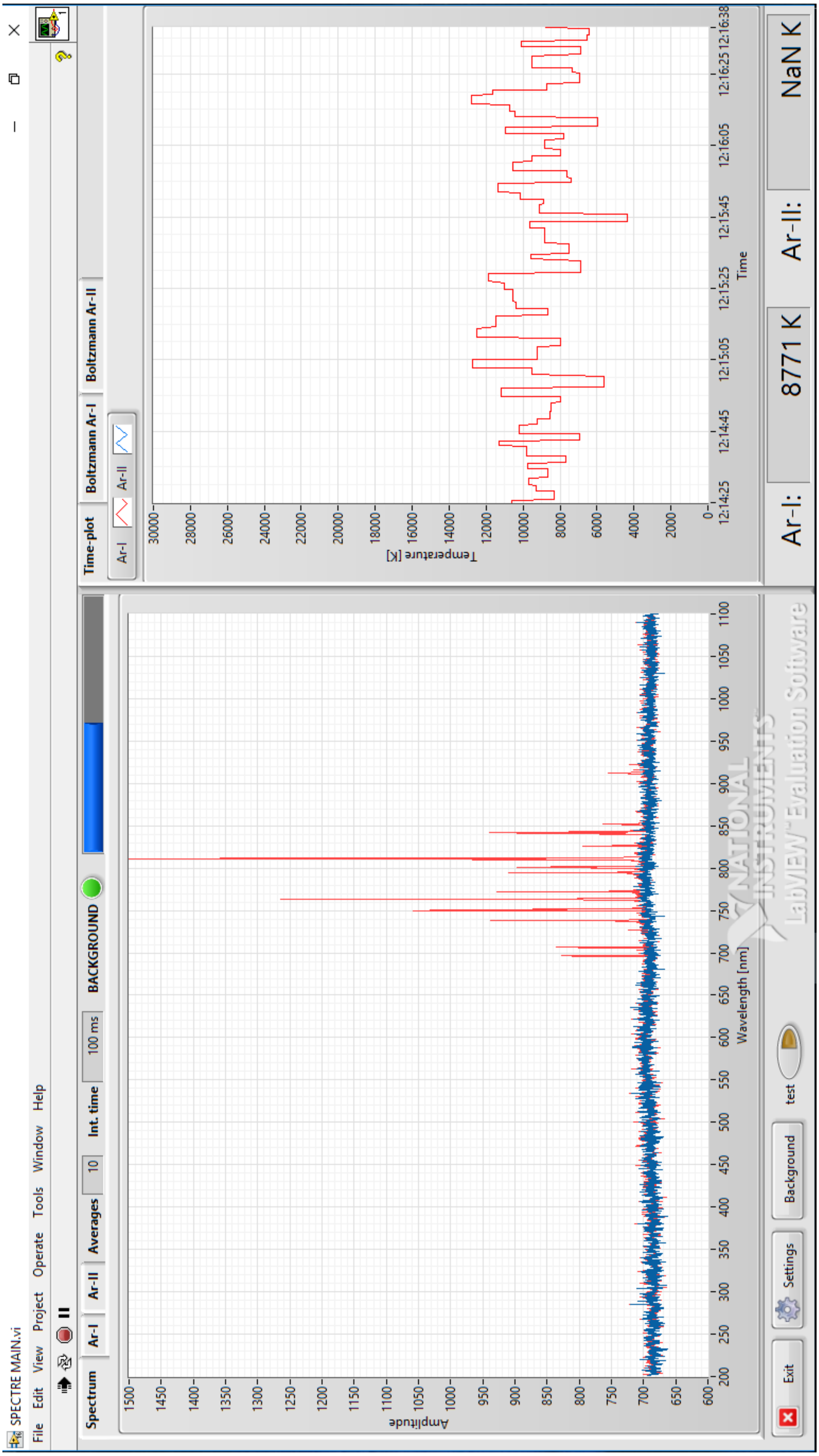

Averages 10

Int. time 100 ms

Ar-I: 8771 K

Ar-II: NaN K

Figure A.11: Screen shot of UI of real-time Boltzmann plot software.

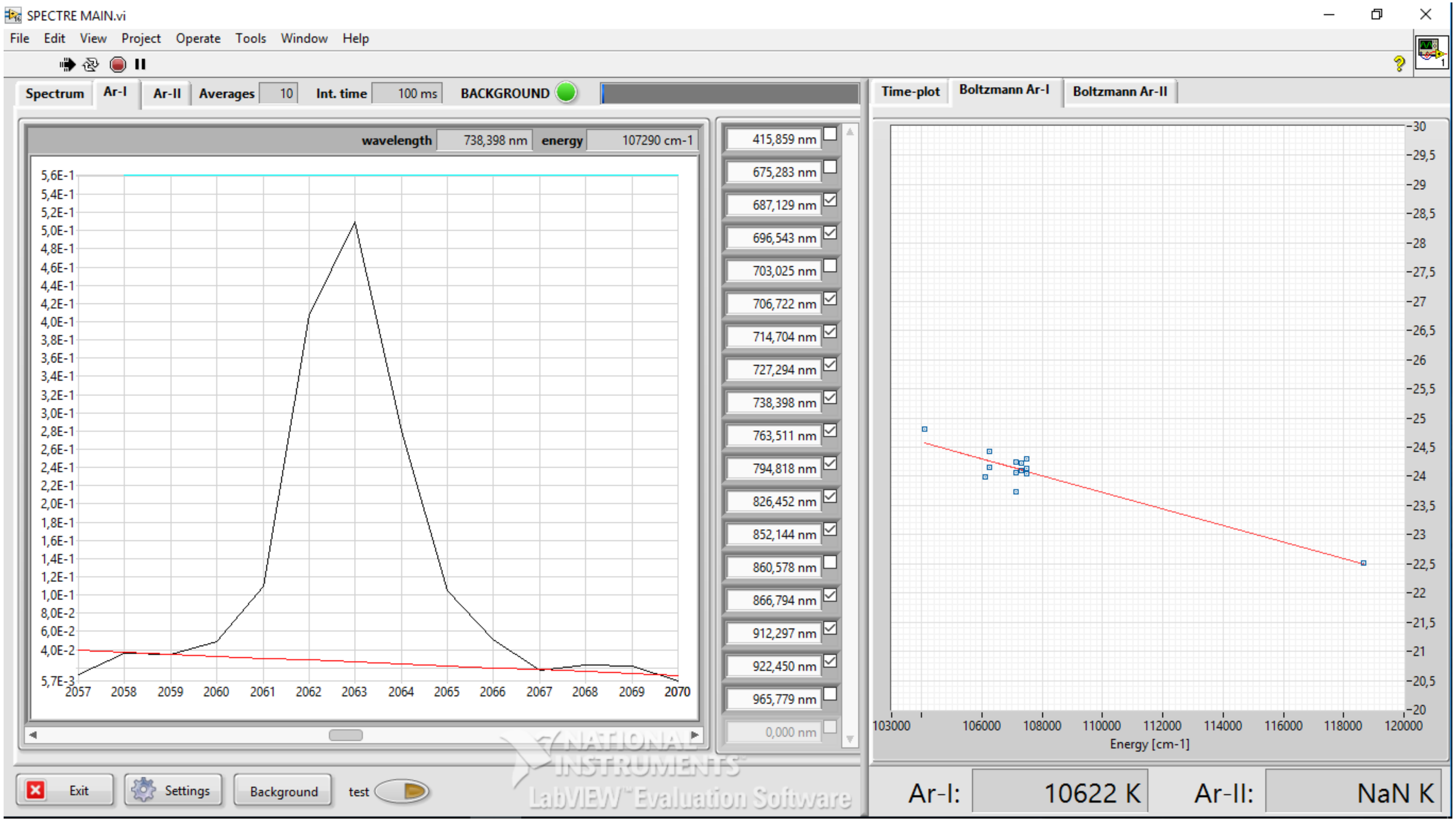

Averages 10

Int. time 100 ms

wavelength 738,398 nm

energy 107290 cm-1

415,859 nm ☐
675,283 nm ☐
687,129 nm ☑
696,543 nm ☑
703,025 nm ☐
706,722 nm ☑
714,704 nm ☑
727,294 nm ☑
738,398 nm ☑
763,511 nm ☑
794,818 nm ☑
826,452 nm ☑
852,144 nm ☑
860,578 nm ☐
866,794 nm ☑
912,297 nm ☑
922,450 nm ☑
965,779 nm ☐
0,000 nm ☐

Ar-I: 10622 K

Ar-II: NaN K

Figure A.12: Screen shot of UI of real-time Boltzmann plot software.

B

Database

This appendix contains a list of all the raw data files used in this report. All raw data files are included digitally. The files are sorted by probe, data, RF power, dimension and axial position or objective where relevant.

EP	14/03/2017	500 W	axial
FP_20170314_120244			
FP_20170314_120906			

EP	14/03/2017	500 W	radial	z80
FP_20170314_120408				
FP_20170314_120613				

FP	16/12/2016	power	radial
FP_20161216_172324			
FP_20161216_172644			
FP_20161216_173104			
FP_20161216_173607			
FP_20161216_173925			
FP_20161216_174252			

FP	30/01/2017	500 W	radial
FP_20170130_123407_Z120			
FP_20170130_123906_Z160			
FP_20170130_131621_Z200			

FP	31/01/2017	650 W	radial	MN
FP_20170131_165057_MNoff_120				
FP_20170131_170129_MNon_120				

FP	14/03/2017	500 W	axial
FP_20170314_113322			

LP	19/01/2017	300 W	stability
LP_20170119_162229			
LP_20170119_162303			
LP_20170119_162335			
LP_20170119_162415			
LP_20170119_162447			
LP_20170119_162524			
LP_20170119_162556			
LP_20170119_162651			
LP_20170119_162727			

LP	30/01/2017	500 W	axial
LP_20170130_111639			
LP_20170130_111718			
LP_20170130_111756			
LP_20170130_111832			
LP_20170130_111907			
LP_20170130_111938			
LP_20170130_112008			
LP_20170130_112037			
LP_20170130_112105			
LP_20170130_112133			

LP	30/01/2017	500 W	radial	z40
LP_20170130_114953				
LP_20170130_115032				
LP_20170130_115111				
LP_20170130_115150				
LP_20170130_115228				
LP_20170130_115306				
LP_20170130_115344				
LP_20170130_115417				
LP_20170130_115448				
LP_20170130_115518				
LP_20170130_115549				
LP_20170130_115619				
LP_20170130_115649				
LP_20170130_115719				
LP_20170130_115751				
LP_20170130_115826				
LP_20170130_115904				
LP_20170130_115943				

LP_20170130_120021
LP_20170130_120059
LP_20170130_120138

LP 30/01/2017 500 W radial z80

LP_20170130_120539
LP_20170130_120618
LP_20170130_120656
LP_20170130_120735
LP_20170130_120812
LP_20170130_120843
LP_20170130_120914
LP_20170130_120947
LP_20170130_121019
LP_20170130_121053
LP_20170130_121132
LP_20170130_121210
LP_20170130_121250
LP_20170130_121329

LP 30/01/2017 500 W radial z120

LP_20170130_122126
LP_20170130_122205
LP_20170130_122244
LP_20170130_122319
LP_20170130_122354
LP_20170130_122430
LP_20170130_122506
LP_20170130_122545
LP_20170130_122624

LP 30/01/2017 500 W radial z160

LP_20170130_124651
LP_20170130_124730
LP_20170130_124809
LP_20170130_124848
LP_20170130_124927
LP_20170130_125006
LP_20170130_125046
LP_20170130_125125
LP_20170130_125204

LP 30/01/2017 500 W radial z200

LP_20170130_130228
LP_20170130_130307
LP_20170130_130346
LP_20170130_130425
LP_20170130_130504
LP_20170130_130543
LP_20170130_130622
LP_20170130_130701
LP_20170130_130741
LP_20170130_130821
LP_20170130_130900

LP 30/01/2017 650 W axial

LP_20170130_204328
LP_20170130_204408
LP_20170130_204447
LP_20170130_204525
LP_20170130_204603
LP_20170130_204637
LP_20170130_204710
LP_20170130_204741
LP_20170130_204812
LP_20170130_204843

LP 30/01/2017 650 W radial z40

LP_20170130_200101
LP_20170130_200140
LP_20170130_200220
LP_20170130_200259
LP_20170130_200337
LP_20170130_200416
LP_20170130_200456
LP_20170130_200528
LP_20170130_200600
LP_20170130_200630
LP_20170130_200700
LP_20170130_200731
LP_20170130_200801
LP_20170130_200832
LP_20170130_200904
LP_20170130_200939
LP_20170130_201018
LP_20170130_201057
LP_20170130_201135
LP_20170130_201214
LP_20170130_201253

LP 31/01/2017 800 W axial

LP_20170131_113051
LP_20170131_113130
LP_20170131_113208
LP_20170131_113244
LP_20170131_113318
LP_20170131_113351
LP_20170131_113423
LP_20170131_113453
LP_20170131_113524
LP_20170131_113554

LP 31/01/2017 800 W radial z40

LP_20170131_115915
LP_20170131_115954
LP_20170131_120033
LP_20170131_120112
LP_20170131_120151
LP_20170131_120225
LP_20170131_120256
LP_20170131_120326
LP_20170131_120356
LP_20170131_120426
LP_20170131_120456
LP_20170131_120526
LP_20170131_120556
LP_20170131_120627
LP_20170131_120703
LP_20170131_120743
LP_20170131_120822

LP 14/03/2017 500 W axial

LP_20170314_113650
LP_20170314_113729
LP_20170314_113808
LP_20170314_113846
LP_20170314_113925
LP_20170314_114004
LP_20170314_114043
LP_20170314_114121
LP_20170314_114200
LP_20170314_114239
LP_20170314_114317

LP_20170314_114354			
LP_20170314_114431			
LP_20170314_114507			
LP_20170314_114542			
LP_20170314_114615			
RFCLP	30/01/2017	500 W	axial
RF_20170130_112646			
RF_20170130_112726			
RF_20170130_112805			
RF_20170130_112844			
RF_20170130_112924			
RF_20170130_113003			
RF_20170130_113040			
RF_20170130_113116			
RF_20170130_113150			
RF_20170130_113222			
RFCLP	30/01/2017	650 W	axial
RF_20170130_203244			
RF_20170130_203324			
RF_20170130_203404			
RF_20170130_203444			
RF_20170130_203523			
RF_20170130_203600			
RF_20170130_203635			
RF_20170130_203709			
RF_20170130_203742			
RF_20170130_203814			
RFCLP	31/01/2017	800 W	axial
RF_20170131_113704			
RF_20170131_113744			
RF_20170131_113823			
RF_20170131_113903			
RF_20170131_113940			
RF_20170131_114013			
RF_20170131_114046			
RF_20170131_114116			
RF_20170131_114147			
RF_20170131_114218			

C

Example Data Files

`LP_20161216_130637.txt`

```
Date: 16/12/2016        Time: 13:06:37
Power [W]: 750.0        Coil 1 [A]: X.X        Coil 2 [A]: X.X        Coil MN [A]: X.X
Z [mm]: 300.0        X [mm]: 0.0        Y [mm]: 0.0
voltage [V]        current [A]
-0100.000       -00052.12E-06
-0099.500       -00052.36E-06
-0099.000       -00052.14E-06
-0098.500       -00051.48E-06
-0098.000       -00051.65E-06
-0097.500       -00051.44E-06
-0097.000       -00051.08E-06
-0096.500       -00051.25E-06
-0096.000       -00050.51E-06
-0095.500       -00050.56E-06
-0095.000       -00050.12E-06
 ........        ............
```

`FP_20161216_165556.txt`

```
Date: 16/12/2016        Time: 16:55:56
Power [W]: 500.0        Coil 1 [A]: X.X        Coil 2 [A]: X.X        Coil MN [A]: X.X

Z [mm]        X [mm]        Y [mm]        T [C]        J [A/m2]        JErr [A/m2]
 175.0        -300.0           0.0         46.5          2.31E-2          2.11E-2
 175.0        -290.0           0.0         46.4          2.39E-2          1.81E-2
 175.0        -280.0           0.0         46.1          1.17E-2          1.74E-2
 175.0        -270.0           0.0         46.1          1.99E-2          2.66E-2
 175.0        -260.0           0.0         46.5          3.74E-2          2.07E-2
 175.0        -250.0           0.0         46.3          2.72E-2          1.70E-2
 175.0        -240.0           0.0         46.7          5.12E-2          1.76E-2
 175.0        -230.0           0.0         46.3          4.88E-2          2.60E-2
 175.0        -220.0           0.0         46.0          4.27E-2          2.03E-2
 175.0        -210.0           0.0         46.0          5.53E-2          1.91E-2
 175.0        -200.0           0.0         46.0          7.03E-2          2.39E-2
 .....          ....           ...         ....   .......          .......
```

EP_20160314_120244.txt

```
Date: 3/14/2017        Time: 12:02:44 PM
Power [W]: 500.0 Coil 1 [A]: X.X Coil 2 [A]: X.X Coil MN [A]: X.X

Z [mm]        X [mm]        Y [mm]        V [V]
 200.0           0.0           0.0         2.48E+1
 195.0           0.0           0.0         2.49E+1
 190.0           0.0           0.0         2.51E+1
 185.0           0.0           0.0         2.52E+1
 180.0           0.0           0.0         2.53E+1
 175.0           0.0           0.0         2.56E+1
 170.0           0.0           0.0         2.57E+1
 165.0           0.0           0.0         2.59E+1
 160.0           0.0           0.0         2.62E+1
 155.0           0.0           0.0         2.65E+1
 150.0           0.0           0.0         2.68E+1
 145.0           0.0           0.0         2.71E+1
 .....           ...     ...   ......
```

D

Addenda

D.1. Electronic Addenda

For the post processing of the data used in this report several MATLAB files where developed. Furthermore the EXCEL sheets developed by Chen have been modified. Table D.1 presents a list of all the digital files that accompany this thesis.

Table D.1: List of electronic files include in this report.

filename	description
MainBRL.m	Main file for applying BRL theory to LP data.
iCurrBRL.m	Function of MainBRL.m, calculates theoretical ion current (eq. 4.21-4.25, 4.27).
iErrorBRL.m	Function of MainBRL.m calculates ion error (eq. 4.28).
eErrorBRL.m	Function of MainBRL.m calculates electron error (eq. 4.29).
TerrBRL.m	Function of MainBRL.m calculates total error.
ImportFile.m	Function of MainBRL.m, MainABR.m and MainBohm.m, imports data from raw data files of LP.
MainABR.m	Main file for applying ABR theory to LP data.
iCurrABR.m	Function of MainABR.m, calculates theoretical ion current (equations 4.33-4.36).
iErrorABR.m	Function of MainABR.m calculates ion error (eq. 4.28).
eErrorABR.m	Function of MainABR.m calculates electron error (eq. 4.29).
TerrABR.m	Function of MainABR.m calculates total error.
MainBohm.m	Main file for applying the planar approximation to LP data.
FP.m	Main file for inferring divergence angles and total current from radial FP profiles.
FPimport.m	Function of FP.m, imports FP data from raw data files.
divangle.m	Function of FP.m, calculates 95% half-angle.
BRL_2017.xlsm	Excel sheet to apply BRL theory to LP data.
ABR_2017.xlsm	Excel sheet to apply ABR theory to LP data.

D.2. Publications

This thesis project is part of a larger research project on magnetic nozzles and helicon thrusters. The experiments that form the core of this report have been conducted in collaboration with dr. Jaume Navarro-Cavallé. The work on spectroscopy (appendix A), in particular the development of the real-time Boltzmann plot software were a collaboration with dr. Yacine Babou. Both topics will be presented on the International Electric Propulsion Conference of October 2017 in Atlanta, Georgia. The approved abstracts for these conference papers are included below.

Experimental performances of a 1 kW HPT by means of plasma diagnosis

Jaume Navarro Cavallé[1*], Mick Wijnen[1], Pablo Fajardo[1], Mario Merino[1], Eduardo Ahedo[1],
[1]*Equipo de Propulsión Espacial y Plasmas (EP2), Universidad Carlos III de Madrid, Spain;*
Víctor Gómez[2], Álvaro Giménez[2], Víctor Sánchez[2], and Mercedes Ruiz[2]
[2]*SENER Ingeniería y Sistemas, Spain;*
Corresponding author: jaume.navarro@uc3m.es

Keyword : Helicon Plasma Thruster, thruster experimental performances

A Helicon Plasma Thruster prototype [1], HTP05 hereafter, rated from 0.5 to 1 kW, had been designed and built by SENER and EP2-UC3M in 2015. The first test campaign (ignition test) was carried out successfully on October 2015 at the Electric Propulsion Lab facilities at ESTEC, ESA. The current work is devoted to explore and assess the thruster performances by means of plasma diagnosis. All results presented here have been obtained during the Winter 2016/17 test campaign performed at the recently inaugurated UC3M-EP2 facilities in Madrid, Spain.

The UC3M-EP2 LAB main vacuum chamber consists of a 3.5 m long and 1.5 m diameter stainless steel vessel, with three cryopanels and two turbomoleculars pumps with a total pumping speed about 37,000 l/s.This allows performing tests at 1.5 mg/s of Argon keeping a background pressures below $2.6 \cdot 10^{-5}$mbar. The employed intrusive plasma diagnostics include: a Langmuir probe (LP), a radio frequency compensated LP (RFCLP), a Faraday probe and an emissive probe. These probes are mounted on a 3 DoF positioning system that allows scans of the whole plume, 0-1500 mm downstream from the thruster exit, and -400 mm to 400 mm on both transversal and vertical direction. Also, a Semion MultiSensor RPA is also available at a fixed position.

With the intrusive diagnostics, plasma density, plasma potential, electron temperature, the electron energy distribution function, the ion energy distribution function, plume divergence (Example in Fig 1a), and the total ion beam current (Example in Fig 2) are measured at different positions in the magnetized plume of the HPT05. All these plasma properties are obtained for several magnetic topologies and magnetic intensities, RF power levels, and mass flow rates. The main objective is to identify these parameters that optimize the HPT05 thrust capabilities. Different plasma operational modes,(inductive, helicon mode, etc.) are identified and the mode variation conditions are assessed as well. Experimental results could be compared with those obtained from analytical and numerical models for the Helicon Plasma Thruster [2] and Magnetic Nozzle [3] developed by EP2 during last years.

Finally, some optical diagnostics, such as optical spectroscopy and high-speed imaging, are also implemented, mainly for assessing the plasma properties at the plasma production region (within the helicon source).

References

1) Navarro-Cavallé, J; Merino, M. et al. “Maiden tests of the HPT05 Helicon Plasma Thruster Prototype” Space propulsion 2016, ROME, ITALY / 2–6 MAY 2016, SP2016 3125014.
2) Ahedo, Eduardo, and Navarro-Cavallé, Jaume. "Helicon thruster plasma modeling: Two-dimensional fluid-dynamics and propulsive performances."*Physics of Plasmas” (1994-present)* 20.4 (2013): 043512.

3) Ahedo, E., and M. Merino. "Two-dimensional supersonic plasma acceleration in a magnetic nozzle."*Physics of Plasmas" (1994-present)*17.7 (2010): 073501.

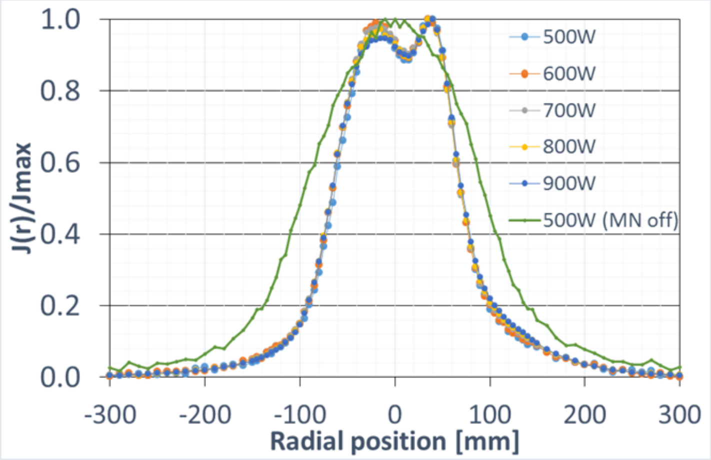

Figure 1. Normalized ion flux on a transversal plane at z = 200mm from the HPT exhaust section, for several levels of RF transmitted power. Each curve is normalized with its maximum measured flux. This proves that plume divergence does not depend on the RF power coupled to the plasma, but on the magnetic field strength at the MN stage (green case is obtained with the MN coil turned off).

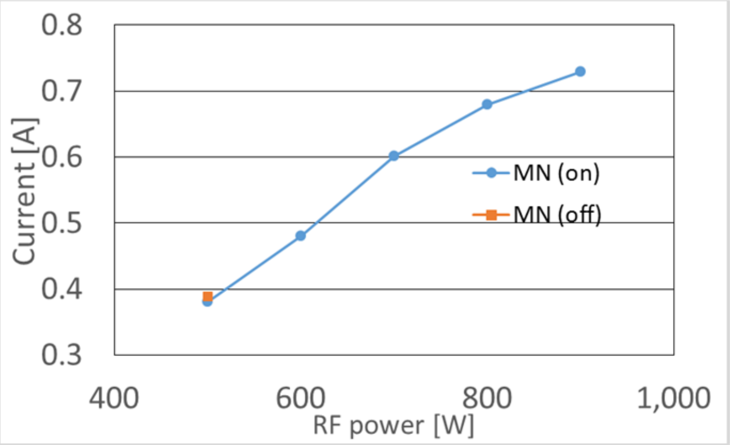

Figure 2. Ion beam total current (measured at z = 200 mm from the HPT exhaust section) as function of the RF transmitted power. The total current with or without MN is similar, so it means that the amount of plasma produced upstream within the source is practically the same, and it does not depend on the MN field strength.

Optical Emission Spectroscopy diagnosis of helicon plasma thruster operating with argon

Yacine Babou, Mick Wijnen, Jaume Navarro-Cavallé, Eduardo Ahedo

Equipo de Propulsión Espacial y Plasmas, Departamento de Bioingeniería Ingeniera Aeroespacial, Universidad Carlos III de Madrid, 28911, Madrid, Spain

Corresponding author : ybabou@ing.uc3m.es

Key words : Helicon Plasma Thurster, Argon plasma jet, Optical Emisison Spectroscopy, non-equilibrium plasma.

Electric propulsion systems based on helicon radio-frequency plasma source, is a promising step in the technological evolution of electric propulsion (electrode-less, high ionization levels, ...). However such system requires so far substantial improvement and optimization that rely on dedicated experimental investigations undertaken on ground facilities. Numerous diagnostic methods can be adopted to measure physical quantities relevant to characterize Helicon Plasma Thruster (HPT) performances including, the plasma production, its confinement and acceleration.

As a rule, particle density, energy distribution and flux are obtained in a standard manner by means of probes (electrostatic/Langmuir, etc). Although well-suited for the plume region, such intrusive diagnostics is less applicable to internal part of a thruster, where any probe would perturbate irremediably the plasma production and transport processes. Optical diagnostics, because non-intrusive, overcome the inherent drawbacks of probes (and intrusive diagnostics) therefore they stand a valuable alternative for plasma characterization. Nowadays, Optical Emission Spectroscopy (OES) technique is commonly applied to probe the excited states density and rebuild plasma excitation temperature almost effortlessly, at the conditional of an adequate optical access. In this frame, ion density and electron temperature can be fairly estimated, by means of appropriate processing of the measured radiative signature.

The present work addresses the characterization by means of OES of the plasma produced by the HPT developed jointly by SENER and UC3M (a detailed description of the system is published elsewhere [1]). This contribution will document the experimental investigations for HPT working with argon in various operating conditions (e.g. applied power) and configurations (e.g. magnetic topology). The reported investigations are intended to identify the correlations between the plasma radiative signature and plasma parameters (namely ne and Te) depending on the operating conditions.

The experimental setup (**Fig. 1**) includes a series of optical probes arranged to perform axial characterization of the plasma throughout the different stages of the thruster, including the rear region close to the injection plate, the region of plasma production, the magnetic throat region and the far plume region up to light extinction. The plasma light is recorded with a spectrometer

OceanOptics USB4000 with a spectral resolution of about 1.0 nm FWHM, optimized for detection in UV and visible spectral ranges. In complement to radiative signature characterization, high-speed imaging measurements in a multi-directional view fashion will be also performed in order to assess the plasma intensity distribution and possible fluctuation or instable dynamics in the 10 kHz range.

Starting from measured spectral intensities of Ar and when available Ar+, the excitation temperature of the plasma is determined by means of the Boltzmann plot method (**Fig. 2**). In addition, the density of metastable and resonant states will be evaluated by means of a new approach, independent of the involved excitation processes, hence bypassing the substantial lack of excitation cross-section, that affects the reliability of traditional Collisional-Radiative model. In this frame, the ion to neutral ratio densities are estimated for the comprehensive set of investigated experimental conditions.

The relation between the investigated experimental conditions and the excited levels distribution is analyzed and the inferred plasma parameters are discussed, by considering also probe measurements carried out besides, to draw lines of improvements in the assessment of HPT performances starting from radiative signature analysis.

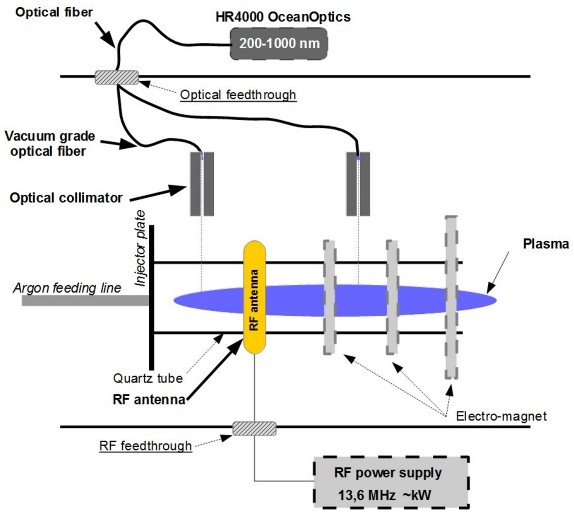

Figure 1: Skectch of experimental setup.

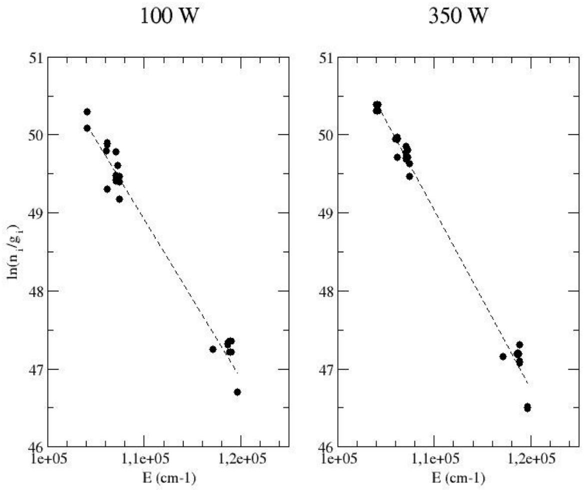

Figure 2: Typical Boltzmann plot (Argon lines)

[1] Navarro-Cavallé, J; Merino, M. et al. “Maiden tests of the HPT05 Helicon Plasma Thruster Prototype” Space propulsion 2016, ROME, ITALY / 2–6 MAY 2016, SP2016 3125014.

References

[1] E. Ahedo and M. Merino. Two-dimensional supersonic plasma acceleration in a magnetic nozzle. *Physics of Plasmas*, 17(07), July 2010. doi: 10.1063/1.3442736.

[2] Eduardo Ahedo. Double-layer formation and propulsive assessment for a three-species plasma expanding in a magnetic nozzle. *Physics of Plasmas*, 18(3):033510, 2011. doi: http://dx.doi.org/10.1063/1.3567159. URL `http://scitation.aip.org/content/aip/journal/pop/18/3/10.1063/1.3567159`.

[3] Eduardo Ahedo and Jaume Navarro-Cavallé. Helicon thruster plasma modeling: Two-dimensional fluid-dynamics and propulsive performances. *Physics of Plasmas (1994-present)*, 20(4):043512, 2013.

[4] JE Allen, RLF Boyd, and P Reynolds. The collection of positive ions by a probe immersed in a plasma. *Proceedings of the Physical Society. Section B*, 70(3):297, 1957.

[5] S.A. Andersen, V.O. Jensen, P. Nielsen, and N. D'Angelo. Continuous supersonic plasma wind tunnel. *The Physics of Fluids*, 12(3), March 1969.

[6] Yasser Azziz. *Experimental and Theoretical Characterization of a Hall Thruster Plume*. PhD thesis, Massachusetts Institute of Technology, June 2007.

[7] Oleg. V Batishchev. Mini-helicon plasma thruster characterization. In *44th AIAA Joint Propulsion Conference & Exhibit*, 2008.

[8] Brian E Beal, Alec D Gallimore, James M Haas, and William A Hargus. Plasma properties in the plume of a hall thruster cluster. *Journal of Propulsion and Power*, 20(6):985–991, 2004.

[9] Edgar A. Bering, Benjamin W. Longmier, Chris S. Olsen, Jared P. Squire, and Franklin R. Chang Díaz. Performance studies of the VASIMR® VX-200. In *49th AIAA Aerospace Sciences Meeting*, 2011. doi: 10.2514/6.2011-1071.

[10] A. Boschi and F. Magistrelli. Effect of a r.f, signal on the characteristic of a langmuir probe. *Il Nuovo Cimento (1955-1965)*, 29(2):487–499, 1963. ISSN 1827-6121. doi: 10.1007/BF02750367. URL `http://dx.doi.org/10.1007/BF02750367`.

[11] Rod W Boswell, Kazunori Takahashi, Christine Charles, and Igor D Kaganovich. Non-local electron energy probability function in a plasma expanding along a magnetic nozzle. *Frontiers in Physics*, 3:14, 2015.

[12] Roderick Boswell and Christine Charles. Plasma beam generator, 2004.

[13] Daniel L Brown and Alec D Gallimore. Evaluation of ion collection area in faraday probes. *Review of Scientific Instruments*, 81(6):063504, 2010.

[14] Daniel L Brown, Mitchell LR Walker, James Szabo, Wensheng Huang, and John E Foster. Recommended practice for use of faraday probes in electric propulsion testing. *Journal of Propulsion and Power*, 2016.

[15] Murat Celik. Spectral measurements of inductively coupled and helicon discharge modes of a laboratory argon plasma source. *Spectrochimica Acta Part B: Atomic Spectroscopy*, 66(2):149–155, 2011.

[16] Murat Alp Çelik. *Experimental and computational studies of electric thruster plasma radiation emission*. PhD thesis, Massachusetts Institute of Technology, 2007.

[17] C. Charles and R. Boswell. Current-free double-layer formation in a high-density helicon discharge. *Applied Physics Letters*, 82(9), March 2003.

[18] C. Charles, R. W. Boswell, P. Alexand, C. Costa, and O. Sutherland. Helicon double layer thrusters. In *42nd AIAA Joint Propulsion Conference & Exhibit*, 2006.

[19] Christine Charles. High density conics in a magnetically expanding helicon plasma. *Applied Physics Letters*, 96(5):051502, 2010.

[20] F. F. Chen. Langmuir probe analysis for high density plasmas. *Physiscs of Plasmas*, 8(6), June 2001. doi: 10.1063/1.1368874.

[21] Francis F Chen. Numerical computations for ion probe characteristics in a collisionless plasma. *Journal of Nuclear Energy. Part C, Plasma Physics, Accelerators, Thermonuclear Research*, 7(1): 47, 1965.

[22] Francis F. Chen. Plasma ionization by helicon waves. *Plasma Physics and Controlled Fusion*, 33 (4):339–364, 1991.

[23] Francis F Chen. Abr probe analysis program - excel, 2000. URL `http://www.seas.ucla.edu/ltptl/Programs/esp_abr.xls`.

[24] Francis F Chen. Brl probe analysis program - excel, 2000. URL `http://www.seas.ucla.edu/ltptl/Programs/esp_brl.xls`.

[25] Francis F Chen. Langmuir probes in rf plasma: surprising validity of oml theory. *Plasma Sources Science and Technology*, 18(3):035012, 2009.

[26] Francis F Chen, John D Evans, and Donald Arnush. A floating potential method for measuring ion density. *Physics of Plasmas*, 9(4):1449–1455, 2002.

[27] Francis F Chen, John D Evans, and Wade Zawalski. Calibration of langmuir probes against microwaves and plasma oscillation probes. *Plasma Sources Science and Technology*, 21(5):055002, 2012.

[28] Kyeong-Koo Chi, T E Sheridan, and R W Boswell. Resonant cavity modes of a bounded helicon discharge. *Plasma Sources Science and Technology*, 8(3):421, 1999. doi: 10.1088/0963-0252/8/3/312/.

[29] Aiki Chiba, Kazunori Takahashi, Atsushi Komuro, and Akira Ando. Characterization of helicon plasma thruster performance operated for various rare gas propellants. *Journal of Propulsion and Power*, 31(3):962–965, June 2015. doi: 10.2514/1.B35609.

[30] Kyu-Sun Chung. Mach probes. *Plasma Sources Science and Technology*, 21(6):063001, 2012.

[31] Richard Courant and David Hilbert. *Methods of mathematical physics*, volume 1. CUP Archive, 1965.

[32] Daniel G. Courtney, Simon Dandavino, and Herbert Shea. Performance and applications of ionic electrospray micro-propulsion prototypes. In *AIAA Space 2015 conference and exposition*, 2015.

[33] Christopher A. Deline, Roger D. Bengtson, Boris N. Breizman, Mikhail R. Tushentsov, Jonathan E. Jones, D. Greg Chavers, Chris C. Dobson, and Branwen M. Schuettpelz. Plume detachment from a magnetic nozzle. *Physics of Plasmas*, 16(3):033502, 2009. doi: 10.1063/1.3080206.

[34] Robert Eckman, Lawrence Byrne, Nikolaos A Gatsonis, and Eric J Pencil. Triple langmuir probe measurements in the plume of a pulsed plasma thruster. *Journal of Propulsion and Power*, 17(4): 762–771, 2001.

[35] Alexander Kramida et al. Atomic spectra database, September 2016. URL `https://www.nist.gov/pml/atomic-spectra-database`.

[36] Francis. Helicon ddischarge and sources: a review. *Plasma Sources Science and Technology*, 24(1), January 2015. doi: `10.1088/0963-0252/24/1/014001`.

[37] A. Fruchtman. Electric field in a double layer and the imparted momentum. *Phys. Rev. Lett.*, 96: 065002, Feb 2006. doi: `10.1103/PhysRevLett.96.065002`. URL `http://link.aps.org/doi/10.1103/PhysRevLett.96.065002`.

[38] H Fujita, S Nowak, BA Hoegger, and H Schneider. Potential measurements by an emissive probe in a magnetized plasma. *Physics Letters A*, 78(3):263–265, 1980.

[39] BE Gilchrist, SG Ohler, and AD Gallimore. Flexible microwave system to measure the electron number density and quantify the communications impact of electric thruster plasma plumes. *Review of scientific instruments*, 68(2):1189–1194, 1997.

[40] Dan M. Goebel and Ira Katz. *Fundamentals of Electric Propulsion: Ion and Hall Thrusters*. JPL space science and technology series. Jet Propulsion Laboratory, California Institute of Technology, 2008.

[41] WE Harbaugh. Tungsten, thoriated-tungsten, and thoria emitters. *Electron Tube Design*, pages 90–98, 1962.

[42] Masaaki Inutake, Akira Ando, Kunihiko Hattori, Hiroyuki Tabari, and Tsuyoshi Yagai. Characteristics of a supersonic plasma flow in a magnetic nozzle. *Journal of Plasma and Fusion Research*, 78(10), October 2002.

[43] HA Jones. A temperature scale for tungsten. *Physical review*, 28(1):202, 1926.

[44] 6517B-901-01 Rev. B / June 2009. *Model 6517B Reference Manual*. Keithley Instruments Inc., b edition, June 2009.

[45] David Krejci and Paulo Lozano. Scalable ionic liquid electrospray thrusters for nanosatellites. In *39th Annual AAS GNC Conference*, 2016.

[46] James G Laframboise. *Theory of spherical and cylindrical Langmuir probes in a collisionless, Maxwellian plasma at rest*. PhD thesis, University of Toronto Institute for Aerospace Studies, 1966.

[47] J A Lehane and P C Thonemann. An experimental study of helicon wave propagation in a gaseous plasma. *Proceedings of the Physical Society*, 85(2):301, 1965. doi: `10.1088/0370-1328/85/2/312`.

[48] Michael A Lieberman and Alan J Lichtenberg. *Principles of plasma discharges and materials processing*. John Wiley & Sons, 2005.

[49] Justin M Little and Edgar Choueiri. Influence of the applied magnetic field strength on flow collimation in magnetic nozzles. In *50th AIAA/ASME/SAE/ASEE Joint Propulsion Conference*, page 3912, 2014.

[50] Justin M Little and Edgar Y Choueiri. Critical condition for plasma confinement in the source of a magnetic nozzle flow. *IEEE Transactions on Plasma Science*, 43(1):277–286, 2015.

[51] Benjamin Longmier, Jared Squire, Mark Carter, Leonard Cassady, Tim Glover, Jacob Chancery, Chris Olsen, Andrew Ilin, Greg McCaskill, Franklin Chang-Díaz, et al. Ambipolar ion acceleration in the expanding magnetic nozzle of the vasimr vx-200i. In *45th AIAA/ASME/SAE/ASEE Joint Propulsion Conference & Exhibit*, page 5359, 2009.

[52] Benjamin W. Longmier, Jared P. Squire, Leonard D. Cassady, Maxwell G. Ballenger, Mark D. Carter, Chris Olsen, Andrew V. Ilin, Tim W. Glover, Greg E. McCaskill, Franklin R. Chang Dí, Edgar A. Bering, and Juan Del Valle. VASIMR® VX-200 performance measurements and helicon throttle tables using argon and krypton. In *32nd International Electric Propulsion Conference*, 2011.

[53] M Martinez-Sanchez, J Navarro-Cavallé, and E Ahedo. Electron cooling and finite potential drop in a magnetized plasma expansion. *Physics of Plasmas*, 22(5):053501, 2015.

[54] Stéphane Mazouffre. Electric propulsion for satellites and spacecraft: established technologies and novel approaches. *Plasma Sources Science and Technology*, 25(3):033002, 2016. URL `http://stacks.iop.org/0963-0252/25/i=3/a=033002`.

[55] Mario Merino and Eduardo Ahedo. Plasma detachment in a propulsive magnetic nozzle via ion demagnetization. *Plasma Sources Science and Technology*, 23(3):032001, 2014.

[56] Mario Merino and Eduardo Ahedo. Influence of electron and ion thermodynamics on the magnetic nozzle plasma expansion. *IEEE Transactions on Plasma Science*, 43(1), January 2015.

[57] Mario Merino and Eduardo Ahedo. Influence of electron and ion thermodynamics on the magnetic nozzle plasma expansion. *IEEE Transactions on Plasma Science*, 43(1):244–251, 2015.

[58] Mario Merino and Eduardo Ahedo. Towards thrust vector control with a 3d steerable magnetic nozzle. In *34th International Electric Propulsion Conference (Electric Rocket Propulsion Society, Fairview Park, OH, 2015)*, 2015.

[59] Mario Merino, Jaume Navarro, S Casado, E Ahedo, Victor Gómez, M Ruiz, E Bosch, and JG del Amo. Design and development of a 1 kw-class helicon antenna thruster. In *34th International Electric Propulsion Conference, IEPC-2015-297 (Electric Rocket Propulsion Society, Fairview Park, OH, 2015)*, 2015.

[60] Harold M Mott-Smith and Irving Langmuir. The theory of collectors in gaseous discharges. *Physical review*, 28(4):727, 1926.

[61] Jaume Navarro-Cavallé, Eduardo Ahedo, Mario Merino, Víctor Gómez, Mercedes Ruiz, and José Antonio Gonzalez del Amo. Helicon plasma thrusters: prototypes and advances on modelling. In *33^{rd} International Electric Propulsion Conference*, 2013.

[62] Christopher S Olsen, Maxwell G Ballenger, Mark D Carter, Franklin R Chang Diaz, Matthew Giambusso, Timothy W Glover, Andrew V Ilin, Jared P Squire, Benjamin W Longmier, Edgar A Bering, et al. Investigation of plasma detachment from a magnetic nozzle in the plume of the vx-200 magnetoplasma thruster. *IEEE Transactions on Plasma Science*, 43(1):252–268, 2015.

[63] Sabrina Pottinger, Vaios Lappas, Christine Charles, and Roderick Boswell. Performance characterization of a helicon double layer thruster using direct thrust measurements. *Journal of Physics D: Applied Physics*, 44(23), March 2011. doi: 10.1088/0022-3727/44/23/235201.

[64] Donald Rapp and William E Francis. Charge exchange between gaseous ions and atoms. *The Journal of Chemical Physics*, 37(11):2631–2645, 1962.

[65] Garrett Reed, William Hargus, and Mark Cappelli. Microwave interferometry (90 ghz) for hall thruster plume density characterization. In *41st AIAA/ASME/SAE/ASEE Joint Propulsion Conference & Exhibit*, page 4399, 2005.

[66] Bryan Reid and Alec Gallimore. Langmuir probe measurements in the discharge channel of a 6-kw hall thruster. In *44th AIAA/ASME/SAE/ASEE Joint Propulsion Conference & Exhibit*, page 4920, 2008.

[67] Bryan Michael Reid. *The influence of neutral flow rate in the operation of Hall thrusters*. PhD thesis, University of Michigan, 2009.

[68] SK Saha, S Chowdhury, MS Janaki, A Ghosh, AK Hui, and S Raychaudhuri. Plasma density accumulation on a conical surface for diffusion along a diverging magnetic field. *Physics of Plasmas*, 21(4):043502, 2014.

[69] JP Sheehan and N Hershkowitz. Emissive probes. *Plasma Sources Science and Technology*, 20 (6):063001, 2011.

[70] JP Sheehan, Yevgeny Raitses, Noah Hershkowitz, Igor D Kaganovich, and Nathaniel J Fisch. The use of electric probe techniques for electric potential measurements in plasma thrusters. In *32nd International Electric Propulsion Conference, IEPC-2011-174, (Wiesbaden, Germany)*, 2011.

[71] JP Sheehan, BW Longmier, EA Bering, CS Olsen, JP Squire, MG Ballenger, MD Carter, LD Cassady, FR Chang Díaz, TW Glover, et al. Temperature gradients due to adiabatic plasma expansion in a magnetic nozzle. *Plasma Sources Science and Technology*, 23(4):045014, 2014.

[72] JP Sheehan, Timothy A Collard, Frans H Ebersohn, and Benjamin W Longmier. Initial operation of the cubesat ambipolar thruster. In *34th International Electric Propulsion Conference, IEPC-2015-243, (Hyogo-Kobe, Japan)*, 2015.

[73] Nareg Sinenian. *Propulsion mechanisms in a helicon plasma thruster*. PhD thesis, Massachusetts Institute of Technology, 2008.

[74] Z Sternovsky, S Robertson, and M Lampe. The contribution of charge exchange ions to cylindrical langmuir probe current. *Physics of Plasmas*, 10(1):300–309, 2003.

[75] Zoltan Sternovsky, Scott Robertson, and Martin Lampe. Ion collection by cylindrical probes in weakly collisional plasmas: theory and experiment. *Journal of applied physics*, 94(3):1374–1381, 2003.

[76] Isaac D Sudit and Francis F Chen. Rf compensated probes for high-density discharges. *Plasma Sources Science and Technology*, 3(2):162, 1994.

[77] George P. Sutton and Oscar Bilarz. *Rocket Propulsion Elements*. John Wiley & Sons, 8th edition, 2010.

[78] Kazunori Takahashi, Christine Charles, Rod Boswell, Wes Cox, and Rikizo Hatakeyama. Transport of energetic electrons in a magnetically expanding helicon double layer plasma. *Applied Physics Letters*, 94(19):191503, 2009.

[79] Kazunori Takahashi, Christine Charles, Rod Boswell, and Akira Ando. Performance improvement of a permanent magnet helicon plasma thruster. *Journal of Physics D: Applied Physics*, 46(35):352001, 2013. URL `http://stacks.iop.org/0022-3727/46/i=35/a=352001`.

[80] Kazunori Takahashi, Christine Charles, and Rod W Boswell. Approaching the theoretical limit of diamagnetic-induced momentum in a rapidly diverging magnetic nozzle. *Physical review letters*, 110(19):195003, 2013.

[81] Kazunori Takahashi, Atsushi Komuro, and Akira Ando. Measurement of plasma momentum exerted on target by a small helicon plasma thruster and comparison with direct thrust measurement. *Review of Scientific Instruments*, 86(2):023505, 2015.

[82] Kazunori Takahashi, Aiki Chiba, Atsushi Komuro, and Akira Ando. Experimental identification of an azimuthal current in a magnetic nozzle of a radiofrequency plasma thruster. *Plasma Sources Science and Technology*, 25(5):055011, 2016.

[83] E. Y. Wang, N. Hershkowitz, T. Intrator, and C.ee Forest. Techniques for using emitting probes for potential measurement in rf plasmas. *Review of Scientific Instruments*, 57(10):2425–2431, 1986. doi: `10.1063/1.1139088`.

[84] Timothy Ziemba, John Carscadden, John Slough, James Prager, and Robert Winglee. High power helicon thruster. In *41^{st} AIAA Joint Propulsion Conference*, 2005.

[85] Maurice Joseph Zucrow and Joe D Hoffman. *Gas Dynamics*, volume 1. New York: Wiley, 1976.